Novel algorithms for strongly correlated quantum systems in and out of equilibrium

Alice Moutenet

INSTITUT POLYTECHNIQUE DE PARIS

NNT : 2020IPPAX026

Thèse de doctorat

Nouveaux algorithmes pour l'étude des propriétés d'équilibre et hors d'équilibre des systèmes quantiques fortement corrélés

Thèse de doctorat de l'Institut Polytechnique de Paris
préparée à l'École polytechnique

École doctorale n°626 de l'Institut Polytechnique de Paris (ED IP Paris)
Spécialité de doctorat : Physique

Thèse présentée et soutenue à Paris, le 3 juillet 2020, par

ALICE MOUTENET

Composition du Jury :

Sylvain Capponi Professeur, Université Paul Sabatier de Toulouse	Président Rapporteur
Philipp Werner Professeur, Université de Fribourg	Rapporteur
Laura Messio Maître de conférences, Sorbonne Universités	Examinatrice
Marco Schiró Chargé de recherche, CEA-Saclay	Examinateur
Antoine Georges Professeur, Collège de France	Directeur de thèse
Michel Ferrero Chargé de recherche, École polytechnique	Co-directeur de thèse

Acknowledgments

First and foremost, I would like to thank my PhD advisors Antoine Georges and Michel Ferrero for always believing in me since my first research internship as a Master student in 2015. The past three years were extremely rich as I pursued several projects using many different techniques. You were always here to guide me while giving me the freedom to develop my own ideas. I am also deeply grateful for the opportunity to follow Antoine to his new lab, therefore spending a full year at the Flatiron Institute in New York.

Antoine, thank you for always managing to find time in your extremely busy schedule to discuss ongoing projects. These years under your supervision have been an amazing opportunity to learn from your impressive knowledge about physics and methods.

Michel, thank you for always seeing the glass half full under any circumstance, debugging my codes when I was desperate, and answering all of my silly questions (all of that with a coffee, of course). After years of hard work you also managed to make me use a qwerty keyboard, Vim, and cycle to work!

Our team in Collège de France has an amazing spirit and I was glad to be part of it. Giacomo, Thomas, Orazio, Alfred, it was great to share an office with you. Together with Wei, Minjae, Hanhim, Pascal, Fedor, Renaud, Alaska, Leonid, I will miss our coffee breaks that extended in long physics discussions, and of course the wine we shared to celebrate new publications! Thomas, Sophie, Priyanka, you were almost gone when I arrived but I enjoyed very much the time spent with you. I would also like to thank Françoise and Carmen who make our administrative life so easy.

It was also always a pleasure to spend time at the Centre de Physique Théorique in École polytechnique, together with the teams of Silke Biermann, Laurent Sanchez-Palencia and Karyn Le Hur.

I am grateful to Olivier Parcollet, who acted as a third supervisor during my time in New York. Thank you for getting me interested in out-of-equilibrium physics and algorithmic problems, and for helping me settling in this incredible city.

Because you made my stay at the Flatiron Institute unforgettable, thank you Paula and Mary-Kate. Diane, I found a true friend in you and dearly miss our lunches together as well as our long discussions in the corridor. You all could always bring a smile to my face.

Teresa and Alex, spending a year with you was so much more than just sharing an apartment. Thank you for the evenings on the roof, the skiing, the fishing, the laughing... I will never forget you!

Merci Papa, Maman, pour m'avoir toujours soutenue dans mes études et dans mes choix personnels. Merci surtout à toi, Papa, de m'avoir donné le goût des sciences qui m'a permis d'arriver là où je suis aujourd'hui. Je me souviens, enfant, t'avoir un jour demandé en quoi consistait un doctorat, ce à quoi tu as répondu qu'il s'agissait "d'apporter une contribution nouvelle à la science". J'espère te convaincre à travers ces pages que j'ai atteint ce but.

Merci Martin pour toutes ces années passées ensemble. Merci d'avoir supporté mes crises existentielles sur la thèse et mon avenir alors que l'on était pendus à un relais en falaise. Tu auras toujours été une oreille attentive et un soutien sans faille, même confiné dans 40m^2 avec une doctorante en fin de rédaction !

Merci également à tous mes amis, sans qui la vie serait bien triste !

Contents

Abstract

Strongly correlated quantum systems exhibit striking physical properties that cannot be described by standard one-body theories, such as band theory for instance. To understand the origin of these phenomena, all particles have to be treated together with their interactions: one talks about the many-body problem. If modern analytical methods give a qualitative understanding of the mechanisms at work in these materials, numerical approaches can provide quantitative and reliable results. This Thesis is about developing novel algorithms to study strongly correlated materials, both in and out of equilibrium.

First, we focus on the equilibrium properties of the layered perovskite Sr_2IrO_4, a compound isostructural to the superconducting cuprate La_2CuO_4. Using a continuous-time quantum Monte Carlo algorithm as an impurity solver in a 2-site dynamical mean-field theory setup, we are able to precisely compare photoemission results to experimental data. Moreover, we prove the existence of a pseudogap and describe the electronic structure of this material upon doping.

Then, in order to address the thermodynamic limit of lattice problems, we develop extensions of determinant Monte Carlo algorithms to compute dynamical quantities such as the self-energy. We show how a factorial number of diagrams can be regrouped in a sum of determinants, hence drastically reducing the fermionic sign problem. By comparing results for the two-dimensional Hubbard model with those obtained from diagrammatic Monte Carlo, we show that we can reach higher perturbation orders and greater accuracy for the same computational effort.

In the second part, we turn to the description of nonequilibrium phenomena in correlated systems, where the emergence of even richer physics can be expected. Such materials are very difficult to model because the time evolution has to be solved on top of the quantum many-body problem. We start by revisiting the real-time diagrammatic Monte Carlo recent advances in a new basis where all vacuum diagrams directly vanish. In an importance sampling procedure, this implies that only interaction times in the vicinity of the measurement time contribute, and such an algorithm can directly address the long-time limit needed in the study of steady states in out-of-equilibrium systems. We also present a detailed discussion on the origin and limitations of the fermionic sign problem in real-time algorithms.

Finally, we study the insulator-to-metal transition induced by an electric field in Ca_2RuO_4, which coexists with a structural transition. As numerically exact methods are still too primitive to capture the complex physics of this multi-orbital material, we develop a steady-state quantum impurity solver based on the Non-Crossing Approximation, that we couple with a dynamical mean-field theory setup. This allows us to compute the current as a function of crystal-field splitting in this material, and we present encouraging preliminary results in and out of equilibrium.

Résumé

Les systèmes d'électrons fortement corrélés sont le siège de phénomènes physiques fascinants qui ne peuvent être expliqués par une théorie des bandes. Afin de comprendre ces propriétés, il faut traiter l'ensemble des particules et leurs interactions : on parle du problème à N corps. Les méthodes analytiques modernes permettent d'obtenir une compréhension qualitative des mécanismes à l'œuvre dans ces matériaux, mais il est nécessaire d'employer des méthodes numériques pour obtenir des résultats fiables et quantitatifs. Cette Thèse porte sur le développement de nouveaux algorithmes pour l'étude des propriétés d'équilibre et hors d'équilibre des systèmes d'électrons fortement corrélés.

Nous nous intéressons tout d'abord aux propriétés d'équilibre de la pérovskite Sr_2IrO_4, un matériau structurellement équivalent au cuprate supraconducteur La_2CuO_4. Nous utilisons un algorithme de Monte Carlo en temps continu comme solveur d'impureté dans un modèle de champ moyen dynamique à deux sites, ce qui nous permet de comparer précisément nos résultats théoriques à des expériences de photoémission. Nous mettons également en évidence l'existence d'un pseudogap et décrivons la structure électronique de ce matériau en fonction du dopage.

Nous développons ensuite des extensions aux algorithmes de Monte Carlo déterminantaux pour l'étude de quantités dynamiques comme l'énergie propre. Nous montrons qu'il est possible de regrouper un nombre factoriel de diagrammes en une somme de déterminants, réduisant ainsi fortement le problème de signe fermionique. En comparant nos résultats pour le modèle de Hubbard bidimensionnel à ceux obtenus par le Monte Carlo diagrammatique, nous montrons que le même temps de calcul permet d'atteindre des ordres de perturbation plus élevés et une meilleure précision.

Dans un deuxième temps, nous décrivons les systèmes fortement corrélés hors d'équilibre, où nous nous attendons à l'émergence d'une physique encore plus riche. Il est très difficile de modéliser ces matériaux car l'évolution temporelle doit être traitée en plus du problème à N corps quantique. Nous commençons par revisiter le Monte Carlo diagrammatique en temps réel dans une nouvelle base qui permet aux diagrammes du vide de s'annuler directement. Au cours d'un échantillonnage statistique, cette propriété implique que seuls contribuent les temps en interaction proches du temps de mesure. Ceci permet d'atteindre la limite de long temps nécessaire à l'étude des états stationnaires des systèmes hors d'équilibre. Nous discutons également en détail l'origine et les limitations du problème de signe fermionique dans les algorithmes en temps réel.

Pour terminer, nous étudions la transition métal-isolant induite par un champ électrique de Ca_2RuO_4, qui coexiste avec une transition structurelle. Les méthodes numériques exactes étant encore trop primitives pour rendre compte d'une physique aussi complexe que celle de ce matériau, nous développons un solveur d'impureté quantique stationnaire basé sur "l'approximation sans croisement", que nous couplons à une théorie du champ moyen dynamique. Ceci nous permet de calculer le courant en fonction du champ crystallin dans ce matériau, et nous présentons d'encourageants résultats préliminaires à l'équilibre ainsi que hors d'équilibre.

Notations

ω_n	Matsubara frequency
τ	Imaginary time
t	Real time
ω	Real frequency
$\mathcal{H}$	Hamiltonian
$\mathcal{S}$	Action
Z	Partition function
G	Interacting Green's function
g	Noninteracting Green's function
Σ	Self-energy
Δ	Hybridization function
$\hat{}$	Matrix form
U	Coulomb repulsion between electrons
γ	Hopping amplitude
σ	Spin of an electron
β	Inverse temperature
$\mathfrak{c}$	Monte Carlo configuration
DMFT	Dynamical Mean-Field Theory
MC	Monte Carlo
CT-QMC	Continuous-Time Quantum Monte Carlo
DiagMC	Diagrammatic Monte Carlo
NCA	Non-Crossing Approximation

Part I

Context and Overview

Chapter 1

General Introduction

Condensed matter physics aims at studying organized forms of matter and predicting the properties of materials based on their microscopic structure. As theoreticians, our ultimate goal would be to start from the positions of atoms and electrons in order to understand why a given compound might conduct electricity, reflect light, or − in the case of superconductors − levitate above a magnet.

We typically deal with $10^{22} - 10^{23}$ particles: A sand grain indeed contains a number of atoms comparable to the number of stars within the observable universe! Macroscopic phenomena therefore emerge from the collective structure and motion of all these building blocks. As an example, let us consider diamond and graphite (from which pencils are made). Both are only made of carbon atoms, one of the simplest elements in nature. Still, because they crystallize in very different structures, one compound is transparent, extremely hard and insulating, while the other one is black, brittle and conducts electricity. Recently, even more exotic materials have been engineered solely from carbon atoms, among which fullerenes, carbon nanotubes, and graphene. One can easily be convinced that this whole bestiary cannot be predicted from the properties of a single atom. As P.W. Anderson beautifully summarized in an eponymous article in 1972: "More is different." [8]

In many systems, particles can however be described as if they were *independent*. For example, it is often a good approximation to assume that a given electron does not "see" individually all other electrons, but rather that its motion only depends on an effective medium constructed from the general structure of the material and the overall presence of other particles. This way of describing the system, called band theory, works remarkably well for a wide range of materials, and allows one to understand properties of simple metals as well as semiconductors.

Strongly correlated materials cannot be described by band theory, usually because *interactions* between electrons become important. This is for instance the case for Mott insulators, in which the electrons remain localized because the cost in Coulomb energy is too high for them to move. If the reader ever had to ride the subway in Paris or New York at rush hour, he or she might have been unable to enter the train. However, there technically *is* some space left if you were to pile commuters on top of one another! But "human interaction", of course, prevents you from doing so. As soon as electronic correlations come into play, we have to consider the full system where all particles influence each other: this is the quantum many-body problem.

The full Hamiltonian describing a piece of matter containing N_a atoms and N_e electrons is actually very easy to write

$$\begin{aligned}\mathcal{H} = &\sum_{i=1}^{N_a} \frac{\mathbf{P}_i^2}{2M_i} + \sum_{i=1}^{N_e} \frac{\mathbf{p}_i^2}{2m_e} + \frac{1}{2} \sum_{1\leq i\neq j\leq N_e} \frac{e^2}{4\pi\epsilon_0 |\mathbf{r}_i - \mathbf{r}_j|} \\ &- \sum_{i=1}^{N_a}\sum_{j=1}^{N_e} \frac{Z_i e^2}{4\pi\epsilon_0 |\mathbf{R}_i - \mathbf{r}_j|} + \frac{1}{2} \sum_{1\leq i\neq j\leq N_a} \frac{Z_i^2 e^2}{4\pi\epsilon_0 |\mathbf{R}_i - \mathbf{R}_j|},\end{aligned} \tag{1.1}$$

where an electron, with mass m_e, is located at $\mathbf{r}_i$ and has a momentum $\mathbf{p}_i$, while an atom, with a number of protons Z_i and a mass M_i, is located at $\mathbf{R}_i$ and has momentum $\mathbf{P}_i$. ϵ_0 is the dielectric constant.

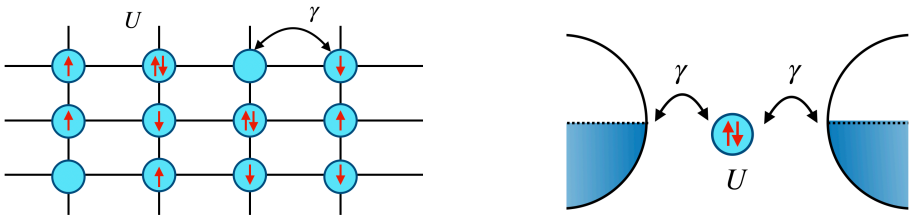

(a) Hubbard model

(b) Quantum dot model

Figure 1.1 – Minimal models used to describe strongly correlated materials.

The wavefunction ψ of the system is then obtained through Schrödinger equation

$$i\hbar\frac{\partial\psi}{\partial t} = \mathcal{H}\psi. \tag{1.2}$$

As compact as this expression looks like, ψ actually has... 10^{23} variables, and all the atoms of the universe would not provide enough matter to store it on hard drives! Without additional symmetries, it is in practice impossible to directly solve this model when N_a and N_e exceed 16. [1] This paradigm led Paul Dirac to state in 1929: [43]

> The underlying physical laws necessary for the mathematical theory of a large part of physics and the whole of chemistry are thus completely known, and the difficulty is only that the exact application of these laws leads to equations much too complicated to be soluble. It therefore becomes desirable that approximate practical methods of applying quantum mechanics should be developed, which can lead to an explanation of the main features of complex atomic systems without too much computation.

This is the path we choose in this Thesis: We start from minimal models that contain the key ingredients to capture the physics we are interested in. As these remain impossible to solve analytically, we then develop numerical methods to study their properties. Let us now give some examples of exciting physical phenomena that would not exist without strong correlations and introduce the most common models we use to describe them.

1.1 Interesting properties of strongly correlated materials and toy models

Materials where strong correlations matter are often complex: they either imply sophisticated layered structures, heavy atoms, or multiple orbitals. However, as theoreticians, we like to design models that seem to oversimplify the problem at hand, but actually minimally include key ingredients to see the physics emerge: this is the infamous *spherical cow*. In the case of strongly correlated materials, two competing energy scales are at the heart of their rich physics: the kinetic energy that comes from the motion of the electrons in the material, and the potential energy coming from the Coulomb interaction between electrons.

Let us see how they give rise to some of the most intriguing phenomena of condensed matter physics.

1.1.1 High-temperature superconductivity

Superconductivity was first discovered in 1911 by Kamerlingh Onnes, who realized that mercury's resistivity drops to zero when cooled down below 4.2K. Usually, current in a material comes with energy losses due to particles colliding (this is the reason why laptops heat up for instance). In superconductors, electrons form a state where they flow smoothly without any collision: the current they create then lasts forever, under the condition that the system is kept at low enough temperature. Materials such as mercury are known as "conventional superconductors", and their critical temperatures are low, reaching at most 10K for simple metals. A microscopic explanation of this phenomenon was found by Bardeen, Cooper, and

1. See Chapter 2 for more details.

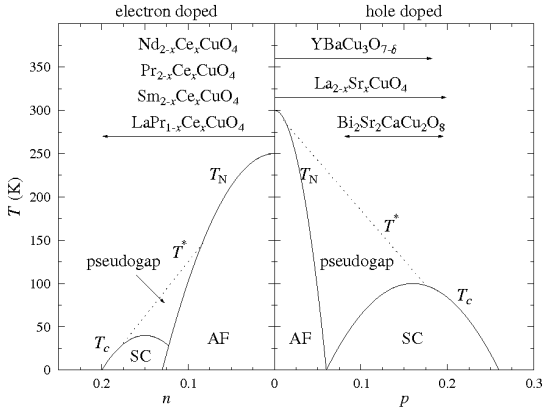

(a) Phase diagram of common superconductors, as as function of electron and hole doping. [182]

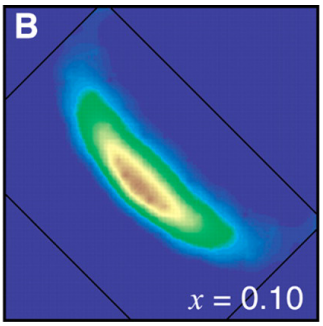

(b) Spectral intensity of $Ca_{2-x}Na_xCuO_2Cl_2$, $x = 0.10$, in the top right corner of the Brillouin zone. [149]

Figure 1.2 – Some properties of high-temperature superconductors.

Schrieffer who were awarded the Nobel prize in 1972.

In the late 1980s, a new type of superconductivity was discovered in layered ceramics, cuprates, composed of copper-oxygen planes separated by bigger atoms. Their critical temperature was found to reach up to 150K, hence their name of high-temperature, or unconventional, superconductors. The low energy band structure of these materials is characterized by a half-filled energy band, however cuprates are Mott insulators with a sizable energy gap of 2 eV (not a natural candidate when looking for a new superconductor!) [121].

The *Hubbard model*, depicted in Fig. 1.1a, is widely used to describe the two-dimensional properties of cuprates. It describes a square lattice where electrons can hop between different sites with amplitude γ, and experience the Coulomb repulsion U when being on the same physical site. Its Hamiltonian writes

$$\mathcal{H} = -\gamma \sum_{ij,\sigma} c^\dagger_{i\sigma} c_{j\sigma} + U \sum_i n_{i\uparrow} n_{i\downarrow} \tag{1.3}$$

where $c^\dagger_{i\sigma}$ (resp. $c_{i\sigma}$) is the operator creating (resp. annihilating) an electron with spin σ on site i, and $n_{i\sigma} = c^\dagger_{i\sigma} c_{i\sigma}$ is the density operator.

A very rich and complex phase diagram, with a superconducting dome, appears when doping either with holes or electrons, as is sketched in Fig. 1.2a. Apart from superconductivity, another salient phenomenon in cuprates is the appearance of a 'pseudogap' in the underdoped part of the phase diagram, whose origin is still very debated today. It was first observed in 1989 as a sharp decrease in the Nuclear Magnetic Resonance (NMR) response [3], but it is also characterized by a suppression of coherent quasiparticles in the antinodal region of the Brillouin zone. This yields a momentum-differentiation of the spectral intensity and so-called Fermi arcs that were observed both experimentally, see Fig. 1.2b, and theoretically [149, 48].

1.1.2 Hund's metals

Rich physics also emerges when studying multi-orbital materials. In these systems, the energy scale associated with the intra-atomic exchange, the Hund's coupling J, also has to be considered. J influences the electronic correlations as it lowers the effective Coulomb repulsion when two electrons are on different orbitals with parallel spins as opposed to when they are on the same orbital.

The importance of Hund's coupling was pointed out early on for insulators [162, 163]. More recently, its relevance to the physics of multi-orbital correlated metals was emphasized, starting with two pioneering papers [172, 70]. It quickly became apparent that Hund's coupling plays a crucial role in a broad family of materials, including transition-metal oxides of the $4d$ series such as ruthenates (especially Sr_2RuO_4 [111]), as well as iron pnictides or chalcogenides (for a review, see *e.g.* Ref. [54]). The term 'Hund's metals',

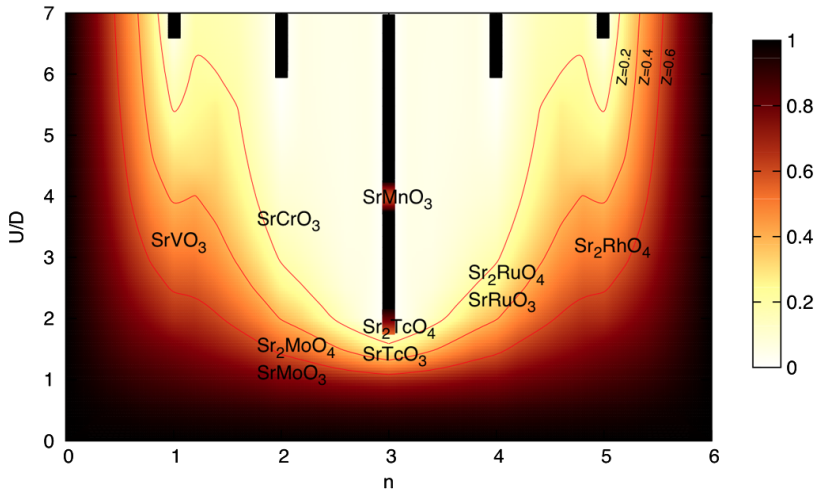

Figure 1.3 – Colour map of the degree of correlation (as measured by the quasiparticle weight z) for a Hubbard-Kanamori model with 3 orbitals. U/D is the Coulomb interaction normalized to the half-bandwidth, and n is the number of electrons per site. $J = 0.15U$. Black bars are the Mott insulating regions. [42]

coined in Ref. [186], is generically used to refer to these strongly correlated but itinerant systems. Several of these materials also display superconductivity – with distinctive properties in comparison to single band cuprates given their multi-band nature.

The atomic Hamiltonian describing the t_{2g} orbitals of these systems is called the *Kanamori Hamiltonian* and writes [78, 58, 155]

$$\begin{aligned}\mathcal{H} = &\sum_{a\sigma} \epsilon_a n_{a\sigma} + J \sum_{a\neq b} \left(d^\dagger_{a\uparrow} d_{b\uparrow} d^\dagger_{b\downarrow} d_{a\downarrow} + d^\dagger_{a\uparrow} d_{b\uparrow} d^\dagger_{a\downarrow} d_{b\downarrow} \right) \\ &+ U \sum_a n_{a\uparrow} n_{a\downarrow} + (U - 2J) \sum_{a\neq b} n_{a\uparrow} n_{b\uparrow} + (U - 3J) \sum_{a<b,\sigma} n_{a\sigma} n_{b\sigma}.\end{aligned} \tag{1.4}$$

Here $a = xy, xz, yz$ denotes one of the t_{2g} orbitals, $d^\dagger_{a\sigma}$ (resp. $d_{a\sigma}$) creates (resp. destroys) an electron on orbital a with spin σ, and $n_{a\sigma} = d^\dagger_{a\sigma} d_{a\sigma}$ is the number operator. ϵ_a is the energy level of orbital a, U the Coulomb interaction and J the Hund's coupling. When a hopping term is introduced on a lattice composed of different sites described by the above model, one talks about the *Hubbard-Kanamori* Hamiltonian.

Recent theoretical studies show that the Hund's coupling plays a crucial role in multi-orbital metals with moderate Coulomb interaction U. The Hund's coupling has been characterized as being '*Janus faced*', since it is responsible for two competing effects. It indeed drives the system away from the Mott transition, but at the same time it makes the system more correlated by decreasing the quasiparticle coherent scale [42, 54]. This is summarized in Fig. 1.3 for a Hubbard-Kanamori model with 3 orbitals. The 'degree of correlation' [2] is studied as a function of U and of the number of electrons n in the orbitals. Light yellow denotes a strongly correlated material while darker colors are the sign of a good metal with relatively few interactions. The value of the Hund's coupling is set to $J = 0.15U$ and black bars denote Mott insulating regimes. Specific materials are schematically placed on the diagram.

1.1.3 Quantum dots

Up to now, we have presented physical phenomena occurring in lattice systems, where many strongly correlated sites are connected together. Quantum dots, on the other hand, are made of a single atom encapsulated between large noninteracting reservoirs, as depicted in Fig. 1.1b. Electrons can hop between the impurity and the leads, but only experience Coulomb repulsion on the impurity. The first experimental realization of such a system was obtained at the interface of GaAs/AlGaAs heterostructures [40, 56, 57, 145].

2. As measured by the quasiparticle weight z, see Section 2.1.3 for more details.

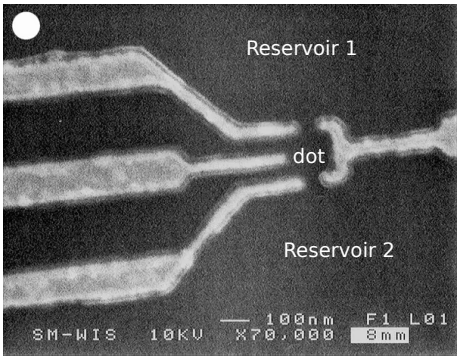

Figure 1.4 – Top view of a quantum dot (middle) created at the interface between two reservoirs (top and bottom). [57]

A top view of this setup in provided in Fig. 1.4, where we see the dot (middle part) connected by tunnel junctions to the reservoirs (top and bottom).

In the case of a left (L) and a right (R) lead, and the impurity being a single-energy level ϵ, the Hamiltonian of a quantum dot writes

$$\mathcal{H} = \epsilon \sum_{\sigma} d_{\sigma}^{\dagger} d_{\sigma} + U n_{d\uparrow} n_{d\downarrow} - \sum_{\substack{\mathbf{k}\sigma \\ \alpha=L,R}} \gamma_{\mathbf{k}} \left(d_{\sigma}^{\dagger} c_{\alpha\mathbf{k}\sigma} + \text{h.c.} \right) + \sum_{\substack{\mathbf{k}\sigma \\ \alpha=L,R}} \epsilon_{\mathbf{k}\alpha} c_{\alpha\mathbf{k}\sigma}^{\dagger} c_{\alpha\mathbf{k}\sigma} \tag{1.5}$$

where $d_{\sigma}^{\dagger}$ (resp. d_{σ}) is the operator creating (resp. annihilating) an electron with spin σ on the impurity, and $n_{d\sigma} = d_{\sigma}^{\dagger} d_{\sigma}$ is the density operator. $c_{\alpha\mathbf{k}\sigma}^{\dagger}$ (resp. $c_{\alpha\mathbf{k}\sigma}$) is the operator creating (resp. annihilating) an electron with spin σ in the α lead with a momentum $\mathbf{k}$. The $\epsilon_{\mathbf{k}\alpha}$ describe the energy spectra of the leads, $\gamma_{\mathbf{k}}$ is a hopping term between the impurity and the leads, and U is the Coulomb repulsion. Note that this model is easily driven out-of-equilibrium by changing the filling of the two leads. When only one lead is present, it is called the *Anderson impurity model* and was originally used to describe magnetic impurities in materials [7]. It is nowadays one of the basic blocks of Dynamical Mean-Field Theory, as we will discuss in the next Chapter.

One of the most studied phenomena in quantum dots is the Kondo effect [40, 56, 57, 145]. The local magnetic moment of the impurity antiferromagnetically couples with the bath electrons, resulting in the formation of a spin singlet between the atom and the bath. At low enough temperature, the impurity moment is screened and the scattering rate of the bath electrons increases: This results in an enhancement of transport properties. In the presence of strong correlations, the current can however be easily suppressed through Coulomb blockade [1]. Understanding the interplay between electronic correlations and the Kondo effect is thus of great interest to build new nanoelectronic devices.

Quantum dots have also been considered as possible candidates for the construction of quantum qubits [97, 127].

1.1.4 $U = 0$ and $\gamma = 0$ limits: towards perturbation expansion

We have seen that, in the study of strongly correlated systems, two parameters matter and actually compete with each other:

— the hoppping term $\gamma > 0$, that allows electrons to move in the material, [3]

— the Coulomb repulsion $U > 0$ between electrons.

Setting either the Coulomb repulsion or the hopping amplitude to zero is interesting, as both these limits are completely understood from a theoretical point of view. If $U = 0$, correlations vanish and electrons freely flow in the material. This problem can be solved using band theory and electrons behave as plane waves. If $\gamma = 0$, atoms become independent and electrons are then strongly localized. It is interesting

3. Note that the hopping term is usually denoted t but, as we will consider out-of-equilibrium physics, we keep this variable to denote times.

to note that the wave-particle duality of electrons, one of the key principles of quantum mechanics, is embodied in these two limits.

The richness of the physics observed in strongly correlated materials comes from values of U and γ that are typically comparable, so that we cannot easily discard one of the two. However, these two limits pave the way for the methods we develop in this Thesis. Among the many theoretical approaches to the quantum many-body problem, we choose to focus on perturbation expansions, either in U or γ,[4] therefore taking advantages of a well-understood starting point. Note that these approaches are not truncated explicitly at a given order, such as second-order perturbation theory for instance, as we express physical quantities as infinite series that we then resum.

1.2 Overview of the Thesis

Chapter 2 aims at giving a broad overview of the formalism and techniques used to study strongly correlated materials. We start with the imaginary-time formalism for equilibrium physics, introducing Green's functions, spectral functions, self-energies and hybridization functions. We then review modern computational methods for the many-body problem, before presenting the Dynamical Mean-Field Theory (DMFT) approximation.

This manuscript is then divided in four independent parts that correspond to four different physics project that were studied during the Thesis.

First, we focus on the equilibrium properties of the layered perovskite Sr_2IrO_4, a compound isostructural to the superconducting cuprate La_2CuO_4. In Chapter 3, we present recent angular resolved photoemission spectra that reveal a strong momentum differentiation in the Brillouin zone. Then, we construct a minimal model of the low-energy electronic structure of doped Sr_2IrO_4. Correlations are included using a 2-site dynamical mean-field theory setup where an hybridization-based quantum Monte Carlo algorithm is used as impurity solver.

In Chapter 4, the effects of doping on the electronic structure of this material are studied. A rapid collapse of the Mott gap is found, and we prove the existence of a pseudogap which causes the momentum differentiation of the spectral intensity. There is an overall excellent qualitative agreement between our results and experimental data.

In a second part, we address new developments in determinant Monte Carlo algorithms for fermionic systems. In Chapter 5, we start by a general introduction to continuous-time quantum Monte Carlo algorithms. These are based on an expansion of the partition function Z either in the Coulomb repulsion (CT-INT) or the hybridization function (CT-HYB), and they aim at sampling the quantity of interest (Green's function, density, self-energy, ...) at different perturbation orders using contributions to Z as weights in a Monte Carlo sampling.

These methods being mainly limited to quantum impurity problems, we introduce in Chapter 6 an alternative and complementary technique that can directly be used on the lattice. Diagrammatic Monte Carlo algorithms are based on an expansion in U and they compute physical quantities such as the Green's function by sampling diagrammatic contributions. Recently, the Connected Determinant (CDet) algorithm has been shown to greatly improve the fermionic sign problem when computing correlators by regrouping topologies of diagrams in a sum of 3^n determinants at order n.

When studying strongly correlated systems, one however needs to go beyond the study of Green's functions and compute dynamical quantities such as the self-energy. In Chapter 7, we therefore present an extension of the CDet algorithm that allows to sum contributions from one-particle-irreducible diagrams in the Monte Carlo weight using determinants. By comparing results for the two-dimensional Hubbard model with those obtained from state-of-the-art Diagrammatic Monte Carlo, we show that we can reach higher perturbation orders and greater accuracy for the same computational effort.

We then move to the description of nonequilibrium phenomena in correlated systems. Such materials are very difficult to model because the time evolution has to be solved on top of the quantum many-body problem. In Chapter 8, we start by introducing the Keldysh formalism to compute observables in real time. Then, we present an early attempt of real-time quantum Monte Carlo algorithm which is a direct extension

4. Technically, it will be an expansion in the hybridization function Δ and not in the hopping γ, see later for more details.

of CT-INT on the Keldysh contour. It suffers from a dynamical sign problem that prevents the technique from reaching long times. A route explored to cure this problem is the real-time diagrammatic quantum Monte Carlo algorithm that directly samples contributions to the density using an explicit summation of 2^n determinants at order n in the Monte Carlo weight. This exponential sum has been shown to cancel vacuum diagrams, greatly reduce the sign problem, and allow the computation of observables in the infinite-time steady-state limit.

This exponential scaling of the computation of the Monte Carlo weight limits our capability to compute high orders with great precision. In Chapter 9, we show that we can obtain the cancellation of diagrams and the long-time clusterization property without summing an exponential number of terms. Using the Larkin-Ovchinnikov (LO) basis, we rewrite the integrand as a sum of 4^n determinants, but show that diagrammatic rules in this basis are such that every diagram has the clusterization property. In other words, the elimination of vacuum diagrams is directly achieved in the diagrammatics without the need of an exponential sum. When implementing this property in a Monte Carlo algorithm, we face a huge sign problem originating from massive cancellations between LO configurations that are only performed stochastically.

In Chapter 10, we present a detailed discussion on the origin and limitations of the fermionic sign problem in this algorithm. More specifically, we are interested in understanding whether there is a way of regrouping contributions in the LO basis that would optimize it and thus reduce the overall error bar. We start by exhibiting grouping patterns found heuristically before presenting a machine learning approach based on deep Haar scattering networks. We are able to greatly reduce the obtained variance, but not enough to compete with the original real-time diagrammatic quantum Monte Carlo algorithm.

The last part of the Thesis focuses on the study of the insulator-to-metal transition driven by an electric-field in Ca_2RuO_4. Its transition indeed appears to be driven at room temperature using a dry-battery level voltage, resulting in a suprisingly low threshold field $E_{\text{th}} \sim 40$ V/cm. The multiorbital nature of this material and the need to reach the steady-state limit prevent us from using the numerically exact diagrammatic methods that are still too primitive. It is therefore desirable to use a more economical way to solve the quantum impurity model that still captures the essential physics of the system. In Chapter 11, we present the Non-Crossing Approximation (NCA), a simple approximation in the hybridization function that analytically sums a subset of diagrams without crossing hybridization lines. We first present the equilibrium version of NCA to introduce the formalism, before exposing the out-of-equilibrium equations on the full Baym-Kadanoff triple contour.

As we are only interested in the steady-state regime of Ca_2RuO_4 driven out-of-equilibrium, we would like to avoid solving the full transient regime. In Chapter 12, we first present an out-of-equilibrium version of the NCA approximation working on the Keldysh contour. We then derive the infinite-time limit of the equations in order to obtain a solver directly tackling the non-equilibrium steady-state limit. These algorithms are benchmarked by computing the current flowing through a quantum dot.

In Chapter 13, we start by presenting the recent experiments where a switching from the insulating state to a metallic one is observed when applying an electric field. We reexpress the effects of the static electric field as a linear voltage drop in the material, which allows us to construct a tight-binding model for the material in the steady-state regime. Correlations are introduced using the dynamical mean-field approximation, and we use the long-time limit NCA impurity solver developed in Chapter 12. Preliminary results are then presented both for the equilibrium and out-of-equilibrium material.

Chapter 2

Overview of many-body techniques for strongly correlated systems

This Chapter aims at giving a broad overview of the formalism and techniques used to study strongly correlated materials. We start by reviewing the imaginary-time formalism for equilibrium physics, introducing Green's functions, spectral functions, self-energies and hybridization functions. Note that the introduction to the Keldysh formalism to compute observables in real-time is postponed to Chapter 8. We then review modern computational methods for the many-body problem, before presenting the Dynamical Mean-Field Theory (DMFT) approximation.

2.1 Basic equilibrium formalism

In this Section, we introduce the theoretical objects and notations used throughout this Thesis. For a complete introduction to the many-body formalism, see for instance Ref. [25].

In the following, we consider a system described by a Hamiltonian $\mathcal{H}$ with inverse temperature β. $c^\dagger_{\mathbf{k}a}$ (resp. $c_{\mathbf{k}a}$) creates (resp. annihilates) a fermion with momentum $\mathbf{k}$, a being a composite index denoting other possible degrees of freedom: spin, orbital, ...

2.1.1 Green's function

Introducing the Heisenberg representation $c_{\mathbf{k}a}(\tau) = e^{\tau\mathcal{H}} c_{\mathbf{k}a} e^{-\tau\mathcal{H}}$, the imaginary-time Green's function, also called Matsubara Green's function, is defined for every momentum $\mathbf{k}$ in the Brillouin zone, $\tau \in [0, \beta]$, as

$$G_{ab}(\mathbf{k}, \tau) = -\left\langle T_\tau c_{\mathbf{k}a}(\tau) c^\dagger_{\mathbf{k}b}(0) \right\rangle, \tag{2.1}$$

where the time-ordering operator T_τ is

$$T_\tau c_{\mathbf{k}a}(\tau) c^\dagger_{\mathbf{k}b}(\tau') = \theta(\tau - \tau') c_{\mathbf{k}a}(\tau) c^\dagger_{\mathbf{k}b}(\tau') - \theta(\tau' - \tau) c^\dagger_{\mathbf{k}a}(\tau') c_{\mathbf{k}b}(\tau). \tag{2.2}$$

In the following, we use the $\hat{}$ notation to denote a matrix form. The Green's function is extended to all real numbers as being antiperiodic of period β

$$\hat{G}(\mathbf{k}, \tau + \beta) = -\hat{G}(\mathbf{k}, \tau). \tag{2.3}$$

The Fourier transform of the Matsubara Green's function is

$$\hat{G}(\mathbf{k}, i\omega_n) = \int_0^\beta e^{i\omega_n \tau} \hat{G}(\mathbf{k}, \tau) \mathrm{d}\tau, \tag{2.4}$$

where the discrete frequency variables ω_n are called Matsubara frequencies and satisfy

$$\omega_n = \frac{(2n+1)\pi}{\beta}, n \in \mathbf{Z}. \tag{2.5}$$

The Green's function for spinless fermions described by a band dispersion $\epsilon_{\mathbf{k}}$ is for instance

$$G(\mathbf{k}, i\omega_n) = \frac{1}{i\omega_n + \mu - \epsilon_{\mathbf{k}}}, \tag{2.6}$$

where μ is the chemical potential of the system.

The real-frequency Green's function [1] can be obtained from its Matsubara counterpart using analytical continuation

$$\hat{G}(\omega) = \hat{G}(i\omega_n \to \omega + i\eta), \tag{2.7}$$

where η is a positive infinitesimal. Although this procedure is well defined on paper, it involves in practice the inversion of a nearly-singular matrix. This is responsible for huge error bars on $\hat{G}(\omega)$ that are difficult to quantify and possibly biased, especially for large ω. As most equilibrium algorithms work in imaginary time and/or frequency, it is therefore of paramount importance to pursue the development of methods that are able to directly compute equilibrium properties in real time / frequency.

2.1.2 Spectral function

The spectral function is defined as

$$\hat{A}(\mathbf{k}, \omega) = -\frac{1}{\pi}\text{Im}\hat{G}(\mathbf{k}, \omega). \tag{2.8}$$

Experimentalists can probe the trace of this observable using Angular-Resolved PhotoEmission Spectroscopy (ARPES), shining light on the material and determining the momentum of the extracted electrons. Examples of such spectral intensities are displayed in Chapter 3 where we present the physics of Sr_2IrO_4.

Noticing that

$$A_{ab}(\mathbf{k}, \omega = 0) = \lim_{\omega \to 0} -\frac{1}{\pi}\text{Im}G_{ab}(\mathbf{k}, \omega) = \lim_{i\omega_n \to 0} -\frac{1}{\pi}\text{Im}G_{ab}(\mathbf{k}, i\omega_n), \tag{2.9}$$

the inspection of the extrapolation of the imaginary part of the Matsubara Green's function in the $T = 0$ limit provides a criterion to distinguish between a metal and an insulator:

— If Im Tr $\left[\hat{G}(i\omega_n)\right] \to 0$ when $i\omega_n \to 0$, no states are present at the Fermi level and the system is an insulator,

— If Im Tr $\left[\hat{G}(i\omega_n)\right] \to C \neq 0$ when $i\omega_n \to 0$, the system is a metal.

In the case of spinless fermions described by a band dispersion $\epsilon_{\mathbf{k}}$, A simply writes

$$A(\mathbf{k}, \omega) = \delta(\omega + \mu - \epsilon_{\mathbf{k}}). \tag{2.10}$$

In real materials, these peaked dispersions are dampened by the finite lifetime of the particles.

2.1.3 Self-energy and hybridization function

When studying strongly correlated materials, it is useful to introduce the noninteracting Green's function $\hat{g}$, always denoted by a lower case letter throughout this Thesis. The effect of correlations in the system are then encoded in the self-energy $\hat{\Sigma}$ defined through Dyson's equation

$$\hat{\Sigma}(\mathbf{k}, i\omega_n) = \hat{g}(\mathbf{k}, i\omega_n)^{-1} - \hat{G}(\mathbf{k}, i\omega_n)^{-1}. \tag{2.11}$$

Labelling $\hat{\epsilon}_{\mathbf{k}}$ the noninteracting energy dispersion in the system, μ the chemical potential, and $\mathbf{1}$ the identity matrix, the fully interacting Green's function of the system then writes

$$\hat{G}(\mathbf{k}, i\omega_n) = \left[(i\omega_n + \mu)\mathbf{1} - \hat{\epsilon}_{\mathbf{k}} - \hat{\Sigma}(\mathbf{k}, i\omega_n)\right]^{-1}. \tag{2.12}$$

If the system is noninteracting, $\hat{\Sigma}$ is null and $\hat{G} = \hat{g}$.

1. Technically the retarded component of the real-frequency Green's function. See Chapters 8 and 9 for a full introduction to real-time formalism.

It is instructive to consider the scalar case and expand the self-energy at first order

$$\Sigma(\mathbf{k}, i\omega_n) = \Sigma'_{\mathbf{k}} + i\Sigma''_{\mathbf{k}} + i\omega_n(1 - z_{\mathbf{k}}^{-1}), \tag{2.13}$$

where $\Sigma'_{\mathbf{k}} = \lim_{i\omega_n \to 0} \mathrm{Re}\Sigma(\mathbf{k}, i\omega_n)$ and $\Sigma''_{\mathbf{k}} = \lim_{i\omega_n \to 0} \mathrm{Im}\Sigma(\mathbf{k}, i\omega_n)$. The Green's function then writes

$$G(\mathbf{k}, i\omega_n) = \frac{z_{\mathbf{k}}}{i\omega_n + z_{\mathbf{k}}(\mu - \epsilon_{\mathbf{k}} - \Sigma'_{\mathbf{k}}) - iz_{\mathbf{k}}\Sigma''_{\mathbf{k}}}. \tag{2.14}$$

The energy bands are thus shifted by the real part of the self-energy and renormalized by $z_{\mathbf{k}}$, as well as dampened by the imaginary part of the self-energy times $z_{\mathbf{k}}$. In the uniform case, if $z \sim 1$ there is almost no difference with the noninteracting case and the system has a well-defined energy dispersion. On the other hand, if $z \sim 0$ the spectral weight at the Fermi level is suppressed and a gap opens: the system is a Mott insulator. z is therefore often used as order parameter to study the Mott transition.

When the strongly interacting system we study is coupled to a bath, this can be encoded in a hybridization function $\hat{\Delta}$, so that the noninteracting Green's function writes

$$\hat{g}(\mathbf{k}, i\omega_n) = \left[(i\omega_n + \mu)\mathbf{1} - \hat{\epsilon}_{\mathbf{k}} - \hat{\Delta}(i\omega_n)\right]^{-1}. \tag{2.15}$$

The full Green's function is

$$\hat{G}(\mathbf{k}, i\omega_n) = \left[(i\omega_n + \mu)\mathbf{1} - \hat{\epsilon}_{\mathbf{k}} - \hat{\Delta}(i\omega_n) - \hat{\Sigma}(\mathbf{k}, i\omega_n)\right]^{-1}. \tag{2.16}$$

$\hat{\Delta}$ will prove useful for many lattice systems in the context of dynamical mean-field theory, where a site is singled out and treated as an impurity self-consistently embedded in the material, see Section 2.3.

Let us consider the case of the quantum dot located between a left and a right lead introduced in Section 1.1.3 as an example. The hybridization function takes the form

$$\Delta_\sigma(i\omega_n) = \sum_{\alpha=L,R} \sum_{\mathbf{k}} \frac{\gamma_{\mathbf{k}}^2}{i\omega_n - \epsilon_{\mathbf{k}\alpha}}. \tag{2.17}$$

2.2 Overview of numerical approaches

Computational methods for many-body quantum systems have seen considerable progress in the last 30 years thanks to new algorithms as well as new concepts and approximations. As the development of numerical techniques plays a central role in this Thesis, we provide here a broad overview of modern algorithms used to tackle the many-body problem in and out of equilibrium. Those might either be used successfully on full lattice systems (such as the Hubbard model of Section 1.1.1) or for quantum impurity problems. The latter will turn particularly useful in the context of dynamical mean-field theory that we present next.

First, semi-analytical approximate methods, such as Iterated Perturbation Theory (IPT) [53] or the Noncrossing Approximation (NCA) [81, 59, 90, 131, 16, 17, 69] provide fast and easy-to-implement quantum impurity solvers. These techniques consist in keeping a subclass of contributions to the self-energy in a perturbation expansion. The error introduced by these approximations cannot be precisely quantified, and they are nowadays considered as too primitive for the study of correlated systems at equilibrium. They are however still largely employed when modelling out-of-equilibrium phenomena where numerically exact methods cannot reach relevant regimes of parameters yet [45, 95, 102, 126]. NCA will for instance be used in Chapter 13 to describe Ca_2RuO_4 subject to an electric-field.

A large class of methods are interested in the ground state properties of materials, hence working in the $T = 0$ limit. All of these techniques are nonperturbative in the system parameters.

Exact Diagonalization (ED) directly addresses the Schrödinger equation $\mathcal{H}\psi = E\psi$ on a lattice system of N sites using an iterative matrix eigenvalue solver, such as Lanczos algorithm. It provides a versatile and unbiased method, but is very much limited by the number of sites that can be treated. The current record is set at $N = 50$ interacting spins using symmetries and many computational tricks [179].

The Numerical Renormalization Group (NRG) approach aims at treating the small energy scales of an impurity coupled to a bath through a logarithmic discretization of the bath [180, 27, 28]. The system is then diagonalized starting from the impurity site alone and iteratively adding degrees of freedom of the bath. The exponentially growing Hilbert space is truncated by only keeping the lowest-lying many-particle states.

The Density Matrix Renormalization Group (DMRG) method is also based on a truncation of the Hilbert space using a bond dimension D [176, 177]. It has a very natural interpretation in one dimension, where the wavefunction is represented by a product of matrices of size $D \times D$. The method can treat system sizes up to several hundreds of sites and its accuracy can be systematically controlled by increasing D. Extensions for $T \neq 0$ or dimensions higher than 1 (called tensor networks) face strong limitations due to entanglement entropy [164, 165].

All of these methods have been extended to treat time-dependent impurity Hamiltonians [5, 6, 146] as well as transport through open systems [4] but remain strongly limited by the size of the Hilbert space and the entanglement entropy, and can therefore only treat low dimensions and low temperatures.

On the other hand, many numerical methods start from well-defined limits at high temperature and try to reach lower temperatures using Monte Carlo techniques. In all these algorithms, the contributions to the quantity we accumulate, such as the Green's function or the partition function, have alternating signs due to the anticommutation relations between fermionic operators. This leads to cancellations between individual measurements and exponentially growing errors: it is the *sign problem*. More details are provided in Section 5.3.1.

The auxiliary-field quantum Monte Carlo (AF-QMC) algorithm tries to recover the ground state wavefunction by applying the $e^{-\beta\mathcal{H}}$ operator to an initial wavefunction and taking the $\beta \to \infty$ limit [188, 151, 150]. This method uses imaginary-time path integrals that are stochastically evaluated with the help of auxiliary fields introduced by a Hubbard-Stratanovich transformation. The inherent sign problem can be managed using a constrained-path approximation, but this can introduce a systematic error that has to be controlled.

Continuous-time quantum Monte Carlo (CT-QMC) algorithms have been a breakthrough in finding solutions of quantum impurity problems [139, 140, 171, 173, 61, 62]. These methods are based on a perturbation expansion of the partition function, but do not truncate the series at a specific order so that they are numerically exact in the limit of long computational time. The two most popular approaches, that we present in more details in Chapter 5, are the CT-INT, based on an expansion in the Coulomb repulsion U, and the CT-HYB, based on an expansion in the hybridization function Δ. Both methods face a strong limitation with the system size N. The hybridization expansion is limited because of the exponentially growing size of the Hilbert space, while the interaction expansion faces an average perturbation order in the sampling of the partition function scaling as $U\beta N$.

Diagrammatic Monte Carlo methods can directly address the thermodynamic limit, that is the limit of infinite system size with fixed density of particles. Based on an expansion in the Coulomb interaction U, they compute physical quantities, such as the Green's function, by directly sampling their diagrammatic contributions [129, 130, 88, 73, 22, 135]. A strong reduction of the sign problem has recently been achieved in algorithms using a sum of determinants to express contributions from different topologies of diagrams [135, 110, 168]. These ideas are exposed in Chapters 6 and 7.

Early attempts of real-time quantum Monte Carlo algorithms were direct extensions of the CT-QMC methods on the Keldysh contour. They sampled the partition function Z, both using strong-coupling and weak-coupling expansions [112, 175, 174, 144]. They however faced a 'dynamical' sign problem that worsens when trying to reach longer times. Current efforts to build real-time quantum Monte Carlo methods mainly explore two routes: the inchworm algorithm [37, 35, 36, 32, 33, 9, 21] and the so-called diagrammatic QMC [128, 15, 14, 109]. The latter is the subject of Chapters 8 and 9.

Considerable efforts have recently been put in comparing the strengths and limitations of many of the above methods on lattice models [93, 143].

2.3 DMFT or the importance of the quantum impurity problem

In Sections 1.1.3 and 2.2, we have presented quantum impurity models and efficient techniques to solve them. An important effort has indeed been made in this direction because one can design a mapping be-

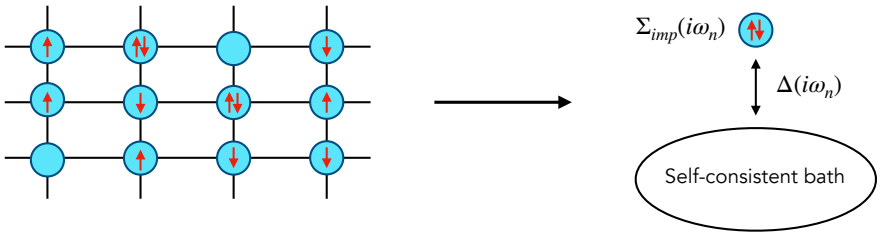

Figure 2.1 – DMFT mapping of a lattice site to an impurity self-consistently embedded into a bath.

tween the full lattice problem and a single site embedded in a bath: this is the Dynamical Mean-Field Theory (DMFT). For a complete review on the subject, see Ref. [53].

Let us consider a lattice system. According to Section 2.1, the interacting Green's function writes

$$\hat{G}(\mathbf{k}, i\omega_n) = \left[(i\omega_n + \mu)\mathbf{1} - \hat{\epsilon}_{\mathbf{k}} - \hat{\Sigma}(\mathbf{k}, i\omega_n)\right]^{-1}, \tag{2.18}$$

where $\hat{\epsilon}_{\mathbf{k}}$ is the energy dispersion of the noninteracting system, μ the chemical potential and $\hat{\Sigma}(\mathbf{k}, i\omega_n)$ the lattice self-energy. The key idea is then to isolate a single lattice site and embed it into an effective bath with which it can exchange electrons through a hybridization function $\hat{\Delta}(i\omega_n)$, as depicted in Fig. 2.1. The impurity Green's function is

$$\hat{G}_{\text{imp}}(i\omega_n) = \left[(i\omega_n + \mu)\mathbf{1} - \hat{\epsilon}_d - \hat{\Delta}(i\omega_n) - \hat{\Sigma}_{\text{imp}}(i\omega_n)\right]^{-1}. \tag{2.19}$$

The embedding requires the local Green's function on the lattice to be equal to the impurity one

$$G_{\text{loc}} = \sum_{\mathbf{k}} \hat{G}(\mathbf{k}, i\omega_n) = \hat{G}_{\text{imp}}(i\omega_n). \tag{2.20}$$

At this point, the equations are still exact as we have only introduced a *representation* of the local Green's function as an impurity coupled to a bath, and the above equation should be understood as a functional equation that determines the hybridization function.

The DMFT approximation consists in stating that the lattice self-energy does not depend on $\mathbf{k}$ and is given by the impurity model self-energy

$$\hat{\Sigma}(\mathbf{k}, i\omega_n) = \hat{\Sigma}_{\text{imp}}(i\omega_n). \tag{2.21}$$

The hybridization function now has to be self-consistently adjusted in order for Eq. (2.20) to be satisfied.

Note that the 'dynamical' refers to the ability of this approximation to handle different time scales or energy scales involved in the excitation spectra of the system, and not to out-of-equilibrium physics. This scheme is exact in the atomic limit ($\hat{\Delta} = 0$) as well as in the noninteracting case ($\hat{\Sigma} = 0$), so that it is thought to be a good candidate to obtain physical results in the intermediate regime where both the interaction and the hybridization matter. This approximation has also been shown to be exact in the limit of infinite lattice coordination (Bethe lattice). Moreover, as it approximates the lattice self-energy by the impurity one, it yields meaningful results for systems that have a localized self-energy.

In practice, this approximation is solved using the following iterative scheme:

1. Start from a noninteracting local Green's function $\hat{g}(i\omega_n)$.
2. Solve the impurity model in order to obtain $\hat{\Sigma}_{\text{imp}}(i\omega_n)$.
3. Construct the local interacting Green's function

$$G_{\text{loc}} = \sum_{\mathbf{k}} \left[(i\omega_n + \mu)\mathbf{1} - \hat{\epsilon}_{\mathbf{k}} - \hat{\Sigma}_{\text{imp}}(i\omega_n)\right]^{-1}. \tag{2.22}$$

4. Construct the new noninteracting Green's function using Dyson's equation

$$\hat{g}(i\omega_n) = \left[\hat{G}^{-1}_{\text{loc}}(i\omega_n) + \hat{\Sigma}_{\text{imp}}(i\omega_n)\right]^{-1}. \tag{2.23}$$

5. Loop until convergence.

Extensions of DMFT have been developed in order to go beyond Eq. (2.21). A first approach is to add more sites in the impurity model. In the Dynamical Cluster Approximation (DCA) formulation, the Brillouin zone is thus partitioned into area tiles and the self-energy is approximated as a piecewise function of momentum in each tile [72, 71, 99]. The Cellular Dynamical-Mean Field Theory (CDMFT) scheme considers on the other hand a real-space cluster extension of the self-energy [87, 99]. Translational symmetry is however usually broken and periodization schemes have to be used. In Chapter 4, we use 2-site CDMFT to study the electronic properties of electron-doped Sr_2IrO_4.

Another route is to include spatial correlations by making a higher order object than the self-energy local. In DΓA, the two-particle analog of the self-energy, the fully irreducible two-fermion scattering vertex Λ, is assumed to be purely local [80, 159]. In TRILEX, it is the three-leg interaction vertex that is assumed to be local [12, 13]. Both methods are computationally heavy due to the evaluation of these higher order vertices.

The DMFT approximation has also been extended to study out-of-equilibrium strongly correlated systems [10], and we will use it in Chapter 13 to model Ca_2RuO_4 subject to an electric field.

Part II

Pseudogap and electronic structure of electron-doped Sr_2IrO_4

Chapter 3

Experiments and Model

In Chapter 1, we presented the properties of high-temperature superconductors. One of the biggest challenges of modern condensed matter physics consists in understanding the emergence of the pseudogap and its interplay with superconductivity. In this respect, the Sr_2IrO_4 iridate is a very interesting playground as it closely resembles these materials.

It is indeed isostructural to La_2CuO_4 [133], and its low-energy electronic structure is well described by a single half-filled band because of strong spin-orbit (SO) coupling as shown by electronic structure calculations in the Local Density Approximation (LDA) [83, 100]. Angular Resolved PhotoEmission Spectroscopy (ARPES), optical spectroscopy, and resonant inelastic X-ray scattering experiments [83, 84, 41, 24, 158] as well as scanning tunneling microscopy [120] demonstrate that the ground-state of this material is a Mott insulator. This conclusion is also supported by electronic structure calculations taking into account electronic correlations [100, 187, 94].

In this Chapter, we present recent ARPES experiments emphasizing a momentum-differentiation of the spectral intensity in the Brillouin zone, and we develop a minimal model to capture the physics of Sr_2IrO_4. Results concerning the electronic structure of this material upon doping are presented in the next Chapter.

3.1 Motivation

3.1.1 Material

Sr_2IrO_4 is a layered transition metal oxide. The electronic configuration of the Ir^{4+} ions is $\{Xe\}4f^{14}5d^5$ and the compound crystallizes in the K_2NiF_4 tetragonal structure, as La_2CuO_4 or Sr_2RhO_4, with planar

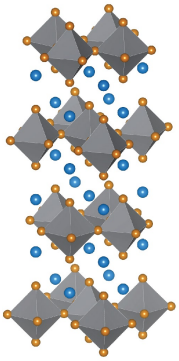

(a) Sr_2IrO_4 structure. Orange dots denote oxygen atoms, and blue ones strontium atoms. Iridium atoms are located at the center of the octahedra. [31]

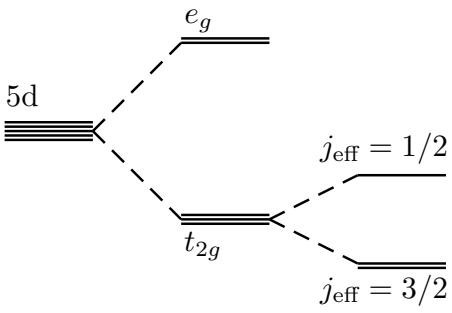

(b) $5d$ levels splitting due to the crystal field and spin-orbit coupling.

Figure 3.1

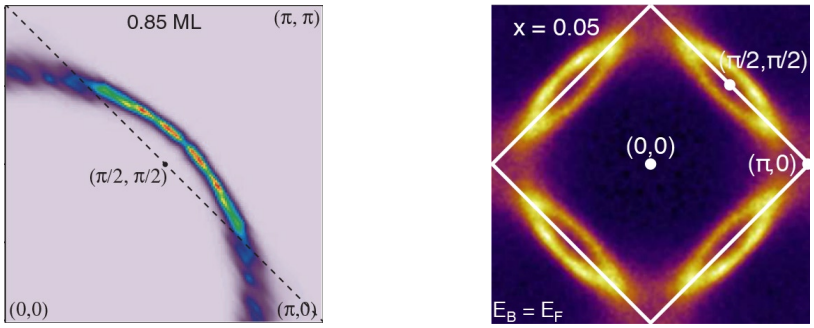

(a) 0.85 Potassium monolayer deposited on the parent compound. [85]

(b) La substitution: $(Sr_{1-x}La_x)_2IrO_4$ for $x = 0.05$. [41]

Figure 3.2 – ARPES experiments on electron-doped samples of Sr_2IrO_4.

IrO_2 layers forming a square lattice of Ir^{4+} ions [133]. The IrO_6 octahedra are rotated about the c-axis by ~ 11 deg., generating a doubled unit cell [39]. The structure of this material is sketched on Fig. 3.1a. The iridium ions are at the center of the grey octahedra defined by the position of the oxygen atoms (orange). The strontium atoms (blue) separate the layers in the material.

The $5d^5$ electronic configuration would naively yield a metallic state in a band theory approach. Sr_2RhO_4, having an identical atomic arrangement with nearly the same lattice constants and bond angles, is indeed found to be a Fermi liquid metal [167]. Sr_2IrO_4 however has a very strong spin-orbit (SO) coupling, a property which was shown to modify the electronic structure near the Fermi level in $5d$ systems [152, 138, 184, 100, 187].

As pictured in Fig. 3.1b, the $5d$ structure of Sr_2IrO_4 is indeed split in two e_g and three t_{2g} bands due to the crystal field. Through the action of spin-orbit, the t_{2g} manifold then splits into a low-lying effective momentum $j_{\text{eff}} = 3/2$ quadruplet, and a higher-lying effective total angular momentum $j_{\text{eff}} = 1/2$ doublet. This compound then effectively reduces to a half-filled $j_{\text{eff}} = 1/2$ single band near the Fermi surface, a configuration which makes it prone to the opening of a Mott gap as a result of repulsive interactions.

As a result, despite very different electronic structures, the effective low-energy physics of Sr_2IrO_4 can be described by the same minimal model as developed for cuprates. One of the outstanding questions concerning this material is therefore to discover if this analogy can be extended to the metallic phase, and especially if we can find high-temperature superconductivity and the occurence of a pseudogap.

3.1.2 Photoemission experiments

The noninteracting Fermi surface of this material being electron-like, the hole-doped regime of high-T_c cuprates (see for instance Fig. 1.2) is to be compared with the electron-doped regime of Sr_2IrO_4. Several experimental groups performed ARPES measurements on this material to investigate the doped compound further [85, 41, 24, 158]. We reproduce in Fig. 3.2 the spectral intensity at the Fermi surface obtained by growing a potassium layer on top of the undoped material (Fig. 3.2a), and by performing a La substitution of the Sr atoms, $(Sr_{1-x}La_x)_2IrO_4$ (Fig. 3.2b). The spectral intensity exhibits a strong momentum differentiation, leading to the appearance of pockets in the 'nodal' region located around $(\pi/2, \pi/2)$, while the ARPES spectra in the 'antinodal' region around $(\pi, 0)$ are suggestive of a pseudogap. [1]

More insight is gained from probing the quasiparticle bands below the Fermi surface, see Fig. 3.3, where the fully gapped parent insulator (*left*) is compared to the doped system at $x = 0.05$ (*right*). The intensity is displayed along the nodal (*top*) and antinodal (*bottom*) directions. A clear 'collapse' of the Mott gap is found upon doping, that is the two bands become much closer to each other. In the doped compound, bands around $(\pi/2, \pi/2)$ extrapolate to a Dirac point at -0.1 eV and cross the Fermi surface with linear dispersion, resulting in the sharp pockets observed in Fig. 3.2b. Along the antinodal direction, bands shift towards the Fermi energy with a rather round and spread behavior.

1. Note that the 'nodal/antinodal' terminology is inherited from the cuprate context and does not refer to the nodes of a superconducting gap – up to now no unambiguous evidence of superconductivity has been established.

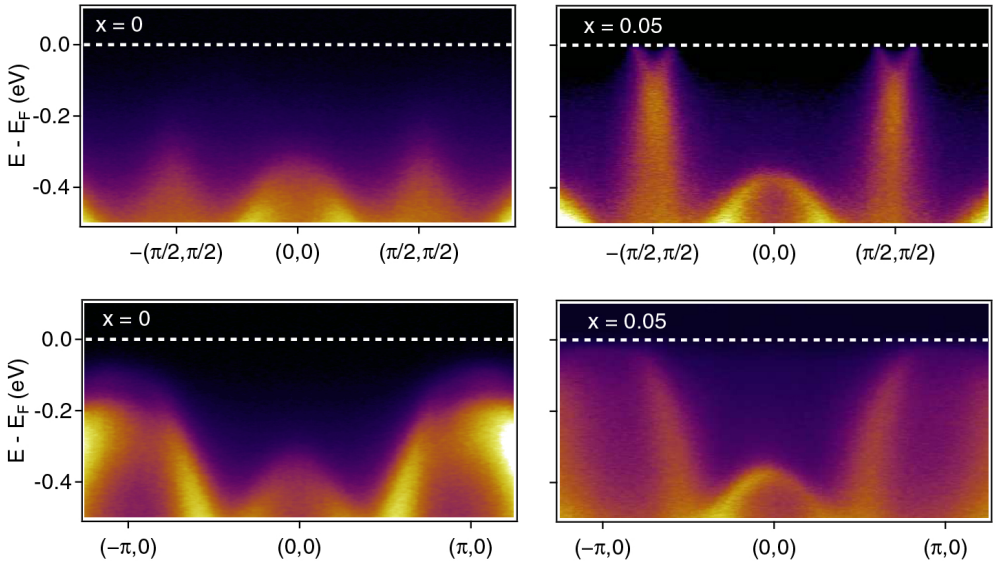

Figure 3.3 – ARPES experiments probing the spectral intensity below the Fermi surface of Sr_2IrO_4, both for the insulating parent compound (*left*) and the electron-doped material (*right*). Intensities are shown along the nodal (*upper panels*) and the antinodal (*lower panels*) directions. [41]

Note that, because of the stoichiometry of the material, the $x = 0.05$ La doping in the experiments of Ref. [41] corresponds to a nominal electron doping of 10%.

In the following Section, we construct a theoretical model for the low-energy electronic structure of doped Sr_2IrO_4, and we then treat electronic correlation effects in the framework of cellular dynamical mean-field theory (CDMFT). In the next Chapter, we present our results, demonstrating the existence of a pseudogap and reproducing the momentum-differentiation in the Fermi surface spectral intensity maps (see Fig. 4.4).

3.2 Minimal model

3.2.1 Tight-binding model

Our starting point is the tight-binding (TB) model introduced in Refs. [76, 30] describing t_{2g} bands in the presence of a spin-orbit coupling. Because of the rotation of the IrO_6 octahedra around the c-axis, the Sr_2IrO_4 unit cell is composed of two inequivalent sites A and B. The tight-binding Hamiltonian is then written as

$$\mathcal{H}_0 = \sum_{\mathbf{k}\in \mathrm{RBZ}} \psi^\dagger_{\mathbf{k}} H_0(\mathbf{k}) \psi_{\mathbf{k}}, \tag{3.1}$$

where the momentum sum is over the $\sqrt{2} \times \sqrt{2}$ reduced Brillouin zone and the components of $\psi_{\mathbf{k}}$ are the electron annihilation operators for all 12 orbitals in the unit cell $\{c_{\mathbf{k}\tau\alpha\sigma} | \tau = A, B; \alpha = d_{xy}, d_{yz}, d_{zx}; \sigma = \uparrow, \downarrow\}$. It is convenient to order the basis according to $(c_{Ad_{xy}\uparrow}, c_{Ad_{yz}\downarrow}, c_{Ad_{zx}\downarrow}, [A \leftrightarrow B])$ followed by their time-reversed partners $([\uparrow\leftrightarrow\downarrow])$. There is no coupling between these two blocks as the system is time-reversal invariant and we can thus only consider the first half of the basis, taking into account that all bands are two-fold degenerate.

The remaining 6×6 tight-binding matrix H_0 writes

$$H_0(\mathbf{k}) = \begin{pmatrix} O(\mathbf{k}) & P(\mathbf{k}) \\ P^\dagger(\mathbf{k}) & O(\mathbf{k}) \end{pmatrix}, \tag{3.2}$$

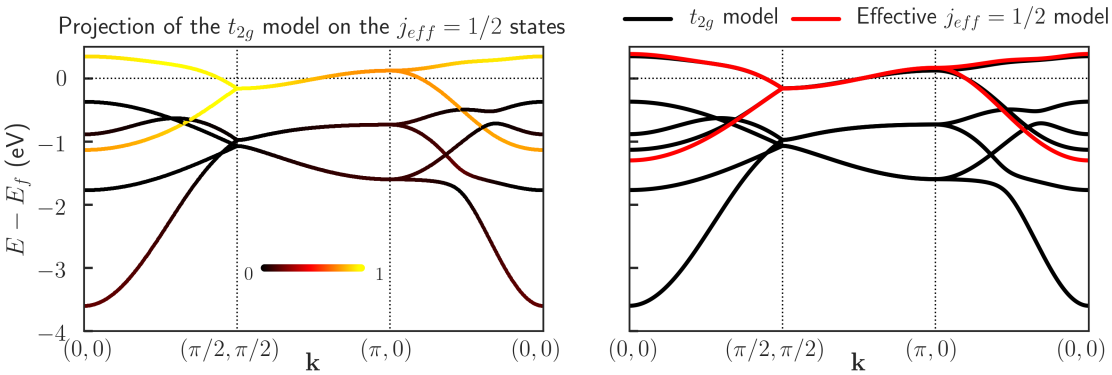

Figure 3.4 – *Left:* Projection of the tight-binding model for the t_{2g} bands (Eq. (3.2)) on the j_{eff} = 1/2 states. The value of the projection ranges from 0 (black) to 1 (yellow). *Right:* Comparison between the full t_{2g} model and the effective $j_{\text{eff}} = 1/2$ model from Eq. (3.10) with $E = 0$.

where P describes the hopping part of the Hamiltonian

$$P(\mathbf{k}) = e^{-i\frac{k_x+k_y}{2}} \begin{pmatrix} -4\gamma_1(\mathbf{k}) & 0 & 0 \\ 0 & -2\gamma_2(\mathbf{k}) & 0 \\ 0 & 0 & -2\gamma_3(\mathbf{k}) \end{pmatrix}, \tag{3.3}$$

with $\gamma_1(\mathbf{k}) = \gamma_0 \cos\frac{k_x}{2} \cos\frac{k_y}{2}$, $\gamma_2(\mathbf{k}) = \gamma_0 \cos\frac{k_x+k_y}{2}$ and $\gamma_3(\mathbf{k}) = \gamma_0 \cos\frac{k_x-k_y}{2}$. Here $\mathbf{k} = (k_x, k_y)$ is expressed in terms of the reciprocal vectors forming the reduced Brillouin zone.

O describes the on-site part of the Hamiltonian. It includes the spin-orbit coupling $\lambda \mathbf{L}_i \cdot \mathbf{S}_i$ and reads

$$O(\mathbf{k}) = \begin{pmatrix} \Delta_t + e_1(\gamma_1(\mathbf{k})/\gamma_0)^2 & \lambda/2 & -i\lambda/2 \\ \lambda/2 & 0 & -i\lambda/2 \\ i\lambda/2 & i\lambda/2 & 0 \end{pmatrix}, \tag{3.4}$$

where Δ_t is an on-site energy difference of the d_{xy} orbital relative to d_{yz} and d_{zx}, and λ is the spin-orbit coupling parameter. The additional term $e_1(\gamma_1/\gamma_0)^2$ accounts for the hybridization between d_{xy} and $d_{x^2-y^2}$ [76]. In the following we consider $\Delta_t = 0.15$ eV, $\gamma_0 = 0.35$ eV, $e_1 = -1.5$ eV and $\lambda = 0.57$ eV. It has been shown that these values yield a band structure in good agreement with LDA+SO calculations [76, 41].

We plot in Fig. 3.4 (*left*) the six bands resulting from the diagonalization of $H_0(\mathbf{k})$ along the $(0,0) - (\pi/2,\pi/2) - (\pi,0) - (0,0)$ path of the full Brillouin zone. When the eigenvalues are projected on the $j_{\text{eff}} = 1/2$ states

$$\left| j_{\text{eff}} = \frac{1}{2}, \pm\frac{1}{2} \right\rangle = \mp\frac{1}{\sqrt{3}} \left[|d_{xy}, \pm\rangle \pm (|d_{yz}\rangle, \mp) \pm i|d_{zx}, \mp\rangle) \right], \tag{3.5}$$

it can be seen that the low-energy bands essentially have $j_{\text{eff}} = 1/2$ character, as highlighted in Refs [83, 76, 30, 41]. It is therefore natural to look for an effective reduced 2×2 Hamiltonian describing these states.

3.2.2 Effective $j_{\text{eff}} = 1/2$ model

We rewrite H_0 in the basis $(|\frac{1}{2}, \frac{1}{2}\rangle_A, |\frac{1}{2}, \frac{1}{2}\rangle_B, |\frac{3}{2}, \frac{1}{2}\rangle_A, |\frac{3}{2}, \frac{1}{2}\rangle_B, |\frac{3}{2}, -\frac{3}{2}\rangle_A, |\frac{3}{2}, -\frac{3}{2}\rangle_B)$

$$H_0(\mathbf{k}) = \begin{pmatrix} H_{1/2}(\mathbf{k}) & M(\mathbf{k}) \\ M^\dagger(\mathbf{k}) & H_{3/2}(\mathbf{k}) \end{pmatrix}, \tag{3.6}$$

where, labelling $l(\mathbf{k}) = e^{-i\frac{k_x+k_y}{2}}$, $u_1(\mathbf{k}) = l(\mathbf{k})\gamma_1(\mathbf{k})$, $u_2(\mathbf{k}) = l(\mathbf{k})\left(\gamma_2(\mathbf{k}) - \gamma_3(\mathbf{k})\right)$,

$$H_{1/2}(\mathbf{k}) = \begin{pmatrix} \frac{1}{3}\left[\Delta_t + e_1\left(\frac{\gamma_1(\mathbf{k})}{\gamma_0}\right)^2\right] + \lambda & -\frac{8}{3}u_1(\mathbf{k}) \\ -\frac{8}{3}u_1^\dagger(\mathbf{k}) & \frac{1}{3}\left[\Delta_t + e_1\left(\frac{\gamma_1(\mathbf{k})}{\gamma_0}\right)^2\right] + \lambda \end{pmatrix}, \tag{3.7}$$

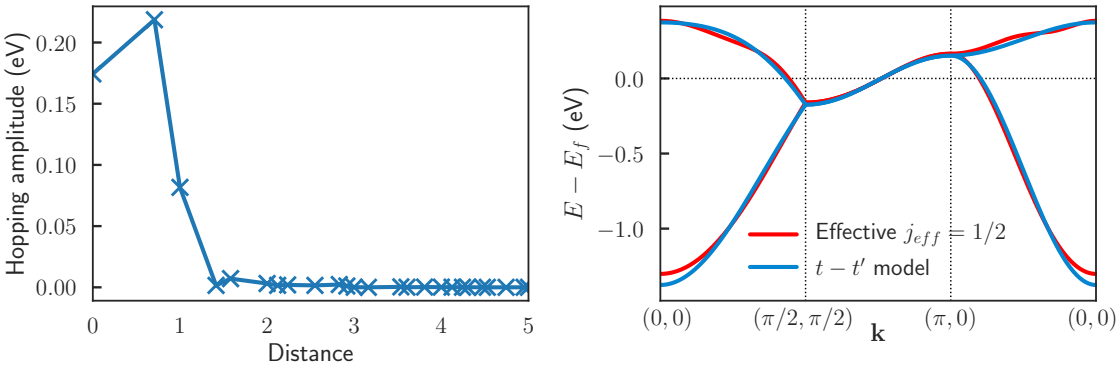

Figure 3.5 – *Left:* Real-space hopping amplitudes of effective $j_{\text{eff}} = 1/2$ Hamiltonian with respect to the distance (the inter-site distance is normalized to 1). *Right:* Comparison between the effective $j_{\text{eff}} = 1/2$ bands with $E = 0$ and the folded dispersion obtained by keeping only the nearest and next-nearest neighbor hopping terms (resp. $\gamma = -0.219$ eV, $\gamma' = -0.082$ eV).

$$M^\dagger(\mathbf{k}) = \begin{pmatrix} -\frac{\sqrt{2}}{3}\left[\Delta_t + e_1\left(\frac{\gamma_1(\mathbf{k})}{\gamma_0}\right)^2\right] & \frac{2\sqrt{2}}{3}u_1(\mathbf{k}) \\ \frac{2\sqrt{2}}{3}u_1^\dagger(\mathbf{k}) & -\frac{\sqrt{2}}{3}\left[\Delta_t + e_1\left(\frac{\gamma_1(\mathbf{k})}{\gamma_0}\right)^2\right] \\ 0 & \frac{1}{\sqrt{3}}u_2(\mathbf{k}) \\ \frac{1}{\sqrt{3}}u_2^\dagger(\mathbf{k}) & 0 \end{pmatrix}, \tag{3.8}$$

and

$$H_{3/2}(\mathbf{k}) = \begin{pmatrix} \frac{2}{3}\left[\Delta_t + e_1\left(\frac{\gamma_1(\mathbf{k})}{\gamma_0}\right)^2\right] - \frac{\lambda}{2} & -\frac{10}{3}u_1(\mathbf{k}) & 0 & \frac{1}{\sqrt{3}}u_2(\mathbf{k}) \\ -\frac{10}{3}u_1(\mathbf{k}) & \frac{2}{3}\left[\Delta_t + e_1\left(\frac{\gamma_1(\mathbf{k})}{\gamma_0}\right)^2\right] - \frac{\lambda}{2} & \frac{1}{\sqrt{3}}u_2^\dagger(\mathbf{k}) & 0 \\ 0 & \frac{1}{\sqrt{3}}u_2(\mathbf{k}) & -\frac{\lambda}{2} & -2u_1(\mathbf{k}) \\ \frac{1}{\sqrt{3}}u_2^\dagger(\mathbf{k}) & 0 & -2u_1^\dagger(\mathbf{k}) & -\frac{\lambda}{2} \end{pmatrix}. \tag{3.9}$$

An effective Hamiltonian is then obtained by projecting H_0 onto the $j_{\text{eff}} = 1/2$ subspace

$$H^{\text{eff}}_{1/2}(\mathbf{k}) = H_{1/2}(\mathbf{k}) + M(\mathbf{k})\left[E \times \mathbf{1}_{4\times4} - H_{3/2}(\mathbf{k})\right]^{-1} M^\dagger(\mathbf{k}), \tag{3.10}$$

where $\mathbf{1}_{4\times4}$ is the 4×4 unit matrix and E an energy scale that is adjusted in order to best match the original band structure.

While it is difficult to obtain a compact expression for this reduced Hamiltonian, one can easily diagonalize $H^{\text{eff}}_{1/2}$ numerically for every $\mathbf{k}$ point of interest. This is shown (red lines) in Fig. 3.4 (*right*) together with the complete t_{2g} band structure (black lines) for $E = 0$. The effective model appears to be in excellent agreement with the two low-energy bands exhibiting a $j_{\text{eff}} = 1/2$ character.

As mentioned earlier, the Sr_2IrO_4 crystal has a two-atom unit cell, and we expressed the tight-binding models above in the reduced Brillouin zone in order to make contact with experiments. Let us however emphasize that all sites are actually equivalent from a purely electronic point of view in these models. An inspection of the band structure in the reduced Brillouin zone indeed reveals that it results from the folding of half as many bands defined over the full Brillouin zone. This can be seen e.g. from the degeneracy of the bands along the $(\pi/2, \pi/2) - (\pi, 0)$ path. As a result, the effective model in Eq. (3.10) can be written as a simple tight-binding model on a square lattice

$$\mathcal{H}^{\text{TB}}_{1/2} = \sum_{ij} \gamma_{ij} c_i^\dagger c_j, \tag{3.11}$$

where the hopping amplitudes γ_{ij} are shown as a function of the distance $|i - j|$ in Fig. 3.5 (*left*). We obtain a good approximation of the band structure by only keeping the nearest and next-nearest neighbor hopping

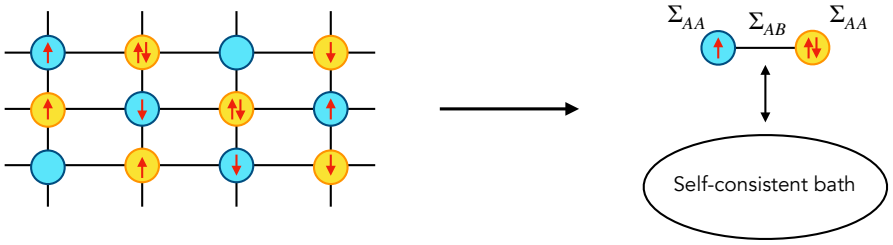

Figure 3.6 – Cellular DMFT approximation.

terms (for an almost perfect agreement it is necessary to keep 8 hopping parameters). This yields the simple energy dispersion

$$\epsilon(\mathbf{k}) = \epsilon_0 + 2\gamma(\cos k_x + \cos k_y) + 4\gamma' \cos k_x \cos k_y, \tag{3.12}$$

where $\epsilon_0 = -0.174$ eV, $\gamma = -0.219$ eV, $\gamma' = -0.082$ eV and $\mathbf{k} = (k_x, k_y)$ is now expressed in the basis of the *full* Brillouin zone. The folding of this band in the reduced Brillouin zone is shown together with the effective $j_{\text{eff}} = 1/2$ band structure previously derived in Fig. 3.5 (*right*). Let us mention that a similar tight-binding model was derived in Ref. [170] with the difference that the $d_{x^2-y^2}$ admixture was not included in their work.

In the following, we use the effective Hamiltonian derived in Eq. (3.10), $\mathcal{H}^{\text{eff}}_{1/2} = \sum_{\mathbf{k}} H^{\text{eff}}_{1/2}(\mathbf{k})$, to describe the low-energy excitations of the system.

3.3 Introducing correlations: Cellular DMFT

We model the effect of electronic correlations in Sr_2IrO_4 by introducing an energy cost for having two electrons on the same Ir atom

$$\mathcal{H} = \mathcal{H}^{\text{eff}}_{1/2} + U \sum_{i,\tau} n_{i\tau\uparrow} n_{i\tau\downarrow}, \tag{3.13}$$

where $n_{i\tau\sigma}$ is the occupation number on the $j_z = \sigma$ orbital of the Ir atom $\tau = A, B$ in the unit cell i. In the following we use $U = 2$ eV [76, 41] and a temperature $T = 1/\beta = 1/200$ eV $\simeq 58$ K.

This model is studied using cellular dynamical mean-field theory [87, 53]: The original lattice Hamiltonian (3.13) is mapped on a two-site auxiliary cluster model embedded in a self-consistent medium (see Fig. 3.6). The self-energy of the cluster model $\Sigma_{\tau,\tau'}$ is used to construct an approximation of the lattice self-energy where only intra unit cell components are non-vanishing, i.e. $\Sigma^{\text{latt}}_{i\tau,i\tau'} = \Sigma_{\tau,\tau'}$. Note that the orbitals at sites A and B are electronically equivalent and therefore $\Sigma_{AA} = \Sigma_{BB}$ and $\Sigma_{AB} = \Sigma_{BA}$. We obtain the following expression for the lattice Green's function

$$\hat{G}^{\text{latt}}(i\omega_n, \mathbf{k}) = \left\{ (i\omega_n + \mu)\mathbf{1} - H^{\text{eff}}_{1/2}(\mathbf{k}) - \hat{\Sigma}(i\omega_n) \right\}^{-1}, \tag{3.14}$$

where $\mathbf{k}$ is defined in the reduced Brillouin zone and both $\hat{G}^{\text{latt}}$ and $\hat{\Sigma}$ are 2×2 matrices associated with the two Ir atoms in the unit cell. The CDMFT self-consistency imposes that the cluster Green's function $\hat{G}$ be the same as the unit cell Green's function of the lattice:

$$\hat{G}(i\omega_n) = \sum_{\mathbf{k}\in\text{RBZ}} \hat{G}^{\text{latt}}(i\omega_n, \mathbf{k}) = \sum_{\mathbf{k}\in\text{RBZ}} \left\{ (i\omega_n + \mu)\mathbf{1} - H^{\text{eff}}_{1/2}(\mathbf{k}) - \hat{\Sigma}(i\omega_n) \right\}^{-1}. \tag{3.15}$$

These quantities can be expressed in the basis $\{|\frac{1}{2}, \frac{1}{2}\rangle_A, |\frac{1}{2}, \frac{1}{2}\rangle_B\}$ of the $j_{\text{eff}} = 1/2$ orbitals on sites A and B. However, because A and B are electronically equivalent, it is convenient to work in the basis $\mathcal{B}$ of even and odd combinations of the $j_{\text{eff}} = 1/2$ orbitals, defined by

$$\left| \pm \right\rangle = \frac{1}{\sqrt{2}} \left(\left| \frac{1}{2}, \frac{1}{2} \right\rangle_A \pm \left| \frac{1}{2}, \frac{1}{2} \right\rangle_B \right). \tag{3.16}$$

In this basis, the cluster self-energy is diagonal because A and B sites are electronically equivalent

$$\hat{\Sigma}(i\omega_n) = \begin{pmatrix} \Sigma_+(i\omega_n) & 0 \\ 0 & \Sigma_-(i\omega_n) \end{pmatrix}. \tag{3.17}$$

Note that for a given $\mathbf{k}$ point, $\hat{G}^{\mathrm{latt}}(i\omega_n, \mathbf{k})$ is not diagonal. One can however show that, for a generic 2×2 diagonal matrix $\mathcal{M}$ in the $\mathcal{B}$ basis, $\sum_{\mathbf{k}\in\mathrm{RBZ}} \left[H^{\mathrm{eff}}(\mathbf{k}) + \mathcal{M}\right]^{-1}$ is a diagonal matrix too. As a result, the CDMFT self-consistency Eq. (3.15) implies that both cluster quantities $\hat{G}$ and $\hat{\Sigma}$ are diagonal in the $\mathcal{B}$ basis.

This equation is solved iteratively in the following way: At the iteration step n, the quantum impurity model is described by a diagonal noninteracting Green's function $\hat{g}^{(n)}$ and a local interaction Hamiltonian that has the following expression in the $\mathcal{B}$ basis

$$\mathcal{H}^{\mathrm{int}} = \frac{U}{2} \sum_{s=\pm} \left(n_{s\uparrow} n_{s\downarrow} + n_{s\uparrow} n_{\bar{s}\downarrow} + c^\dagger_{s\uparrow} c^\dagger_{s\downarrow} c_{\bar{s}\downarrow} c_{\bar{s}\uparrow} + c^\dagger_{s\uparrow} c^\dagger_{\bar{s}\downarrow} c_{s\downarrow} c_{\bar{s}\uparrow} \right). \tag{3.18}$$

This cluster model is solved using the CT-HYB quantum impurity solver[2] [148, 171, 173, 62], directly in the $\mathcal{B}$ basis. It yields both the cluster Green's functions $\hat{G}^{(n)}$ and self-energies $\hat{\Sigma}^{(n)}$. The self-consistency condition is used to construct a local diagonal lattice Green's function

$$\hat{G}^{(n)}_{\mathrm{loc}}(i\omega_n) = \sum_{\mathbf{k}\in\mathrm{RBZ}} \left\{ (i\omega_n + \mu)\mathbf{1} - H^{\mathrm{eff}}_{1/2}(\mathbf{k}) - \hat{\Sigma}^{(n)}(i\omega_n) \right\}^{-1}. \tag{3.19}$$

This allows one to get a new expression for the noninteracting cluster Green's function $\hat{g}$ via Dyson's equation

$$\left[\hat{g}^{(n+1)}\right]^{-1} = \left[\hat{G}^{(n)}_{\mathrm{loc}}\right]^{-1} + \hat{\Sigma}^{(n)}. \tag{3.20}$$

This procedure is iterated until convergence. Codes were developed using the TRIQS library [123].

This model is used to introduce electronic correlations on top of the tight-binding Hamiltonian $\mathcal{H}^{\mathrm{eff}}_{1/2}$. In the next Chapter, we present the electronic structure obtained when doping the Mott insulator Sr_2IrO_4. A strong momentum differentiation is found in the Brillouin zone, as well as the onset of a pseudogap.

2. An introduction to continous-time quantum Monte Carlo solvers is provided in Chapter 5.

Chapter 4

Electronic structure and emergence of a pseudogap

In this Chapter, we present results concerning the effects of correlations on the electronic structure of the Mott insulator Sr_2IrO_4 upon electron doping. The electronic structure displays a strong momentum-space differentiation at low doping level: The Fermi surface consists of pockets centered around $(\pi/2, \pi/2)$, while a pseudogap opens near $(\pi, 0)$. Its physical origin is shown to be related to short-range spin correlations. The pseudogap closes upon increasing doping, but a differentiated regime characterized by a modulation of the spectral intensity along the Fermi surface persists to higher doping levels. The work presented in this Chapter has been published in Ref. [108], the full text being reproduced in Appendix VII.

We recall the parameters we use in our calculations: $\Delta_t = 0.15$ eV, $\gamma_0 = 0.35$ eV, $e_1 = -1.5$ eV, $\lambda = 0.57$ eV, $U = 2$ eV and $T = 1/\beta = 1/200$ eV $\simeq 58$ K.

4.1 Doping regimes

4.1.1 Density and spectral intensity

As discussed in Section 3.3, the cluster quantities $\hat{G}$ and $\hat{\Sigma}$, obtained by solving the CDMFT equations, can be expressed in the basis of even and odd combinations of the $j_{\text{eff}} = 1/2$ orbitals, where they are

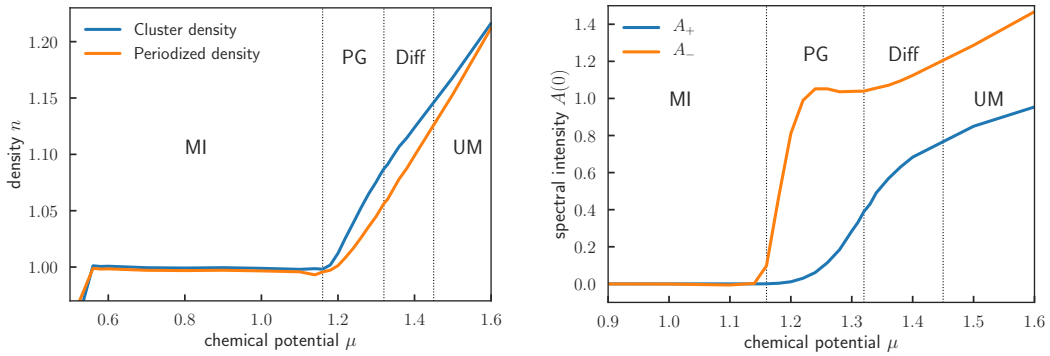

(a) Density of states as a function of the chemical potential μ.

(b) Spectral intensity at the Fermi level $A(0)$ as a function of the chemical potential μ.

Figure 4.1 – Dotted lines separate the four doping regimes: the Mott-insulating phase (MI), the pseudogap regime (PG), the differentiation region (Diff), and the uniform metal (UM).

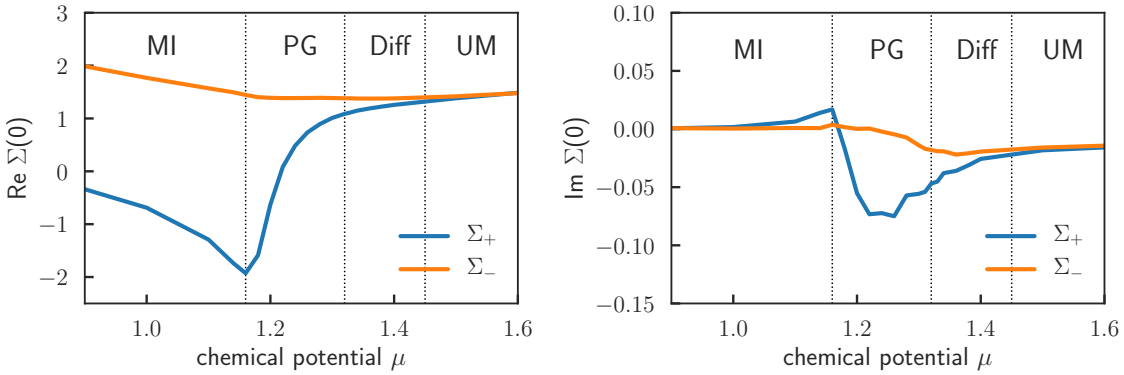

Figure 4.2 – Extrapolation to zero frequency of the real part (*left*) and of the imaginary part (*right*) of the self-energy $\Sigma(i\omega_n)$ as a function of the chemical potential μ. Dotted lines separate the four doping regimes: the Mott-insulating phase (MI), the pseudogap regime (PG), the differentiation region (Diff), and the uniform metal (UM).

diagonal

$$\hat{G} = \begin{pmatrix} G_+ & 0 \\ 0 & G_- \end{pmatrix} \qquad \hat{\Sigma} = \begin{pmatrix} \Sigma_+ & 0 \\ 0 & \Sigma_- \end{pmatrix}. \tag{4.1}$$

As we discuss later, $G_\pm$ and $\Sigma_\pm$ have a direct physical interpretation. The physics close to the node $(\pi/2, \pi/2)$ is indeed essentially controlled by G_- and Σ_- while the physics at the antinode $(\pi, 0)$ is controlled by G_+ and Σ_+. The reason for this, anticipating on Sec. 4.3 and Fig. 4.7, is that the nodal Fermi-surface pocket at $(\pi/2, \pi/2)$ is associated with the upper band (which has an antibonding/odd character) while the nodal states are associated with the lower bonding band with even character. The analysis of these quantities will reveal the existence of four distinct regimes upon doping: a Mott insulator phase (MI), a pseudogap regime (PG), a differentiation region (Diff) and finally a uniform Fermi liquid state (UM).

The electronic density n is shown as a function of the chemical potential μ in Fig. 4.1a (blue curve). It displays a clear plateau at $n = 1$ for μ between 0.56 eV and 1.16 eV, confirming that the system is a Mott insulator at half-filling [83, 100, 187]. The width of the plateau $\simeq 0.6$ eV is consistent with Ref. [24].

In Fig. 4.1b and 4.2 are displayed the spectral intensities $A_\pm(\omega = 0)$ at the Fermi level as well as the zero-frequency self-energies $\Sigma_\pm(\omega = 0)$ as a function of the chemical potential μ. These quantities are obtained by extrapolating to zero Matsubara frequencies results obtained by Monte Carlo

$$A_\pm(0) = -\frac{1}{\pi} \lim_{i\omega_n \to 0} \mathrm{Im} G_\pm(i\omega_n), \tag{4.2}$$

$$\Sigma_\pm(0) = \lim_{i\omega_n \to 0} \Sigma_\pm(i\omega_n). \tag{4.3}$$

For completeness, we have included plots of the Matsubara frequency Green's functions and self-energies for several chemical potentials in Appendix A.1.

4.1.2 The four doping regimes

These results allow to identify four distinct doping regimes. For chemical potentials smaller than $\mu = 1.16$ eV, the system is in a Mott insulating regime and both the even (+) and odd (−) components of the spectral intensity at the Fermi level are zero, $A_\pm(0) = 0$ (also both Matsubara Green's functions $G_\pm(i\omega_n)$ have clear insulating character, see Appendix A.1). This is compatible with the location of the Mott plateau in Fig. 4.1a.

Correlation effects are especially visible in the real parts of the self-energies. As both imaginary parts vanish, the effective low-energy band structure is split by the real parts of the self-energy in Eq. (3.15) and no excitations exist at zero frequency. More precisely, the quasiparticle equation

$$\det\left\{(\omega + \mu)\mathbf{1} - H^{\mathrm{eff}}_{1/2}(\mathbf{k}) - \hat{\Sigma}(\omega)\right\} = 0 \tag{4.4}$$

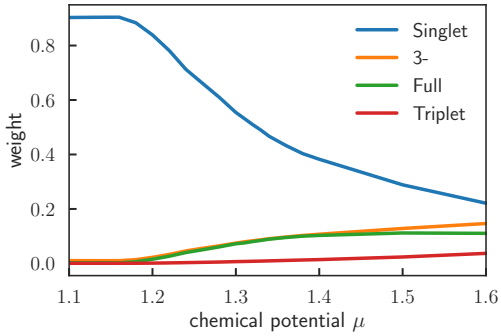

Figure 4.3 – Statistical weights of states dominating the Monte Carlo sampling on the dimer cluster of the CDMFT approach, as a function of the chemical potential μ. The dominant state is found to be the 2-electron inter-site singlet (blue). As doping level is increased, the three-electrons odd parity state catches up, denoted here as $3-$ (orange) $-$ as well as the fully occupied state (green), while the 2-electron triplet state (red) has a smaller weight. Other contributions are negligible.

has no solutions at $\omega = 0$ for all values of $\mathbf{k}$.

When μ lies between 1.16 eV and 1.32 eV, the system enters a *pseudogap* regime. The even component of the Green's function, that provides a coarse-grained picture of the physics close to the antinode $\mathbf{k} = (\pi, 0)$, maintains its insulating character ($A_+(0) = 0$) while the odd component, describing the nodal region close to $\mathbf{k} = (\pi/2, \pi/2)$, becomes metallic ($A_-(0) \neq 0$). This describes a metal that only has coherent quasiparticles close to the node. Antinodal particles are suppressed by lifetime effects, as can be seen from the negative imaginary part of the even self-energy $\mathrm{Im}\Sigma_+(0)$. It reaches -0.1 eV in Fig. 4.2, while $\mathrm{Im}\Sigma_-(0)$ remains very small. This regime is very reminiscent of the pseudogap region of superconducting cuprates, and we indeed show below that the spectral function exhibits a pseudogap at $\mathbf{k} = (\pi, 0)$ in this region.

As the electron doping is further increased, for $1.32 \leq \mu \leq 1.45$ eV, spectral weight starts to appear in $A_+(0)$, an indication that quasiparticles form at the antinode as well. However, there are still visible differences between the even and odd components of the self-energies. [1] The regime is therefore characterized by a visible $\mathbf{k}$-space differentiation where lifetime effects are stronger at the antinode than at the node ($\mathrm{Im}\Sigma_+(0) < \mathrm{Im}\Sigma_-(0)$) but do not completely destroy quasiparticles.

Eventually, for μ above 1.45 eV, a uniform metallic regime settles where both self-energies are identical and $\mathbf{k}$-space differentiation has disappeared. This regime would be well described by a single-site DMFT calculation.

It should be emphasized that boundaries delimiting these different regimes correspond to crossovers and hence are here defined in a qualitative manner.

The physical mechanism responsible for the formation of the pseudogap and the strong nodal-antinodal dichotomy observed at low doping can be revealed by studying the many-body states associated with the 2-site cluster. Calculating these states' histogram, we identify those that contribute most to the stochastic sampling within the CT-HYB quantum impurity solver. This is shown in Fig. 4.3, where it is clear that the system is dominated by the intra-dimer singlet state at low doping levels. This is a strong indication that physics in this regime is governed by the formation of short-range antiferromagnetic correlations between neighboring sites.

4.2 Fermi surface and pseudogap

4.2.1 Periodization of the self-energy

Within CDMFT, the lattice Green's function given by Eq. (3.14) breaks translational symmetry [87], hence making a direct comparison to momentum-resolved ARPES experiments difficult. The lattice self-energy in CDMFT only having components inside a unit cell but not between different unit cells is the

1. See also Appendix A.1.

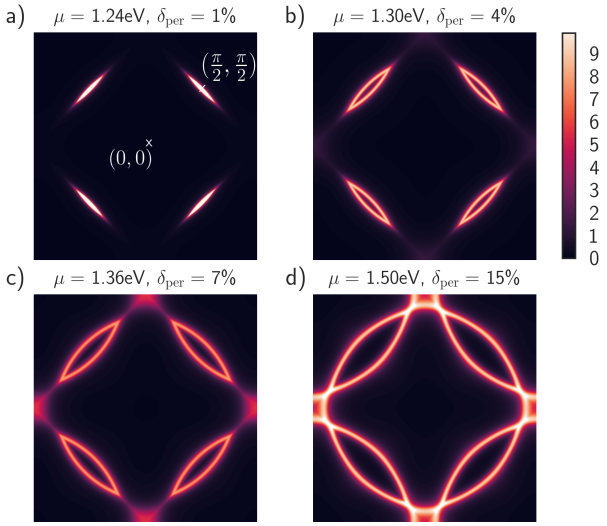

Figure 4.4 – Spectral intensity at the Fermi surface upon increasing doping level.

reason for the symmetry breaking. A natural way to restore the translational symmetry is to *periodize* the self-energy by propagating the intersite contribution Σ_{AB} over all links on the lattice. An artefact of this scheme is that it prevents the formation of a Mott insulator and gives a wrong description of the low-doping physics.[2] We therefore design a different periodization that yields physical results and preserves the existence of the Mott insulator. In this scheme, the lattice self-energy is given by

$$\tilde{\Sigma}^{\text{latt}}(i\omega_n, \mathbf{k}) = \begin{pmatrix} \Sigma_{AA} & \Sigma_{AB} \times e^{-i\frac{k_1+k_2}{2}} \\ \Sigma_{AB} \times e^{i\frac{k_1+k_2}{2}} & \Sigma_{AA} \end{pmatrix}, \tag{4.5}$$

where $\mathbf{k} = (k_1, k_2)$ is expressed in the reduced Brillouin zone. With this self-energy, we then define a periodized lattice Green's function $\tilde{G}^{\text{latt}}$ according to

$$\tilde{G}^{\text{latt}}(i\omega_n, \mathbf{k}) = \left\{ i\omega_n + \mu - H^{\text{eff}}_{1/2}(\mathbf{k}) - \tilde{\Sigma}^{\text{latt}}(i\omega_n, \mathbf{k}) \right\}^{-1}. \tag{4.6}$$

This Green's function preserves all the symmetries of the lattice and will be the basis of our analysis below.

As a consistency check we first compute in Fig. 4.1a the electronic density n as a function of μ obtained from $\tilde{G}$ (orange curve). Comparing it to the cluster density (blue curve) discussed in Sec. 4.1, we see that plateaus at $n = 1$ match well, confirming the existence of a Mott insulator within our periodization scheme. However, the periodized density generally has a slightly lower value compared to the cluster density for a given chemical potential. In the following, we discuss our results for specific values of μ and thus indicate two corresponding values of the electron doping: the cluster and the periodized one (resp. δ_{cluster} and δ_{per}).

4.2.2 Spectral intensities

We plot in Fig. 4.4 the spectral intensity at the Fermi surface for four values of the chemical potential. At small doping levels, for $\mu \leq 1.30$ eV, nodal pockets with coherent quasiparticles develop while the antinodal intensity is completely suppressed. A close inspection of the spectral function at $\mathbf{k} = (\pi, 0)$ for $\mu = 1.30$ eV confirms the presence of a clear pseudogap, as discussed previously: Fig. 4.5 shows the leading edge of the spectrum being shifted away from zero energy. We attribute its formation to short-range antiferromagnetic correlations (manifested here as the dominance of inter-site singlet dimer formation in our cluster as revealed by the histogram of states, see Fig. 4.3).

As the electron doping is increased, the $(\pi/2, \pi/2)$ pockets grow and spectral intensity starts to appear around $(\pi, 0)$, see panel c) of Fig. 4.4, leading to an extension of the Fermi surface over the Brillouin zone.

2. See Appendix A.2 for more details.

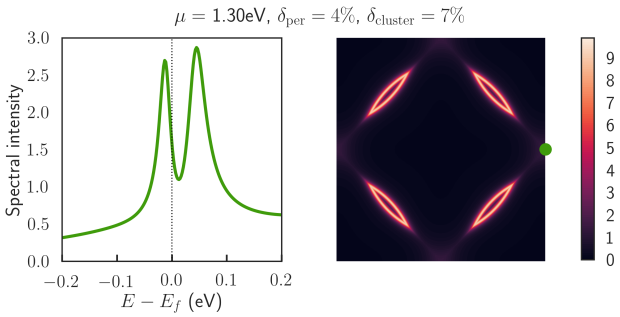

Figure 4.5 – *Left:* Spectral intensity $\mathrm{Tr}A(\omega, \mathbf{k}_{\mathrm{AN}})$ (Energy Distribution Curve - EDC) at the antinode $\mathbf{k}_{\mathrm{AN}} = (\pi, 0)$ for $\mu = 1.3$ eV. *Right:* Spectral intensity at the Fermi surface for the same μ.

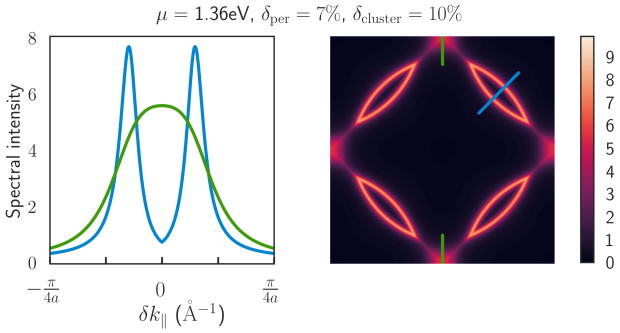

Figure 4.6 – *Left:* Spectral intensity at the Fermi surface $\mathrm{Tr}A(\omega = 0, \mathbf{k})$ (Momentum Distribution Curve - MDC) for $\mu = 1.36$ eV taken along the nodal (blue) and the antinodal (green) directions. *Right:* Spectral intensity at the Fermi surface for the same μ.

Quasiparticles are however far more incoherent and broader at the antinode, as can be seen from momentum cuts across the node or the antinode (Fig. 4.6). While sharp coherent quasiparticles are found at the node, those at the antinode display a lower spectral intensity that is broadened over a greater region of $\mathbf{k}$-space. This corresponds to the momentum-differentiation regime introduced above.

At larger doping, the self-energy becomes finally uniform and the resulting Fermi surface displays coherent quasiparticles both at the node and the antinode, as shown in the panel d) of Fig. 4.4.

4.3 Electronic band structure

4.3.1 Quasiparticle bands

We now turn to an analysis of the dispersion of quasiparticle bands in Sr_2IrO_4. This requires to analytically continue our imaginary-frequency data to the real axis. We use Padé approximants [166] to find $\tilde{\Sigma}^{\mathrm{latt}}(\omega, \mathbf{k})$ from the knowledge of the periodized lattice self-energy $\tilde{\Sigma}^{\mathrm{latt}}(i\omega_n, \mathbf{k})$. The resulting band structure is shown in Fig. 4.7 where we compare the insulating state at $\mu = 0.8$ eV (*left*) and the electron doped state at $\mu = 1.36$ eV, $\delta_{\text{per}} = 7\%$, $\delta_{\text{cluster}} = 10\%$ (*right*). On the upper panels, we show the noninteracting bands obtained by diagonalizing the TB + SO Hamiltonian $\mathcal{H}^{\mathrm{eff}}_{1/2}$ (dashed lines) and the quasiparticle bands obtained from the solutions of

$$\det\left\{(\omega + \mu)\mathbf{1} - H^{\mathrm{eff}}_{1/2}(\mathbf{k}) - \tilde{\Sigma}^{\mathrm{latt}}(\omega, \mathbf{k})\right\} = 0. \tag{4.7}$$

Bands are plotted along the $(\pi, \pi) - (\pi/2, \pi/2) - (0, 0) - (\pi, 0) - (2\pi, 0)$ path of the full Brillouin zone. Lower panels display the corresponding total spectral intensity $\mathrm{Tr}A(\omega, \mathbf{k})$.

In the insulating region, the Mott gap is clearly visible. The band structure indicates that correlation effects have split the original noninteracting bands. This is compatible with the observation that, at $\mu =$

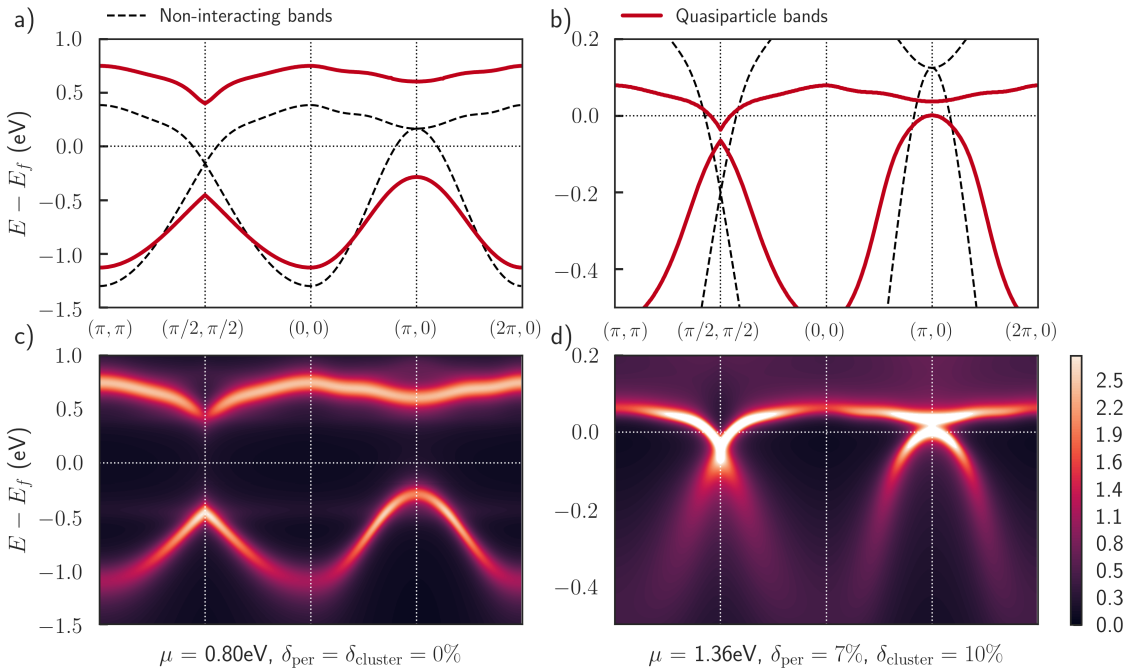

Figure 4.7 – Band dispersion of the insulating (a-c), $\mu = 0.8$eV, and doped (b-d), $\mu = 1.36$ eV, Sr_2IrO_4. *Upper panels:* Comparison between the non-interacting bands obtained from the TB + SO Hamiltonian $\mathcal{H}^{\rm eff}_{1/2}$ (dashed lines) and the quasiparticle bands. *Lower panels:* Spectral intensities.

0.8 eV, the cluster self-energies take very different values $\mathrm{Re}\Sigma_+(0) \neq \mathrm{Re}\Sigma_-(0)$. Lifetime effects are also not very strong and the bands are fairly coherent, consistent with the fact that $\mathrm{Im}\Sigma_\pm(0) \simeq 0$. The top of the lower band is located at $\simeq -0.4$ eV at the node and at $\simeq -0.2$ eV at the antinode. This in in good agreement with the position of the bands observed in ARPES experiments and presented in Fig. 3.3.

There is a direct gap to the unoccupied states of the order of 0.8 eV at $\mathbf{k} = (\pi/2, \pi/2)$, while the smallest overall gap is indirect and of order 0.6 eV. Note that the latter value is consistent with the width of the Mott plateau in Fig. 4.1a.

As we move to the doped region, the Mott gap first closes at the nodal point $\mathbf{k} = (\pi/2, \pi/2)$ and the quasiparticle bands merge. The crossing of the upper band at two points close to $(\pi/2, \pi/2)$ is a signature of the pocket seen in the previous spectral intensities. Around these points, a clear renormalization of the Fermi velocities by a factor $1/4$ is visible as compared to the non-interacting bands. For $\mu = 1.36$ eV there is still a gap between the bands at $\mathbf{k} = (\pi, 0)$ but the lower band just reaches the Fermi level, yielding some antinodal spectral weight. It is interesting to note that the correlation effects are much stronger on the lower band than on the upper band. Quasiparticles are then better defined at $(\pi/2, \pi/2)$ (they correspond to a crossing of the upper band) than at $(\pi, 0)$ where they are associated with the lower band. This is explained by the fact that the physics of the lower band is mainly controlled by the cluster Σ_+, while the upper band is controlled by Σ_-. As a result, the larger negative imaginary part of Σ_+ (see Fig. 4.2) induces stronger lifetime effects at the antinode, while the smaller imaginary part of Σ_- maintains coherent quasiparticles at the node.

This 'collapse' of the Mott gap (i.e the two bands becoming much closer to each other) is also found in the ARPES experiments, see Fig. 3.3. The location of the top of the band at the 'node' (-0.4 eV) and 'antinode' (-0.2 eV) are in good quantitative agreement with the experiments, as well as the rather round and spread behavior of the band at the node. On the other hand, the nodal part does not appear to be as narrow as it is observed.

We finally display in Fig. 4.8 a spectral intensity map along the $(\pi/2, \pi/2) - (\pi, 0)$ Brillouin zone path, which corresponds to the path along which the non-interacting bands are degenerate. ARPES data along this path have not appeared in print to our knowledge, and our results could be useful in the context of future

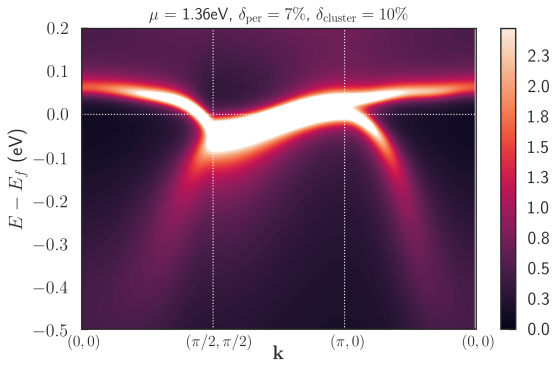

Figure 4.8 – Spectral intensity of the doped compound ($\mu = 1.36$eV) along the degenerate path $(0,0) - (\pi/2,\pi/2) - (\pi,0) - (0,0)$ in the full Brillouin zone

analysis of ARPES experiments.

4.3.2 Discussion and conclusions

Overall, there is excellent qualitative agreement between our results and ARPES experiments conducted on doped Sr_2IrO_4. The 'nodal-antinodal' differentiation and formation of a pseudogap near the 'antinode' is also consistent with the experimental observations [41, 85]. Here, the pseudogap is linked to short-range spin correlations, which would indicate the same physical origin as in superconducting cuprates (see e.g. Refs. [64, 183] for recent studies). Note that our results are also in good agreement with the recent theoretical approach from Ref. [101].

The value of the interaction parameter $U = 2$ eV for which we chose to perform our calculations should also be discussed in the context of experimental measurements, especially determinations of the Mott gap. With this value, we find a Mott gap which is indirect and of order ~ 0.6 eV $-$ corresponding to the transition between the top of the lower Hubbard band at $(\pi, 0)$ and the bottom of the upper Hubbard band at $(\pi/2, \pi/2)$ in Fig. 4.7a. It is also the width of the Mott plateau in Fig. 4.1a. The value of the optical gap would be slightly larger. In Ref. [24], Sr_2IrO_4 was studied under both hole (Rh) and electron (La) doping, allowing for a determination of a Mott gap of order 0.7 eV, in rather good agreement with the present work. Optical spectroscopy measurements (see e.g Fig. 4 in Ref. [83]) do reveal a sharp increase of absorption in that frequency range, but a rather slow onset of the optical conductivity is observed with spectral weight below this scale, possibly suggesting a significantly smaller value of the actual gap (although a precise determination is difficult). This suggests that the value of U used in the present work may be a bit too large. Accordingly, we note that the Fermi surface renormalizations obtained above appear to be somewhat larger than the values reported in Ref. [41].

Part III

Developments in determinant Monte Carlo algorithms for fermionic systems

Chapter 5

Continuous-time quantum Monte Carlo algorithms for fermionic systems

As presented in Chapter 2, quantum impurity problems play an important role in strongly correlated physics, either as representations of quantum dots, or as auxiliary problems used within the Dynamical Mean-Field Theory (DMFT) framework. However, designing robust methods to solve impurity problems over a wide range of temperatures and energy scales is in itself a great challenge.

Continuous-time quantum Monte Carlo (CT-QMC) algorithms [139, 140, 171, 173, 61, 62] have been a breakthrough in finding solutions of quantum impurity problems [53, 86, 72, 96, 87, 99]. These methods are based on a perturbation expansion of the partition function. The latter is then used as a probability distribution function in a Monte Carlo sampling of the quantity of interest (Green's function, density, ...). The series is not explicitly truncated at a specific order so that they are numerically exact in the limit of long computational time.

In this Chapter, we focus on two of them: the CT-INT, based on an expansion in the Coulomb repulsion U, and the CT-HYB, based on an expansion in the hybridization function Δ.

5.1 Perturbation expansion of the partition function

We consider a correlated impurity coupled to uncorrelated bath. Its Hamiltonian writes

$$\mathcal{H} = \mathcal{H}^0_{\rm loc} + \mathcal{H}^I_{\rm loc} + \mathcal{H}_{\rm hyb} + \mathcal{H}_{\rm bath}, \tag{5.1}$$

with $\mathcal{H}^0_{\rm loc}$ describing the non-interacting quadratic part of the impurity, $\mathcal{H}^I_{\rm loc}$ the correlations on the impurity, $\mathcal{H}_{\rm bath}$ the non-interacting bath, and $\mathcal{H}_{\rm hyb}$ the hybridization between the impurity and the bath.

For the sake of simplicity in upcoming formulas, we consider the single-impurity single-orbital Anderson model [7], whose Hamiltonian is

$$\mathcal{H} = \sum_\sigma \epsilon d^\dagger_\sigma d_\sigma + U n_{d\uparrow} n_{d\downarrow} + \sum_{\mathbf{k}\sigma} \left(\gamma_{\mathbf{k}} c^\dagger_{\mathbf{k}\sigma} d_\sigma + \text{h.c.} \right) + \sum_{\mathbf{k}\sigma} \epsilon_{\mathbf{k}} c^\dagger_{\mathbf{k}\sigma} c_{\mathbf{k}\sigma}, \tag{5.2}$$

where ϵ is the energy level of the impurity, $d^\dagger_\sigma$ (resp. d_σ) is the creation (resp. annihilation) operator for an electron with spin σ on the impurity, $\epsilon_{\mathbf{k}}$ describes the energy spectrum of the bath, $c^\dagger_{\mathbf{k}\sigma}$ (resp. $c_{\mathbf{k}\sigma}$) is the creation (resp. annihilation) operator for an electron with spin σ and momentum $\mathbf{k}$ in the bath, and finally $\gamma_{\mathbf{k}}$ is a coupling constant between the energy level of momentum $\mathbf{k}$ of the bath and the impurity.

This can be reformulated as an action using an imaginary-time path integral [119]

$$\begin{aligned} \mathcal{S} = \sum_\sigma \int_0^\beta \mathrm{d}\tau d^\dagger_\sigma(\tau) \left(\partial_\tau + \epsilon\right) d_\sigma(\tau) + U \int_0^\beta \mathrm{d}\tau \; n_{d\uparrow}(\tau) n_{d\downarrow}(\tau) \\ + \sum_\sigma \int_0^\beta \mathrm{d}\tau \mathrm{d}\tau' d^\dagger_\sigma(\tau) \Delta_\sigma(\tau - \tau') d_\sigma(\tau') \end{aligned} \tag{5.3}$$

The hybridization function Δ is defined in Matsubara frequency as $\Delta_\sigma(i\omega_n) = \sum_{\mathbf{k}} \frac{|\gamma_{\mathbf{k}}|^2}{i\omega_n - \epsilon_{\mathbf{k}}}$. The partition function is then expressed as an integral over Grassmann variables

$$Z = \int \mathcal{D}[d_\sigma^\dagger, d_\sigma] e^{-\mathcal{S}}, \tag{5.4}$$

and the interacting Green's function of the impurity is

$$G_\sigma(\tau) = -\frac{1}{Z}\int \mathcal{D}[d_\sigma^\dagger, d_\sigma] e^{-\mathcal{S}} d_\sigma(\tau) d_\sigma^\dagger(0) = -\frac{1}{\beta}\frac{\delta \ln Z}{\delta \Delta_\sigma(-\tau)}. \tag{5.5}$$

Eq. (5.4) is the starting point of the development of CT-QMC algorithms, which construct a perturbation expansion of the partition function, either in the Coulomb interaction U or in the hybridization function Δ. This expansion is then used in an importance sampling of another quantity of interest such as the Green's function.

5.1.1 Expansion in the Coulomb interaction

We define the bare part of the action to be

$$\begin{aligned} \mathcal{S}_0 &= \sum_\sigma \int_0^\beta \mathrm{d}\tau d_\sigma^\dagger(\tau)\left(\partial_\tau + \epsilon\right) d_\sigma(\tau) + \sum_\sigma \int_0^\beta \mathrm{d}\tau \mathrm{d}\tau' d_\sigma^\dagger(\tau)\Delta_\sigma(\tau-\tau') d_\sigma(\tau') \\ &= -\sum_\sigma \int_0^\beta \mathrm{d}\tau \mathrm{d}\tau' d_\sigma^\dagger(\tau) g_\sigma^{-1}(\tau-\tau') d_\sigma(\tau'), \end{aligned} \tag{5.6}$$

where $g_\sigma^{-1}(i\omega_n) = i\omega_n - \epsilon - \Delta_\sigma(i\omega_n)$ is the noninteracting Green's function. The associated partition function is $Z_0 = \int \mathcal{D}[d_\sigma^\dagger, d_\sigma] e^{-\mathcal{S}_0}$ and the average of an operator A with respect to $\mathcal{S}_0$ is

$$\langle A \rangle_0 = \int \mathcal{D}[d_\sigma^\dagger, d_\sigma] e^{-\mathcal{S}_0} A. \tag{5.7}$$

The partition function of the full system now rewrites

$$\begin{aligned} Z &= \int \mathcal{D}[d_\sigma^\dagger, d_\sigma] e^{-\mathcal{S}} = Z_0 \left\langle T_\tau e^{-U\int_0^\beta \mathrm{d}\tau n_{d\uparrow}(\tau) n_{d\downarrow}(\tau)} \right\rangle_0 \\ &= Z_0 \sum_n \int_0^\beta \mathrm{d}\tau_1 \ldots \mathrm{d}\tau_n \frac{(-U)^n}{n!} \prod_\sigma \left\langle T_\tau n_{d\sigma}(\tau_1)\ldots n_{d\sigma}(\tau_n)\right\rangle_0 . \end{aligned} \tag{5.8}$$

Because $\mathcal{S}_0$ describes a noninteracting system, we use Wick's theorem [178] to express the above expectation values as determinants

$$Z = Z_0 \sum_n \int_0^\beta \mathrm{d}\tau_1 \ldots \mathrm{d}\tau_n \frac{(-U)^n}{n!} \det D_n^\uparrow \det D_n^\downarrow, \tag{5.9}$$

where $(D_n^\sigma)_{ij} = g_\sigma(\tau_i - \tau_j)$. Note that the $1/n!$ factor, originating from the expansion of the exponential, ensures the convergence of the series. We are not considering a "weak-coupling" limit here: the series is infinite and not explicitly truncated at low orders.

As we will discuss in more detail in Section 5.2, the CT-INT algorithm samples the partition function (5.9) using Monte Carlo techniques in order to compute the physical quantities of interest [139, 62].

5.1.2 Expansion in the hybridization function

The local part of the action is defined to be

$$\mathcal{S}_{\mathrm{loc}} = \sum_\sigma \int_0^\beta \mathrm{d}\tau d_\sigma^\dagger(\tau)\left(\partial_\tau + \epsilon\right) d_\sigma(\tau) + U\int_0^\beta \mathrm{d}\tau\, n_{d\uparrow}(\tau) n_{d\downarrow}(\tau), \tag{5.10}$$

associated with the local Hamiltonian

$$\mathcal{H}_{\rm loc} = \sum_\sigma \epsilon d_\sigma^\dagger d_\sigma + U n_{d\uparrow} n_{d\downarrow}. \tag{5.11}$$

This action is not quadratic in the d operators, and Wick's theorem cannot be applied. The local partition function is $Z_{\rm loc} = {\rm Tr}\left(-e^{\beta \mathcal{H}_{\rm loc}}\right)$ and the average of an operator A with respect to $\mathcal{S}_{\rm loc}$ is

$$\langle A \rangle_{\rm loc} = \frac{{\rm Tr}\left(e^{-\beta \mathcal{H}_{\rm loc}} A\right)}{Z_{\rm loc}}. \tag{5.12}$$

In this expansion, the partition function of the full system writes

$$\begin{aligned} Z &= Z_{\rm loc} \left\langle T_\tau e^{-\sum_\sigma \int_0^\beta {\rm d}\tau {\rm d}\tau' d_\sigma^\dagger(\tau)\Delta_\sigma(\tau-\tau')d_\sigma(\tau')} \right\rangle_{\rm loc} \\ &= {\rm Tr}\left(T_\tau e^{-\beta H_{\rm loc}} \prod_\sigma \sum_n \frac{(-1)^n}{n!} \int_0^\beta {\rm d}\tau_1 \dots {\rm d}\tau_n' \prod_{i=1}^n d_\sigma^\dagger(\tau_i)\Delta_\sigma(\tau_i - \tau_i')d_\sigma(\tau_i') \right). \end{aligned} \tag{5.13}$$

This expression can be simplified as

$$\begin{aligned} Z = \sum_{n_\uparrow, n_\downarrow} \int_0^\beta {\rm d}\tau_1^\uparrow \dots {\rm d}\tau_{n_\uparrow}^{'\uparrow} \int_0^\beta {\rm d}\tau_1^\downarrow \dots \tau_{n_\downarrow}^{'\downarrow} \left(\prod_\sigma \frac{\det \hat{\Delta}_n^\sigma}{(n_\sigma!)^2} \right) \times \\ {\rm Tr}\left(T_\tau e^{-\beta H_{\rm loc}} \prod_\sigma d_\sigma^\dagger(\tau_i^\sigma) d_\sigma(\tau_i^{'\sigma}) \right), \end{aligned} \tag{5.14}$$

where $\left(\hat{\Delta}_n^\sigma\right)_{ij} = \Delta_\sigma(\tau_i^\sigma - \tau_j^{'\sigma})$. We see that the evaluation of the partition function now relies on a trace over atomic states, which will severely restrict the number of orbitals that can be considered. Note once again that the $1/(n_\sigma!)^2$ factor ensures the convergence of the series.

The CT-HYB algorithm now aims at sampling the partition function (5.14) using Monte Carlo techniques (see below), in order to compute physical quantities of interest [171, 173, 62].

5.2 Evaluating the partition function: Monte Carlo sampling

In both expansions, the partition function is written as an infinite series with some expansion parameter (either the Coulomb repulsion or the hybridization function)

$$Z = \sum_n Z_n, \tag{5.15}$$

where the order-n contribution can be written as a multi-dimensional integral over "inner variables" x_i

$$Z_n = \int {\rm d}x_1 \dots {\rm d}x_n \; Z(x_1, \dots, x_n). \tag{5.16}$$

Evaluating multi-dimensional integrals is a very complex problem, and an efficient way to tackle it is by using a Monte Carlo sampling. In this Section, we recall the basics of such procedures on a general level, [1] and focus on the two perturbation expansions we saw above by describing the CT-INT and CT-HYB algorithms.

5.2.1 Monte Carlo basics

Let us start with a simple 1D example: the evaluation of the integral of a function f defined on the real axis. We decompose f as $\omega \times g$, such that ω can be interpreted as a probability distribution function: $\omega \geq 0$ and $\int \omega = 1$. The Monte Carlo sampling consists in rewriting the integral over f in the following way:

$$\int {\rm d}x \; f(x) = \int {\rm d}x \; \omega(x) g(x) \sim \sum_{\mathfrak{c}}^{\rm MC} g(\mathfrak{c}). \tag{5.17}$$

1. For a detailed introduction to Monte Carlo methods, see for instance [91] and [89].

Instead of computing $\omega \times g$ for all points x on the real axis, we evaluate g over a subset of points **distributed according to** ω. Each of these points is called a *configuration* and denoted $\mathfrak{c}$. We define the *weight* of a configuration as $w_{\mathfrak{c}} = \omega(\mathfrak{c})$. Note that we add a 'MC' superscript on the sum to denote that it is computed using Monte Carlo techniques. When there is a possible ambiguity, we might also specify which function is used as a weight. [2]

For a finite number N of uncorrelated configurations visited, the Monte Carlo sum only provides an estimate of the final result (hence the $\sim$ notation). However, the central limit theorem states that the standard deviation of the distribution scales as $1/\sqrt{N}$, meaning that for a long enough computational time, the algorithm will converge to the exact value of the integral. Methods following this property are called *numerically exact*.

Going back to the problem at hand, we define a configuration to be the perturbation order n as well as a set of inner variables:

$$\mathfrak{c} = \{n; x_1, \dots, x_n\}. \tag{5.18}$$

Those will typically be the imaginary time variables that appear in Eqs. (5.9) and (5.14). The weight of a configuration is chosen to be $w_{\mathfrak{c}} = |Z(x_1, \dots, x_n)| = |Z(\mathfrak{c})|$, so that the order-$n$ contribution to the partition function writes

$$Z_n = \int \mathrm{d}x_1 \dots \mathrm{d}x_n \ |Z(x_1, \dots, x_n)| \operatorname{sgn}\left(Z(x_1, \dots, x_n)\right) \sim \sum_{\mathfrak{c}}^{\mathrm{MC}} \operatorname{sgn} Z(\mathfrak{c}). \tag{5.19}$$

For the **CT-INT** algorithm, which aims at sampling Eq. (5.9), we define a configuration by the perturbation order n and a set of imaginary times: $\mathfrak{c} = \{n; \tau_1, \dots, \tau_n\}$, and the Monte Carlo weight is

$$w_{\mathfrak{c}} = \frac{U^n}{n!} \left| \det D_n^{\uparrow} \det D_n^{\downarrow} \right|. \tag{5.20}$$

The partition function now rewrites

$$Z = Z_0 \sum_{\mathfrak{c}}^{\mathrm{MC}} (-1)^n \operatorname{sgn} \left(\prod_{\sigma} \det D^{\sigma}(\mathfrak{c}) \right). \tag{5.21}$$

For the **CT-HYB** algorithm, which aims at sampling Eq. (5.14), a configuration is defined by the perturbation orders $n_\uparrow$ and $n_\downarrow$, and n_σ "segments" $\{\tau_i^\sigma, \tau_i'^\sigma\}$ for each spin: $\mathfrak{c} = \{n_\uparrow, n_\downarrow; \{\tau_i^\sigma, \tau_i'^\sigma\}_{1 \le i \le n_\sigma}\}$, and the Monte Carlo weight is

$$w_{\mathfrak{c}} = \left| \left(\prod_{\sigma} \frac{\det \hat{\Delta}_n^{\sigma}}{(n_\sigma!)^2} \right) \times \operatorname{Tr} \left(T_\tau e^{-\beta H_{\mathrm{loc}}} \prod_{i\sigma} d_\sigma^\dagger(\tau_i^\sigma) d_\sigma(\tau_i'^\sigma) \right) \right|. \tag{5.22}$$

The partition function now rewrites

$$Z = \sum_{\mathfrak{c}}^{\mathrm{MC}} \operatorname{sgn} \left(\left(\prod_{\sigma} \det \hat{\Delta}^{\sigma}(\mathfrak{c}) \right) \times \operatorname{Tr} \left(T_\tau e^{-\beta H_{\mathrm{loc}}} \prod_{i\sigma} d_\sigma^\dagger(\tau_i^\sigma) d_\sigma(\tau_i'^\sigma) \right) \right). \tag{5.23}$$

In the CT-QMC algorithms, we therefore accumulate the sign of the partition function over configurations sampled according to the absolute value of Z. The partition function can then be seen as a 'tool' to move into configuration space, the main goal of the algorithm being the sampling of physical quantities such as the density or the Green's function, see Section 5.2.3. In fermionic simulations, $Z(\mathfrak{c})$ often becomes negative due to the anticommutation relations between fermionic operators, which can lead to a drastic increase in error bars known as the *sign problem*. We discuss this effect in more detail in Sec. 5.3.1.

2. This will be the case in Chapter 9 where we discuss out-of-equilibrium diagrammatic MC algorithms.

5.2.2 Markov chain

In a Monte Carlo algorithm, new configurations have to be chosen in order to efficiently sample the probability distribution function. A common way to do so is to construct a Markov chain in configuration space using the Metropolis-Hastings algorithm [107, 67]. Knowing the probability $T_{\mathfrak{c}\mathfrak{c}'}$ to propose configuration $\mathfrak{c}'$ after configuration $\mathfrak{c}$, the new configuration $\mathfrak{c}'$ is accepted or rejected according to the Metropolis ratio

$$p_{\mathfrak{c}\to\mathfrak{c}'}^{\text{accept}} = \min\left(1, \frac{T_{\mathfrak{c}'\mathfrak{c}} w_{\mathfrak{c}'}}{T_{\mathfrak{c}\mathfrak{c}'} w_{\mathfrak{c}}}\right). \tag{5.24}$$

For the **CT-INT**, two kinds of moves are in general enough for the algorithm to be ergodic: the insertion and the removal of an imaginary time. Common moves for the **CT-HYB** are the addition of a new segment, the removal of an existing one, and the cutting of a segment into two new ones.

5.2.3 Measurements

The sampling of Z is generally used as a tool to measure more interesting quantities for the model we are considering: the Green's function, the density, the self-energy... Let us denote such an object by $\mathcal{M}$, that we express in the form

$$\mathcal{M} = \int \mathrm{d}x_1 \dots \mathrm{d}x_n \, \mathcal{M}(x_1, \dots, x_n) Z(x_1, \dots, x_n) \sim \sum_{\mathfrak{c}}^{\text{MC}} \mathcal{M}(\mathfrak{c}) \text{sgn}\, Z(\mathfrak{c}). \tag{5.25}$$

In the Monte Carlo algorithm, configurations are therefore sampled according to $w_{\mathfrak{c}} = |Z(\mathfrak{c})|$, but we can measure any quantity of interest by accumulating $\mathcal{M}(\mathfrak{c})\text{sgn}\, Z(\mathfrak{c})$.

Let us consider the specific case of the Green's function, which is linked to the partition function through Eq. (5.5). Combining this with Eq. (5.21), gives the expression of G in the **CT-INT** algorithm

$$G_\sigma(\tau) = g_\sigma(\tau) - \frac{1}{\beta Z} g_\sigma(-\tau)^2 \sum_{\mathfrak{c}\in\mathcal{C}}^{\text{MC}} (-1)^n \sum_{ij} \left(D^\sigma(\mathfrak{c})\right)^{-1}_{ij} \delta(\tau_i - \tau_j + \tau) \times \text{sgn}\left(\prod_{\sigma'} \det D^{\sigma'}(\mathfrak{c})\right) \tag{5.26}$$

For the **CT-HYB** algorithm, the Green's function is obtained as

$$\begin{aligned} G_\sigma(\tau) = &- \frac{1}{\beta Z} \sum_{\mathfrak{c}\in\mathcal{C}}^{\text{MC}} \sum_{ij} (\hat{\Delta}_\sigma(\mathfrak{c}))^{-1}_{ij} \delta(\tau_i - \tau_j + \tau) \\ &\times \text{sgn}\left(\left(\prod_{\sigma'} \det \hat{\Delta}^{\sigma'}(\mathfrak{c})\right) \text{Tr}\left(T_\tau e^{-\beta H_{\text{loc}}} \prod_{\sigma'} d^\dagger_{\sigma'}(\tau_i^{\sigma'}) d_{\sigma'}(\tau_i'^{\sigma'})\right)\right) \end{aligned} \tag{5.27}$$

Note that in both algorithms, a given configuration will only allow us to accumulate contributions at imaginary times that correspond to the difference of two τ_i because of the delta function.

5.3 Strengths and limitations of CT-QMC algorithms

5.3.1 The fermionic sign problem

In all CT-QMC algorithms, the physical quantity we accumulate, such as the Green's function, is proportional to the *sign* of the partition function. In fermionic simulations, individual contributions to Z may have alternating signs due to the anticommutation relations between operators that can lead to cancellations between individual measurements and exponentially growing errors.

To quantify this effect, we reproduce here the argument of Ref. [62]. Let us consider the average value of the sign of contributions to the partition function

$$\langle \text{sgn} \rangle = \frac{\int \mathrm{d}x_1 \dots \mathrm{d}x_n \, \text{sgn}\left(Z(x_1, \dots, x_n)\right) |Z(x_1, \dots, x_n)|}{\int \mathrm{d}x_1 \dots \mathrm{d}x_n \; |Z(x_1, \dots, x_n)|} = \frac{Z}{\overline{Z}} = e^{-\beta \Delta F}, \tag{5.28}$$

where $\bar{Z}$ is the partition function of the system without sign problem, and ΔF the difference in free energy between this system and the original one. The variance of the sign is

$$\text{var sgn} = \langle \text{sgn}^2 \rangle - \langle \text{sgn} \rangle^2 = 1 - e^{-2\beta \Delta F}, \tag{5.29}$$

which is very close to 1 as soon as the system is quantitatively different from the bosonic system. The relative error after N masurements is defined as the error bar divided by the mean value

$$\Delta \text{sgn} = \frac{\sqrt{\text{var sgn}}}{\sqrt{N}} \times \frac{1}{\langle \text{sgn} \rangle} \simeq \frac{e^{\beta \Delta F}}{\sqrt{N}}. \tag{5.30}$$

This equation shows why we talk about a sign *problem*: the relative error grows exponentially when increasing the system size or decreasing the temperature. Though it depends on the representation chosen, its magnitude is an inherent property of the system at hand. For example, the Anderson impurity problem has no sign problem. More generally, it worsens when the number of sites of orbitals in the system increases. Impurity problems thus tend to have less severe sign problems than comparable finite-size lattice models. It is believed to be nondeterministic polynomial (NP) hard [160].

In this Thesis, one of our main focus is the development of novel quantum algorithms, both in imaginary and real time, that aim at taming this sign problem by taking care of cancellations directly in the computation of the MC weight.

Redefinition of non-interacting propagators: the α-shift

In the interaction-expansion based CT-INT algorithm, the sign problem can be strongly mitigated, or even completely cured in some cases, by a redefinition of both the local interaction and the noninteracting propagators [140, 128, 137, 183].

The action of Eq. (5.3) and (5.6) can be seen as a function of U

$$\mathcal{S}[U] = -\sum_{\sigma} \int_0^{\beta} \mathrm{d}\tau \mathrm{d}\tau' d_{\sigma}^{\dagger}(\tau) g_{\sigma}^{-1}(\tau - \tau') d_{\sigma}(\tau') + U \int_0^{\beta} \mathrm{d}\tau \; n_{d\uparrow}(\tau) n_{d\downarrow}(\tau). \tag{5.31}$$

Let us label U_{φ} the physical value of U that we are interested in. In order to optimize the sign problem, we introduce a modified action depending on two scalars $\alpha_{\uparrow}$ and $\alpha_{\downarrow}$

$$\begin{aligned} \tilde{\mathcal{S}}[U] = -\sum_{\sigma} \int_0^{\beta} \mathrm{d}\tau \mathrm{d}\tau' d_{\sigma}^{\dagger}(\tau) \left[g_{\sigma}^{-1}(\tau - \tau') - U_{\varphi} \alpha_{\bar{\sigma}} \delta(\tau - \tau') \right] d_{\sigma}(\tau') \\ + U \int_0^{\beta} \mathrm{d}\tau (n_{\uparrow}(\tau) - \alpha_{\uparrow})(n_{d\downarrow}(\tau) - \alpha_{\downarrow}), \end{aligned} \tag{5.32}$$

so that $\mathcal{S}[U = U_{\varphi}] = \tilde{\mathcal{S}}[U = U_{\varphi}]$ up to an unessential constant. The series in U of $\tilde{\mathcal{S}}$ is therefore fundamentally different from the one of $\mathcal{S}$, but both coincide for the physical value of the interaction we are interested in.

Upon the implementation of this α-shift, the partition function still writes

$$Z = Z_0 \sum_n \int_0^{\beta} \mathrm{d}\tau_1 \dots \mathrm{d}\tau_n \frac{(-U)^n}{n!} \det D_n^{\uparrow} \det D_n^{\downarrow}, \tag{5.33}$$

except now $(D_n^{\sigma})_{ij} = \tilde{g}_{\sigma}(\tau_i - \tau_j) - \alpha_{\sigma} \delta_{ij}$, where $\tilde{g}$ is the redefined noninteracting propagator

$$\tilde{g}_{\sigma}(i\omega_n) = \frac{1}{i\omega_n - \epsilon - \Delta_{\sigma}(i\omega_n) - U_{\varphi} \alpha_{\bar{\sigma}}}. \tag{5.34}$$

Tuning α can then drastically reduce the sign problem.

5.3.2 Domains of application

Let us first discuss in what regimes the CT-INT and CT-HYB algorithms work best [62].

The CT-HYB algorithm, due to the expansion in the hybridization expansion, can treat arbitrarily complicated interactions, and it does not have a strong limitation in temperature. However, the implementation of the trace in Eq. (5.14) requires dealing with matrices whose sizes grow exponentially with the Hilbert space, hence limiting the number of orbitals and sites accessible. The algorithm also suffers from a very strong sign problem if the hybridization function has off-diagonal components. As a result, it is often used to describe the properties of systems with partially filled d and f shells, where it can treat the full complexity of general multiplet interactions. For example, it has recently allowed precise computations of the Hall coefficient in Sr_2RuO_4 [189]. The results on the electronic structure of Sr_2IrO_4 presented at the beginning of this Thesis were also obtained using this algorithm.

The CT-INT algorithm, however, scales as a power law with system size, which makes it more suitable for clusters extensions of dynamical mean-field theory. On the other side, it faces strong limitations in temperature and it is mostly limited to density-density interactions. The auxiliary-field version of this algorithm has for example been used to compute the superconducting phase diagram of the 2D Hubbard model [63].

Taking a broader perspective, one of the reasons for the success of the continuous-time quantum Monte Carlo algorithms is that they are based on a perturbation expansion of the partition function Z. As we saw previously, contributions to Z can be reorganized into determinants that effectively sum a factorial number of perturbation diagrams and automatically take care of some cancellations between them. As a result, large perturbation orders can be computed.

Sampling the partition function is also a drawback of CT-QMC algorithms. As useful as they are to solve impurity problems, these methods face a strong limitation with the system size N. For the CT-HYB, we have seen that it is the size of the Hilbert space that prevents us to reach large systems. For the CT-INT, the average perturbation order in the sampling of the partition function scales as $U\beta N$. In realistic systems, it is then common to reach perturbation order 100 to 200. In both cases, the algorithm faces an exponential sign problem.

Those limitations are the reason why novel methods have been developed, that directly work in the thermodynamic limit by sampling the diagrammatic expansion of the quantities of interest on the lattice, as we present in the next Chapter.

Chapter 6

Towards the thermodynamic limit: diagrammatic Monte Carlo algorithms

The continuous-time quantum Monte Carlo algorithms presented in Chapter 5 work remarkably well for quantum impurity models but face strong limitations when it comes to problems defined on large (or infinite) lattices. It is therefore desirable to develop methods that can address the thermodynamic limit, that is the limit of infinite system size with fixed density of particles.

In this Chapter, we present alternative and complementary methods to CT-QMC algorithms. Based on an expansion in the Coulomb interaction U, they directly sample contributions to the physical quantities, such as the Green's function, and not the partition function. A pictorial representation in terms of Feynman diagrams is used, hence their name of 'diagrammatic' algorithms [129, 130, 88, 73, 22, 135]. We also describe recent advances that show how one can use determinants to sum all topologies of diagrams relevant for correlators in the Monte Carlo weight [135].

In the following, we consider lattice models described by a noninteracting action $\mathcal{S}_0$ and a local interaction of the form $Un_{i\uparrow}n_{i\downarrow}$ where i is a site index. The noninteracting Green's function associated with $\mathcal{S}_0$ is labelled g.

6.1 Diagrammatic Monte Carlo

We start with a brief introduction to Feynman diagrams, before showing how we expand physical quantities such as the Green's function or the self-energy as infinite series of diagrams. We then present diagrammatic Monte Carlo that aims at stochastically sampling the individual contributions to these series.

6.1.1 Introduction to Feynman diagrams: the expansion of the partition function revisited

We have seen in Section 5.1.1 that the partition function can be expressed as a series in the Coulomb interaction U

$$Z = Z_0 \sum_n \int \mathrm{d}x_1 \dots \mathrm{d}x_n \frac{(-U)^n}{n!} \left\langle \prod_\sigma T_\tau n_\sigma(x_1) \dots n_\sigma(x_n) \right\rangle_0 , \tag{6.1}$$

where x_i is now a composite index encapsulating both the position on the lattice and the imaginary time: $x_i = (\vec{r}_i, \tau_i)$. The notation $\int \mathrm{d}x_i$ is a compact way of writing $\int_0^\beta \mathrm{d}\tau_i \sum \vec{r}_i$.

Instead of rewriting the average value $\langle \dots \rangle_0$ as a product of determinants, we now choose to represent it using Feynman diagrams. [1] It is a powerful method that illustrates operator contractions in Wick's theorem, therefore expressing each term of the perturbation series as a picture composed of noninteracting lines and

1. For a complete introduction to Feynman diagrams and their construction, we refer the reader to [119] and [25].

interaction vertices. They are composed of two main ingredients: straight lines represent noninteracting Green's functions

$$x_2 \xrightarrow{\sigma} x_1 \quad = g_\sigma(x_1, x_2), \tag{6.2}$$

and interaction vertices are pictured by wiggly lines between propagators with opposite spins. Note that every fermion loop in a Feynman diagram brings an additional (-1) factor.

For example, the following diagram is a compact way to represent an order-2 contribution to the partition function:

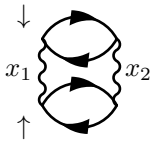

$$= U^2 \int \mathrm{d}x_1 \mathrm{d}x_2 \prod_\sigma g_\sigma(x_1, x_2) g_\sigma(x_2, x_1). \tag{6.3}$$

Eq. (6.1) can now be rewritten as

$$\frac{Z}{Z_0} = \sum_n \int \mathrm{d}x_1 \dots \mathrm{d}x_n \sum_{\mathcal{F} \in \mathcal{F}_n} \mathcal{F}(x_1, \dots, x_n), \tag{6.4}$$

where $\mathcal{F}_n$ represents all possible diagrams at order n. Contributions to the partition function indeed involve all topologies of diagrams, whether they are connected or disconnected. These are called *vacuum diagrams*, and there are $(n!)^2$ of them at order n.

This expression can be evaluated using Monte Carlo techniques, where we sample both the interaction vertices *and* the diagram topology, and then measure the value of each diagram associated with a given set of x_i. Such an algorithm would however yield very large error bars, as many Feynman diagrams do cancel each other: this is the fermionic sign problem described in Section 5.3.1. The strength of the CT-INT algorithm was to rewrite this sum over diagrams as a product of determinants to take care of the cancellations. Note that it also allowed to sum a factorial number of diagrams in a polynomial time, $O(n^3)$.

In the remainder of this Section, we present a similar construction using Feynman diagrams for physical observables. In this case, there is no obvious way to rewrite the sum over diagrams using determinants, and the algorithm which directly samples them turns out to be very efficient.

6.1.2 Diagrammatic expansion of physical observables

Computing correlators

A general correlation function $\mathcal{C}$ of two operators A and B is defined as

$$\mathcal{C}(x_{\text{out}}, x_{\text{in}}) = -\langle T_\tau B(x_{\text{out}}) A(x_{\text{in}}) \rangle. \tag{6.5}$$

We can also expand it as a series in the Coulomb repulsion U:

$$\begin{aligned} \mathcal{C}(x_{\text{out}}, x_{\text{in}}) &= -\frac{1}{Z} \int \mathcal{D}[d^\dagger, d] e^{-\mathcal{S}} B(x_{\text{out}}) A(x_{\text{in}}) \\ &= -\frac{Z_0}{Z} \sum_n \frac{(-U)^n}{n!} \int \mathrm{d}x_1 \dots \mathrm{d}x_n \left\langle T_\tau \left[\prod_\sigma n_\sigma(x_1) \dots n_\sigma(x_n) \right] B(x_{\text{out}}) A(x_{\text{in}}) \right\rangle_0 . \end{aligned} \tag{6.6}$$

As for the partition function, these average values with respect to the noninteracting system may be represented as an infinite sum of Feynman diagrams. The main difference with Z is that only *connected* topologies now subsist in the computation of correlators.

To illustrate this, let us consider the example of the Green's function

$$\begin{aligned} G_\sigma(x_{\text{out}}, x_{\text{in}}) = -\frac{Z_0}{Z} \sum_n \frac{(-U)^n}{n!} \int \mathrm{d}x_1 \dots \mathrm{d}x_n \left\langle T_\tau n_{d\sigma}(x_1) \dots n_{d\sigma}(x_n) d_\sigma(x_{\text{out}}) d^\dagger_\sigma(x_{\text{in}}) \right\rangle_0 \\ \times \left\langle T_\tau n_{d\bar{\sigma}}(x_1) \dots n_{d\bar{\sigma}}(x_n) \right\rangle_0 , \end{aligned} \tag{6.7}$$

where $d_\sigma^\dagger(x_i)$ (resp. $d_\sigma(x_i)$) is the operator creating (resp. annihilating) a spin-σ fermion at x_i, and $\bar{\sigma} = 1-\sigma$. Using the linked-cluster theorem, G itself can be represented as an infinite sum of Feynman diagrams

$G_\sigma(x_{\text{out}}, x_{\text{in}}) =$ 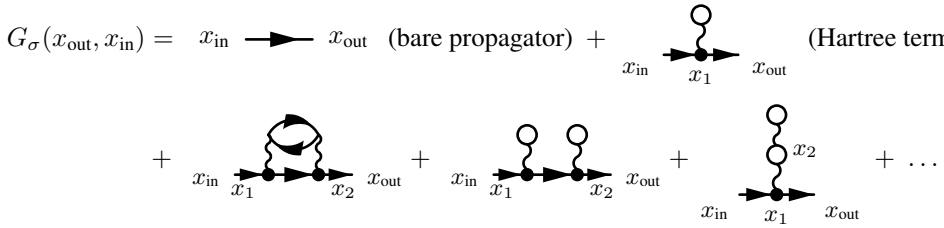 (6.8)

which can be formally written as

$$G_\sigma(x_{\text{out}}, x_{\text{in}}) = \sum_n \int \mathrm{d}x_1 \dots \mathrm{d}x_n \sum_{\mathcal{F} \in \mathcal{F}_n^{\text{conn}}} \mathcal{F}(x_{\text{out}}, x_{\text{in}}; x_1, \dots, x_n), \tag{6.9}$$

where $\mathcal{F}_n^{\text{conn}}$ represents *connected* topologies at order n.

Beyond correlators: what about the self-energy?

Let us consider the self-energy

$$\Sigma_\sigma = g_\sigma^{-1} - G_\sigma^{-1}. \tag{6.10}$$

It can be represented as an infinite series of Feynman diagrams

$\Sigma_\sigma =$ 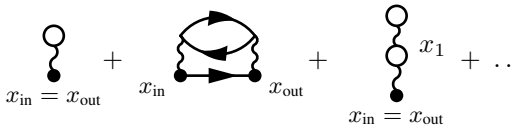 (6.11)

where only *one-particle irreducible* (1PI) diagrams appear, that is diagrams that do not become two independent pieces when a straight line is cut. This equation can be formally written as

$$\Sigma_\sigma(x_{\text{out}}, x_{\text{in}}) = \sum_n \int \mathrm{d}x_1 \dots \mathrm{d}x_n \sum_{\mathcal{F} \in \mathcal{F}_n^{\text{1PI}}} \mathcal{F}(x_{\text{out}}, x_{\text{in}}; x_1, \dots, x_n), \tag{6.12}$$

where $\mathcal{F}_n^{\text{1PI}}$ represents one-particle irreducible topologies at order n.

6.1.3 Diagrammatic Monte Carlo

The order-n contribution to a generic physical observable $\mathcal{M}$ can therefore be expressed as a multi-dimensional integral over interaction vertices and topologies of Feynman diagrams

$$\mathcal{M}_n(x_{\text{out}}, x_{\text{in}}) = \int \mathrm{d}x_1 \dots \mathrm{d}x_n \sum_{\mathcal{F} \in \bar{\mathcal{F}}_n} \mathcal{F}(x_{\text{out}}, x_{\text{in}}; x_1, \dots, x_n), \tag{6.13}$$

where $\bar{\mathcal{F}}_n$ is the family of order-n diagrams that are either connected, 1PI, ... given the quantity we want to compute.

According to Section 5.2, Eq. (6.13) can be evaluated using stochastic sampling *via* Monte Carlo techniques: this is the diagrammatic Monte Carlo (DiagMC) algorithm [129, 130, 88, 73, 22, 135]. A configuration is defined to be the perturbation order n, interaction vertices, and a Feynman diagram topology [2]

$$\mathfrak{c} = \{n; x_1, \dots, x_n; \mathcal{F}\}. \tag{6.14}$$

The weight is then

$$w_{\mathfrak{c}} = |\mathcal{F}(x_{\text{out}}, x_{\text{in}}; x_1, \dots, x_n)| = |\mathcal{F}(x_{\text{out}}, x_{\text{in}}; \mathfrak{c})|\,, \tag{6.15}$$

so that

$$\mathcal{M}_n(x_{\text{out}}, x_{\text{in}}) \sim \sum_{\mathfrak{c}}^{\text{MC}} \text{sgn}\, \mathcal{F}(x_{\text{out}}, x_{\text{in}}; \mathfrak{c}). \tag{6.16}$$

2. One can also choose to add the external vertices x_{in} and x_{out} in the configuration to sample them as well.

New configurations are proposed through a Metropolis-Hastings algorithm, defining a Markov chain in the space of Feynman diagrams. Usual updates are the insertion or the removal of a wiggly line. Note that the new diagram has to belong to $\bar{\mathcal{F}}_n$, and keeping track of the allowed topologies is a complicated algorithmic problem in itself.

DiagMC thus directly computes the quantity of interest thanks to a stochastic sampling of Feynman diagrams. Sampling individual topologies brings a severe sign problem, which typically limits the number of orders accessible to $n \sim 7$, although this may be enough for some applications. The series can become divergent, especially for large interactions, as poles appear in the complex plane. Resummation techniques then have to be used in order to evaluate the series beyond its convergence radius [183, 14, 136].

As stressed earlier, the most important aspect of the CT-INT algorithm presented in Chapter 5 is the use of determinants that allows to sum an exponential number of diagrams in a polynomial time. As determinants describe all topologies of diagrams, they are well suited for the partition function but their use is less straightforward when computing quantities such as the Green's function or the self-energy.

6.2 Computing correlators using determinants: the CDet algorithm

In this Section, we describe recent advances from Ref. [135] that show how one can use determinants to sum all topologies of diagrams in the MC weight relevant for correlators: this is the Connected Determinant (CDet) algorithm. The next Chapter presents our advances concerning the use of determinants to compute dynamical quantities such as the self-energy.

6.2.1 Formalism

Let us consider a generic correlation function $\mathcal{C}$ defined according to Eq. (6.5). At a given order n in the perturbation series, a diagram contributing to $\mathcal{C}(x_{\text{out}}, x_{\text{in}})$ is characterized by the set of its internal vertices $V = \{x_1, ..., x_n\}$ where x_l is associated with the l-th interaction vertex. In the standard DiagMC technique, we have seen that individual connected diagrams are stochastically sampled in a way that preserves their connectivity, with a probability given by the absolute value of their contribution to $\mathcal{C}(x_{\text{out}}, x_{\text{in}})$. This technique however yields a severe sign problem.

The idea of the CDet algorithm is to regroup *all* diagrams sharing the same internal vertices V in a contribution $\mathcal{C}_V(x_{\text{out}}, x_{\text{in}})$, and then stochastically sample the sets V. The stochastic weight of this group of diagrams in the Monte Carlo sampling of $\mathcal{C}(x_{\text{out}}, x_{\text{in}})$ is the absolute value of their sum, which is only a function of V. One could naturally expect that summing this factorial number of diagrams would come with a factorial cost, but it was shown that it can actually be achieved exponentially [135].

The sum of connected diagrams entering $\mathcal{C}_V(x_{\text{out}}, x_{\text{in}})$ is expressed as the sum of *all* diagrams (connected and disconnected ones) from which the disconnected components are recursively subtracted . This can be formalized as follows

$$\mathcal{C}_V(x_{\text{out}}, x_{\text{in}}) = \mathcal{D}_V(x_{\text{out}}, x_{\text{in}}) - \sum_{S \subsetneq V} \mathcal{C}_S(x_{\text{out}}, x_{\text{in}}) \mathcal{D}_{V \setminus S}(\varnothing),$$

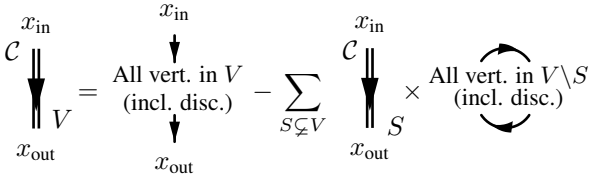

(6.17)

where $\mathcal{D}_V(x_{\text{out}}, x_{\text{in}})$ denotes the sum of all diagrams (including disconnected ones) with internal vertices V, external vertices x_{in} and x_{out}. $\mathcal{D}_V(\varnothing)$ is the sum of all diagrams with vertices V and no external vertices. The cancellation of disconnected diagrams is illustrated in the second line of Eq. (6.17). A key feature of this recursive sum is that $\mathcal{D}_V$ terms can be expressed as determinants (hence at a polynomial computational cost) [134]. At a given perturbation order n, the computational cost of evaluating a given $\mathcal{C}_V(x_{\text{out}}, x_{\text{in}})$ is $O(3^n)$.

First, determinants $\mathcal{D}_S$ are computed for all subsets S of V. It has been shown that this can be done with a total effort $O(2^n)$ [60, 168]. The leading complexity however comes from the progressive computation,

from low to high orders, of the $\mathcal{C}_S$. More precisely, if all $\mathcal{C}_{S'}$ are known for subsets S' with less than $p \leq n$ vertices, one can compute a given p-order $\mathcal{C}_S$ using Eq. (6.17) with $V = S$, in 2^p operations (see r.h.s of Eq. (6.17)). This has to be done for all the $\binom{n}{p}$ subsets S at order p before computing contributions at the next order $p+1$. The final result is obtained when this has been done for all $p \leq n$ and the leading complexity of the algorithm to compute $\mathcal{C}_V(x_{\text{out}}, x_{\text{in}})$ is therefore $\sum_{p=0}^{n} \binom{n}{p} 2^p = 3^n$. This complexity can in principle be improved to $O(n^2 2^n)$ using fast subset convolutions [19].

Note that this idea of cancelling disconnected diagrams will be revisited in Chapter 8 for out-of-equilibrium diagrammatic quantum Monte Carlo algorithms, where correlators are expressed as a sum of 2^n determinants thanks to Keldysh diagrammatic techniques [128].

6.2.2 Monte Carlo implementation

Once Eq. (6.17) has been established, the Monte Carlo implementation is quite straightforward. A configuration is the perturbation order n, external vertices x_{out} and x_{in},[3] and a set of n internal vertices

$$\mathfrak{c} = \{n; x_{\text{out}}, x_{\text{in}}; x_1, \ldots, x_n\}. \tag{6.18}$$

The MC weight is then $w_{\mathfrak{c}} = |\mathcal{C}_V(x_{\text{out}}, x_{\text{in}})| = |\mathcal{C}(\mathfrak{c})|$, so that the order-$n$ contribution to $\mathcal{C}$ is obtained by sampling the sign of each exponential sum of determinants. The computation of $w_{\mathfrak{c}}$ is numerically expensive and is at the origin of the exponential complexity of the algorithm. In order to compute it, we have seen that we need the values of all $\mathcal{C}_s(x_{\text{out}}, x_{\text{in}})$ with $S \subsetneq V$. We therefore recursively compute all these contributions starting from $S = \varnothing$ and store them in a 2^n array.

We use a standard Metropolis [107] algorithm to generate a Markov chain distributed according to $w_{\mathfrak{c}}$. Remembering that x is a composite index for a site index and an imaginary time, $x = (i, \tau)$, a new configuration $\mathfrak{c}'$ is proposed by applying one of the following updates to a given configuration $\mathfrak{c}$:

1. Pick one of the interaction vertices in $\mathfrak{c}$ and change its position and imaginary time. One can increase the probability of the move being accepted by choosing a new position either among the neighbors of the chosen vertex or from a Gaussian distribution. The imaginary time can be chosen uniformly.
2. Remove a randomly chosen internal interaction vertex from $\mathfrak{c}$.
3. Add a new internal interaction vertex in $\mathfrak{c}$. The new lattice site can be chosen from a Gaussian distribution around the center of gravity of the vertices in $\mathfrak{c}$. The imaginary time can be chosen with uniform probability.

Note that the use of an α-shift that redefines the noninteracting propagator and the interaction vertex, as introduced in Section 5.3.1, allows to greatly improve the convergence properties of the perturbation series in some regimes of parameters [183].

This algorithm will sample the configurations according to the weights $w_{\mathfrak{c}}$, however it is necessary to normalize the result. To do so, it is convenient to restrict the Monte Carlo simulation to only two consecutive orders, m and $m+1$. A vertex can be added (resp. removed) only if the current $\mathfrak{c}$ is at order m (resp. $m+1$). In the lowest order m the following normalization quantity is measured

$$\mathcal{N}_m = \sum_{x_{\text{in}}, x_{\text{out}}} \sum_{V_m} \left| \mathcal{C}_{V_m}(x_{\text{out}}, x_{\text{in}}) \right|, \tag{6.19}$$

while at order $m+1$, both $\mathcal{N}_{m+1}$ and the contribution to $\mathcal{C}$ are measured. The knowledge of the expected value for $\mathcal{N}_m$ allows us to find the normalization factor and obtain a normalized value for the contribution to $\mathcal{C}$ and $\mathcal{N}_{m+1}$ at order $m+1$. The latter can then be used to normalize a further simulation at orders $m+1$ and $m+2$, and so on. The contribution at $m = 0$ is computed analytically, allowing for a precise determination of $\mathcal{N}_0$.

In the specific case of a single correlated site, useful for benchmark purposes for instance, it is possible to restrict the simulation to a fixed order m and propose updates that only change the imaginary time of a randomly chosen interaction vertex. The normalization is obtained by computing an integral whose value is known. The simple choice

$$\mathcal{I}_m = \int_0^\beta \mathrm{d}\tau_{\text{in}} \mathrm{d}\tau_{\text{out}} \mathrm{d}\tau_1 \ldots \mathrm{d}\tau_m = \beta^{m+2}$$

3. So that we can stochastically sample $\mathcal{C}(x_{\text{out}}, x_{\text{in}})$ without doing multiple MC runs.

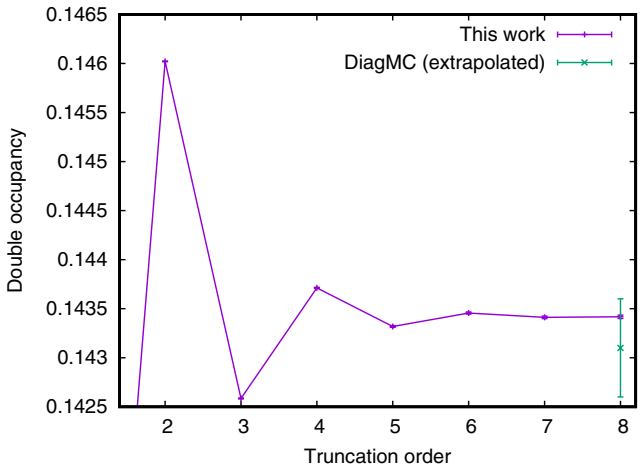

Figure 6.1 – Double occupancy as a function of truncation order computed with the CDet algorithm, for the 2D Hubbard model, $\beta = 8$, $U = 2$ and $n = 0.875$, from [135]. The DiagMC number is taken from [93].

turns out to provide a good normalization.

6.2.3 Comparison to DiagMC

The CDet approach leads to an important reduction of statistical error with respect to the DiagMC and has allowed for great progress in the computation of static properties. For instance, we reproduce in Fig. 6.1 the double occupancy for the two-dimensional Hubbard model as a function of the perturbation order [135]. The inverse temperature is $\beta = 8$, the Coulomb interaction $U = 2$, and the density $n = 0.875$. Comparing it with DiagMC benchmarks from Ref. [93], the error bars are found to be one order of magnitude smaller when using the CDet algorithm.

This method, however, has to be adapted in order to efficiently compute the frequency-dependence of dynamical quantities, such as the Green's function or the self-energy. We investigate how this can be achieved in the next Chapter.

Chapter 7

New diagrammatic algorithms for dynamical quantities in fermionic systems

In this Chapter, we are interested in the computation of frequency-dependent ('dynamical') quantities using determinantal algorithms, focusing on the self-energy Σ as it encodes electronic correlations. We introduce and compare three different algorithms. Two of them are directly based on the CDet approach presented in the previous Chapter, one using Dyson's equation, the other one equations of motion (EOM) for the Green's function. A generalization of the use of determinants to directly sample one-particle-irreducible (1PI) diagrams is then derived, the corresponding algorithm being labelled ΣDet. This work has been published in Ref. [110], the full text being reproduced in Appendix VII.

7.1 CDet-based approaches to self-energy computation

7.1.1 Dyson's equation

The most straightforward way to compute the self-energy Σ_σ is to first compute the Green's function G_σ with the CDet algorithm and then use Dyson's equation $\Sigma_\sigma = g_\sigma^{-1} - G_\sigma^{-1}$, where g_σ is the noninteracting Green's function. We show in Section 7.6 that it is very difficult to obtain precise data with this method because of the inversion of G that dramatically increases the stochastic noise.

7.1.2 Equations of motion

We present a diagrammatic approach to compute the self-energy based on the computation of a different correlator with the CDet algorithm. Let us first write the self-energy as the sum of a constant Hartree term and a frequency-dependent part

$$\Sigma_\sigma(x_{\text{out}}, x_{\text{in}}) = \Sigma_\sigma^H \, \delta_{x_{\text{in}}, x_{\text{out}}} + \tilde{\Sigma}_\sigma(x_{\text{out}}, x_{\text{in}}). \tag{7.1}$$

We recall that x is a combined index (i, τ), where i is the lattice site and τ the imaginary time. The Hartree term contribution is given by

$$\Sigma_\sigma^H = U G_{\bar{\sigma}}(0^-) =$$

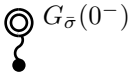

(7.2)

It can be directly computed from the knowledge of the Green's function $G_{\bar{\sigma}}$ which is a connected correlator that can be obtained from Eq. (6.17). The self-energy Σ_σ can then be recursively computed using the following expression

$$\Sigma_\sigma = \Sigma_\sigma^H + \bar{F}_\sigma - \Sigma_\sigma G_\sigma \Sigma_\sigma, \tag{7.3a}$$

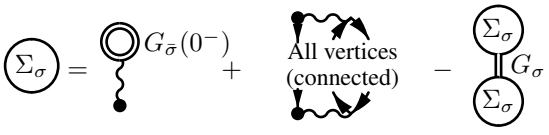

(7.3b)

where the correlation function $\bar{F}_\sigma$ is defined by

$$\bar{F}_\sigma(x_{\text{out}}, x_{\text{in}}) = -U^2 \langle T_\tau n_{\bar{\sigma}} c_\sigma(x_{\text{out}}) n_{\bar{\sigma}} c_\sigma^\dagger(x_{\text{in}}) \rangle. \tag{7.4}$$

Eq. (7.3) can be derived from the equations of motion (EOM) for the Green's function, as detailed in Appendix B.1 [26, 65]. It has a simple diagrammatic interpretation, see the second line of Eq. (7.3), that illustrates how 1PI diagrams are isolated. Indeed, according to Eq. (7.1), the self-energy is the sum of contributions with a single external vertex (Hartree term Σ_σ^H) and contributions with two external vertices ($\tilde{\Sigma}_\sigma$). The former is easy to compute, and the latter is the sum of all 1PI diagrams with two external vertices. The term $\bar{F}_\sigma$ on the r.h.s of Eq. (7.3) represents the sum of *all connected* diagrams with the same external vertices as $\tilde{\Sigma}_\sigma$. From this, one then has to subtract all non-1PI diagrams, which can always be expressed in the form $\Sigma_\sigma G_\sigma \Sigma_\sigma$.

We now transform the above equation in order to be able to compute the contributions to the self-energy at a given perturbation order just from the knowledge of the contributions to $\bar{F}_\sigma$ and Σ_σ^H. We first multiply Eq. (7.3) by g_σ on the right and we obtain

$$\Sigma_\sigma g_\sigma = \Sigma_\sigma^H g_\sigma + \bar{F}_\sigma g_\sigma - \Sigma_\sigma G_\sigma \Sigma_\sigma g_\sigma. \tag{7.5}$$

Reorganizing the terms,

$$\bar{F}_\sigma g_\sigma + \Sigma_\sigma^H g_\sigma = \Sigma_\sigma [g_\sigma + G_\sigma \Sigma_\sigma g_\sigma] = \Sigma_\sigma G_\sigma. \tag{7.6}$$

Substituting this expression for $\Sigma_\sigma G_\sigma$ in Eq. (7.3), we find

$$\Sigma_\sigma = \Sigma_\sigma^H + \bar{F}_\sigma - [\bar{F}_\sigma g_\sigma + \Sigma_\sigma^H g_\sigma] \Sigma_\sigma. \tag{7.7}$$

Contributions to the self-energy can be recursively computed for all perturbation orders. Because $\bar{F}_\sigma$ is at least of order 2 in U and Σ_σ^H is at least of order 1 in U, the computation of contribution to the self-energy at order n on the l.h.s can indeed be obtained from the knowledge of contributions to $\bar{F}$ and to the self-energy at orders strictly lower than n on the r.h.s. As a result, Σ can be computed without any inversion and there is no noise amplification as in Dyson's equation. We therefore expect this approach to be more efficient than the one presented in Section 7.1.1.

The algorithm is implemented by computing the Green's function G_σ and the correlator $\bar{F}_\sigma$ using the CDet algorithm. As it is based on the equations of motion, we will use the label 'EOM' to unambiguously refer to this method. Then, Eq. (7.7) is used to recursively compute the contributions to Σ_σ at a given order. As we use the CDet algorithm to obtain two correlators, and the self-energy is only computed in a post-processing part, the complexity of this algorithm naturally scales as $O(3^n)$.

7.2 Generalizing the CDet to 1PI diagrams: the ΣDet algorithm

We now introduce an extension of the CDet algorithm to efficiently compute the sum of all one-particle irreducible diagrams of a perturbation series. At a given perturbation order n in the interaction U, a self-energy diagram is characterized by x_{in}, x_{out}, its internal interaction vertices $V = \{x_1, \ldots, x_{n-2}\}$, and the adjacency matrices that connect the vertices. Note that we choose $n-2$ points in the set of internal vertices V because x_{in} and x_{out} both carry an interaction vertex as well.

We wish to group all diagrams that share the same internal vertices V into a contribution $\Sigma_V^\sigma(x_{\text{out}}, x_{\text{in}})$ so that

$$\begin{aligned} \Sigma_\sigma(x_{\text{out}}, x_{\text{in}}) &= \sum_V \Sigma_V^\sigma(x_{\text{out}}, x_{\text{in}}) \\ &= \sum_V \left(\Sigma_V^{H,\sigma}\, \delta_{x_{\text{in}}, x_{\text{out}}} + \tilde{\Sigma}_V^\sigma(x_{\text{out}}, x_{\text{in}}) \right). \end{aligned} \tag{7.8}$$

The contribution $\Sigma_V^\sigma(x_{\text{out}}, x_{\text{in}})$ is theoretically a sum of a factorial number of diagrams, but we express it with the help of a recursion, very much in the spirit of Section 6.2, that only involves connected correlators that can be computed with exponential effort using Eq. (6.17). The numerical effort to obtain $\Sigma_V^\sigma(x_{\text{out}}, x_{\text{in}})$ will then turn out to also be exponential.

Based on Eq. (7.3), the frequency-dependent part of the self-energy $\tilde{\Sigma}^\sigma_V(x_{\text{out}}, x_{\text{in}})$ can be expressed *via* the following recursive formula

$$\tilde{\Sigma}^\sigma_V(x_{\text{out}}, x_{\text{in}}) = \bar{F}^\sigma_V(x_{\text{out}}, x_{\text{in}}) - \sum_{\substack{x'\in V \\ S\subseteq V\setminus\{x'\} \\ S'=V\setminus(S\cup\{x'\})}} F^\sigma_{S'}(x_{\text{out}}, x')\tilde{\Sigma}^\sigma_S(x', x_{\text{in}}) - \sum_{\substack{S\subseteq V \\ S'=V\setminus S}} F^\sigma_{S'}(x_{\text{out}}, x_{\text{in}}) \left(UG^{\bar{\sigma}}_S(0^-)\right) \tag{7.9a}$$

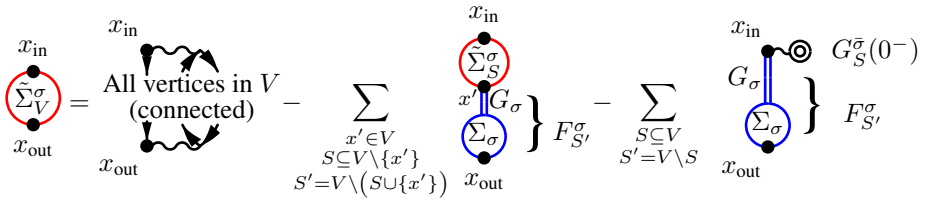

(7.9b)

where the correlation function F_σ is given by [27]

$$F_\sigma(x_{\text{out}}, x_{\text{in}}) = \Sigma_\sigma G_\sigma(x_{\text{out}}, x_{\text{in}}) \tag{7.10}$$

$$= -U\langle T_\tau n_{\bar{\sigma}} c_\sigma(x_{\text{out}}) c^\dagger_\sigma(x_{\text{in}})\rangle, \tag{7.11}$$

and $\bar{F}_\sigma$ by Eq. (7.4). The starting point of the recursion is the order-2 diagram

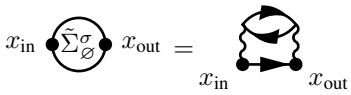

(7.12)

The second line of Eq. (7.9) illustrates the cancellation of non-1PI diagrams. The self-energy contributions $\tilde{\Sigma}^\sigma_V$ that are calculated recursively are indicated as red circles, while blue diagrams correspond to the correlation function $F_\sigma = \Sigma_\sigma G_\sigma$. An explicit example of this formula at third order is shown in Appendix B.2. Let us note that, in this formula, the starting point of the recursion is already an order-2 diagram while it is an order-0 diagram in Eq. (6.17), justifying a set V with $n-2$ vertices.

The first term $\bar{F}^\sigma_V(x_{\text{out}}, x_{\text{in}})$ on the r.h.s of Eq. (7.9) is the contribution to the correlation function $\bar{F}_\sigma(x_{\text{out}}, x_{\text{in}})$ for the set of internal vertices V. It is the sum of all connected diagrams that have interaction vertices at x_{in}, x_{out} and all $x \in V$ as interaction vertices. In order to obtain the contributions to the self-energy $\tilde{\Sigma}^\sigma_V(x_{\text{out}}, x_{\text{in}})$, one has to subtract from this term all diagrams that are not 1PI. These ones can be expressed in the form

$$\Sigma_\sigma G_\sigma \Sigma_\sigma = F_\sigma \Sigma_\sigma = F_\sigma(\Sigma^H_\sigma + \tilde{\Sigma}_\sigma), \tag{7.13}$$

and there are therefore two families of diagrams to subtract for a given set of vertices V: first all terms $F^\sigma_{S'}(x_{\text{out}}, x_{\text{in}})\Sigma^{H,\sigma}_S$ such that $S \sqcup S' = V$, then all terms $F^\sigma_{S'}(x_{\text{out}}, x')\tilde{\Sigma}^\sigma_S(x', x_{\text{in}})$ such that $S \sqcup \{x'\} \sqcup S' = V$. In the latter family, note that $S \subsetneq V$ is a proper subset of V, so that the calculation of $\tilde{\Sigma}^\sigma_V$ involves only some $\tilde{\Sigma}^\sigma_S$ that have been previously computed in the recursion.

We have therefore derived a recursive formula for the contributions $\tilde{\Sigma}^\sigma_V(x_{\text{out}}, x_{\text{in}})$ that involves the computation of only connected correlation functions. The recursion is completed in two steps. First, all correlators $\bar{F}_\sigma$, F_σ and G_σ have to be enumerated, the main effort coming from the F^σ_S that have to be computed for all pairs of external vertices (as a consequence of the explicit use of an intermediate vertex point x' in Eq. (7.9)). The computational cost for the precomputation is thus dominated by $n^2 3^n$. Second, the recursion has to be implemented, as in the CDet, by computing the contributions $\tilde{\Sigma}^\sigma_S$ starting from low to higher orders. At a given order p, it takes an effort $p2^p$ to get a given $\tilde{\Sigma}^\sigma_S(x', x_{\text{in}})$. This has to be done for all subsets S at order p and all x' before computing contributions at the next order $p+1$ and requires a total effort $\binom{n}{p}p^2 2^p$. All in all the recursion will take $\sum_{p=0}^n \binom{n}{p}p^2 2^p$ with a complexity $n^2 3^n$. The leading complexity of the algorithm is then $O(n^2 3^n)$.

We show in Section 7.6 that despite this additional n^2 factor, this method leads to smaller error bars compared to the approaches from Section 7.1. It also gives more accurate results than the state-of-the-art DiagMC calculations for the same computational effort.

7.3 Monte Carlo implementation

In this Section, we describe how to compute the different quantities that appear in the algorithms presented above using a Monte Carlo (MC) method. [1] We generically denote the function we want to compute as $\mathcal{M}_\sigma$. The Green's function G_σ has to be computed for all three approaches. In addition $\bar{F}_\sigma$ must be computed for the equations of motion algorithm and $\tilde{\Sigma}_\sigma$ for the direct sampling of the self-energy (ΣDet). We write $\mathcal{M}_\sigma$ as a sum over all contributions described by a set V_m with m internal vertices

$$\mathcal{M}_\sigma(x_{\text{out}}, x_{\text{in}}) = \sum_{m=0}^{\infty} \sum_{V_m} \mathcal{M}^\sigma_{V_m}(x_{\text{out}}, x_{\text{in}}). \tag{7.14}$$

Note that a configuration with m internal vertices contributes, in the perturbation series in U, to the coefficient of order $n = m$ for the Green's function, $n = m + 1$ for F_σ and $n = m + 2$ for $\tilde{\Sigma}_\sigma$.

In order to compute $\mathcal{M}_\sigma(x_{\text{out}}, x_{\text{in}})$, we stochastically generate Monte Carlo configurations that sample the r.h.s terms of the sum. A configuration $\mathfrak{c}$ is described by the number of internal vertices m, the spin σ and the set of all vertices

$$\mathfrak{c} = \{m; \sigma; x_{\text{in}}, x_{\text{out}}; x_1, \dots, x_m\}, \tag{7.15}$$

and its weight in the Monte Carlo sampling is

$$w_\mathfrak{c} = \left|\mathcal{M}^\sigma_{V_m}(x_{\text{out}}, x_{\text{in}})\right|. \tag{7.16}$$

We use a standard Metropolis [107] algorithm to generate a Markov chain distributed according to $w_\mathfrak{c}$. Starting from a given $\mathfrak{c}$, a new configuration $\mathfrak{c}'$ is following the same updates as the CDet ones described in Section 6.2.2, as well as the flipping of the spin $\sigma \leftarrow 1-\sigma$. The new configuration $\mathfrak{c}'$ is accepted or rejected with the usual Metropolis ratio

$$p^{\text{accept}}_{\mathfrak{c}\to\mathfrak{c}'} = \min\left(1, \frac{T_{\mathfrak{c}'\mathfrak{c}}\, w_{\mathfrak{c}'}}{T_{\mathfrak{c}\mathfrak{c}'}\, w_\mathfrak{c}}\right), \tag{7.17}$$

where $T_{\mathfrak{c}\mathfrak{c}'}$ is the probability to propose $\mathfrak{c}'$ after $\mathfrak{c}$.

As detailed in Section 6.2.2, results have to be normalized, so that we restrict the Monte Carlo simulation to only two consecutive orders. Let us note that statistical errors in the normalization factor propagate from one order to the other. One must therefore be careful in the computation of error bars using e.g. a binning or jackknife analysis. An α-shift can also be used to improve the fermionic sign problem and the convergence of the series, see Section 5.3.1.

7.4 Models

In the following Sections, we present actual computations of the self-energy according to the implementations described in Sections 7.1 and 7.2. For clarity, we use the following convention for names and colors: Dyson (green) denotes the use of Dyson's equation, EOM (orange) of the equations of motion and ΣDet (blue) the use of the direct calculation of the self-energy from the sum of 1PI diagrams. Red symbols denote benchmarks, as introduced below.

We consider two models in the following. The first is a single correlated electronic level, that we will refer to as a Hubbard atom, described by the Hamiltonian

$$\mathcal{H}_{\text{atom}} = U n_\uparrow n_\downarrow + \epsilon(n_\uparrow + n_\downarrow), \tag{7.18}$$

where n_σ is the number of the spin-σ fermion, U the onsite repulsion and ϵ the energy of the electronic level. This model has an analytical solution and allows us to both benchmark and compare the different methods introduced above. We use $\beta = 10$, $U = 1$, $\epsilon = -0.2$.

The second model is the prototypical two-dimensional Hubbard model given by

$$\mathcal{H}_{\text{Hubbard}} = -\gamma \sum_{\langle i,j\rangle\sigma} c^\dagger_{i\sigma} c_{j\sigma} + U \sum_i n_{i\uparrow} n_{i\downarrow}, \tag{7.19}$$

1. For a complete introduction to Monte Carlo techniques, see Section 5.2.

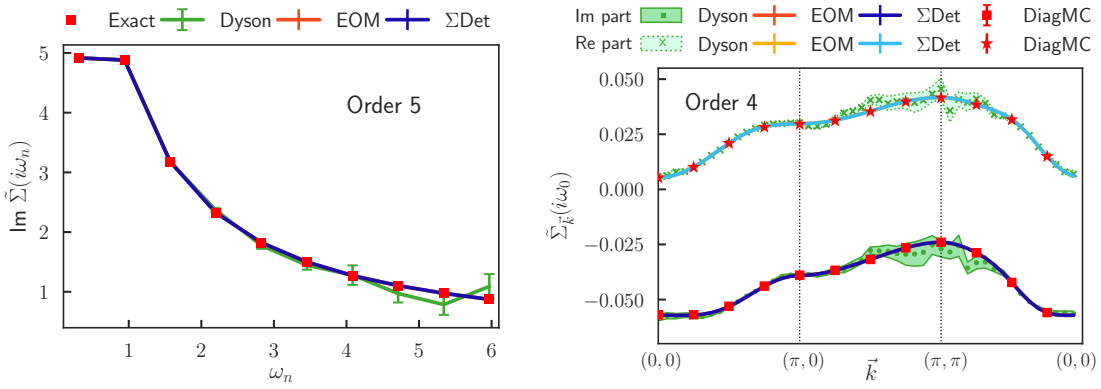

(a) Hubbard atom $\tilde{\Sigma}(i\omega_n)$ at order 5.

(b) Hubbard model self-energy at the first Matsubara frequency $\tilde{\Sigma}_{\vec{k}}(i\omega_0)$ at order 4.

Figure 7.1 – Benchmarks with the analytical solution (*left*) and DiagMC simulations (*right*).

where $c^\dagger_{i\sigma}$ creates a spin-σ electron on the site i of a square lattice, $\gamma > 0$ is the nearest-neighbor hopping and U is the onsite interaction. This is the model that we eventually aim to solve in its thermodynamic limit (infinite lattice). In our results, $\gamma = 1$ will be our energy unit. On the lattice, results from our approaches are compared to results obtained by Wei Wu using the standard DiagMC algorithm [129, 130, 88, 73, 22]. This implementation of the algorithm has been benchmarked and used in earlier calculations, see e.g. Ref. [183]. We use a 32×32 lattice with $\beta\gamma = 2$,[2] $U = 4\gamma$, $\mu = 0$ and a uniform α-shift $\alpha_\uparrow = \alpha_\downarrow = 1.53\gamma$.

7.5 Benchmarks

We present benchmarks for the three methods and check their theoretical complexity. We first consider the simple problem of a Hubbard atom. Its self-energy is given by

$$\Sigma_\sigma(i\omega_n) = \langle n_{\bar{\sigma}}\rangle U + \frac{\langle n_{\bar{\sigma}}\rangle(1 - \langle n_{\bar{\sigma}}\rangle)U^2}{i\omega_n - \epsilon - (1 - \langle n_{\bar{\sigma}}\rangle)U}, \tag{7.20}$$

and the contributions to $\tilde{\Sigma}(i\omega_n)$ at different orders in U can be computed analytically. In Fig. 7.1a, we show results for the contributions to $\tilde{\Sigma}(i\omega_n)$ at order 5 as obtained from the proposed algorithms. Red squares are the analytical solution, and all simulations lasted 1200 CPU hours. The results clearly agree with the analytical values within the error bars.

Next we consider the Hubbard model on a 32×32 square lattice. In Fig. 7.1b we plot the momentum-dependent self-energy $\tilde{\Sigma}_{\vec{k}}(i\omega_0)$ at its first Matsubara frequency along the $\vec{k} = (0,0) - (\pi,0) - (\pi,\pi) - (0,0)$ path of the Brillouin zone. Results are shown at order 4. The DiagMC simulation lasted 400 CPU hours, while all other simulations lasted 1440 CPU hours. Results agree with the benchmark DiagMC calculation within error bars.

A measurement of the time to perform one MC step allows us to study the complexity of the algorithms. This is shown on a semilog scale in Fig. 7.2, where the time for a single step is shown both for the direct measurement of the self-energy using the ΣDet and for the measurement of G using the CDet, that is then used in Dyson's equation. Each curve is fitted by its expected high-n behavior: $\gamma_\Sigma n^2 3^n$ for the ΣDet (dotted red line) and $\gamma_G 3^n$ for Dyson (dashed red line), where $\gamma_G = 0.0464$ and $\gamma_\Sigma = 0.0012$ are implementation-dependent constants. We know that the EOM method has twice the CDet complexity so we consider these two methods together in this study. The expected high-order behavior $n^2 3^n$ for the self-energy measurement and 3^n for the CDet is found.

At smaller perturbation orders, the asymptotic behavior is not yet settled. At orders smaller than 5, the self-energy measurement takes less time mainly because the algorithm starts at order 2 (The recursion starts

2. For this value of β the Hubbard model is in its thermodynamic limit on this lattice.

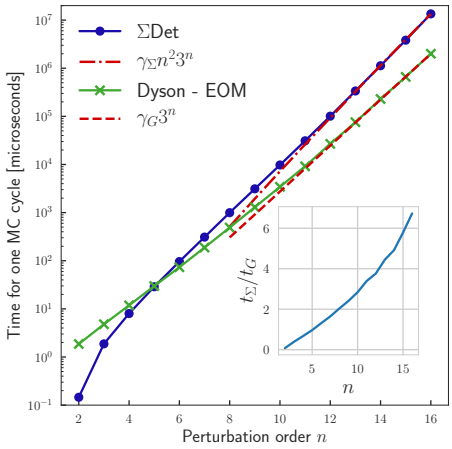

Figure 7.2 – Comparison of the time for one Monte Carlo cycle (in microseconds) between the direct accumulation of the self-energy and the computation of the Green's function using CDet, as a function of the perturbation order n. *Inset*: Ratio of the time of one MC cycle for the ΣDet (t_Σ) and for the CDet (t_G).

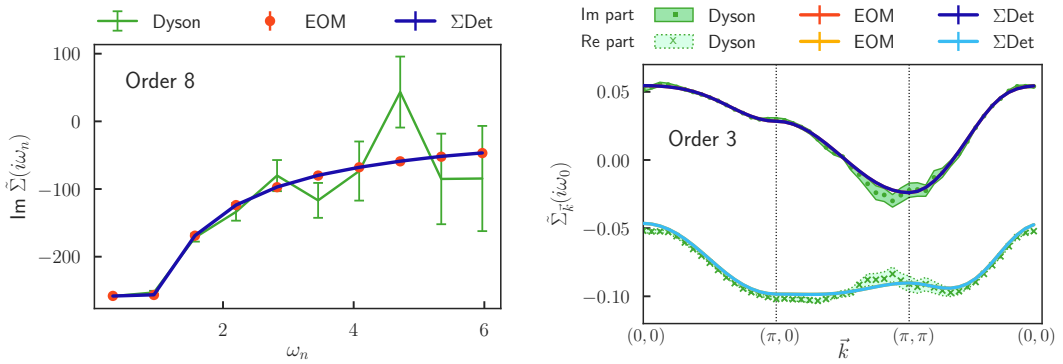

(a) Hubbard atom $\tilde{\Sigma}(i\omega_n)$ at order 8.

(b) Hubbard model self-energy at the first Matsubara frequency $\tilde{\Sigma}_{\vec{k}}(i\omega_0)$ at order 3.

Figure 7.3 – Amplification of the numerical noise in Dyson's equation.

with the pair-bubble diagram, see Eq. (7.12)). On the contrary, the CDet algorithm for the Green's function starts at order 0. As a consequence, the direct measurement of the self-energy is only about a factor 3 slower than the CDet approach at order 10 (see inset of Fig. 7.2) which is the order that is currently accessible with reasonable error bars.

7.6 Results

We now compare the three different methods between them, showing that ΣDet performs better both on the isolated atom and on the lattice. This method is finally shown to also improve state-of-the-art results from recent DiagMC calculations.

We recall the regimes of parameters used: $\beta = 10$, $U = 1$ and $\epsilon = -0.2$ for the Hubbard atom; $\beta = 2$, $U = 4$, $\mu = 0$ for the Hubbard model.

7.6.1 Comparison with Dyson's equation

Until now, no dynamical quantities have been computed with the CDet algorithm and it is therefore instructive to see how the use of Dyson's equation compares to the calculation of the self-energy from the

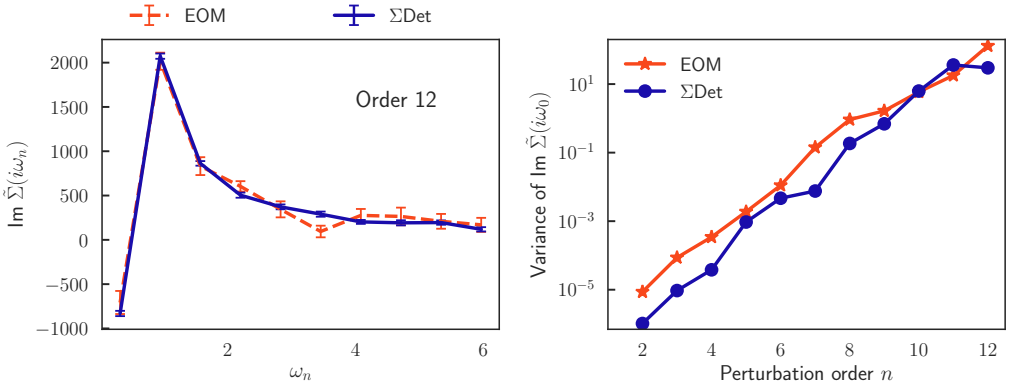

Figure 7.4 – Comparison between EOM and ΣDet for the Hubbard atom. *Left:* Hubbard atom self-energy at order 12. *Right:* Variance of $\tilde{\Sigma}$ at the first Matsubara frequency.

EOM and ΣDet methods. All simulations lasted 120 CPU hours.

We first consider the Hubbard atom. Fig. 7.3a shows the contribution to the imaginary part of the Matsubara frequency self-energy $\tilde{\Sigma}_\sigma(i\omega_n)$ at perturbation order 8. The direct measurement of the self-energy and the EOM method yield results that have very small error bars (smaller than the symbol size) and that are in perfect agreement (both curves lie on top of one another). In contrast, starting from the Green's function as obtained by Eq. (6.17), the results for the self-energy display large statistical errors that increase with the Matsubara frequency index. The reason is simple and expected: when Dyson's equation is used to compute the self-energy, there is an amplification of the numerical noise because of the inversion of the Green's function. In practice, it becomes quickly impossible to obtain accurate data. This is problematic because it would for instance make the analytical continuation of the results to the real axis very difficult.

Fig. 7.3b shows results for the two-dimensional Hubbard model. At order 3, the contribution to the self-energy taken at the first Matsubara frequency ω_0 obtained from ΣDet on the $\vec{k} = (0,0) - (\pi,0) - (\pi,\pi) - (0,0)$ path in the Brillouin zone is in perfect agreement with the EOM method, and error bars for both methods are very small (smaller than symbol size, both curves being on top). The computation of Σ_σ from the Green's function is noisier. Error bars actually increase with the Matsubara frequency index when using Dyson's equation, resulting in reasonable results only for the first few frequencies even for small perturbation orders. Again, the reason for this large noise is the amplification due to the inversion of the Green's function. Also, on the lattice, a direct measurement of the self-energy has the advantage of mainly sampling fairly local diagrams. Indeed, at a temperature $T = \gamma/2$, the self-energy very quickly vanishes for non-local components. The same is not true for the Green's function that has a slower decay; its stochastic sampling is therefore less efficient.

7.6.2 Comparison between the equations of motion and the direct sampling of the self-energy

We now compare the use of equations of motion (EOM) to the direct sampling of the self-energy expressed as a sum of 1PI diagrams (ΣDet). It is not clear at first which method is more efficient, as the ΣDet allows for a precise cancellation of diagrams and directly samples the quantity of interest but scales as $n^2 3^n$, while the EOM method cancels diagrams on average but has a better scaling as 3^n. All simulations lasted 120 CPU hours.

We first consider the Hubbard atom. In Fig. 7.4 (*left*) are shown the contributions to the imaginary part of the Matsubara frequency $\tilde{\Sigma}_\sigma(i\omega_n)$ at order 12 for both methods. The equations of motion method has error bars about one order of magnitude greater than the ΣDet ones. In order to quantify the efficiency more accurately, we plot in Fig. 7.4 (*right*) the variance at the first Matsubara frequency ω_0 as a function of the perturbation order for both methods. We see from this plot that ΣDet performs better at low perturbation order, and that both methods tend to become equivalent at higher orders.

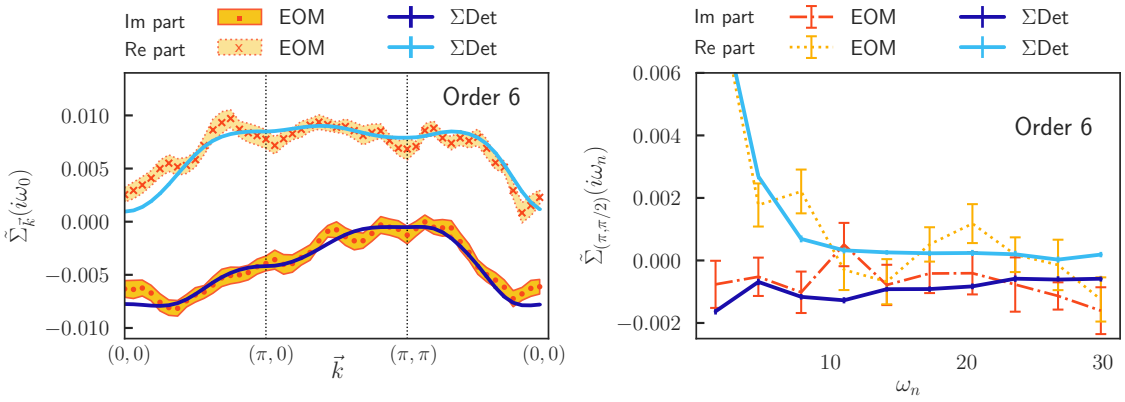

Figure 7.5 – Hubbard model self-energy at order 6. *Left:* Self-energy at the first Matsubara frequency $\tilde{\Sigma}_{\vec{k}}(i\omega_0)$. *Right:* Self-energy as a function of $i\omega_n$ at $\vec{k} = (\pi, \pi/2)$.

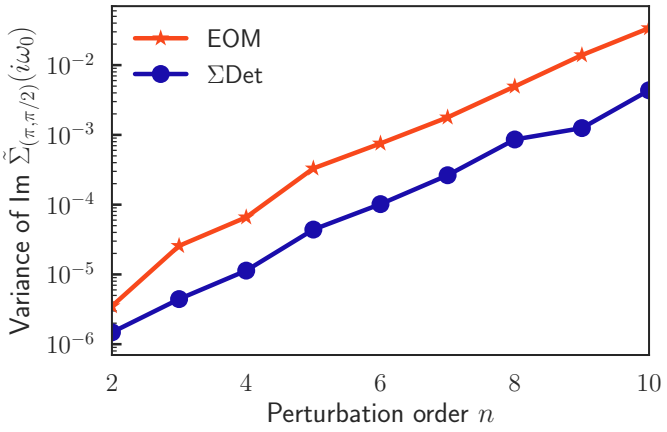

Figure 7.6 – Variance of the imaginary part of the Hubbard model self-energy Im $\tilde{\Sigma}_{(\pi,\pi/2)}(i\omega_0)$.

The comparison of the resulting self-energies on the lattice Hubbard model (Fig. 7.5) shows an even more pronounced difference between the two approaches. At order 6, the contribution to the self-energy taken at the first Matsubara frequency (*left*) obtained from ΣDet on the chosen path $\vec{k} = (0,0) - (\pi,0) - (\pi,\pi) - (0,0)$ in the Brillouin zone is very well converged and the error bars for this method are very small (smaller than symbol size). The computation of Σ_σ from the equations of motion is less accurate, even if it agrees with the ΣDet within its error bars. We then look at the Matsubara frequency evolution for a given reciprocal lattice vector $\vec{k} = (\pi, \pi/2)$ (right panel of Fig. 7.5). The error bar for the EOM method is seen to be large for all Matsubara frequencies.

To be quantitative, we plot in Fig. 7.6 the variance at the first Matsubara frequency ω_0 for this same value of $\vec{k} = (\pi, \pi/2)$ as function a of the perturbation order. We see from this plot that ΣDet always performs better than the EOM method, by about one order of magnitude.

We believe the explanation for this behavior comes from two ingredients. First, the cancellation of non-one-particle-irreducible diagrams is done *on average* in the EOM approach, while it is exact in the ΣDet algorithm. The latter is therefore more efficient to measure the self-energy, and it is particularly visible on the lattice that has more degrees of freedom. Second, the self-energy Σ_σ is more local on the lattice than the correlator $\bar{F}$. Hence the direct MC sampling of the self-energy still performs better even though its numerical complexity is increased by a factor n^2. Let us note here that the EOM approach could be useful in the context of the real-time algorithm of Ref. [128]. There the complexity of the EOM approach would be 2^n while a direct self-energy approach would scale as $n^2 3^n$.

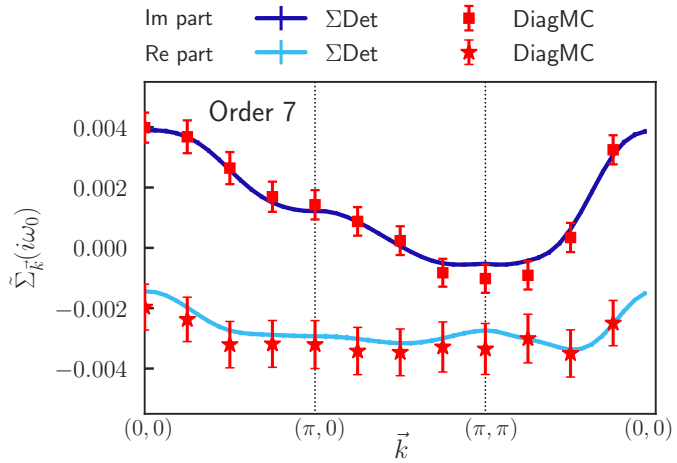

Figure 7.7 – Hubbard model self-energy at the first Matsubara frequency $\tilde{\Sigma}_{\vec{k}}(i\omega_0)$ at order 7.

7.6.3 Comparison between ΣDet and DiagMC algorithms

As the direct calculation of the self-energy ΣDet proves to be a very accurate method to get the self-energy, it is natural to compare it to the state-of-the-art DiagMC results on the two-dimensional Hubbard model. To this end, we compute in Fig. 7.7 the contribution to the first Matsubara frequency ω_0 of the self-energy at perturbation order 7 for the ΣDet (blue) method and compare it to the DiagMC (red) results obtained by Wei Wu. Simulations lasted 1440 CPU hours for the ΣDet and 4000 CPU hours for the DiagMC. Error bars at this perturbation order, the highest currently reachable with DiagMC techniques, are much smaller with the ΣDet algorithm than with the standard DiagMC approach for simulations of the same length.

This algorithm cancelling directly non-1PI diagrams in the MC sampling is therefore an interesting alternative to the current diagrammatic Monte Carlo approach.

As a final illustration of the method, we compute contributions to the local self-energy up to order 9 on the 2D Hubbard model with the parameters discussed above: $\beta = 2$, $U = 4$, $\mu = 0$. The resummed self-energy is shown in Fig. 7.8. We observe that, with a reasonable choice of the α-shift ($\alpha_\uparrow = \alpha_\downarrow = 1.53$), one can completely converge the results with an uncertainty below 1%. In this high-temperature, low electronic correlations examples, other approaches, such as determinant quantum Monte Carlo (DQMC) [20], also converge and can be used as benchmarks.

In the regime of parameters used in Ref. [183] to study the onset of the pseudogap in the Hubbard model, the ΣDet algorithm would perform well to reach lower temperatures in the computation of contributions to the perturbation series. The latter however becomes strongly divergent as poles appear in the complex plane. An equally difficult algorithmic challenge thus consists in using resummation techniques to evaluate the series beyond its convergence radius and recent developments addressing this problem should be considered [168, 14, 136].

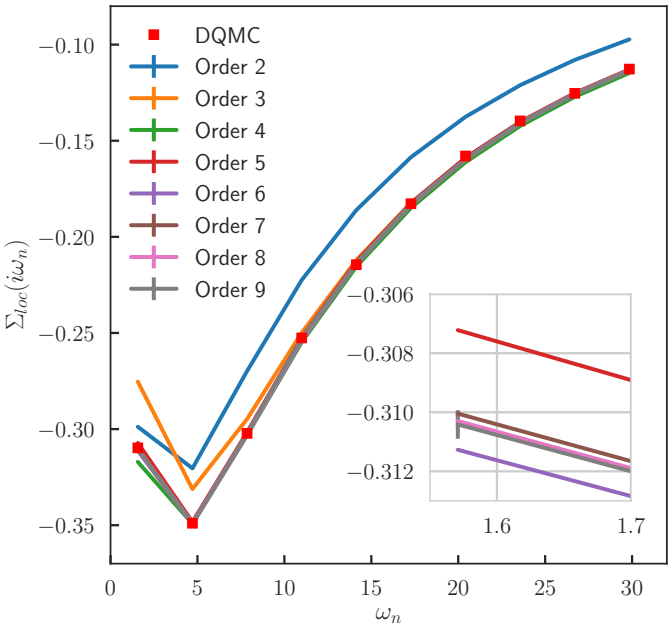

Figure 7.8 – Imaginary part of the local lattice self-energy $\Sigma_{\text{loc}}(i\omega_n)$ as a function of Matsubara frequency, as computed using k orders, with $k = 2, \ldots, 9$. The red squares are results obtained from DQMC (error bars are smaller than the symbol size). Inset: Zoom on the first Matsubara frequency. The discrete time interval in DQMC is $\Delta\tau = 1/32$.

Part IV

Determinant Monte Carlo algorithms for out-of-equilibrium physics

Chapter 8

Introduction to Keldysh formalism and real-time quantum Monte Carlo algorithms

Up to this point, we have only considered strongly correlated systems at equilibrium, therefore developing formalisms and methods working in imaginary time and/or Matsubara frequencies. We have seen that such advances allow us to understand detailed properties of materials and consider unbiased numerical solutions, for instance of the 2D Hubbard model.

By contrast, the nonequilibrium properties of strongly correlated quantum systems are much less well understood, despite many experimental realizations. [1] The basic formalism has been developed in the early 1960s by Schwinger, Kadanoff, Baym and Keldysh but, since then, mostly approximate approaches have been proposed. The formulation of numerically exact methods is therefore of paramount importance.

In this Chapter, we start by introducing the Keldysh formalism to compute observables in real time, before presenting state-of-the-art Monte Carlo algorithms to sample them.

8.1 The Keldysh contour

In this section, we briefly motivate and describe the Keldysh formalism for real-time Green's functions. For a complete introduction to nonequilibrium physics, see for example Ref. [153] or [77].

8.1.1 Motivation

Let us consider a strongly correlated system prepared in a noninteracting state at $t < 0$, described by the Hamiltonian $\mathcal{H}_0$. We denote its density matrix ρ_0. If the initial state is at equilibrium, then $\rho_0 = e^{-\beta\mathcal{H}_0}/\mathrm{Tr}\left(e^{-\beta\mathcal{H}_0}\right)$. Otherwise, ρ_0 does not have a simple expression as a function of $\mathcal{H}_0$, and simply describes how states are populated.

At $t = 0$, interactions in the system are turned on through a term $V(t)$. The full Hamiltonian of the system therefore writes

$$\mathcal{H} = \mathcal{H}_0 + \theta(t)V(t). \tag{8.1}$$

Let us consider an observable A, with Heisenberg representation $A(t) = e^{i\mathcal{H}t}Ae^{-i\mathcal{H}t}$. [2] Its average value at a given time $t > 0$ writes

$$\langle A(t)\rangle = \mathrm{Tr}\left(\rho_0 A(t)\right). \tag{8.2}$$

We introduce the interaction picture representation of A

$$A_I(t) = e^{i\mathcal{H}_0 t}Ae^{-i\mathcal{H}_0 t}, \tag{8.3}$$

1. See for example the quantum dots presented in Chapter 1 or the electric-field driven Ca_2RuO_4 from Chapter 13.
2. Note that the above time-dependent $V(t)$ is *not* in the Heisenberg representation.

as well as the evolution operators

$$U(t) = Te^{-i\int_0^t V_I}, \tag{8.4a}$$

$$U^\dagger(t) = \check{T}e^{i\int_0^t V_I}, \tag{8.4b}$$

where T and $\check{T}$ are respectively the time-ordering and anti-time-ordering operators in real time. This leads to the following expression for the average value of A

$$\langle A(t)\rangle = \mathrm{Tr}\left(\rho_0 \check{T}e^{i\int_0^t V_I} A_I(t) T e^{-i\int_0^t V_I}\right). \tag{8.5}$$

As in the imaginary-time case, we would like $\langle A(t)\rangle$ to be expressed as a simple time-ordered product. This can be achieved by working in the Keldysh formalism [147, 82, 132]. In this framework, operators act on the so-called Keldysh contour $\mathcal{C}$ consisting of a forward branch, from the initial time 0 to a given time $t_{\max}$, and a backward branch, from $t_{\max}$ to 0. A Keldysh point k on $\mathcal{C}$ is defined as a pair $k = (t, \alpha)$ with a time $t \in [0, t_{\max}]$ and a Keldysh index $\alpha \in \{\pm\}$ indicating which branch is to be considered. The $+$ (resp. $-$) index denotes the forward (resp. backward) branch, as depicted below.

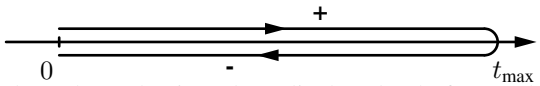

Note that both branches are along the real axis and are displaced only for graphical purposes. In the following, Greek letters refer to $\pm$ indices unless otherwise stated. We define a contour operator $T_\mathcal{C}$ that follows the arrows on the above picture: $T_\mathcal{C}$ coincides with the time-ordering operator T on the $+$ branch, with $\check{T}$ on the $-$ branch, and considers all Keldysh points on the backward branch to be later than points on the forward branch.

The average value of A now takes the form of a time-ordered product on the Keldysh contour $\mathcal{C}$

$$\langle A(t)\rangle = \mathrm{Tr}\left(\rho_0 T_\mathcal{C} e^{-i\int_\mathcal{C} V_I} A_I(t)\right) = \left\langle T_\mathcal{C} e^{-i\int_\mathcal{C} V_I} A_I(t)\right\rangle_0, \tag{8.6}$$

where $-i\int_\mathcal{C} V_I$ is $-i\alpha\int_0^{t_{\max}} V_I$ on the α contour.

Three important properties of the Keldysh contour easily follow from this definition. First, the evolution of an operator on $\mathcal{C}$ does not depend on the branch it is evaluated on

$$A(t,\alpha) = A(t). \tag{8.7}$$

Second, the average value of the product of two operators at two different points of the Keldysh contour is

$$\langle T_\mathcal{C} A(t,\alpha) B(t',\alpha')\rangle = \left\langle T_\mathcal{C} e^{-i\int_\mathcal{C} V_I} A_I(t,\alpha) B_I(t',\alpha')\right\rangle_0. \tag{8.8}$$

Finally, the partition function simply evaluates to 1:

$$Z = \left\langle T_\mathcal{C} e^{-i\int_\mathcal{C} V_I}\right\rangle_0 = 1. \tag{8.9}$$

8.1.2 Green's functions on the Keldysh contour

For the sake of simplicity, we consider in the following interacting electrons on a single energy level. The operator c_σ (resp. $c_\sigma^\dagger$) destroys (resp. creates) an electron with spin $\sigma = \uparrow, \downarrow$. We define the time-dependent Green's function as [3]

$$\hat{G}_\sigma(t,t') = -i\langle T_\mathcal{C} c_\sigma(t) c_\sigma^\dagger(t')\rangle. \tag{8.10}$$

It takes the form of a 2×2 matrix in the $\{\pm\}$ basis: $\hat{G}_\sigma = \begin{pmatrix} G_\sigma^{++} & G_\sigma^{<} \\ G_\sigma^{>} & G_\sigma^{--} \end{pmatrix}$, where

$$G_\sigma^{+-}(t,t') = G_\sigma^{<}(t,t') = i\langle c_\sigma^\dagger(t') c_\sigma(t)\rangle, \tag{8.11a}$$

$$G_\sigma^{-+}(t,t') = G_\sigma^{>}(t,t') = -i\langle c_\sigma(t) c_\sigma^\dagger(t')\rangle, \tag{8.11b}$$

$$G_\sigma^{++}(t,t') = -i\langle T c_\sigma(t) c_\sigma^\dagger(t')\rangle, \tag{8.11c}$$

$$G_\sigma^{--}(t,t') = -i\langle \check{T} c_\sigma(t) c_\sigma^\dagger(t')\rangle. \tag{8.11d}$$

3. The notation $\hat{}$ denotes a matrix form.

Out of those four Green's functions, only two are independent as we have

$$G_\sigma^{++}(t,t') = \theta(t-t')G_\sigma^{>}(t,t') + \theta(t'-t)G_\sigma^{<}(t,t'), \tag{8.12a}$$
$$G_\sigma^{--}(t,t') = \theta(t'-t)G_\sigma^{>}(t,t') + \theta(t-t')G_\sigma^{<}(t,t'). \tag{8.12b}$$

At equilibrium, the greater and lesser components only depend on the time difference $t-t'$ and their Fourier transforms are related through the fluctuation-dissipation theorem

$$G^{<}(\omega) = -e^{-\beta\omega}G^{>}(\omega). \tag{8.13}$$

8.2 Diagrammatics of an expansion in the Coulomb interaction U

The interaction term, turned on at $t = 0$, is considered to be $V(t) = Un_\uparrow n_\downarrow$, where $n_\sigma = c_\sigma^\dagger c_\sigma$ is the density operator, and U is the Coulomb interaction. We want to construct perturbation series in U for physical observables of interest. As in the equilibrium case, [4] let us start from the partition function. From now on, we omit the interaction representation subscript I for clarity. Because the interaction term is local in time, its expansion in powers of U writes $Z = \sum_{n\geq 0} Z_n$,

$$Z_n = (-iU)^n \int_0^{t_{\max}} \mathrm{d}t_1 \dots \mathrm{d}t_n \sum_{\alpha_1\dots\alpha_n} \alpha_1 \dots \alpha_n \prod_\sigma \left\langle T_\mathcal{C} \prod_{i=1}^{n} c_\sigma^\dagger(t_i,\alpha_i) c_\sigma(t_i,\alpha_i) \right\rangle_0, \tag{8.14}$$

where integrals over times are now considered to be ordered ($t_1 < \dots < t_n$), hence cancelling the $1/n!$ factor coming from the expansion of the exponential.

Every term in this expression can be pictorially represented using Feynman diagrams obeying rules we now briefly summarize. [5] A straight line represents a noninteracting Green's function, denoted by a lower case letter

$$t',\beta \xrightarrow{\ \sigma\ } t,\alpha \quad = ig_\sigma^{\alpha\beta}(t-t'). \tag{8.15}$$

Note that the extra i factor compared to the imaginary time comes from the definition of real-time Green's functions, Eq. (8.11), so that the line is a $\langle cc^\dagger \rangle$ correlator.

Because the interaction has the local form $Un_\uparrow n_\downarrow$, an interaction vertex is characterized by a single Keldysh point $\{t,\alpha\}$ and the indices of the four legs all have to be equal to the Keldysh index α

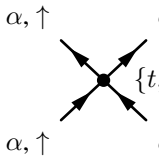

$$= -i\alpha U. \tag{8.16}$$

Hence, for every interaction time t, there are two possible vertices.

Finally, note that each fermion loop in a Feynman diagram brings an additional (-1) factor.

According to Eq. (8.14), Z is now expressed as the sum of all topologies of diagrams, both connected and disconnected. The property of Eq. (8.9) implies that all contributions of order $n > 0$ vanish:

$$\forall n > 0, \int_0^{t_{\max}} \mathrm{d}t_1 \dots \mathrm{d}t_n \sum_{\alpha_1\dots\alpha_n} \alpha_1 \dots \alpha_n \prod_\sigma \left\langle T_\mathcal{C} \prod_{i=1}^{n} c_\sigma^\dagger(t_i,\alpha_i) c_\sigma(t_i,\alpha_i) \right\rangle_0 = 0. \tag{8.17}$$

Vacuum diagrams thus cancel when summing over all topologies and integrating over times at a given order.

In the following, as we develop new algorithms for the real-time many-body problem, we will be interested in the computation of the simplest of correlators: the density of $\uparrow$ spins at the end point of the Keldysh contour $\mathcal{C}$

$$d = c_\uparrow^\dagger(t_{\max}) c_\uparrow(t_{\max}). \tag{8.18}$$

4. See Chapter 5.
5. For a full derivation of Feynman diagrams representation out-of-equilibrium, see for instance Ref. [153].

According to Eq. (8.11), d is proportional to the lesser component of the Green's function

$$d = -iG^{<}_{\uparrow}(t_{\max}, t_{\max}) = -iG^{+-}(t_{\max}, t_{\max}). \tag{8.19}$$

The expansion in powers of U of the density takes the form $d = \sum_{n\geq 0} d_n$, where

$$\begin{aligned} d_n = (-iU)^n \int_0^{t_{\max}} \mathrm{d}t_1 \dots \mathrm{d}t_n \sum_{\alpha_1 \dots \alpha_n} \alpha_1 \dots \alpha_n \left\langle T_{\mathcal{C}} \prod_{i=1}^{n} c^{\dagger}_{\downarrow}(t_i, \alpha_i) c_{\downarrow}(t_i, \alpha_i) \right\rangle_0 \\ \times \left\langle T_{\mathcal{C}} \prod_{i=1}^{n} \left[c^{\dagger}_{\uparrow}(t_i, \alpha_i) c_{\uparrow}(t_i, \alpha_i) \right] c^{\dagger}_{\uparrow}(t_{\max}, +) c_{\uparrow}(t_{\max}, -) \right\rangle_0 . \end{aligned} \tag{8.20}$$

We can therefore represent d as the sum of all connected diagrams ending with a measurement vertex bearing time $t_{\max}$, such that the ingoing and outgoing Keldysh indices are respectively $+$ and $-$:

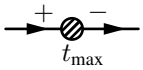

(8.21)

This representation will automatically form a fermion loop linked to the measurement, hence bringing a (-1) when the density is computed. This is consistent with Eq. (8.19): at order 0, the density is $-ig^{<}_{\uparrow}(0)$, but the straight line represent and $i\hat{g}$. To give a concrete example, the following diagram evaluates to

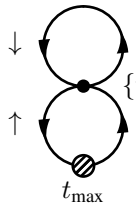

$$\{t, \alpha\} = (-1)^2 \int_0^{t_{\max}} \mathrm{d}t \sum_{\alpha} (-i\alpha U)\, ig^{+\alpha}_{\uparrow}(t_{\max} - t)\, ig^{\alpha -}_{\uparrow}(t - t_{\max})\, ig^{\alpha\alpha}_{\downarrow}(0). \tag{8.22}$$

8.3 Continuous-time quantum Monte Carlo algorithms

The task at hand is to numerically sample the order-n contribution to the density, see Eq. (8.20). As described in Chapter 5, continuous-time quantum Monte Carlo methods provide very efficient and flexible tools to solve impurity problems at equilibrium. Early attempts of real-time quantum Monte Carlo algorithms therefore were direct extensions of those on the Keldysh contour. They sampled the partition function Z, both using strong-coupling and weak-coupling expansions [112, 175, 174, 144].

Let us briefly summarize the original algorithm based on the expansion in the Coulomb interaction U [10, 175]. Using Wick's theorem, one can rewrite Eq. (8.14) using determinants constructed from the noninteracting Green's function $\hat{g}$

$$Z_n = \int_0^{t_{\max}} \mathrm{d}t_1 \dots \mathrm{d}t_n \sum_{\alpha_1 \dots \alpha_n} Z_n(\{t_i, \alpha_i\}_{1\leq i\leq n}), \tag{8.23}$$

where

$$Z_n(\{t_i, \alpha_i\}_{1\leq i\leq n}) = \alpha_1 \dots \alpha_n (iU)^n \prod_{\sigma} \det \left[g^{\alpha_i \alpha_j}_{\sigma}(t_i - t_j) \right]_{1\leq i,j\leq n}. \tag{8.24}$$

The evaluation of such a multi-dimensional integral is well handled by standard Monte Carlo techniques. [6] We define a configuration by the perturbation order n and n points on the Keldysh contour

$$\mathfrak{c} = \{n; t_1, \dots, t_n; \alpha_1, \dots \alpha_n\}. \tag{8.25}$$

The weight of a configuration is chosen to be $w_{\mathfrak{c}} = |Z(\mathfrak{c})| = |Z_n(\{t_i, \alpha_i\}_{1\leq i\leq n})|$, so that the order-$n$ contribution to the partition function is evaluated as

$$Z_n \sim \sum_{\mathfrak{c}}^{\mathrm{MC}} \mathrm{sgn} Z(\mathfrak{c}). \tag{8.26}$$

6. See Section 5.2 for a complete introduction to Monte Carlo methods.

New configurations are then constructed using an importance sampling based on the Metropolis-Hastings algorithm [107, 67].

Concerning the density measurement, Eq. (8.20) can also be rewritten using determinants

$$d_n = \int_0^{t_{\max}} \mathrm{d}t_1 \dots \mathrm{d}t_n \sum_{\alpha_1 \dots \alpha_n} d_n(\{t_i, \alpha_i\}_{1 \leq i \leq n}), \tag{8.27}$$

where

$$d_n(\{t_i, \alpha_i\}_{1 \leq i \leq n}) = -\alpha_1 \dots \alpha_n i^{n+1} U^n \prod_\sigma \det \mathcal{D}_\sigma(\{t_i, \alpha_i\}_{1 \leq i \leq n}). \tag{8.28}$$

These determinants now have to take into account the density measurement at $t_{\max}$:

$$\mathcal{D}_\uparrow(\{t_i, \alpha_i\}_{1 \leq i \leq n}) = \begin{pmatrix} \left[g_\uparrow^{\alpha_i \alpha_j}(t_i - t_j)\right]_{1 \leq i,j \leq n} & \begin{matrix} g_\uparrow^{\alpha_1 -}(t_1 - t_{\max}) \\ \vdots \\ g_\uparrow^{\alpha_n -}(t_n - t_{\max}) \end{matrix} \\ \begin{matrix} g_\uparrow^{+\alpha_1}(t_{\max} - t_1) & \dots & g_\uparrow^{+\alpha_n}(t_{\max} - t_n) \end{matrix} & g_\uparrow^{+-}(0) \end{pmatrix}, \tag{8.29}$$

and

$$\mathcal{D}_\downarrow(\{t_i, \alpha_i\}_{1 \leq i \leq n}) = \left[g_\downarrow^{\alpha_i \alpha_j}(t_i - t_j)\right]_{1 \leq i,j \leq n}. \tag{8.30}$$

The order-n contribution to the density is then simply expressed as

$$d_n \sim \sum_{\mathfrak{c}}^{\mathrm{MC}} \frac{d(\mathfrak{c})}{|Z(\mathfrak{c})|}. \tag{8.31}$$

The main issue these historical algorithms are facing is the "dynamical" sign problem arising from the expansion of the evolution operator $e^{-i\mathcal{H}t}$: the convergence of the perturbation theory is oscillatory rather than exponential (as it is in the equilibrium case when expanding $e^{-\tau\mathcal{H}}$). This results in a sign problem which severely limits the maximum perturbation order on the real-time branches, and prevents the algorithms from reaching the long-time steady-state limit in several regimes of parameters [175, 10]. It is worth noting that weak-coupling CT-QMC has however enabled some pioneering nonequilibrium studies of the Hubbard model [44, 161].

Current efforts to build real-time quantum Monte Carlo methods mainly explore two routes: the inchworm algorithm [37, 35, 36, 32, 33, 9, 21] and the so-called diagrammatic QMC [128, 15, 14] that we present in the next Section.

8.4 Diagrammatic quantum Monte Carlo algorithm

First introduced in Ref. [128], the real-time diagrammatic QMC algorithm directly samples contributions to the density (and not the partition function) using an explicit summation over Keldysh indices α_i, which makes the computation of the weight scale as 2^n for a given perturbation order n. However, this exponential sum has been shown to cancel vacuum diagrams, a property also used in recent diagrammatic equilibrium QMC methods, [7] and to allow the direct computation of observables in the infinite-time steady-state limit. In this Section, we review the basis of this algorithm and we propose in the next Chapter new developments based on it.

Note that, as in equilibrium (see Chapter 6), the series for the density may not be convergent for the parameters considered. We will not tackle this question in this Thesis and refer the reader to Refs. [14, 15] concerning resummation techniques in real time.

8.4.1 Cancellation of vacuum diagrams and steady-state limit

Cancellation of vacuum diagrams when summing over Keldysh indices

We have seen earlier that, when summing over Keldysh indices and integrating over times, contributions to the partition function vanish at each perturbation order n. Reexpressed in terms of determinants, this

7. As we have seen in Chapters 6 and 7.

means

$$\forall n > 0, \int_0^{t_{\max}} \mathrm{d}t_1 \dots \mathrm{d}t_n \sum_{\alpha_1 \dots \alpha_n} \alpha_1 \dots \alpha_n \prod_\sigma \det \left[g_\sigma^{\alpha_i \alpha_j}(t_i - t_j) \right]_{1 \leq i,j \leq n} = 0. \tag{8.32}$$

Let us now consider a given set of n ordered interacting times $t_1 < \dots < t_n$. The matrix $\left[g_\sigma^{\alpha_i \alpha_j}(t_i - t_j) \right]_{1 \leq i,j \leq n}$ actually does not change when the Keldysh index associated with t_n, α_n, is flipped for $+$ to $-$. Indeed, as t_n is the largest time, we have

$$g_\sigma^{\alpha_i -}(t_i - t_n) = \delta_{\alpha_i +} g_\sigma^<(t_i - t_n) + \delta_{\alpha_i -} g_\sigma^>(t_i - t_n) = g_\sigma^{\alpha_i +}(t_i - t_n), \tag{8.33a}$$

$$g_\sigma^{-\alpha_i}(t_n - t_i) = \delta_{\alpha_i +} g_\sigma^>(t_n - t_i) + \delta_{\alpha_i -} g_\sigma^<(t_n - t_i) = g_\sigma^{+\alpha_i}(t_n - t_i), \tag{8.33b}$$

$$g_\sigma^{--}(0) = g_\sigma^{++}(0). \tag{8.33c}$$

This implies

$$\begin{aligned} &\sum_{\alpha_1 \dots \alpha_{n-1}} \alpha_1 \dots \alpha_{n-1} \prod_\sigma \det \left[g_\sigma^{\alpha_i \alpha_j}(t_i - t_j)|_{\alpha_n = +} \right]_{1 \leq i,j \leq n} \\ &\qquad = \sum_{\alpha_1 \dots \alpha_{n-1}} \alpha_1 \dots \alpha_{n-1} \prod_\sigma \det \left[g_\sigma^{\alpha_i \alpha_j}(t_i - t_j)|_{\alpha_n = -} \right]_{1 \leq i,j \leq n}. \end{aligned} \tag{8.34}$$

For every configuration of times $\{t_1, \dots, t_n\}$, vacuum diagrams therefore cancel when performing the explicit 2^n sum over Keldysh indices:

$$\forall n > 0, \forall \{t_1, \dots, t_n\} \in [0, t_{\max}]^n, \sum_{\alpha_1 \dots \alpha_n} \alpha_1 \dots \alpha_n \prod_\sigma \det \left[g_\sigma^{\alpha_i \alpha_j}(t_i - t_j) \right]_{1 \leq i,j \leq n} = 0. \tag{8.35}$$

Note that, in principle, only the summation over the last Keldysh index α_n is needed to obtain the cancellation of the partition function, as was used for example in Ref. [174]. But to obtain the steady-state limit and tame the sign problem in the computation of observables such as the density, the sum over all Keldysh indices is needed (see Eq. (8.38) and the argument below).

As we have seen in Chapters 6 and 7, recent developments in imaginary-time diagrammatic QMC also achieved, through an iterative procedure, the cancellation of disconnected and non one-particle irreducible diagrams at every Monte Carlo step at an exponential cost in the perturbation order [135, 110, 168].

Direct access to the steady-state limit in the density computation

This cancellation of vacuum diagrams when summing over Keldysh indices directly implies the clusterization of interaction times near $t_{\max}$ in the density computation, therefore allowing us to address any measurement time.

Let n be a given perturbation order, and $t_1 < t_2 < \dots < t_n$ n interaction times. Let us assume that the first j times are located far away from the measurement time $t_{\max}$, and that the last $n - j$ times are located in the vicinity of $t_{\max}$. We can formally consider

$$\forall 1 \leq i \leq j, |t_i - t_{\max}| \to \infty. \tag{8.36}$$

Because the Green's function is a local quantity, this means that for all $t \in \{t_1, \dots, t_j\}, t' \in \{t_{j+1}, \dots, t_n; t_{\max}\}$

$$||\hat{g}_\sigma(t - t')|| \to 0, \quad ||\hat{g}_\sigma(t' - t)|| \to 0. \tag{8.37}$$

Remembering that the density is expressed in terms of determinants, Eq. (8.28), we have

$$\begin{aligned} &\sum_{\alpha_1 \dots \alpha_n} \alpha_1 \dots \alpha_n \prod_\sigma \det \mathcal{D}_\sigma(\{t_i, \alpha_i\}_{1 \leq i \leq n}) \\ &\qquad \simeq \left(\sum_{\alpha_1 \dots \alpha_j} \alpha_1 \dots \alpha_j \prod_\sigma \det A_\sigma \right) \left(\sum_{\alpha_{j+1} \dots \alpha_n} \alpha_{j+1} \dots \alpha_n \prod_\sigma \det B_\sigma \right), \end{aligned} \tag{8.38}$$

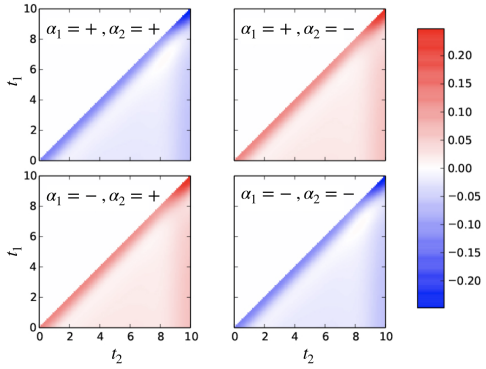

(a) Contributions to $d_2(t_1, t_2; \alpha_1, \alpha_2)$.

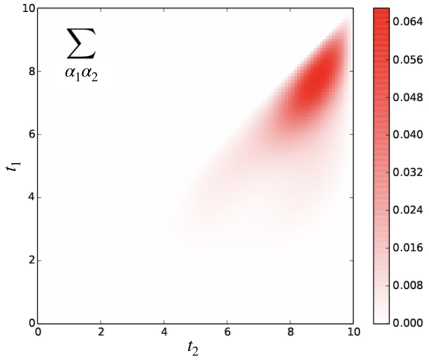

(b) Sum over α_1 and α_2 of $d_2(t_1, t_2; \alpha_1, \alpha_2)$.

Figure 8.1 – Pictorial representation of the clusterization of times around $t_{\max} = 10$ in the density calculation. Adapted from Ref. [128].

with

$$A_\sigma = \left[(\hat{g}_\sigma)_{\alpha_i \alpha_i'}(t_i - t_{i'})\right]_{1 \le i, i' \le j}, \tag{8.39a}$$

$$B_\downarrow = \left[(\hat{g}_\downarrow)_{\alpha_i \alpha_i'}(t_i - t_{i'})\right]_{j+1 \le i, i' \le n}, \tag{8.39b}$$

$$B_\uparrow = \begin{pmatrix} \left[g_\uparrow^{\alpha_i \alpha_i'}(t_i - t_{i'})\right]_{j+1 \le i, i' \le n} & \begin{matrix} g_\uparrow^{\alpha_{j+1} -}(t_{j+1} - t_{\max}) \\ \vdots \\ g_\uparrow^{\alpha_n -}(t_n - t_{\max}) \end{matrix} \\ \begin{matrix} g_\uparrow^{+\alpha_{j+1}}(t_{\max} - t_{j+1}) & \dots & g_\uparrow^{+\alpha_n}(t_{\max} - t_n) \end{matrix} & g_\uparrow^{+-}(0) \end{pmatrix}. \tag{8.39c}$$

However, $\sum_{\alpha_1 \dots \alpha_j} \alpha_1 \dots \alpha_j \prod_\sigma A_\sigma$ is a contribution to Z at order j, and it vanishes according to Eq. (8.35). Therefore

$$\sum_{\alpha_1 \dots \alpha_n} \alpha_1 \dots \alpha_n \prod_\sigma \det \mathcal{D}_\sigma(\{t_i, \alpha_i\}_{1 \le i \le n}) \simeq 0, \tag{8.40}$$

and this proves the clusterization of times around $t_{\max}$ in the computation of the density.

As a direct consequence, Monte Carlo algorithms based on an importance sampling will only consider interaction times near $t_{\max}$: They can address *any measurement time*, including the steady-state limit, when earlier methods were limited to short-term measurements [112, 175, 174, 144].

To better understand understand this phenomenon, a pictorial representation of this cancellation is reproduced from Ref. [128] in Fig. 8.1. Let us consider perturbation order $n = 2$, for which the contribution to the density writes

$$d_2(t_1, t_2; \alpha_1, \alpha_2) = iU^2 \alpha_1 \alpha_2 \prod_\sigma \det \mathcal{D}_\sigma, \tag{8.41}$$

In Fig. 8.1a, this quantity is plotted as a function of $t_1 \in [0, 10]$ and $t_2 < t_1$ for the different Keldysh indices α_1 and α_2. Contributions are uniformly distributed in time, and they can either be positive or negative. In Fig. 8.1b the sum over Keldysh indices of these four terms is plotted: Huge cancellations indeed appear, and we witness the clusterization of times around $t_{\max}$.

8.4.2 Details of the Monte Carlo implementation

Direct sampling of the density

A configuration $\mathfrak{c}$ is determined by a given perturbation order n and a set of n interaction times (and *not* Keldysh points as in Section 8.3): $\mathfrak{c} = \{n; t_1, \dots, t_n\}$. The contribution to d_n of a given configuration is

$$d_n(t_1, \dots t_n) = -i^{n+1} U^n \sum_{\alpha_1 \dots \alpha_n} \alpha_1 \dots \alpha_n \prod_\sigma \det \mathcal{D}_\sigma(\{t_i, \alpha_i\}_{1 \le i \le n}). \tag{8.42}$$

In the Monte Carlo algorithm, configurations are sampled stochastically according to their weight, which we choose to be $w_{\mathfrak{c}} = |d(\mathfrak{c})| = |d_n(t_1, \ldots, t_n)|$. We then have

$$d_n = \int_0^{t_{\max}} \mathrm{d}t_1 \ldots \mathrm{d}t_n \; d_n(t_1, \ldots, t_n) \propto \sum_{\mathfrak{c}}^{\mathrm{MC}} \operatorname{sgn} d(\mathfrak{c}). \tag{8.43}$$

The heart of the algorithm consists in computing the sum of determinants over Keldysh indices

$$s_{\mathfrak{c}} = -i^{n+1} \sum_{\alpha_1 \ldots \alpha_n} \alpha_1 \ldots \alpha_n \prod_{\sigma} \det \mathcal{D}_\sigma(\{t_i, \alpha_i\}_{1 \leq i \leq n}). \tag{8.44}$$

It was pointed out in Ref. [128] that fast updates of determinants can be applied in this context using a Gray code, so that the overall complexity scales as $2^n n^2$. However, some of the matrices in this sum are close to singular, propagating numerical errors. We found that, for all practical purposes, computing each determinant of the sum from scratch actually leads to smaller error bars in the computation of the density, even though it theoretically scales as $2^n n^3$.

As detailed in Section 5.2, we use a standard Metropolis algorithm [107] to generate Markov chains distributed according to the weights $w_{\mathfrak{c}}$. Starting from an order-n configuration $\mathfrak{c}$, a new configuration $\mathfrak{c}'$ is proposed according to one of the following two Monte Carlo updates:

1. Add a new interaction time t, that we choose according to a Cauchy law ρ (see below). The Metropolis ratio is
$$\frac{T_{\mathfrak{c}'\mathfrak{c}} w_{\mathfrak{c}'}}{T_{\mathfrak{c}\mathfrak{c}'} w_{\mathfrak{c}}} = \frac{1/(n+1)}{\rho(t)} \frac{U^{n+1}|s_{\mathfrak{c}'}|}{U^n |s_{\mathfrak{c}}|} = \frac{U}{(n+1)\rho(t)} \left| \frac{s_{\mathfrak{c}'}}{s_{\mathfrak{c}}} \right|. \tag{8.45}$$
2. Remove a randomly chosen interaction time t. The Metropolis ratio is
$$\frac{T_{\mathfrak{c}'\mathfrak{c}} w_{\mathfrak{c}'}}{T_{\mathfrak{c}\mathfrak{c}'} w_{\mathfrak{c}}} = \frac{n\rho(t)}{U} \left| \frac{s_{\mathfrak{c}'}}{s_{\mathfrak{c}}} \right|. \tag{8.46}$$

Proposition of times

We have shown previously that times clusterize around $t_{\max}$. It is therefore more efficient to propose times located around it instead of uniformly distributed between 0 and $t_{\max}$. We consider a Cauchy law determined by two parameters t_0 and a

$$\rho(t) = \frac{1}{C} \frac{1}{1 + \left(\frac{t - t_0}{a}\right)^2}. \tag{8.47}$$

C is a normalization factor such that the integral of ρ between 0 and $t_{\max}$ is 1. $C = a\,[C_2 - C_1]$, where $C_1 = \arctan\left(-\frac{t_0}{a}\right)$ and $C_2 = \arctan\left(\frac{t_{\max} - t_0}{a}\right)$.

To obtain a new time that follows this probability law, one can perform these three steps:

1. Choose a random number u uniformly distributed between 0 and 1.
2. Construct
$$x = \frac{1}{2} + \frac{1}{\pi} \left[(1-u)C_1 + uC_2\right], \tag{8.48}$$
uniformly distributed between $\frac{1}{2} + \frac{1}{\pi} C_1$ and $\frac{1}{2} + \frac{1}{\pi} C_2$.
3. Compute
$$t = t_0 + a \tan\left(\pi \left(x - \frac{1}{2}\right)\right), \tag{8.49}$$
distributed between 0 and $t_{\max}$ according to ρ.

The parameters t_0 and a are then obtained by fitting the 1D projection of times visited by the Monte Carlo, accumulated during the first part of the computation.

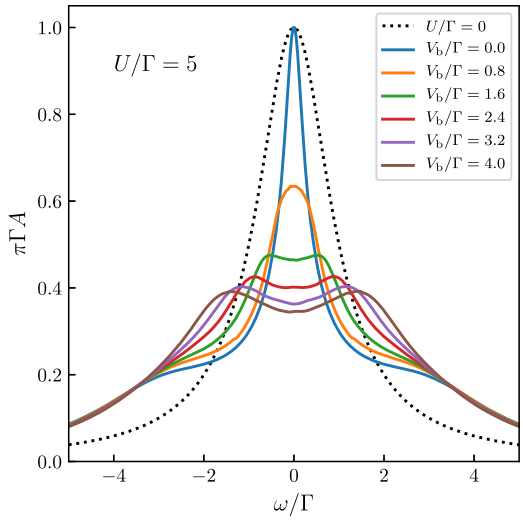

Figure 8.2 – Out-of-equilibrium spectral functions for a half-filled ($\epsilon_d/\Gamma = 0$) impurity coupled to two leads with a voltage bias V_b. The interaction strength is $U/\Gamma = 5$. The noninteracting spectral function is shown as a dotted line. [14]

Redefinition of noninteracting propagators

As shown in Section 5.3.1, there is some freedom in the choice of the noninteracting propagator used to construct the perturbation expansion through the α-shift. [8] The redefinition of the interaction term is taken into account by subtracting α on the diagonal of the determinants, the shift in the chemical potential being absorbed in a redefinition of the noninteracting propagators. In particular, it was shown that α can strongly modify the radius of convergence of the perturbation series [128, 183].

Normalization procedure

As Monte Carlo results need to be normalized, we restrict our calculation to two consecutive orders, n and $n+1$, and a time or vertex can be added (resp. removed) only if the current configuration $\mathfrak{c}$ is at order n (resp $n+1$). We measure both the density (d_n and d_{n+1}) and a normalization factor (η_n and η_{n+1}). The latter is chosen to be the sum of the weights

$$\eta_n \propto \sum_{\mathfrak{c}}^{\mathrm{MC}} w_{\mathfrak{c}}, \tag{8.50}$$

where the proportionality constant is the same as in the calculation of d_n. If $\tilde{d}_n$ and $\tilde{\eta}_n$ are the unrenormalized sums of the contributions accumulated in the Monte Carlo procedure, then the normalized values for d_n and η_n are obtained as

$$d_{n+1} = \frac{\eta_n}{\tilde{\eta}_n}\tilde{d}_{n+1}; \qquad \eta_{n+1} = \frac{\eta_n}{\tilde{\eta}_n}\tilde{\eta}_{n+1}, \tag{8.51}$$

and η_n is then used to normalize the following simulation between orders $n+1$ and $n+2$. The lowest order is computed analytically to close the equations.

8.4.3 Example of numerical results

The problem at hand being much more complicated to treat, real-time diagrammatic methods are still in their infancy compared to their equilibrium counterparts. The algorithm presented above has therefore only been applied to quantum impurity models. Static quantities were first computed, and, more recently, the Green's function has been addressed [15, 14, 104]. We present in this Section out-of-equilibrium spectral functions for a quantum dot between two noninteracting leads as computed in Ref. [14].

8. Note that in this context α *does not* denote a Keldysh index but a scalar, in order to be consistent with the existing literature.

A correlated quantum impurity with energy level ϵ_d is placed on site $i = 0$ of a 1D chain, between two non-interacting leads ($i > 0$ and $i < 0$). The Hamiltonian of the system is

$$\mathcal{H} = \epsilon_d(n_\uparrow + n_\downarrow) + U\theta(t)\left(n_\uparrow - \frac{1}{2}\right)\left(n_\downarrow - \frac{1}{2}\right) + \sum_{i=-\infty}^{+\infty} \gamma_i \left(c_{i\sigma}^\dagger c_{i+1\sigma} + \text{ h.c.}\right), \tag{8.52}$$

where $c_{i\sigma}^\dagger$ (resp. $c_{i\sigma}$) creates (resp. annihilates) an electron with spin σ on site i of the chain, and $n_\sigma = c_{0\sigma}^\dagger c_{0\sigma}$ is the density operator on the impurity. γ_i is a hopping constant between adjacent sites of the chain. We set $\gamma_i = 1$ except for $\gamma_0 = \gamma_{-1} = \gamma$ which connect the impurity to the leads.

The tunneling rate $\Gamma = 2\pi\gamma^2\rho_F$ from the impurity to the electrons is introduced, where ρ_F is the density of states of the electron reservoirs at the Fermi level. In the following, Γ is our energy unit.

Let us consider the half-filled impurity ($\epsilon/\Gamma = 0$) subject to a bias-voltage V_b, the interaction being set to $U/\Gamma = 5$. We reproduce in Fig. 8.2 the out-of-equilibrium spectral functions obtained using the real-time diagrammatic Monte Carlo algorithm for different values of V_b. The black dotted line represents the noninteracting spectral function. The Kondo resonance at $V_b = 0$ is seen to be split into two broad peaks when the voltage bias is increased, as was expected from NCA and perturbative calculations [181, 51].

Note that, up to error bars that are smaller than symbol size, this plot is an exact solution of the model described by Eq. (8.52) and a bias-voltage V_b in the steady-state regime.

Chapter 9

Novel quantum Monte Carlo algorithms in the Larkin-Ovchinnikov basis

We have seen in the previous Chapter that summing over Keldysh indices in the real-time diagrammatic quantum Monte Carlo allows to reach the long-time limit in the computation of contributions to the perturbation theory. However, the exponential scaling of the Monte Carlo weight limits our capability to compute high orders with great precision (we typically are limited to 10 of them). Even though Bayesian techniques can overcome noise amplification occurring in the resummation of the series [14], this prevents the algorithm from reaching very large U.

In this Chapter, we show that we can obtain the cancellation of diagrams and the long-time clusterization property without summing an exponential number of terms. Using the Larkin-Ovchinnikov (LO) basis in Keldysh space, we rewrite the integrand as a sum of 4^n determinants, but we show that diagrammatic rules in this basis are such that every diagram has the clusterization property. In other words, the elimination of vacuum diagrams is directly achieved in the diagrammatics without the need of an exponential sum. We then implement and compare different Monte Carlo algorithms based on this mathematical property. This work has been published in Ref. [109], the full text being reproduced in Appendix VII.

9.1 Green's functions in the Larkin-Ovchinnikov formalism

Starting from the expression of the Green's function $\hat{G}_\sigma$ on the Keldysh contour we define its counterpart in the LO basis through the following transformation [82, 92]

$$\hat{G}^{\mathrm{LO}}_\sigma(t,t') = L^\dagger \tau_3 \hat{G}_\sigma(t,t') L, \tag{9.1}$$

where $L = \frac{1}{\sqrt{2}}\begin{pmatrix} 1 & 1 \\ -1 & 1 \end{pmatrix}$ and $\tau_3 = \begin{pmatrix} 1 & 0 \\ 0 & -1 \end{pmatrix}$. The Green's function now takes the 2×2 form

$$\hat{G}^{\mathrm{LO}}_\sigma = \begin{pmatrix} R_\sigma & K_\sigma \\ 0 & A_\sigma \end{pmatrix}, \tag{9.2}$$

where R, K, and A are respectively the retarded, Keldysh and advanced Green's functions defined as

$$R_\sigma(t,t') = -i\theta(t-t')\langle\{c_\sigma(t), c^\dagger_\sigma(t')\}\rangle, \tag{9.3a}$$
$$A_\sigma(t,t') = i\theta(t'-t)\langle\{c_\sigma(t), c^\dagger_\sigma(t')\}\rangle, \tag{9.3b}$$
$$K_\sigma(t,t') = -i\langle[c_\sigma(t), c^\dagger_\sigma(t')]\rangle. \tag{9.3c}$$

The advanced and retarded Green's functions are linked through

$$A_\sigma(t,t') = R^*_\sigma(t',t), \tag{9.4}$$

so that we only have two independent functions in this basis. A common choice is to work with R and K. The Keldysh index $\alpha \in \{\pm\}$ is replaced by an LO index 0 or 1. In the following, l will always denote such

an index unless otherwise stated.

R, A and K are related to the $\pm$ Green's functions of Eq. (8.11) through

$$R_\sigma(t,t') = G_\sigma^{++}(t,t') - G_\sigma^{<}(t,t') = G_\sigma^{>}(t,t') - G_\sigma^{--}(t,t'), \tag{9.5a}$$
$$A_\sigma(t,t') = G_\sigma^{++}(t,t') - G_\sigma^{>}(t,t') = G_\sigma^{<}(t,t') - G_\sigma^{--}(t,t'), \tag{9.5b}$$
$$K_\sigma(t,t') = G_\sigma^{++}(t,t') + G_\sigma^{--}(t,t') = G_\sigma^{>}(t,t') + G_\sigma^{<}(t,t'). \tag{9.5c}$$

At equilibrium, the fluctuation-dissipation theorem now takes the form

$$K_\sigma(\omega) = \tanh\left(\frac{\beta\omega}{2}\right)\left[R_\sigma(\omega) - A_\sigma(\omega)\right]. \tag{9.6}$$

9.2 Diagrammatics of an expansion in the Coulomb interaction U

As in the previous Chapter, we consider an interaction term, turned on at $t = 0$, of the form $V(t) = Un_\uparrow n_\downarrow$. First, we describe a set of naive rules, but show that they bring eight possible diagrams for each interaction vertex. Then we introduce a redefinition of the bare propagator that allows to reduce the number of diagrams.

9.2.1 Naive diagrammatic rules

Diagrammatic rules in the LO basis are obtained by applying the transformation from Eq. (9.1) to the rules derived in Section 8.2, keeping in mind that, for a given set of interacting times, the sum over LO indices has to be the same as the sum over Keldysh indices.

First, a straight line represents a non-interacting Green's function

$t', l' \xrightarrow{\sigma} t, l \quad = i\,(\hat{g}_\sigma)_{ll'}\,(t-t').$ (9.7)

To derive the expression of the 4-leg interaction vertex, we first note that the sum of the different $\{\pm\}$ configurations from Eq. (8.16) can be written in the $\mathcal{H}_\uparrow \otimes \mathcal{H}_\downarrow$ space, in the form

$$-iU\left(m_+ \otimes m_+ - m_- \otimes m_-\right), \tag{9.8}$$

where $m_+ = \begin{pmatrix} 1 & 0 \\ 0 & 0 \end{pmatrix}$ and $m_- = \begin{pmatrix} 0 & 0 \\ 0 & 1 \end{pmatrix}$ are matrices in the $\{\pm\}$ basis, and $\mathcal{H}_\sigma$ is the Hilbert space for spin σ. The m_+ and m_- matrices transform as

$$L^\dagger \tau_3 m_+ L = \frac{1}{2}\begin{pmatrix} 1 & 1 \\ 1 & 1 \end{pmatrix} = \frac{1}{2}\tau_\uparrow, \tag{9.9a}$$
$$L^\dagger \tau_3 m_- L = \frac{1}{2}\begin{pmatrix} -1 & 1 \\ 1 & -1 \end{pmatrix} = \frac{1}{2}\tau_\downarrow. \tag{9.9b}$$

Hence the sum of different LO contributions can be written

$$-\frac{iU}{4}\left(\tau_\uparrow \otimes \tau_\uparrow - \tau_\downarrow \otimes \tau_\downarrow\right). \tag{9.10}$$

We write $\tau_\uparrow = \tau + \mathbf{1}$ and $\tau_\downarrow = \tau - \mathbf{1}$, where $\tau = \begin{pmatrix} 0 & 1 \\ 1 & 0 \end{pmatrix}$ and $\mathbf{1}$ is the 2×2 identity matrix. The above sum can then be rewritten [1]

$$-\frac{iU}{2}(\mathbf{1} \otimes \tau + \tau \otimes \mathbf{1}). \tag{9.11}$$

Diagramatically, this means that the two sides of an interaction vertex (associated to opposite spins) are now asymmetric: if we have the identity flowing on the σ side, then the $\bar{\sigma}$ side bears the τ part of the interaction.

1. Note that this is consistent with Ref. [18].

An interaction vertex in the LO basis can therefore be represented as

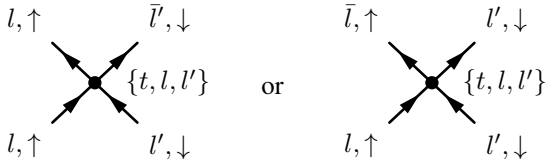

(9.12)

There are eight possible configurations for a given interaction time t, and therefore 8^n at perturbation order n, instead of 2^n in the $\{\pm\}$ basis. This is a drastic increase, especially as we want to overcome this exponential scaling. We see next that we can reduce the number of diagrams to 4^n by redefining the noninteracting propagator.

However, it is important to stress at this point that each vacuum diagram already vanishes in this formalism. Indeed, as we will show in Section 9.3, it is *the identity part* of the vertex, already present in Eq. (9.11), that is essential in the proof of the cancellation of vacuum diagrams and the clusterization of times in the computation of observables.

9.2.2 Redefinition of the noninteracting propagator and reduction of the number of diagrams

In order to reduce the number of indices involved in the diagrammatics, we first rewrite the sum of LO contributions to the 4-leg vertex in the form

$$-\frac{iU}{4}\left(\tau_\uparrow\otimes\tau_\uparrow-\tau_\downarrow\otimes\tau_\downarrow\right)=-\frac{iU}{2}\left(\mathbf{1}\otimes\tau_\downarrow+\tau_\uparrow\otimes\mathbf{1}\right). \tag{9.13}$$

Noticing that $\tau_\uparrow$ and $\tau_\downarrow$ are rank-1 matrices: $\tau_\uparrow = v_\uparrow v_\uparrow^\top$ with $v_\uparrow = \begin{pmatrix}1\\1\end{pmatrix}$ and $\tau_\downarrow = v_\downarrow(-v_\downarrow^\top)$ with $v_\downarrow = \begin{pmatrix}1\\-1\end{pmatrix}$, it is possible to absorb the τ_σ part of the vertex in a redefinition of the noninteracting propagator. We store the information about both the bare propagator $\hat{g}_\sigma^{\mathrm{LO}}$ and the nature of the vertices it connects in the form of a 3×3 renormalized matrix $\hat{\tilde{g}}_\sigma$. With the convention that $\sigma=\uparrow$ should be understood as $+1$ and $\sigma=\downarrow$ as -1, the different components of this matrix are

$$i\left(\hat{\tilde{g}}_\sigma\right)_{ll'}(t-t') = \quad t',l' \xrightarrow{\ \sigma\ } t,l \quad = i\left(\hat{g}_\sigma^{\mathrm{LO}}\right)_{ll'}(t-t'), \tag{9.14a}$$

$$i\left(\hat{\tilde{g}}_\sigma\right)_{l2}(t-t') = \quad t',\tau_\sigma \xrightarrow{\ \sigma\ } t,l \quad = i\left(\hat{g}_\sigma^{\mathrm{LO}}(t-t')v_\sigma\right)_l, \tag{9.14b}$$

$$i\left(\hat{\tilde{g}}_\sigma\right)_{2l}(t-t') = \quad t',l' \xrightarrow{\ \sigma\ } t,\tau_\sigma \quad = i\left(\sigma v_\sigma^\top \hat{g}_\sigma^{\mathrm{LO}}(t-t')\right)_l, \tag{9.14c}$$

$$i\left(\hat{\tilde{g}}_\sigma\right)_{22}(t-t') = \quad t',\tau_\sigma \xrightarrow{\ \sigma\ } t,\tau_\sigma \quad = i\sigma v_\sigma^\top \hat{g}_\sigma^{\mathrm{LO}}(t-t')v_\sigma. \tag{9.14d}$$

We obtain

$$\hat{\tilde{g}}_\sigma = \begin{pmatrix} r_\sigma & k_\sigma & r_\sigma+\sigma k_\sigma \\ 0 & a_\sigma & \sigma a_\sigma \\ \sigma r_\sigma & \sigma k_\sigma + a_\sigma & \sigma[r_\sigma+a_\sigma]+k_\sigma \end{pmatrix}. \tag{9.15}$$

Note that this 3×3 form of the Green's function comes from the absorption of the τ_σ part of the vertex and has nothing to do with the Baym-Kadanoff L-shaped contour used in thermal real-time computations.

An LO vertex can therefore be characterized by a tuple $\{t, i_\tau, l\}$, where $t\in[0,t_{\max}]$, $i_\tau\in\{-1,1\}$ and $l\in\{0,1\}$. $i_\tau=1$ (resp. -1) indicates that the $\uparrow$ (resp. $\downarrow$) spin is carrying the $\tau_\uparrow$ (resp. $\tau_\downarrow$) side, and l is the LO index entering the identity-part of the vertex. To simplify upcoming equations, we express the indices of $\hat{\tilde{g}}_\uparrow$ and $\hat{\tilde{g}}_\downarrow$ at a vertex $\{t,i_\tau,l\}$ in the form of two composite indices $L^\uparrow$ and $L^\downarrow$:

$$L^\sigma = \begin{cases} 2 & \text{if } i_\tau=\sigma, \\ l & \text{otherwise.} \end{cases} \tag{9.16}$$

With this convention, the interaction vertex, now proportional to $\frac{\mathbf{1}\otimes\tau_\downarrow+\tau_\uparrow\otimes\mathbf{1}}{2}$, has the following diagrammatic representation

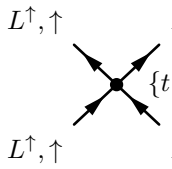

$$= -\frac{iU}{2}\left(\delta_{i_\tau 1}\delta_{L^\uparrow 2}\delta_{L^\downarrow l} + \delta_{i_\tau -1}\delta_{L^\downarrow 2}\delta_{L^\uparrow l}\right). \tag{9.17}$$

As there are two possible choices both for i_τ and for l, there are 4^n LO configurations for a given set of n interaction times. This is a huge gain compared to the 8^n configurations of the naive diagrammatics, but still has to be compared with the 2^n possibilities of the $\{\pm\}$ basis. However, we show in Section 9.3 that vacuum diagrams now directly cancel in this formalism, without the need to perform an explicit sum over indices.

9.2.3 Equal times: the special case of the closed loop

In order to have complete diagrammatic rules, we need to specify the equal-time limit of $\hat{\tilde{g}}$, that is the expression of $r_\sigma(0)$, $a_\sigma(0)$ and $k_\sigma(0)$. Once again, we want the LO formalism to be consistent with the $\{\pm\}$ one when summing over indices.

Let us start with the expression of the following fermionic bubble in the $\{\pm\}$ basis

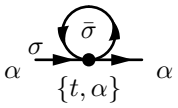

$$= \alpha U g^{\alpha\alpha}_{\bar{\sigma}}(0) = \alpha U g^{<}_{\bar{\sigma}}(0), \tag{9.18}$$

the last equality being due to the form of the interaction term. Furthermore, an interaction of the form $hc^\dagger_\sigma c_\sigma$ in the Hamiltonian would give rise to 2-leg vertices of the form

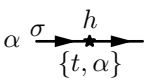

$$= -i\alpha h. \tag{9.19}$$

These do not appear directly in the diagrammatics but allow us to reformulate the above fermionic bubble as a 2-leg vertex with a $iUg^<_{\bar{\sigma}}(0)$ field

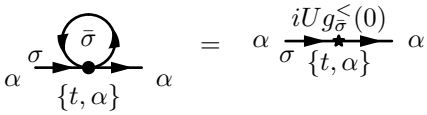

(9.20)

Now we are going to express both sides of this equality in the LO basis to understand what conditions $r_\sigma(0)$, $a_\sigma(0)$ and $k_\sigma(0)$ must fulfil.

First, the fermionic bubble (left side of Eq. (9.20)) is expressed in the LO basis as

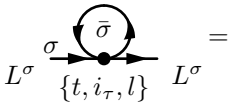

$$= \frac{U}{2}\delta_{L^\sigma 2}\left[r_{\bar{\sigma}}(0) + a_{\bar{\sigma}}(0)\right] + \frac{U}{2}\delta_{L^\sigma l}\left[\bar{\sigma} r_{\bar{\sigma}}(0) + \bar{\sigma} a_{\bar{\sigma}}(0) + k_{\bar{\sigma}}(0)\right]. \tag{9.21}$$

Then, we note that the sum over Keldysh indices of the 2-leg vertex in the $\{\pm\}$ basis, Eq. (9.19), reads $-ih(m_+ - m_-)$ in both $\mathcal{H}_\uparrow$ and $\mathcal{H}_\downarrow$ spaces. As $m_+ - m_-$ transforms into the 2×2 identity matrix in the LO basis, a 2-leg vertex is simply characterized by an interaction time t and an LO index l. A term $hc^\dagger_\sigma c_\sigma$ in the Hamiltonian would then give rise to the following vertex

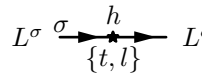

$$= -ih\delta_{L^\sigma l}. \tag{9.22}$$

The 2-leg vertex with a $iUg^<_{\bar{\sigma}}(0)$ field, right side of Eq. (9.20), is therefore expressed in the LO basis as

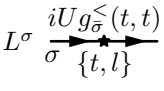

$$= Ug^<_{\bar{\sigma}}(0)\delta_{L^\sigma l}. \tag{9.23}$$

In order for Eq. (9.21) and Eq. (9.23) to be equal, the retarded, advanced and Keldysh Green's functions therefore have to satisfy

$$k_\sigma(0) = 2g^<_\sigma(0), \tag{9.24a}$$
$$r_\sigma(0) + a_\sigma(0) = 0. \tag{9.24b}$$

In the following, we work with a stronger requirement, setting

$$r_\sigma(0) = a_\sigma(0) = 0. \tag{9.25}$$

We see in Section 9.3 that this choice allows every vacuum diagram in the LO basis to vanish.

9.2.4 Density of $\uparrow$ spins at $t_{\max}$

In order to understand how to write the density of $\uparrow$ electrons in the LO basis, we use the following property of the Keldysh formalism: the average value of an operator does not depend on the branch of $\mathcal{C}$ where it is computed.

Considering d on the $+$ branch of the contour, the computation of the density can be understood as the action of the m_+ matrix in the $\{\pm\}$ basis, which transforms in the $\frac{1}{2}\tau_\uparrow$ matrix in the LO basis according to Eq. (9.9a). Hence we can represent the measurement vertex as a "special" interaction vertex at time $t_{\max}$ with $i_\tau = 1$, and no l:

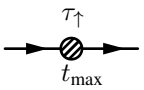

(9.26)

This representation will automatically form a fermion loop linked to the measurement, hence bringing a (-1) when the density is computed, which is consistent with Eq. (8.21). For example, the following diagram evaluates to

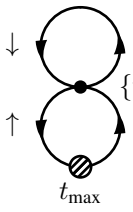

$$\{t, i_\tau, l\} = (-1)^2 \left(-\frac{iU}{4}\right) \int_0^{t_{\max}} \mathrm{d}t \sum_l \Big[i(\hat{\tilde{g}}_\uparrow)_{22}(t - t_{\max})\; i(\hat{\tilde{g}}_\uparrow)_{22}(t_{\max} - t)\; i(\hat{\tilde{g}}_\downarrow)_{ll}(0) + i(\hat{\tilde{g}}_\uparrow)_{l2}(t - t_{\max})\; i(\hat{\tilde{g}}_\uparrow)_{2l}(t_{\max} - t)\; i(\hat{\tilde{g}}_\downarrow)_{22}(0) \Big]. \tag{9.27}$$

One can easily check that this is consistent with Eq. (8.22).

The order-n contribution to the density can be written in terms of determinants as

$$d_n = \int \mathrm{d}t_1 \dots \mathrm{d}t_n \sum_{\substack{i_{\tau_1} \dots i_{\tau_n} \\ l_1 \dots l_n}} d_n\left(\{t_i, i_{\tau_i}, l_i\}_{1 \le i \le n}\right), \tag{9.28}$$

where

$$d_n\left(\{t_i, i_{\tau_i}, l_i\}_{1 \le i \le n}\right) = -\frac{i^{n+1} U^n}{2^{n+1}} \prod_\sigma \det \mathcal{D}^{\mathrm{LO}}_\sigma(\{t_i, i_{\tau_i}, l_i\}_{1 \le i \le n}). \tag{9.29}$$

These matrices are defined by taking into account the measurement time $t_{\max}$

$$\mathcal{D}^{\mathrm{LO}}_\uparrow(\{t_i, i_{\tau_i}, l_i\}_{1 \le i \le n}) = \begin{pmatrix} & & (\hat{\tilde{g}}_\uparrow)_{L_1^\uparrow 2}(t_1 - t_{\max}) \\ \left[(\hat{\tilde{g}}_\uparrow)_{L_i^\uparrow L_j^\uparrow}(t_i - t_j)\right]_{1 \le i,j \le n} & & \vdots \\ & & (\hat{\tilde{g}}_\uparrow)_{L_n^\uparrow 2}(t_n - t_{\max}) \\ (\hat{\tilde{g}}_\uparrow)_{2L_1^\uparrow}(t_{\max} - t_1) & \dots & (\hat{\tilde{g}}_\uparrow)_{2L_n^\uparrow}(t_{\max} - t_n) \quad (\hat{\tilde{g}}_\uparrow)_{22}(0) \end{pmatrix}, \tag{9.30}$$

and

$$\mathcal{D}^{\mathrm{LO}}_{\downarrow}(\{t_i, i_{\tau_i}, l_i\}_{1\leq i\leq n}) = \left[(\hat{\tilde{g}}_{\downarrow})_{L_i^{\downarrow}L_j^{\downarrow}}(t_i - t_j)\right]_{1\leq i,j\leq n}. \tag{9.31}$$

We emphasize here that, for a given set of interacting times $\{t_1, \ldots, t_n\}$, contributions to d summed over Keldysh indices are equal to the ones summed over LO indices

$$\sum_{\alpha_1\ldots\alpha_n} d_n\left(\{t_i, \alpha_i\}_{1\leq i\leq n}\right) = \sum_{\substack{i_{\tau_1}\ldots i_{\tau_n}\\ l_1\ldots l_n}} d_n\left(\{t_i, i_{\tau_i}, l_i\}_{1\leq i\leq n}\right). \tag{9.32}$$

This property will prove extremely useful in Section 9.5 to understand the performance of the Monte Carlo algorithms in the LO basis.

9.3 Direct cancellation of vacuum diagrams and steady-state limit

Now that we have established the diagrammatic rules in the LO formalism, we can show the following property: *every vacuum diagram vanishes*, without any summation required. As in the $\{\pm\}$ basis, this allows the computation of observables in the infinite-time steady-state limit, but this time without the 2^n exponential cost.

9.3.1 Direct cancellation of all vacuum diagrams

The order-n expansion of the partition function in the Coulomb repulsion U is obtained by transforming Eq. (8.23) in the LO basis:

$$Z_n = \int_0^{t_{\max}} \mathrm{d}t_1 \ldots \mathrm{d}t_n \sum_{\substack{i_{\tau_1}\ldots i_{\tau_n}\\ l_1\ldots l_n}} Z_n\left(\{t_i, i_{\tau_i}, l_i\}_{1\leq i\leq n}\right), \tag{9.33}$$

where

$$Z_n\left(\{t_i, i_{\tau_i}, l_i\}\right) = \left(\frac{iU}{2}\right)^n \prod_{\sigma} \det\left[(\hat{\tilde{g}}_{\sigma})_{L_i^{\sigma}L_j^{\sigma}}(t_i, t_j)\right]_{1\leq i,j\leq n}. \tag{9.34}$$

Let us consider an order $n \geq 1$ diagram contributing to Z in the LO basis. The interacting times are denoted $t_1, \ldots, t_n$. We assume that, for all $i < n$, $t_i < t_n$.[2] We label σ the spin on the identity side of the $(\mathbf{1}\otimes\tau_{\downarrow} + \tau_{\uparrow}\otimes\mathbf{1})/2$ interaction vertex at t_n, and l the corresponding LO index. For simplicity, we consider $\sigma = \uparrow$, but the derivation would remain similar for $\downarrow$ spin. The interaction vertex takes the form

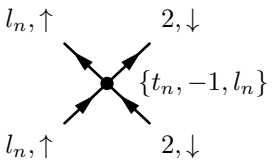

(9.35)

Let us follow the diagrammatic line of spin $\uparrow$. If t_n is surrounded by no other interaction vertex (it is a fermionic bubble), the diagram is then proportional to

$$(\hat{\tilde{g}}_{\uparrow})_{ll}(0) = \delta_{l0} r_{\uparrow}(0) + \delta_{l1} a_{\uparrow}(0) = 0. \tag{9.36}$$

In the case where t_n is surrounded by at least one other interaction vertex, we label its surrounding interaction times (that can be equal) t_i and t_j, $i, j \neq n$, with corresponding composite indices $L_i^{\uparrow}$, $L_j^{\uparrow}$. We then obtain

$$\begin{aligned}(\hat{\tilde{g}}_{\uparrow})_{L_j^{\uparrow}l}(t_j - t_n) = {} & \delta_{L_j^{\uparrow}2}\delta_{l1}\left[k_{\uparrow}(t_j - t_n) + a_{\uparrow}(t_j - t_n)\right] \\ & + \delta_{L_j^{\uparrow}1}\delta_{l1} a_{\uparrow}(t_j - t_n) + \delta_{L_j^{\uparrow}0}\delta_{l1} k_{\sigma}(t_j - t_n),\end{aligned} \tag{9.37}$$

2. We can rearrange indices if this is not the case.

and

$$\begin{aligned}(\hat{\tilde{g}}_\uparrow)_{lL_i^\uparrow}(t_n - t_i) = \delta_{L_i^\uparrow 2}\delta_{l0}\left[r_\uparrow(t_n - t_i) + k_\uparrow(t_n - t_i)\right] \\ + \delta_{L_i^\uparrow 1}\delta_{l0}k_\uparrow(t_n - t_i) + \delta_{L_i^\uparrow 0}\delta_{l0}r_\uparrow(t_n - t_i).\end{aligned} \tag{9.38}$$

The full diagram is then proportional to $\delta_{l0}\delta_{l1} = 0$. Hence every diagram contributing to Z in the LO basis is exactly equal to 0: This formalism *directly cancels vacuum diagrams*.

Finally, we note that this proof relies only on having the identity on one side of the interaction vertex, and not on the explicit contraction with $\tau_\uparrow, \tau_\downarrow$. Had we kept the diagrammatics with $\hat{g}^{\mathrm{LO}}$ lines instead of $\hat{\tilde{g}}$ ones, we would also have obtained the cancellation of vacuum diagrams.

In terms of determinants, these massive cancellations imply

$$\begin{aligned}\forall n > 0, \forall\{t_1, \dots, t_n\} \in [0, t_{\max}]^n, \forall\{i_{\tau_1}, \dots, i_{\tau_n}\} \in \{-1, 1\}^n, \\ \forall\{l_1, \dots, l_n\} \in \{0, 1\}^n, \prod_\sigma \det\left[(\hat{\tilde{g}}_\sigma)_{L_i^\sigma L_j^\sigma}(t_i, t_j)\right]_{1\le i,j\le n} = 0\end{aligned} \tag{9.39}$$

9.3.2 Direct access to the steady-state limit in the density computation

Just as in the $\{\pm\}$ basis, the cancellation of vacuum diagrams directly implies the clusterization of interaction time near $t_{\max}$ in the density computation, therefore allowing us to address any measurement time. The proof is very similar to the one given in Section 8.4.1, without the exponential sum over Keldysh indices.

Let n be a given perturbation order, and $t_1 < t_2 < \cdots < t_n$ n interacting times. Let us assume that the first j times are located far away from the measurement time $t_{\max}$, and that the last $n - j$ times are located in the vicinity of $t_{\max}$. We can formally consider

$$\forall 1 \le i \le j, |t_i - t_{\max}| \to \infty. \tag{9.40}$$

Because the Green's function is a local quantity in time, this means that for all $t \in \{t_1, \dots, t_j\}$, $t' \in \{t_{j+1}, \dots, t_n; t_{\max}\}$

$$||\hat{\tilde{g}}_\sigma(t, t')|| \to 0, \quad ||\hat{\tilde{g}}_\sigma(t', t)|| \to 0. \tag{9.41}$$

We therefore have

$$\prod_\sigma \det \mathcal{D}_\sigma^{\mathrm{LO}}(\{t_i, i_{\tau_i}, l_i\}_{1\le i\le n}) \simeq \prod_\sigma \det A_\sigma \prod_\sigma \det B_\sigma, \tag{9.42}$$

with

$$A_\sigma = \left[(\hat{\tilde{g}})_{L_i^\sigma L_{i'}^\sigma}(t_i - t_{i'})\right]_{1\le i,i'\le j}, \tag{9.43a}$$

$$B_\downarrow = \left[(\hat{\tilde{g}})_{L_i^\downarrow L_{i'}^\downarrow}(t_i - t_{i'})\right]_{j+1\le i,i'\le n}, \tag{9.43b}$$

$$B_\uparrow = \begin{pmatrix} & & (\hat{\tilde{g}}_\uparrow)_{L_{j+1}^\uparrow 2}(t_{j+1} - t_{\max}) \\ \left[(\hat{\tilde{g}}_\uparrow)_{L_i^\uparrow L_{i'}^\uparrow}(t_i - t_{i'})\right]_{j+1\le i,i'\le n} & & \vdots \\ & & (\hat{\tilde{g}}_\uparrow)_{L_n^\uparrow 2}(t_n - t_{\max}) \\ (\hat{\tilde{g}}_\uparrow)_{2L_{j+1}^\uparrow}(t_{\max} - t_{j+1}) & \dots & (\hat{\tilde{g}}_\uparrow)_{2L_n^\uparrow}(t_{\max} - t_n) \quad (\hat{\tilde{g}}_\uparrow)_{22}(0) \end{pmatrix}. \tag{9.43c}$$

However, $\prod_\sigma A_\sigma$ is a contribution to Z at order j, and it vanishes according to Eq. (9.39). Therefore $\prod_\sigma \det \mathcal{D}_\sigma^{\mathrm{LO}} \simeq 0$, and this proves the clusterization of times around $t_{\max}$ in the computation of the density.

Let us note that the cancellation of vacuum diagrams also implies that, out of the 4^n possible configurations for the density, *half of them vanish*.

We consider a given set $\{t_i, i_{\tau_i}, l_i\}_{1\le i\le n}$ of LO vertices at order n, and we assume that for all $i < n$, $t_i < t_n$. If $i_{\tau_n} = 1$, then the $\downarrow$ spin is carrying the identity side of the vertex. As we measure the density on the $\uparrow$ spin, the argument used in the cancellation vacuum diagrams applies again and $\mathcal{D}_\downarrow^{\mathrm{LO}}(\{t_i, i_{\tau_i}, l_i\}_{1\le i\le n})$ is the $n \times n$ null matrix. If $i_{\tau_n} = -1$, the contribution does not vanish. Hence, when computing the density, at every order n and for every set of n interaction times, $4^n/2$ LO configurations are exactly zero.

9.4 Diagrammatic quantum Monte Carlo algorithms

In this Section, we describe how to compute the density d introduced above using quantum Monte Carlo (MC) techniques. We present two different algorithms based on the LO formalism.

9.4.1 Sampling of the density

A configuration $\mathfrak{c}$ is determined by a given perturbation order n and a set of n interaction LO vertices: $\mathfrak{c} = \{n; y_1, \ldots, y_n\}$, where $y_i = \{t_i, i_{\tau_i}, l_i\}$.

In what we define as the *LO algorithm*, we simply sample the contributions to d_n, Eq. (9.29). Because the density is a real quantity, we consider

$$d(\mathfrak{c}) = -\frac{U^n}{2^{n+1}} \mathrm{Re}\left(i^{n+1} \prod_\sigma \det \mathcal{D}_\sigma^{\mathrm{LO}}(\mathfrak{c}) \right). \tag{9.44}$$

Defining the statistical weight of $\mathfrak{c}$ in the Monte Carlo to be $w_{\mathfrak{c}}^{\mathrm{LO}} = |d(\mathfrak{c})|$, then

$$d_n = \int_0^{t_{\max}} \mathrm{d}t_1 \ldots \mathrm{d}t_n \sum_{\substack{i_{\tau_1} \ldots i_{\tau_n} \\ l_1 \ldots l_n}} d(\mathfrak{c}) \propto \sum_{\mathfrak{c}}^{\text{MC LO}} \mathrm{sgn}\, d(\mathfrak{c}). \tag{9.45}$$

The second algorithm that we study is a *mixed algorithm* that samples the configurations according to their LO weight $w_{\mathfrak{c}}^{\mathrm{LO}}$ but computes d_n in the original $\{\pm\}$ basis, from the contributions [3]

$$d^{\pm}(\mathfrak{c}) = U^n s_{\mathfrak{c}}, \tag{9.46}$$

where $s_{\mathfrak{c}}$ is defined in Eq. (8.44). The idea is to use the LO weight to construct the Markov chain, but to measure the exact contribution to d as summed over the 2^n Keldysh indices. We therefore obtain

$$\begin{aligned} d_n &= \int_0^{t_{\max}} \mathrm{d}t_1 \ldots \mathrm{d}t_n d^{\pm}\left(\{t_i\}_{1 \le i \le n}\right) \\ &= \frac{1}{\mathcal{N}} \int_0^{t_{\max}} \mathrm{d}t_1 \ldots \mathrm{d}t_n \sum_{\substack{i_{\tau_1} \ldots i_{\tau_n} \\ l_1 \ldots l_n}} |w_{\mathfrak{c}}^{\mathrm{LO}}| \frac{d^{\pm}(\mathfrak{c})}{|w_{\mathfrak{c}}^{\mathrm{LO}}|} \propto \frac{1}{\mathcal{N}} \sum_{\mathfrak{c}}^{\text{MC LO}} \frac{d^{\pm}(\mathfrak{c})}{|w_{\mathfrak{c}}^{\mathrm{LO}}|}, \end{aligned} \tag{9.47}$$

where $\mathcal{N}$ is the number of non-zero LO configurations. When computing the density, $\mathcal{N} = 4^n/2$ at order n (see Section 9.3.2).

As detailed in Section 5.2, we use a standard Metropolis algorithm [107] to generate Markov chains distributed according to the weight $w_{\mathfrak{c}}^{\mathrm{LO}}$. In both algorithms, starting from an order-n configuration $\mathfrak{c}$, a new configuration $\mathfrak{c}'$ is proposed according to one of the following two Monte Carlo updates:

1. Add a new interaction LO vertex. The new interaction time is chosen according to a Cauchy law (as in the $\pm$ algorithm, see Section 8.4.2), and we randomly choose the i_τ and l indices. The Metropolis ratio is

$$\begin{aligned} \frac{T_{\mathfrak{c}'\mathfrak{c}} w_{\mathfrak{c}'}}{T_{\mathfrak{c}\mathfrak{c}'} w_{\mathfrak{c}}} &= \frac{1/(n+1)}{\rho(t)/4} \frac{U^{n+1}/2^{n+2} |\mathrm{Re}\left(i^{n+2} \prod_\sigma \det \mathcal{D}_\sigma^{\mathrm{LO}}(\mathfrak{c}')\right)|}{|\mathrm{Re}\left(i^{n+1} \prod_\sigma \det \mathcal{D}_\sigma^{\mathrm{LO}}(\mathfrak{c})\right)|} \\ &= \frac{2U}{(n+1)\rho(t)} \left| \frac{\mathrm{Re}\left(i^{n+2} \prod_\sigma \det \mathcal{D}_\sigma^{\mathrm{LO}}(\mathfrak{c}')\right)}{\mathrm{Re}\left(i^{n+1} \prod_\sigma \det \mathcal{D}_\sigma^{\mathrm{LO}}(\mathfrak{c})\right)} \right|. \end{aligned} \tag{9.48}$$

2. Remove a randomly chosen interaction LO vertex from $\mathfrak{c}$. The Metropolis ratio is

$$\frac{T_{\mathfrak{c}'\mathfrak{c}} w_{\mathfrak{c}'}}{T_{\mathfrak{c}\mathfrak{c}'} w_{\mathfrak{c}}} = \frac{n\rho(t)}{2U} \left| \frac{\mathrm{Re}\left(i^{n} \prod_\sigma \det \mathcal{D}_\sigma^{\mathrm{LO}}(\mathfrak{c}')\right)}{\mathrm{Re}\left(i^{n+1} \prod_\sigma \det \mathcal{D}_\sigma^{\mathrm{LO}}(\mathfrak{c})\right)} \right|. \tag{9.49}$$

3. Here the $\pm$ superscript only denotes the $\{\pm\}$ basis and not two different contributions.

9.4.2 Redefinition of noninteracting propagators and renormalization

As shown in Section 5.3.1, there is some freedom in the choice of the noninteracting propagator used to construct the perturbation expansion through the α-shift. [4] The redefinition of the interaction term is taken into account by subtracting α_σ on the diagonal of the determinants $\mathcal{D}^{\mathrm{LO}}_\sigma$. The shift in the chemical potential acts as a diagonal term in the self-energy and hence in

$$\left(\hat{g}^{\mathrm{LO}}_\sigma\right)^{-1} = \begin{pmatrix} r_\sigma^{-1} & -k_\sigma/|r_\sigma|^2 \\ 0 & a_\sigma^{-1} \end{pmatrix}. \tag{9.50}$$

α therefore modifies r_σ and a_σ into

$$\bar{r}_\sigma(\omega) = \left[r(\omega)^{-1} - U_\varphi \alpha_{\bar{\sigma}}\right]^{-1}, \tag{9.51}$$

$$\bar{a}_\sigma(\omega) = \left[a(\omega)^{-1} - U_\varphi \alpha_{\bar{\sigma}}\right]^{-1}. \tag{9.52}$$

As $k_\sigma/|r_\sigma|^2$ is not impacted by the shift, the modified Keldysh Green's function is then

$$\bar{k}_\sigma(\omega) = \left|\frac{\bar{r}_\sigma(\omega)}{r_\sigma(\omega)}\right|^2 k_\sigma(\omega). \tag{9.53}$$

Monte Carlo results also need to be normalized. We therefore restrict our calculation to two consecutive orders and follow the procedure described for the $\pm$ algorithm in Section 8.4.2.

9.5 Results

In this Section, we present actual computations of the density according to the $\pm$ algorithm of Chapter 8, the algorithms described in this Chapter, and we compare their efficiency. We consider an energy level ϵ_d coupled to a bath described by a semi-circular density of states of bandwidth $4D$. The Green's function describing this bath is defined on the complex plane as [53]

$$g_{\mathrm{bath}}(\zeta) = \frac{\zeta - \mathrm{sgn}(\mathrm{Im}\zeta)\sqrt{\zeta^2 - 4D^2}}{2D^2}. \tag{9.54}$$

The noninteracting retarded Green's function of the impurity level is

$$r_\sigma(\omega) = \frac{1}{\omega - \epsilon_d - \gamma^2 g_{\mathrm{bath}}(\omega)}, \tag{9.55}$$

where γ is a coupling term between the energy level and the bath. The Keldysh Green's function is then deduced from Eq. (9.6) using the fluctuation-dissipation theorem.

In the following, $D = 1$ is our energy unit. We consider $\beta = 100$, $\gamma^2 = 0.04$, $\epsilon_d = -0.36$. Electrons on the impurity experience a local Coulomb interaction $U = 1.2$. We choose a uniform α-shift: $\alpha = 0.3$, such that $U\alpha = -\epsilon_d$. The bath being particle-hole symmetric, this creates a shifted retarded Green's function $\bar{r}_\sigma(\omega)$ that is itself particle-hole symmetric (see Eq. (9.51)). However, we have checked that this particular choice of α does not influence our conclusions. The computational effort is 240 CPU*hours for every order.

We provide in Appendix C a table benchmarking the LO and mixed algorithms against the original $\pm$ algorithm as well as the CDet algorithm from Chapter 6. This shows in particular that the LO and mixed methods yield correct results and that we can indeed reach long times without an exponential sum of determinants.

9.5.1 Comparison with the original diagrammatic quantum Monte Carlo algorithm

Our main result is shown in Fig. 9.1 where we compare the relative error bar in the density computation as a function of the perturbation order. Blue dots denote the $\pm$ algorithm, orange stars the LO algorithm, and green dots the mixed algorithm. In all three cases, dotted lines are guides to the eye.

4. Note that in this context α *does not* denote a Keldysh index but a scalar, in order to be consistent with the existing literature.

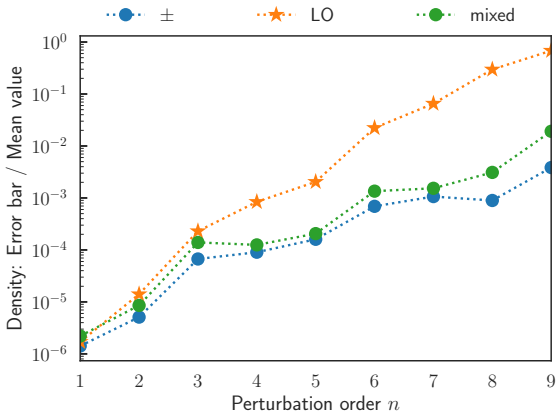

Figure 9.1 – Comparison of the error bar divided by the mean value in a density computation.

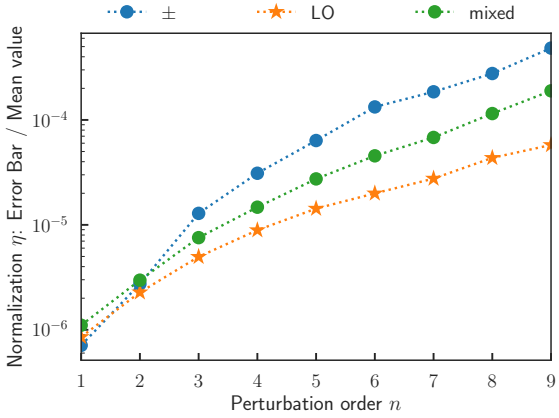

Figure 9.2 – Comparison of the error bar divided by the mean value of the normalization coefficient.

We see that all three relative error bars increase with perturbation order. This can either come from the increasing difficulty of computing the series coefficients, or an error propagation coming from the normalization factor η. We plot in Fig. 9.2 the relative error bar on η, which is much smaller than the final relative error on the density, showing that the latter mainly comes from the increasing difficulty to compute higher order coefficients. Moreover, the LO relative error bars very quickly become much larger than the $\pm$ ones, their difference nearly reaching two orders of magnitude at order 8. The mixed algorithm is found to perform better than the LO algorithm but its error bars slowly grow larger than the $\pm$ ones. This is surprising, as one could have expected to at least gain the decorrelation time over the algorithm of Ref. [128]. We discuss the origin of the error bars in both algorithms in the next Section.

9.5.2 The return of the sign problem

In this Section, we discuss the origin of the large variance in the computation of the density in the LO algorithm in terms of a sign problem in the Monte Carlo sampling and we show how this impacts the error bars of the mixed algorithm.

On the upper panel of Fig. 9.3, we plot as blue dots the non-zero LO contributions to the density sorted according to their absolute value. The left and right panel correspond to two different time configurations (*cf* caption). In both cases, the red line indicates the full sum over all LO indices, normalized to 1 (which coincides with the $\pm$ contribution). The lower panel shows the partial sum, from left to right, of the LO contributions plotted above. The last point, equal to 1 by construction, is emphasized as a red dot. As roughly half of them are positive and half negative, we see that the sum of the LO contributions over the indices for a fixed set of interacting times is characterized by massive cancellations. This is the origin of the large error bar in the Monte-Carlo, *i.e.* another manifestation of the sign problem. Furthermore, the partial

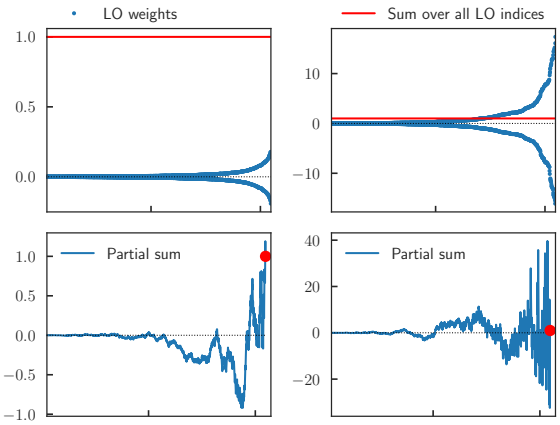

Figure 9.3 – *Upper panel*: Sorted array of the LO contributions according to their absolute value (blue dots) and their sum (red line), normalized to 1. *Lower panel*: Partial sum of the above LO contributions, from left to right, the red dot being the last point, by definition 1. Left panels correspond to the time configuration $T_1 = \{273.2, 277.8, 280.9, 331.7, 366.4, 390.5\}$, and the right panels to $T_2 = \{338.3, 343.2, 366.9, 369.7, 393.9, 394.5\}$. Order 7, $t_{\text{max}} = 400$.

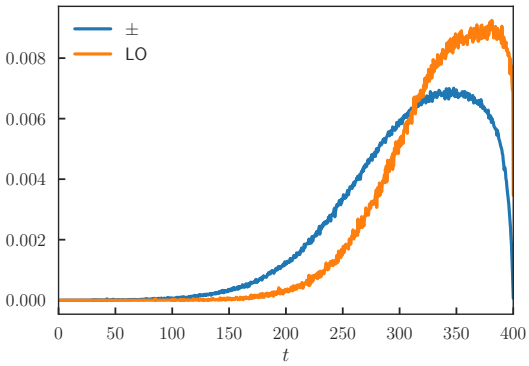

Figure 9.4 – Histograms of the times visited by the Monte Carlo algorithms, projected in one dimension. Order 9, $t_{\text{max}} = 400$.

sum shows that there is no clear feature or cutoff from which one could extract the value of the full sum.

Let us now turn to the mixed algorithm. On both the left and right panels of Fig. 9.3, the sum over all LO indices, which coincides with the $\pm$ contribution, is normalized to 1. However, on the left panel, the contributions of the different LO configurations are small compared to the final result, reaching at most 20% of it. On the right panel, those same contributions are much bigger, reaching up to 1700% of the full sum. Hence the Monte Carlo implemented in the LO basis does not sample the same time configurations as the algorithm in the $\{\pm\}$ basis. This is illustrated in Fig. 9.4 where the histograms of the times visited by the Monte Carlo, projected in one dimension, are plotted for both the $\pm$ algorithm (blue line) and LO one (orange line). First, we observe the clusterization of times proved at the beginning of this article: interaction times contributing to the density tend to be in the vicinity of t_{max}. Then, we see that some times located far away from the measurement but still contributing significantly to the $\pm$ algorithm are almost never visited in the LO algorithm. On the other hand, times close to t_{max} are more sampled in the latter. As times visited by the mixed algorithm coincide with the LO ones, this explains the difference in error bars between the mixed and $\pm$ algorithms observed in Fig. 9.1.

In the next Chapter, we explore in more detail the massive cancellations in the LO algorithm as a function of the LO indices. We show that it is possible to find patterns to regroup them, and therefore

reduce the overall error bar, but this is not enough to compete with the $\pm$ algorithm.

Chapter 10

Grouping determinants to reduce the sign problem

10.1 Motivation

We have seen in the previous Chapter that it is possible to write diagrammatic rules in the Larkin-Ovchinnikov (LO) basis that yield a direct cancellation of vacuum diagrams. As a consequence we can directly tackle the infinite-time steady-state limit when sampling contributions to a physical quantity such as the density.

In the original diagrammatic Quantum Monte Carlo presented in Section 8.4, these properties were also satisfied, but at the cost of an exponential sum over determinants when computing the MC weight: 2^n at a given perturbation order n. It led nonetheless to a drastic reduction of the sign problem compared to original real-time QMC algorithms. Our hope therefore was that the LO algorithm would similarly tame the sign problem and allow the computation of perturbative contributions with a much higher numerical accuracy. We showed in Section 9.5 that error bars are actually exponentially larger than the ones from the $\pm$ algorithm, due to massive cancellations over LO indices that are only performed stochastically.

A natural question arises from these results: Is there a way to sum a number of determinants smaller than 2^n at order n that would yield a smaller error bar than the $\pm$ algorithm? The general problem at hand is sketched in Fig. 10.1. We would like to understand whether there exists an optimal way to partition the determinants in groups of m members that are summed, with $1 < m < 2^n$, in order to minimize the sign problem. Does m have to be exponential in the perturbation order or can it scale polynomially?

In order to address these questions, we are going to explore ways of regrouping determinants in the LO basis that are independent of the interacting times considered. We first exhibit patterns found heuristically before presenting results of a machine learning approach based on Haar scattering. Note that Ref. [157] recently exposed the idea of sorting Feynman diagrams into groups that are likely to contain nearly equal or nearly cancelling contributions at equilibrium.

Throughout this Chapter, we use the same set of parameters as in Section 9.5. We compute contributions to the density of $\uparrow$ states on a single energy level ϵ_d coupled to a bath described by a semi-circular density of states of bandwidth $4D$, g_{bath}. The noninteracting retarded Green's function of the impurity level is

$$r_\sigma(\omega) = \frac{1}{\omega - \epsilon_d - \gamma^2 g_{\mathrm{bath}}(\omega)}, \tag{10.1}$$

where γ is a coupling term between the energy level and the bath.

In the following, $D = 1$ is our energy unit. We consider $\beta = 100$, $\gamma^2 = 0.04$, $\epsilon_d = -0.36$. Electrons on the impurity experience a local Coulomb interaction $U = 1.2$. We choose a uniform α-shift: $\alpha = 0.3$ (see Sec. 8.4.2), such that $U\alpha = -\epsilon_d$. The bath being particle-hole symmetric, this creates a shifted retarded Green's function $\bar{r}_\sigma(\omega)$ that is itself particle-hole symmetric, see Eq. (9.51). In practice, the noninteracting

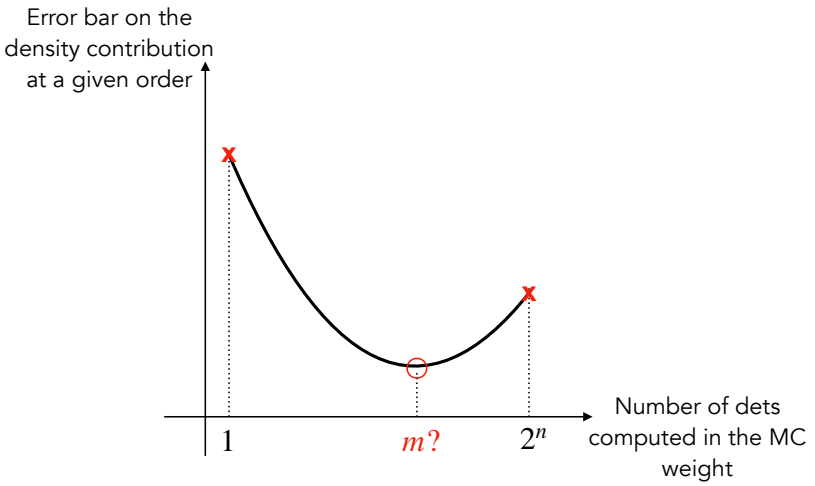

Figure 10.1 – Sketch of the algorithmic problem we are addressing in this Chapter.

Green's functions therefore have the following symmetry relations

$$\bar{k}_\sigma(-t) = -\bar{k}_\sigma(t), \tag{10.2a}$$
$$\bar{r}_\sigma(-t) = -\bar{a}_\sigma(t). \tag{10.2b}$$

We stress that patterns presented below weakly depend on the α-shift but are easier to identify in the particle-hole symmetric case. The computation effort is 240 CPU*hours for each perturbation order. In the following, we omit the $^-$ notation and the spin subscript to keep notations simple.

As a basis for upcoming comparisons, we also recall results obtained for the contributions to the density at a given perturbation order using the $\pm$ and LO algorithms, as presented in Appendix C.

	$\pm$	LO
Order 1	$-1.7013355 \pm 2.4 \times 10^{-6}$	$-1.7013405 \pm 2.9 \times 10^{-6}$
Order 2	$14.472669 \pm 7.4 \times 10^{-5}$	14.47295 ± 0.00020
Order 3	-33.3544 ± 0.0022	-33.3462 ± 0.0077
Order 4	-431.304 ± 0.039	-431.17 ± 0.36
Order 5	5094.46 ± 0.82	5097 ± 10
Order 6	-16166 ± 11	-16337 ± 364
Order 7	-164111 ± 175	-158102 ± 10331
Order 8	$2.2319 \times 10^6 \pm 2.0 \times 10^3$	$1.68 \times 10^6 \pm 5.0 \times 10^5$
Order 9	$-7.850 \times 10^6 \pm 3.0 \times 10^4$	EB $\simeq$ result

10.2 Human learning: Identifying cancellation patterns by hand

10.2.1 The $n = 2$ example

Let us first focus on second perturbation order. LO configurations take the form $\{(t_1, i_{\tau_1}, l_1), (t_2, i_{\tau_2}, l_2)\}$, with $0 \leq t_1 < t_2 \leq t_{\max}$, $(i_{\tau_1}, i_{\tau_2}) \in \{-1, 1\}^2$ and $(l_1, l_2) \in \{0, 1\}^2$. We proved in Section 9.3 that those bearing $i_{\tau_2} = 1$ are exactly equal to zero, so that we only deal with eight nonzero contributions. In this Section, we explicit them to show what cancellations can be obtained.

First, we compute the contribution from the first nonzero configuration

$$\begin{aligned}\prod_\sigma \det \mathcal{D}^{\mathrm{LO}}_\sigma (t_1, 1, 0; t_2, -1, 0) &= k(t_1 - t_2) r(t_2 - t_1) r(t_{\max} - t_2) \\ &\times \left[2g^<(0) k(t_2 - t_{\max}) - (r(t_2 - t_1) + k(t_2 - t_1))(a(t_1 - t_{\max}) + k(t_1 - t_{\max}))\right],\end{aligned} \tag{10.3}$$

and the second one

$$\begin{aligned}\prod_\sigma \det \mathcal{D}^{\mathrm{LO}}_\sigma\left(t_1,1,0;t_2,-1,1\right) &= k(t_1-t_2)r(t_2-t_1)r(t_{\max}-t_2)\\ &\times\left[2g^<(0)k(t_2-t_{\max})+(r(t_2-t_1)+k(t_2-t_1))(a(t_1-t_{\max})+k(t_1-t_{\max}))\right].\end{aligned} \tag{10.4}$$

When summing these two results together, many terms cancel out, and one simply obtains

$$4g^<(0)k(t_2-t_{\max})r(t_{\max}-t_2)k(t_1-t_2)r(t_2-t_1). \tag{10.5}$$

Summing together the two following configurations yields the same result

$$\begin{aligned}&\prod_\sigma \det \mathcal{D}^{\mathrm{LO}}_\sigma\left(t_1,1,1;t_2,-1,0\right)+\prod_\sigma \det \mathcal{D}^{\mathrm{LO}}_\sigma\left(t_1,1,1;t_2,-1,1\right)\\ &\quad=4g^<(0)k(t_2-t_{\max})r(t_{\max}-t_2)k(t_1-t_2)r(t_2-t_1).\end{aligned} \tag{10.6}$$

Even more interesting, the following configurations exactly cancel when grouped together:

$$\prod_\sigma \det \mathcal{D}^{\mathrm{LO}}_\sigma\left(t_1,-1,0;t_2,-1,0\right) = -\prod_\sigma \det \mathcal{D}^{\mathrm{LO}}_\sigma\left(t_1,-1,1;t_2,-1,1\right), \tag{10.7a}$$

$$\prod_\sigma \det \mathcal{D}^{\mathrm{LO}}_\sigma\left(t_1,-1,0;t_2,-1,1\right) = -\prod_\sigma \det \mathcal{D}^{\mathrm{LO}}_\sigma\left(t_1,-1,1;t_2,-1,0\right). \tag{10.7b}$$

One sees from this simple example that it is possible to completely cure the sign problem originating from the LO configurations by grouping two determinants in the Monte Carlo weight. Do some of these cancellations survive for orders larger than 2?

10.2.2 Exact cancellations at half-filling

For the specific case of α that make the non-interacting Green's function particle-hole symmetric, we heuristically find that 2^n contributions exactly cancel each other at perturbation order n. Let us consider n interacting times $t_1 < \cdots < t_n$.

If $n = 2k$ is even, cancelling contributions correspond to those with all i_τ equal to -1. More specifically, defining

$$\mathfrak{c} = \{(t_1,-1,l_1),\ldots,(t_{2k},-1,l_{2k})\}, \tag{10.8a}$$

$$\mathfrak{c}' = \{(t_1,-1,\bar{l}_1),\ldots,(t_{2k},-1,\bar{l}_{2k})\}, \tag{10.8b}$$

we obtain

$$\prod_\sigma \det \mathcal{D}^{\mathrm{LO}}_\sigma\left(\mathfrak{c}\right) = -\prod_\sigma \det \mathcal{D}^{\mathrm{LO}}_\sigma\left(\mathfrak{c}'\right), \tag{10.9}$$

and therefore $d(\mathfrak{c}) + d(\mathfrak{c}') = 0$. Note that this is consistent with Eq. (10.7). If $n = 2k+1$, cancelling contributions correspond to those with all i_τ equal to 1 except the last one associated to the greatest interaction time. In this case, the grouping pattern is

$$\mathfrak{c} = \{(t_1,1,l_1),\ldots,(t_{2k},1,l_{2k}),(t_{2k+1},-1,l_{2k+1})\}, \tag{10.10a}$$

$$\mathfrak{c}' = \{(t_1,1,\bar{l}_1),\ldots,(t_{2k},1,\bar{l}_{2k}),(t_{2k+1},-1,l_{2k+1})\}. \tag{10.10b}$$

We implement these groupings in the computation of the Monte Carlo weight of the LO algorithm, resulting in the order-by-order error bars presented in the table below.

	LO - 2^n exact cancellations at half-filling
Order 1	$-1.7013426 \pm 2.8 \times 10^{-6}$
Order 2	$14.472816 \pm 8.2 \times 10^{-5}$
Order 3	-33.3522 ± 0.0060
Order 4	-431.43 ± 0.24
Order 5	5096.6 ± 8.0
Order 6	-15995 ± 289
Order 7	-156490 ± 8203
Order 8	$2.47 \times 10^6 \pm 3.1 \times 10^5$
Order 9	EB $\simeq$ result

The LO results of Section 10.1 are indeed improved, but we need to find more groupings to fight the exponential scaling of the sign problem.

10.2.3 Cluster patterns

First, we numerically check that on average half of the contributions from the nonzero LO configurations are positive, while the other half are negative. This motivates the idea of summing terms in groups scaling as powers of 2.

Then, we find that families of correlated configurations are mainly defined by the $\{i_{\tau_1}, \dots, i_{\tau_n}\}$ sequence (and not the l coefficients). More specifically, let us define a *cluster* as a set of following i_τs with the same value. For example, in the following order-7 configuration [1]

$$\mathfrak{c} = \{(1,0),(-1,0),(-1,1),(-1,1),(1,1),(1,0),(-1,1)\}, \tag{10.11}$$

we have $i_{\tau_2} = i_{\tau_3} = i_{\tau_4} = -1$, so that they form a cluster of size 3. We observe that the new configuration $\mathfrak{c}'$ obtained by switching the last l of the largest cluster massively cancel the contribution of $\mathfrak{c}$. In this example, it would be defined as

$$\mathfrak{c}' = \{(1,0),(-1,0),(-1,1),(-1,0),(1,1),(1,0),(-1,1)\}. \tag{10.12}$$

When there are several clusters of the same size, the best cancellation is formed when flipping the last l of the rightmost one. For example, the following two configurations should be grouped together

$$\mathfrak{c} = \{(-1,0),(1,0),(-1,1),(-1,1),(1,1),(1,0),(-1,1)\}, \tag{10.13a}$$
$$\mathfrak{c}' = \{(-1,0),(1,0),(-1,1),(-1,1),(1,1),(1,1),(-1,1)\}. \tag{10.13b}$$

We also observe that flipping the very last l, l_n, often yields good cancellations.

We therefore design two Monte Carlo algorithms based on theses ideas:

— The *cluster* LO algorithm. To each configuration $\mathfrak{c}$ proposed by the Monte Carlo, we associate another configuration $\mathfrak{c}'$ in which we flip the last l of the rightmost largest cluster of i_τs. The contribution to the density is the sum of the contributions of $\mathfrak{c}$ and $\mathfrak{c}'$. The order-by-order error bars are presented in the left column of the table below.

— The *cluster and last* LO algorithm. To each configuration $\mathfrak{c}$ proposed by the Monte Carlo, we associate $\mathfrak{c}'$ as in the cluster LO algorithm. If the flipped l was not the last one, we form a group of size 4 associating the other two configurations in which we flip l_n. The order-by-order error bars are presented in the right column of the table below.

	LO - Cluster groupings	LO - Cluster and last groupings
Order 1	$-1.7013394 \pm 3.3 \times 10^{-6}$	$-1.7013394 \pm 3.2 \times 10^{-6}$
Order 2	$14.472762 \pm 7.7 \times 10^{-5}$	$14.472731 \pm 7.3 \times 10^{-5}$
Order 3	-33.3510 ± 0.0033	-33.3476 ± 0.0033
Order 4	-431.146 ± 0.072	-431.322 ± 0.079
Order 5	5095.0 ± 2.4	5096.9 ± 1.9
Order 6	-16256 ± 78	-16170 ± 61
Order 7	-164974 ± 2198	-165426 ± 1588
Order 8	$2.175 \times 10^6 \pm 6.4 \times 10^4$	$2.277 \times 10^6 \pm 5.6 \times 10^4$
Order 9	$-9.5 \times 10^6 \pm 2.1 \times 10^6$	$-8.6 \times 10^6 \pm 1.3 \times 10^6$

Both algorithms give very encouraging results, allowing to reduce the error bar by a factor 10 for the highest perturbation orders compared to the LO results of Section 10.1. But another factor 10 would be needed to challenge the $\pm$ algorithm. Because the number of LO configurations grows exponentially with the perturbation order n, finding groupings by hand proves very difficult for large n. It would therefore be desirable to develop a more systematic search using machine learning techniques, which is the subject of the next Section.

1. In this Section, we drop the interacting times when writing configurations to keep notations short.

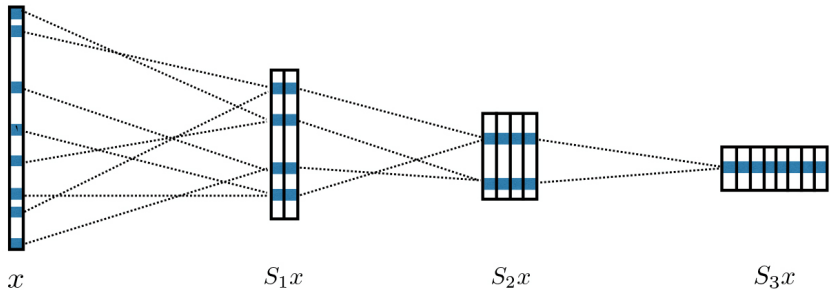

Figure 10.2 – Example of a Haar scattering network. Each layer is obtained by adding or subtracting a pair of coefficients from the previous layer. Note that x is labeled d_T in the text. [34]

10.3 Machine learning: Deep Haar scattering on graphs

Designing an efficient machine learning algorithm to optimize the sign problem by grouping configurations requires to find a proper representation of data and of the optimization function. The work presented in this Section has been driven by discussions with Stéphane Mallat from École Normale Supérieure.

At a given order n, the 4^n LO configurations can be thought of as vertices of a graph, where the edges between vertices define a group that should be summed together when computing the Monte Carlo weight. In this representation, finding groups therefore means learning the *connectivity* of the graph, that is which vertices should be connected together.

Such a problem has been addressed in Ref. [34] using deep Haar scattering. In the following, we reproduce the arguments presented in this article, adapting formulas and procedures to our optimization problem. We then present results for the density computation.

10.3.1 Haar scattering on a graph

Let us consider a given perturbation order n and set of interacting times $T = \{t_1 < \cdots < t_n\}$. A set of LO configurations $\{i_{\tau_i}, l_i\}_{1\leq i\leq n}$ is labelled by a single integer L between 0 and $4^n - 1$. For instance, one can make the following choice at order 1

$$\{-1, 0\} \to 0, \quad \{-1, 1\} \to 1, \quad \{1, 0\} \to 2, \quad \{1, 1\} \to 3. \tag{10.14}$$

The contribution to the density is labelled $d_T(L)$ and writes, see Eq. (9.44),

$$d_T(L) = -\frac{U^n}{2^{n+1}} \mathrm{Re}\left[i^{n+1} \prod_\sigma \det \mathcal{D}^{\mathrm{LO}}_\sigma(T, L) \right]. \tag{10.15}$$

T being fixed, the different $d_T(L)$ define an unweighted graph G whose vertices correspond to the 4^n different values of L.

A Haar scattering is calculated by iteratively applying the following permutation invariant operator to two numbers a and b

$$(a, b) \longrightarrow (a + b, |a - b|). \tag{10.16}$$

This transformation can be applied along a deep network, as depicted in Fig. 10.2. At layer j, the network coefficients are stored in a $(2^{-j}4^n) \times 2^j$ matrix $S_j d_T$, where rows denote a node index and columns a feature type. The input network layer is thus

$$S_0 d_T = \begin{pmatrix} d_T(0) \\ \cdots \\ d_T(4^n - 1) \end{pmatrix}. \tag{10.17}$$

The network layer $j + 1$, $S_{j+1}d_T$, is then computed regroupings the $2^{-j}4^n$ nodes from $S_j d_T$ in $2^{-j-1}4^n$ pairs (a_l, b_l) and applying Eq. (10.16) to each pair $(S_j d_T(a_l, q), S_j d_T(b_l, q))$:

$$S_{j+1}d_T(l, 2q) = S_j d_T(a_l, q) + S_j d_T(b_l, q), \tag{10.18a}$$

$$S_{j+1}d_T(l, 2q + 1) = |S_j d_T(a_l, q) - S_j d_T(b_l, q)|. \tag{10.18b}$$

This transform is iterated up to a maximum depth $J \leq \log_2(4^n)$.

In order to illustrate this construction, we consider the case $n = 1$. The input layer writes

$$S_0 d_T = \begin{pmatrix} d_T(0) \\ d_T(1) \\ d_T(2) \\ d_T(3) \end{pmatrix}. \tag{10.19}$$

We can then choose to pair $d_T(0)$ with $d_T(1)$, and $d_T(2)$ with $d_T(3)$. The following layer in the Haar scattering network would therefore write

$$S_1 d_T = \begin{pmatrix} d_T(0) + d_T(1) & |d_T(0) - d_T(1)| \\ d_T(2) + d_T(3) & |d_T(2) - d_T(3)| \end{pmatrix}. \tag{10.20}$$

Had we choosen to pair $d_T(0)$ with $d_T(2)$, and $d_T(1)$ with $d_T(3)$, the following layer would have been

$$S_1 d_T = \begin{pmatrix} d_T(0) + d_T(2) & |d_T(0) - d_T(2)| \\ d_T(1) + d_T(3) & |d_T(1) - d_T(3)| \end{pmatrix}. \tag{10.21}$$

The task of the machine learning algorithm will be to discriminate between the different possible groupings in order to minimize a cost function we describe next.

10.3.2 Optimization function

We would like to design an algorithm to learn the connectivity of the graph G from a training set of unlabelled examples $\{d_{T_i}\}_i$. The goal of the method is to identify LO configurations that cancel each other, see for instance Section 10.2.3. If the connectivity is known up to scale 2^j, the next scale is therefore obtained by finding optimal pairings $\{a_l, b_l\}$ which minimize the sum of scattering vectors, averaged over the training set $\{d_{T_i}\}_i$:

$$\sum_{l=0}^{2^{-j-1}4^n} \sum_{q=0}^{2^j-1} \sum_i |S_j d_{T_i}(a_l, q) + S_j d_{T_i}(b_l, q)| \,. \tag{10.22}$$

Note the difference with Eq. (6). of Ref. [34], where a difference is used instead of a sum because the authors are interested in scattering vectors that are similar. This is a weighted matching problem which can be solved by the Blossom Algorithm of Edmonds [34, 47, 52].

10.3.3 Results

We use the MATLAB software of Ref. [34], publicly available at *www.di.ens.fr/data/scattering/haar*. As mentioned in the previous Section, a minor modification has to be made in the $haar\_tree\_learn.m$ file to minimize the sum of scattering vectors and not their difference.

We train the algorithm using 2000 examples and look for pairings of size 2 and 4, which respectively correspond to depths $J = 1$ and $J = 2$ of the Haar scattering network. The error bars of the two Monte Carlo implementing the obtained pairings are presented below. As the sign problem is completely cured using groupings of size 2 at order 2 (see Section 10.2.1), we only look for groupings of size 4 starting at $n = 3$.[2]

	LO - Haar size 2	LO - Haar size 4
Order 1	$-1.7013383 \pm 3.3 \times 10^{-6}$	
Order 2	$14.472734 \pm 7.0 \times 10^{-5}$	
Order 3	-33.3560 ± 0.0028	-33.3589 ± 0.0026
Order 4	-431.324 ± 0.061	-431.314 ± 0.057
Order 5	5091.6 ± 3.2	5095.1 ± 1.4
Order 6	-16162 ± 60	-16183 ± 40
Order 7	-167344 ± 1718	-163794 ± 1003

2. We computed contributions to the density up to order 7 due to some MATLAB limitations.

The use of this Haar scattering algorithm yields a small improvement over what we found by hand, but not by a big factor. This means there is no obvious cancellation pattern that we have missed using 'human learning'.

10.4 Conclusion

Finding groupings to reduce the fermionic sign problem in real-time diagrammatic Monte Carlo methods is a very challenging algorithmic problem. It either requires a good physical intuition to find patterns among 4^n contributions, or sophisticated machine learning techniques.

All in all, the error bars managed to be greatly reduced, and one might gain even more by increasing the groupings size. Results from Sections 10.2.3 and 10.3.3 however seem to indicate that the exponential scaling of the sign problem is faster.

Another idea would be to look at the problem from a slightly different angle. Up to now, we focused on the fact that contributions should cancel each other. The algorithms were actually quite successful in this respect. As contributions from many groups became very small, acceptance rates dropped below 5% and correlation times drastically increased at high perturbation orders. The efficiency of the Monte Carlo was therefore greatly reduced.

But the final result, obtained when summing over *all* LO configurations, is a nonzero contribution to the density. What we are interested in is thus a way to group configurations that cancel each other with other ones that actually contribute to the final result. This optimization problem is more subtle than the one we looked at and it is unclear how one could best address it.

Part V

Current-driven transition in Ca_2RuO_4 using steady-state NCA

Chapter 11

Non-Crossing Approximation

In upcoming Chapter 13, we will model the insulator-to-metal transition driven by an electric-field in Ca_2RuO_4 [115, 142, 122], which is one of the numerous examples of recent experimental progress in driving strongly correlated systems out of equilibrium. In such materials, the multiorbital nature and/or the need to reach the steady-state limit prevent us from using the numerically exact methods presented in Chapter 8. It is therefore desirable to use a more economical way to solve the quantum impurity model that still captures the essential physics of the system. Systematic approximations in the hybridization expansion are popular as they give reasonably accurate results while keeping the computational cost at minimum [81, 59, 90, 131, 16, 17, 69].

A simple strong-coupling expansion is called the Non-Crossing Approximation (NCA), as it analytically sums a subset of diagrams without crossing hybridization lines. In this Chapter, we first present the imaginary-time formulation of NCA. This allows us to introduce the formalism and notations, as equations easily generalize to the real-time Baym-Kadanoff contour that we present next. A novel algorithm working directly in the steady-state limit of the equations is then derived in the next Chapter.

In the literature, the most common derivation of NCA equations uses a pseudo-particle representation of the Green's function [38, 16, 46]. We choose here to work with the local states propagator R, following Refs. [10, 141, 125].

11.1 Equilibrium NCA

11.1.1 Local states propagator

We consider a correlated impurity coupled to an uncorrelated bath. Its Hamiltonian writes

$$\mathcal{H} = \mathcal{H}_{\text{loc}} + \mathcal{H}_{\text{hyb}} + \mathcal{H}_{\text{bath}}, \tag{11.1}$$

where $\mathcal{H}_{\text{loc}}$ describes the local physics of the impurity, $\mathcal{H}_{\text{bath}}$ the noninteracting bath, and $\mathcal{H}_{\text{hyb}}$ is a hybridization term between the impurity and the bath. The partition function of the bath is $Z_{\text{bath}} = \text{Tr}\left(e^{-\beta\mathcal{H}_{\text{bath}}}\right)$. The impurity state propagator R is defined as

$$R(\tau) = -\frac{1}{Z_{\text{bath}}}\text{Tr}_{\text{bath}} e^{-\beta\mathcal{H}_{\text{bath}}} e^{-\tau(\mathcal{H}_{\text{loc}}+\mathcal{H}_{\text{hyb}})}. \tag{11.2}$$

It can be interpreted as a projected evolution operator of the atomic states after averaging over the bath states at equilibrium. As in Section 5.1, the quantum impurity can be described using an imaginary-time path integral

$$\begin{aligned}\mathcal{S} = \sum_a \int_0^\beta \mathrm{d}\tau d_a^\dagger(\tau)\partial_\tau d_a(\tau) + \int_0^\beta \mathrm{d}\tau \mathcal{H}_{\text{loc}}\left(d_a^\dagger(\tau), d_a(\tau)\right) \\ + \int_0^\beta \mathrm{d}\tau\mathrm{d}\tau' \sum_{ab} d_a^\dagger(\tau)\Delta_{ab}(\tau-\tau')d_b(\tau'),\end{aligned} \tag{11.3}$$

where Δ is the hybridization function, and $d_a^\dagger$ (resp. d_a) the creation (resp. annihilation) operator on the impurity. a is a composite index for the different degrees of freedom (spin, orbital, ...).

In Chapter 5, we introduced the CT-HYB quantum Monte Carlo algorithm, showing that one can expand and stochastically sample the partition function Z as a series in Δ. In this Section, we are interested in the expansion of the impurity states propagator R. We derive in Appendix D a path-integral representation of its matrix elements which motivates an operator representation as a time-ordered exponential

$$R(\tau) = -T_\tau \exp\left(-\tau\mathcal{H}_{\text{loc}} - \int_0^\tau \mathrm{d}\tau'\mathrm{d}\bar{\tau} \sum_{ab} \Delta_{ab}(\tau'-\bar{\tau}) d_a^\dagger(\tau') d_b(\bar{\tau})\right). \tag{11.4}$$

Note that R is an operator that acts in the Hilbert space and therefore has a $2^N \times 2^N$ matrix representation, where N is the number of states in the system. When setting the hybridization function to zero, we recover the usual local states propagator of an isolated system

$$R_0(\tau) = -e^{-\tau\mathcal{H}_{\text{loc}}}, \tag{11.5}$$

and the partition function is obtained as

$$Z = -\mathrm{Tr} R(\beta). \tag{11.6}$$

Eq. (11.4) yields the following expansion in powers of the hybridization function

$$\begin{aligned} R(\tau) = -\sum_n \frac{(-1)^n}{n!} \int_0^\tau \mathrm{d}\tau_1'\mathrm{d}\bar{\tau}_1 \ldots \mathrm{d}\tau_n'\mathrm{d}\bar{\tau}_n \sum_{\substack{a_1\ldots a_n \\ b_1\ldots b_n}} \left(\prod_{i=1}^n \Delta_{a_i b_i}(\tau_i'-\bar{\tau}_i)\right) \\ \times T_\tau\left(e^{-\tau\mathcal{H}_{\text{loc}}} d_{a_1}^\dagger(\tau_1') d_{b_1}(\bar{\tau}_1) \ldots d_{a_n}^\dagger(\tau_n') d_{b_n}(\bar{\tau}_n)\right). \end{aligned} \tag{11.7}$$

Every term in this expression can be pictorially represented using diagrams in Δ. A straight line denotes a bare propagator

$$0 \longrightarrow \tau \quad = R_0(\tau), \tag{11.8}$$

and a double straight line a full propagator

$$0 \Longrightarrow \tau \quad = R(\tau). \tag{11.9}$$

The hybridization being a retarded function, it is drawn as an oriented dashed line between an annihilation operator d_b and a creation operator $d_a^\dagger$.

$$\bar{\tau}, b \quad \tau', a \quad = \Delta_{ab}(\tau'-\bar{\tau}) d_a^\dagger R_0(\tau'-\bar{\tau}) d_b. \tag{11.10}$$

Each diagram has to be multiplied by $(-1)^{s+f}$, where s is the number of crossings of hybridization lines, and f the number of hybridization lines that go opposite to the overall direction.

For example, the following diagram is an order-2 contribution to R

$$\begin{aligned} 0 \quad \tau \quad = \int_0^\tau \mathrm{d}\tau_1'\mathrm{d}\tau_2'\mathrm{d}\bar{\tau}_1\mathrm{d}\bar{\tau}_2 \sum_{\substack{a_1 a_2 \\ b_1 b_2}} \Delta_{a_1 b_1}(\tau_1'-\bar{\tau}_1)\Delta_{a_2 b_2}(\tau_2'-\bar{\tau}_2) R_0(\tau-\tau_2') \\ \times d_{b_2} R_0(\tau_2'-\bar{\tau}_1) d_{a_1}^\dagger R_0(\bar{\tau}_1-\bar{\tau}_2) d_{a_2}^\dagger R_0(\bar{\tau}_2-\tau_1') d_{b_1} R_0(\tau_1'). \end{aligned} \tag{11.11}$$

From these diagrammatic rules, one sees that the impurity states propagator satisfies a Dyson equation

$$R(\tau) = R_0(\tau) + \int_0^\tau \mathrm{d}\tau'\mathrm{d}\bar{\tau} R_0(\tau-\tau') S(\tau-\bar{\tau}) R(\bar{\tau}), \tag{11.12}$$

$$\Longrightarrow \quad = \quad \longrightarrow \quad + \quad \longrightarrow \!\!\!\!\bullet\!\!\!\!\longrightarrow$$

where the self-energy S associated to R is the sum of all one-particle irreducible diagrams, that is diagrams that cannot be separated into two parts by cutting a single R_0 line. This equation can be rewritten as a first kind integro-differential Volterra equation

$$-\partial_\tau R(\tau) = \mathcal{H}_{\text{loc}} R(\tau) + \int_0^\tau \mathrm{d}\tau' S(\tau - \tau') R(\tau'), \tag{11.13}$$

with initial condition $R(0) = -\mathbf{1}$ where $\mathbf{1}$ is the identity matrix.

11.1.2 Non-Crossing Approximation

The Non-Crossing Approximation (NCA) consists of summing the subset of diagrams without crossing hybridization lines in the strong-coupling expansion of R. For example, the contribution from Eq. (11.11) is not considered. The self-energy S takes the analytical form

$$S(\tau) = -\sum_{ab} \left[d_a^\dagger R(\tau) d_b \Delta_{ab}(\tau) - d_a R(\tau) d_b^\dagger \Delta_{ba}(-\tau) \right] \tag{11.14}$$

$=$  $+$

This approach has the advantage to resum diagrams up to infinite order while keeping a very simple equation for the self-energy. It was shown to perform well in the strong-coupling regime, especially the Mott insulating phase, although it fails to correctly reproduce the Fermi liquid behavior [16, 113].

NCA is also a conserving approximation that can be shown to derive from the Luttinger-Ward functional [16, 69, 141]

$$\Phi[R, \Delta] = -\sum_{ab} \int_0^\beta \mathrm{d}\tau \mathrm{Tr} \left[R(\beta - \tau) d_a R(\tau) d_b^\dagger \right] \Delta_{ba}(\beta - \tau) \tag{11.15}$$

$=$ 

The matrix elements of the self-energy from Eq. (11.14) are indeed obtained through

$$S_{nm}(\tau) = \frac{\delta \Phi[R, \Delta]}{\delta R_{mn}(\beta - \tau)}. \tag{11.16}$$

The NCA impurity Green's function then simply writes

$$G_{ab}(\tau) = \frac{1}{Z} \frac{\delta \Phi[R, \Delta]}{\delta \Delta_{ba}(\beta - \tau)} = -\frac{1}{Z} \mathrm{Tr} \left[R(\beta - \tau) d_a R(\tau) d_b^\dagger \right]. \tag{11.17}$$

11.1.3 Implementation

In order to reduce the size of the matrices we manipulate, we use the symmetries of $\mathcal{H}_{\text{loc}}$ and Δ to block-diagonalize R and S. The Volterra equation (11.13) is diagonal in the block indices, while the NCA equation (11.14) for the self-energy couples blocks together due to the creation and annihilation operators. Denoting Γ a block index, the coupled set of equations to solve now writes

$$-\partial_\tau R^\Gamma(\tau) = \mathcal{H}^\Gamma_{\text{loc}} R^\Gamma(\tau) + \int_0^\tau \mathrm{d}\tau' \; S^\Gamma(\tau - \tau') R^\Gamma(\tau'), \qquad R(0) = -\mathbf{1}, \tag{11.18a}$$

$$S^\Gamma(\tau) = -\sum_{ab} \sum_{\Gamma'} \left[(d_a^\dagger)^{\Gamma\Gamma'} R^{\Gamma'}(\tau) (d_b)^{\Gamma'\Gamma} \Delta_{ab}(\tau) - (d_a)^{\Gamma\Gamma'} R^{\Gamma'}(\tau) (d_b^\dagger)^{\Gamma'\Gamma} \Delta_{ba}(-\tau) \right]. \tag{11.18b}$$

Starting from a guess for $R(\tau)$, these two equations are solved iteratively until convergence. We use the *atom diag* class of the TRIQS library for the block diagonalization as well as the operations on operators of

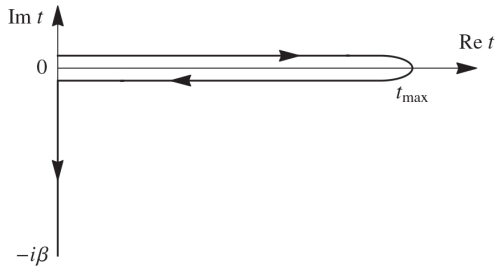

Figure 11.1 – Baym-Kadanoff contour used for out-of-equilibrium NCA. [10]

Eq. (11.18b) [123]. Eq. (11.18a) is solved using a time discretization we now describe.

Let us consider a given block index Γ, and a uniform discretization of the time interval $[0, \tau]$: $\tau_0 < \cdots < \tau_N$, where $\tau_0 = 0$ and $\tau_N = \tau = \tau_0 + N\Delta\tau$. The initial conditions write $R^\Gamma(\tau_0) = -\mathbf{1}$ and $\partial_\tau R^\Gamma(\tau_0) = \mathcal{H}^\Gamma_{\text{loc}}$. Let us now suppose that we know $R^\Gamma(\tau_i)$ and $\partial_\tau R^\Gamma(\tau_i)$ for all $0 \leq i \leq n-1$ and we want to compute $R^\Gamma(\tau_n)$ and $\partial_\tau R^\Gamma(\tau_n)$, where $1 \leq n \leq N$. For convenience, we use the notation $R_i = R^\Gamma(\tau_i)$, $\dot{R}_i = \partial_\tau R^\Gamma(\tau_i)$ and $\mathcal{H} = \mathcal{H}^\Gamma_{\text{loc}}$.

We write

$$R_n = R_{n-1} + \frac{\Delta\tau}{2}\left(\dot{R}_n + \dot{R}_{n-1}\right), \tag{11.19}$$

and use a trapezoidal approximation of the integro-differential equation (11.18a)

$$-\dot{R}_n = \mathcal{H}_{\text{loc}} R_n + \sum_{i=1}^{n-1} \Delta\tau S_{n-i} R_i + \frac{\Delta\tau}{2} S_n R_0 + \frac{\Delta\tau}{2} S_0 R_n. \tag{11.20}$$

We use this equation to replace $\dot{R}_n$ in Eq. (11.19)

$$\begin{aligned} R_n = &\left[\mathbf{1} + \frac{\Delta\tau}{2}\mathcal{H} + \left(\frac{\Delta\tau}{2}\right)^2 S_0\right]^{-1} \\ &\times \left[R_{n-1} + \frac{\Delta\tau}{2}\left(\dot{R}_{n-1} - \frac{\Delta\tau}{2} S_n R_0 - \Delta\tau \sum_{i=1}^{n-1} S_{n-i} R_i\right)\right], \end{aligned} \tag{11.21}$$

and $\dot{R}_n$ is obtained through Eq. (11.20). We reproduce this step until $n = N$.

11.2 Out-of-equilibrium NCA

11.2.1 Formalism

The out-of-equilibrium version of the Non-Crossing Approximation is formulated on an extension of the Keldysh contour presented in Chapter 8, called the Baym-Kadanoff contour and denoted $\bar{\mathcal{C}}$. As depicted in Fig. 11.1, a vertical branch corresponding to imaginary times is added. This allows us to incorporate information on how the state is initially prepared, and more specifically we can choose to start from an equilibrium correlated state at $t = 0$. [10]

A point on $\bar{\mathcal{C}}$ is denoted by z, which can evaluate to $z = (t, +)$ (resp. $(t, -)$) if it is located on the forward (resp. backward) real-time branch, or $z = -i\tau$ if it is on the imaginary-time branch. We introduce the contour operator $T_{\bar{\mathcal{C}}}$ that coincides with $T_{\mathcal{C}}$ introduced in Chapter 8 on the real-time axis, with T_τ on the imaginary-time one, and considers all points on the vertical branch to be later than points on the horizontal branches. This is pictured by the arrows in Fig. 11.1.

The impurity Green's function takes the form of a 3×3 matrix

$$G_{ab}(z, z') = -i\left\langle T_{\bar{\mathcal{C}}} d_a(z) d_b^\dagger(z')\right\rangle = \begin{pmatrix} G_{ab}^{++}(t,t') & G_{ab}^{<}(t,t') & G_{ab}^{\rceil}(t,\tau') \\ G_{ab}^{>}(t,t') & G_{ab}^{--}(t,t') & G_{ab}^{\rceil}(t,\tau') \\ G_{ab}^{\lceil}(\tau,t') & G_{ab}^{\lceil}(\tau,t') & iG_{ab}^{M}(\tau-\tau') \end{pmatrix}. \tag{11.22}$$

It coincides with the 2×2 real-time Green's function defined in Eq. (8.10), and is proportional to the Matsubara Green's function on the imaginary axis, that we label G^M to avoid confusions. We indeed have

$$G_{ab}(-i\tau, -i\tau') = -i \left\langle T_\tau d_a(\tau) d_b^\dagger(\tau') \right\rangle = i G^M_{ab}(\tau, \tau'). \tag{11.23}$$

We also introduce two mixed functions, $G^\rceil$ and $G^\lceil$, that couple the imaginary and real axis. They are not independent as

$$G^\lceil_{ab}(\tau, t) = [G^\rceil_{ba}(t, \beta - \tau)]^\dagger. \tag{11.24}$$

Let us now define a *clockwise* integral on the contour

$$\int_{z'}^{z} \mathrm{d}z_1 f(z_1) = \begin{cases} \displaystyle\int_{z'}^{z} \mathrm{d}z_1 f(z_1) & \text{if } z > z', \\ \displaystyle\int_{0}^{z} \mathrm{d}z_1 f(z_1) + \int_{z'}^{-i\beta} \mathrm{d}z_1 f(z_1) & \text{if } z' > z. \end{cases} \tag{11.25}$$

This allows us to expand the definition of the local states propagator from Eq. (11.4) on the full Baym-Kadanoff contour

$$R(z, z') = -i T_{\bar{\mathcal{C}}} \exp\left(-i \int_{z'}^{z} \mathcal{H}_{\text{loc}}(z_1) \mathrm{d}z_1 - i \int_{z'}^{z} \mathrm{d}z_1 \mathrm{d}z_2 \sum_{ab} \Delta_{ab}(z_1, z_2) d_a^\dagger(z_1) d_b(z_2) \right). \tag{11.26}$$

Note that $\mathcal{H}_{\text{loc}}$ can now be time-dependent, and $d(z)$ is written in the interaction representation with respect to $\mathcal{H}_{\text{loc}}(z)$. R is expressed in terms of a 3×3 matrix involving the different branches of the contour

$$R(z, z') = \begin{pmatrix} R^{++}(t, t') & R^{<}(t, t') & R^\rceil(t, \tau') \\ R^{>}(t, t') & R^{--}(t, t') & R^\rceil(t, \tau') \\ R^\lceil(\tau, t') & R^\lceil(\tau, t') & i R^M(\tau - \tau') \end{pmatrix}. \tag{11.27}$$

One can easily check that $R(-i\tau, -i\tau') = i R^M(\tau - \tau')$, where R^M is the equilibrium propagator defined in Eq. (11.4). The following symmetry relations hold

$$\left(R^{\lessgtr}(t, t') \right)^\dagger = -R^{\lessgtr}(t', t), \tag{11.28a}$$

$$\left(R^\rceil(t, \tau) \right)^\dagger = -R^\lceil(\beta - \tau, t). \tag{11.28b}$$

The bare propagator is defined as

$$R_0(z, z') = -i T_{\bar{\mathcal{C}}} e^{-i \int_{z'}^{z} \mathcal{H}_{\text{loc}}(z_1) \mathrm{d}z_1}, \tag{11.29}$$

and the partition function is

$$Z = -\mathrm{Tr} R^M(\beta) = i \mathrm{Tr}\left[R^<(t, t) \right]. \tag{11.30}$$

The impurity state propagator obeys diagrammatic rules similar to the ones defined in Section 11.1, except that endpoints of propagators are now real or imaginary times z on the contour $\bar{\mathcal{C}}$. R satisfies a Dyson equation involving a self-energy S, which can be written as a Volterra integro-differential equation

$$i\partial_z R(z, z') = \mathcal{H}_{\text{loc}}(z) R(z, z') + \int_{z'}^{z} \mathrm{d}z_1 S(z, z_1) R(z_1, z'). \tag{11.31}$$

Very similar to Eq. (11.14), the Non-Crossing Approximation now consists in removing all diagrams with crossing hybridization lines in the diagrammatrics of R. This corresponds to the following approximation on the self-energy S

$$S(z, z') = i T(z, z') \sum_{ab} \left[d_a^\dagger R(z, z') d_b \Delta_{ab}(z, z') - d_a R(z, z') d_b^\dagger \Delta_{ba}(z', z) \right], \tag{11.32}$$

where we introduce

$$T(z, z') = \begin{cases} 1 & \text{if } z > z', \quad (11.33) \\ -1 & \text{otherwise.} \quad (11.34) \end{cases}$$

This additional factor in the self-energy takes into account the time-ordering product in the definition of R.

Out-of-equilibrium NCA is a conserving approximation as it derives from the Luttinger-Ward functional

$$\Phi[R,\Delta] = i\sum_{ab}\int_0^{-i\beta} \mathrm{d}z\mathrm{d}z'\, T(z,z')\mathrm{Tr}\left[R(z',z)d_a R(z,z')d_b^\dagger\right]\Delta_{ba}(z',z). \tag{11.35}$$

The Green's function is then obtained as

$$G_{ab}(z,z') = \frac{i}{Z}T(z,z')\mathrm{Tr}\left[R(z',z)d_a R(z,z')d_b^\dagger\right]. \tag{11.36}$$

11.2.2 Implementation

Eqs. (11.31) and (11.32) have to be solved iteratively on the different branches of $\bar{\mathcal{C}}$, which, because of the convolution in Dyson's equation, are not independent from each other. There is however a specific order that allows to completely solve one component after the other, that we describe next.

For each component, we again use a block-diagonalisation of $\mathcal{H}_{\text{loc}}$, R and S as described in Section 11.1.3, but we do not specify the block indices in upcoming equations to keep notations short. The imaginary-times interval $[0,\beta]$ is discretized using $M+1$ points, with $\tau_0 = 0$ and $\tau_M = \beta = M\Delta\tau$. The real-time interval $[0, t_{\text{max}}]$ is discretized using $N+1$ points, with $t_0 = 0$ and $t_N = t_{\text{max}} = N\Delta t$.

Equilibrium component

Eqs. (11.31) and (11.32) projected on the vertical imaginary-time axis yield

$$-\partial_\tau R^M(\tau) = \mathcal{H}_{\text{loc}}R^M(\tau) + \int_0^\tau \mathrm{d}\bar{\tau} S^M(\tau-\bar{\tau})R^M(\bar{\tau}), \tag{11.37a}$$

$$S^M(\tau) = -\sum_{ab}\left(d_a^\dagger R^M(\tau)d_b\Delta_{ab}^M(\tau) - d_a R(\tau)d_b^\dagger\Delta_{ba}^M(-\tau)\right), \tag{11.37b}$$

with initial condition $R^M(0) = -\mathbf{1}$. These equations exactly correspond to the equilibrium Non-Crossing Approximation described in Section 11.1.3, and can therefore be solved in the same fashion, independently of the other components of the Baym-Kadanoff contour. This is unsurprising, as this formalism aims at starting the real-time calculations from a correlated state at equilibrium, which therefore has to be solved first.

Greater component

Evaluating Eqs. (11.31) and (11.32) for $z = (t,-)$ and $z' = (t',+)$, we obtain

$$i\partial_t R^>(t,t') = \mathcal{H}_{\text{loc}}(t)R^>(t,t') + \int_{t'}^t \mathrm{d}\bar{t} S^>(t,\bar{t})R^>(\bar{t},t'), \tag{11.38a}$$

$$S^>(t,t') = i\sum_{ab}\left(d_a^\dagger R^>(t,t')d_b\Delta_{ab}^>(t,t') - d_a R^>(t,t')d_b^\dagger\Delta_{ba}^<(t',t)\right), \tag{11.38b}$$

with $R^>(t,t) = -i\mathbf{1}$. These equations look very similar to Eqs. (11.37), but are intrinsically more complicated to solve as they require a time evolution both in t and t'. We choose to self-consistently solve them as we propagate in time, which means that, for a given $1 \le n \le N$, we iterate through these two equations on $[0,t_n]\times[0,t_n]$ until convergence.

The hard computational part relies in the time evolution, Eq. (11.38a). The scheme we use is depicted in Fig. 11.2a. Let us assume we know $R^>(t_j,t_l)$ and $\partial_t R^>(t_j,t_l)$ for all $1 \le j,l < n$ (black crosses in orange square), where $1 \le n \le N$. For simplicity, we introduce the notation $R^>_{j,l} = R^>(t_j,t_l)$, $\dot{R}^>_{j,l} = \partial_t R^>(t_j,t_l)$ and $\mathcal{H}_j = \mathcal{H}_{\text{loc}}(t_j)$.

First, we are going to compute R_{nj} and $\dot{R}_{nj}$ for $0 \le j < n$ (red crosses). For a given j, this is done by evolving points in a scheme similar to the one from Section 11.1.3. We write

$$R^>_{n,j} = R^>_{n-1,j} + \frac{\Delta t}{2}\left(\dot{R}^>_{n,j} + \dot{R}^>_{n-1,j}\right), \tag{11.39}$$

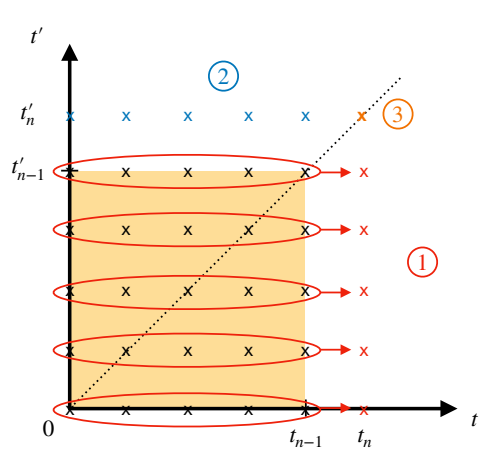

(a) $R^>$ and $R^<$ computation. The known data points (orange square) are first evolved horizontally, yielding the red crosses. Symmetry relations are then used to compute the blue crosses, that are themselves evolved horizontally to get the orange one.

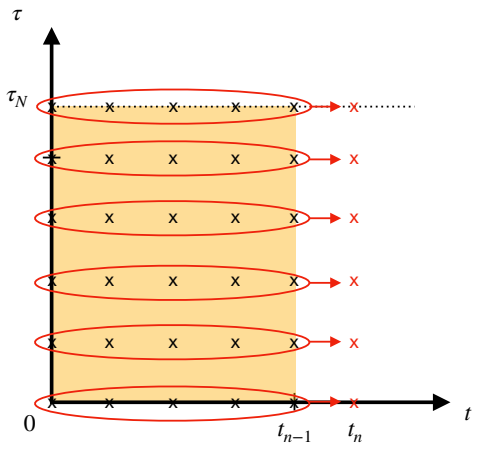

(b) $R^\rceil$ computation. The known data points (orange rectangle) are directly evolved horizontally, yielding the red crosses.

Figure 11.2 – Propagation scheme used for the computation of $R^>$, $R^<$ (*left*) and $R^\rceil$ (*right*).

and use a trapezoidal approximation to evaluate the Volterra equation

$$i\dot{R}^>_{n,j} = \mathcal{H}_n R^>_{n-1,j} + \sum_{l=1}^{n-1} \Delta t S^>_{n-l,j} R^>_{l,j} + \frac{\Delta t}{2} S^>_{n,j} R^>_{0,j} + \frac{\Delta t}{2} S^>_{0,j} R^>_{n,j}. \tag{11.40}$$

Combining these equations, we obtain

$$\begin{aligned} R^>_{n,j} = &\left[\mathbf{1} + i\frac{\Delta t}{2}\mathcal{H}_n + i\left(\frac{\Delta t}{2}\right)^2 S^>_{0,j}\right]^{-1} \\ &\times \left[R^>_{n-1,j} + \frac{\Delta}{2}\left(\dot{R}^>_{n-1,j} - i\frac{\Delta t}{2} S^>_{n,j} R^>_{0,j} - i\Delta t \sum_{l=1}^{n-1} S^>_{n-l,j} R^>_{l,j}\right)\right]. \end{aligned} \tag{11.41}$$

$\dot{R}^>_{n,j}$ is then obtained using Eq. (11.40). Second, we compute R_{jn} and $\dot{R}_{jn}$ for $0 \leq j < n$ (blue crosses), which can be easily achieved using the symmetry relations of $R^>$ (Eq. (11.28a)). Finally, the initial condition of the Volterra equation yields $R^>_{nn} = -i\mathbf{1}$ and $\dot{R}^>_{nn} = -\mathcal{H}_n$.

Mixed component

The coupled equations for the mixed components write

$$i\partial_t R^\rceil(t,\tau) = \mathcal{H}_{\text{loc}}(t) R^\rceil(t,\tau) + \int_0^t \mathrm{d}\bar{t}\, S^>(t,\bar{t}) R^\rceil(\bar{t},\tau) + \int_\tau^\beta \mathrm{d}\bar{\tau}\, S^\rceil(t,\bar{\tau}) R^M(\bar{\tau}-\tau), \tag{11.42a}$$

$$S^\rceil(t,\tau) = -i\sum_{ab}\left(d^\dagger_a R^\rceil(t,\tau) d_b \Delta^\rceil_{ab}(t,\tau) - d_a R^\rceil(t,\tau) d^\dagger_b \Delta^\lceil_{ba}(\tau,t)\right), \tag{11.42b}$$

with initial condition $R^\rceil(0,\tau) = iR^M(\beta-\tau)$. As for the greater components, we choose to self-consistently solve these equations as we propagate in time, which means that, for a given $1 \leq n \leq N$, we loop on them on $[0,t_n] \times [0,\beta]$ until convergence.

Knowing the initial condition for all points on the imaginary-time axis indeed allows a propagation scheme of Eq. (11.42a) slightly different from the one for the greater component, depicted in Fig. 11.2b. Let us assume we know $R^\rceil(t_j,\tau_l)$ and $\partial_t R^\rceil(t_j,\tau_l)$ for all $1 \leq j < n$, $1 \leq l \leq M$ (black crosses in orange rectangle), where $1 \leq n \leq N$. For a given l, $R^\rceil(t_n,\tau_l)$ and $\partial_t R^\rceil(t_n,\tau_l)$ are then simply obtained by propagating points horizontally by descritizing Eq. (11.42a).

Lesser component

Evaluating Eqs. (11.31) and (11.32) for $z = (t, +)$ and $z' = (t', -)$, we obtain

$$i\partial_t R^<(t,t') = \mathcal{H}_{\text{loc}}(t)R^<(t,t') + \int_0^t \mathrm{d}\bar{t} S^>(t,\bar{t})R^<(\bar{t},t') \tag{11.43a}$$
$$- \int_0^{t'} \mathrm{d}\bar{t} S^<(t,\bar{t})R^>(\bar{t},t') - i\int_0^\beta \mathrm{d}\bar{\tau} S^\rceil(t,\bar{\tau})R^\lceil(\bar{\tau},t'),$$
$$S^<(t,t') = -i\sum_{ab}\left(d_a^\dagger R^<(t,t')d_b\Delta_{ab}^<(t,t') - d_a R^<(t,t')d_b^\dagger\Delta_{ba}^>(t',t)\right), \tag{11.43b}$$

with initial condition $R^<(0,0) = iR^M(\beta)$. These equations are structurally very close to the ones for the greater components. There are additional terms in the Volterra equation, but they do not involve the lesser local propagator.

We therefore solve Eqs. (11.43) self-consistently exactly in the same way as Eqs. (11.38), by discretizing points in time. The only difference is that we do not know the diagonal points anymore, so that at the end of the propagation we have to time evolve the points obtained by symmetrization (blue crosses in Fig. 11.2a, yielding the orange one).

Green's functions

At the end of the computation, the Green's functions are simply obtained by projecting Eq. (11.36) on the different branches of the contour

$$G_{ab}^M(\tau) = -\frac{1}{Z}\mathrm{Tr}\left(R(\beta-\tau)d_a R(\tau)d_b^\dagger\right), \tag{11.44a}$$
$$G_{ab}^>(t,t') = \frac{i}{Z}\mathrm{Tr}\left(R^<(t',t)d_a R^>(t,t')d_b^\dagger\right), \tag{11.44b}$$
$$G_{ab}^\rceil(t,\tau) = -\frac{i}{Z}\mathrm{Tr}\left(R^\lceil(\tau,t)d_a R^\rceil(t,\tau)d_b^\dagger\right), \tag{11.44c}$$
$$G_{ab}^<(t,t') = -\frac{i}{Z}\mathrm{Tr}\left(R^>(t',t)d_a R^<(t,t')d_b^\dagger\right). \tag{11.44d}$$

Chapter 12

Steady-state Non-Crossing Approximation

The out-of-equilibrium NCA algorithm presented in the previous Chapter proves extremely useful to compute the transient behaviour of the system studied before it reaches its long-time limit, as for instance in pump-probe experiments. However, when we are only interested in the steady-state regime, as it will be the case for Ca_2RuO_4 in the next Chapter, solving the full time dependence over the triple contour is computationally heavy.

In this Chapter, we first present an out-of-equilibrium version of the NCA approximation working on the Keldysh contour, therefore without the imaginary-time axis, before deriving steady-state equations for the local states propagator R and its self-energy S. In both cases, the proposed algorithms are benchmarked against the technique presented in the previous Chapter. The algorithmic developments presented here have not yet been published.

12.1 Out-of-equilibrium NCA on the Keldysh contour

12.1.1 Formalism

As a first step towards a steady-state solver, let us first derive the out-of-equilibrium NCA equations on the real-time Keldysh contour $\mathcal{C}$ introduced in Chapter 8. In this formalism, there is no imaginary-time axis, so that it is not possible to engineer a correlated state at $t = 0$. This is not an issue as our goal is to study the steady state, which does not depend on the original preparation of the system. The main advantage of this representation is that only the forward and backward branches on the real axis are present, so that we only deal with the greater and lesser components of the local states propagator.

The Volterra equation from Eq. (11.31) simply reduces to

$$i\partial_t R^{>}(t,t') = \mathcal{H}_{\text{loc}} R^{>}(t,t') + \int_{t'}^{t} \mathrm{d}\bar{t} S^{>}(t,\bar{t}) R^{>}(\bar{t},t'), \tag{12.1a}$$

$$i\partial_t R^{<}(t,t') = \mathcal{H}_{\text{loc}} R^{<}(t,t') + \int_{0}^{t} \mathrm{d}\bar{t} S^{>}(t,\bar{t}) R^{<}(\bar{t},t') - \int_{0}^{t'} \mathrm{d}\bar{t} S^{<}(t,\bar{t}) R^{>}(\bar{t},t'), \tag{12.1b}$$

and the NCA approximation on the self-energy becomes

$$S^{\lessgtr}(t,t') = iT(z,z') \sum_{ab} \left(d_a^\dagger R^{\lessgtr}(t,t') d_b \Delta_{ab}^{\lessgtr}(t,t') - d_a R^{\lessgtr}(t,t') d_b^\dagger \Delta_{ba}^{\gtrless}(t',t) \right). \tag{12.2}$$

The greater component continues to verify $R^{>}(t,t) = -i\mathbf{1}$ for all t, but there is no obvious initial condition on $R^{<}(0,0)$ as in the case of the Baym-Kadanoff contour. The starting point therefore has to be provided by hand, which makes this algorithm not well suited for the study of transient behaviours. Moreover, as it requires less computation as its full triple-contour counterpart, it is to be favoured when computing steady-state properties that do not depend on the initial preparation of the system.

The Green's function is then obtained as

$$G_{ab}^{\lessgtr}(t,t') = \frac{i}{Z} T(z,z') \mathrm{Tr} \left(R^{\gtrless}(t',t) d_a R^{\lessgtr}(t,t') d_b^\dagger \right), \tag{12.3}$$

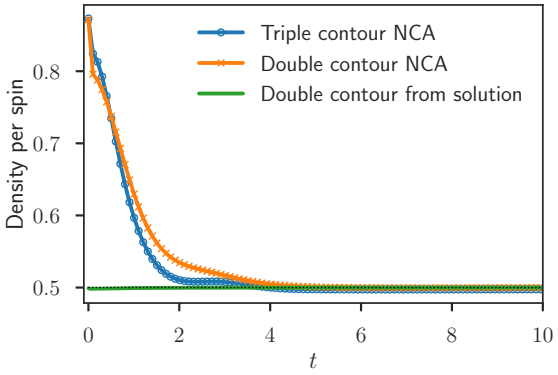

Figure 12.1 – Evolution of the density per spin after a quench from $U = 0$ to $U = 3$ at initial time, using the Baym-Kadanoff version of the NCA equations and the Keldysh one from two different starting points.

where the partition function is

$$Z = i\mathrm{Tr}\left[R^<(t,t)\right]. \tag{12.4}$$

Apart from the computation of the Matsubara and mixed components that are not present anymore, the implementation of these equations is done exactly in the same way as presented in Section 11.2.2.

12.1.2 Benchmark

We consider a two-site Anderson impurity model described by the local Hamiltonian

$$\mathcal{H}_{\mathrm{loc}} = -\mu \sum_{\sigma} \left(n_{\sigma 0} + n_{\sigma 1}\right) - \gamma \sum_{\sigma} \left(d^\dagger_{\sigma 0} d_{\sigma 1} + \text{ h.c.}\right) + U \sum_i n_{i\uparrow} n_{i\downarrow}, \tag{12.5}$$

where $d^\dagger_{\sigma i}$ (resp. $d_{\sigma i}$) creates (resp. annihilates) an electron with spin σ on site i, μ is the chemical potential of the system, γ is a hopping amplitude and U is the Coulomb repulsion. $n_{\sigma i} = d^\dagger_{\sigma i} d_{\sigma i}$ is the density operator. Each site is connected to a bath described by a semi-circular density of states of bandwidth $4D$.

In the following, $D = 1$ is our energy unit, and we have $\beta = 10$, $t_{\mathrm{max}} = 20$, $\mu = 1.5$ and $\gamma = 1$. We consider a quench of the Coulomb interaction U from 0 to 3 at initial time, which means the system is half-filled in the long-time limit.

In Fig. 12.1 is plotted the evolution of the density as a function of time on the $[0, 10]$ interval. Blue circles result from the full Baym-Kadanoff calculation, and orange crosses are obtained in the Keldysh formalism presented above, starting from the same value of $R^<(0,0)$ as the triple-contour calculation. One sees that both algorithms converge towards the same solution, $n = 0.5$, but following a different evolution even if they share the same starting point. The green line is also a two-branch calculation, this time using as starting point the value obtained at the end of the contour, $R^<(t_{\mathrm{max}}, t_{\mathrm{max}})$. This solution is found to already be in the steady-state limit.

In order to verify that the triple-contour and double-contour of the NCA equations indeed yield the same physical quantities at long times, we also plot in Fig. 12.2 the lesser and greater components of the Green's function $G(t_{\mathrm{max}}, t)$ for $t \in [12, t_{\mathrm{max}}]$. As both sites are equivalent, $G_{00}(t,t') = G_{11}(t,t')$ and $G_{01}(t,t') = G_{10}(t,t')$. Full blue and orange lines are obtained using the Keldysh contour formulation of the equations, and lie on top of the green and red dashed lines that result from the full out-of-equilibrium method on the Baym-Kadanoff contour.

12.2 Steady-state NCA

12.2.1 Formalism

If the local Hamiltonian is time-independent, it is possible for the system to reach a well-defined steady-state. All quantities in Eqs. (12.1) and (12.2) then only depend on the time difference $t - t'$. In the Keldysh

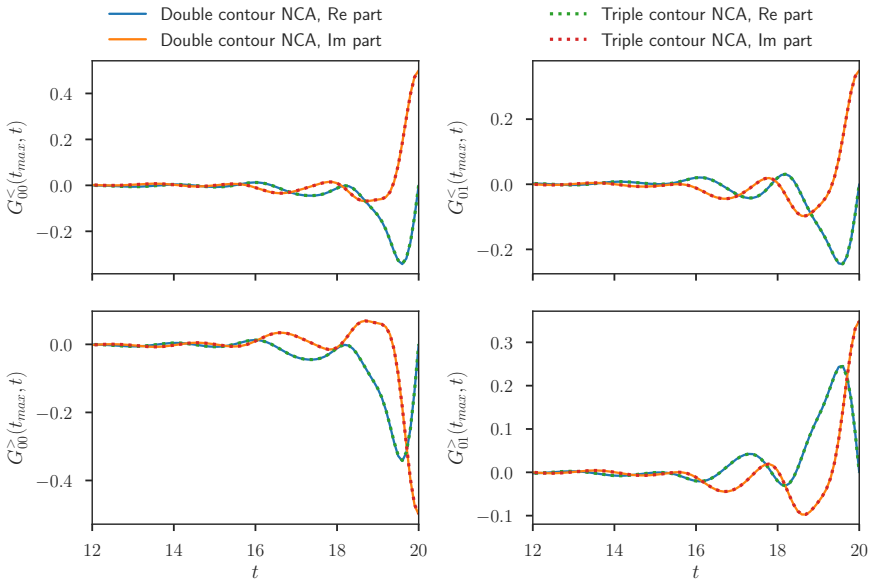

Figure 12.2 – Diagonal and off-diagonal components of the lesser and greater components of the Green's function $G(t_{\max}, t)$ for $t \in [12, t_{\max}]$ after a quench in U from 0 to 3 at initial time.

formalism, this means pushing the starting point of the contour from 0 to $-\infty$, so that the greater and lesser components of the local states propagator write

$$i\partial_t R^>(t) = \mathcal{H}_{\text{loc}} R^>(t) + \int_0^t \mathrm{d}\bar{t} S^>(t-\bar{t}) R^>(\bar{t}), \tag{12.6a}$$

$$i\partial_t R^<(t) = \mathcal{H}_{\text{loc}} R^<(t) + \int_{-\infty}^t \mathrm{d}\bar{t} S^>(t-\bar{t}) R^<(\bar{t}) - \int_{-\infty}^0 \mathrm{d}\bar{t} S^<(t-\bar{t}) R^>(\bar{t}). \tag{12.6b}$$

The NCA equation becomes

$$S^>(t) = i \sum_{ab} \left(d_a^\dagger R^>(t) d_b \Delta^>_{ab}(t) - d_a R^>(t) d_b^\dagger \Delta^<_{ba}(-t) \right), \tag{12.7a}$$

$$S^<(t) = -i \sum_{ab} \left(d_a^\dagger R^<(t) d_b \Delta^<_{ab}(t) - d_a R^<(t) d_b^\dagger \Delta^>_{ba}(-t) \right). \tag{12.7b}$$

We are now interested in computing these different functions between $-t_{\max}$ and $t_{\max}$. The initial condition of the greater component is $R^>(0) = -i\mathbf{1}$. For the lesser component, the initial condition would correspond to the value at $-\infty$ in which the state is initially prepared, but this information is anyway lost once the system has reached the steady state.

In many physical applications, a time evolution is not suited to solve Eq. (12.6) as functions expand to large times while oscillating. We therefore move to frequency space. For the greater component, we introduce $\tilde{R}^>(t) = R^>(t)\theta(t)$, whose spectral function is $iR^>(\omega)/2\pi$, so that

$$\tilde{R}^>(z) = \frac{1}{2\pi} \int_{-\infty}^{+\infty} \frac{iR^>(\omega)}{z-\omega} \mathrm{d}\omega. \tag{12.8}$$

On the real frequency axis, this yields

$$\tilde{R}^>(\omega) = \frac{1}{2\pi} \int_{-\infty}^{+\infty} \frac{iR^>(\omega')}{\omega' - \omega + i\eta} \mathrm{d}\omega'. \tag{12.9}$$

The Volterra equation for $\tilde{R}^>(t)$ is almost identical to that of $R^>(t)$ with an additional delta function and, importantly, infinite bounds for the time integration

$$i\partial_t \tilde{R}^>(t) = \delta(t) + \mathcal{H}_{\text{loc}} \tilde{R}^>(t) + \int_{-\infty}^{+\infty} \mathrm{d}\bar{t}\, \tilde{S}^>(t-\bar{t}) \tilde{R}^>(\bar{t}), \tag{12.10}$$

where $\tilde{S}^>(t) = S^>(t)\theta(t)$. In frequency space, this equation writes

$$\tilde{R}^>(\omega) = \left[\omega - \mathcal{H}_{\text{loc}} - \tilde{S}^>(\omega)\right]^{-1}, \tag{12.11}$$

and the greater component of the local states propagator is then simply obtained as

$$R^>(\omega) = 2i\text{Im}\tilde{R}^>(\omega). \tag{12.12}$$

Eq. (12.6b) can also be rewritten in terms of convolutions in time

$$i\partial_t R^<(t) = \mathcal{H}_{\text{loc}} R^<(t) + \int_{-\infty}^{+\infty} \mathrm{d}\bar{t}\tilde{S}^>(t-\bar{t})R^<(\bar{t}) - \int_{-\infty}^{+\infty} \mathrm{d}\bar{t}S^<(t-\bar{t})\bar{R}^>(\bar{t}), \tag{12.13}$$

where $\bar{R}^>(t) = R^>(t)\theta(-t)$. Moving to Fourier space, one obtains

$$\omega R^<(\omega) = \mathcal{H}_{\text{loc}} R^<(\omega) + \tilde{S}^>(\omega)R^<(\omega) - S^<(\omega)\bar{R}^>(\omega), \tag{12.14}$$

which rewrites

$$R^<(\omega) = -\left[\omega\mathbf{1} - \mathcal{H}_{\text{loc}} - \tilde{S}^>(\omega)\right]^{-1} S^<(\omega)\bar{R}^>(\omega). \tag{12.15}$$

Note that the function being inverted, $\omega\mathbf{1} - \mathcal{H}_{\text{loc}} - \tilde{S}^>(\omega)$, is the same as in Eq. (12.11). We detail in the next Section how these steady-state NCA equations are solved in practice.

Green's functions are then obtained as

$$G^>_{ab}(t) = \frac{i}{Z}\text{Tr}\left(R^<(-t)d_a R^>(t)d_b^\dagger\right), \tag{12.16a}$$

$$G^<_{ab}(t) = -\frac{i}{Z}\text{Tr}\left(R^>(-t)d_a R^<(t)d_b^\dagger\right), \tag{12.16b}$$

where the partition function is

$$Z = i\text{Tr}\left[R^<(0)\right]. \tag{12.17}$$

12.2.2 Implementation

Greater component

The equations for the greater components are

$$\tilde{R}^>(\omega) = \left[\omega - \mathcal{H}_{\text{loc}} - \tilde{S}^>(\omega)\right]^{-1}, \tag{12.18a}$$

$$S^>(t) = i\sum_{ab}\left(d_a^\dagger R^>(t)d_b\Delta^>_{ab}(t) - d_a R^>(t)d_b^\dagger\Delta^<_{ba}(-t)\right). \tag{12.18b}$$

As these do not depend on $R^<$ and $S^<$, they can be solved first, and we choose an iterating scheme going back and forth in Fourier space. Starting from a guess for $R^>(t)$, we use Eq. (12.18b) to obtain $S^>(t)$ from which we construct $\tilde{S}^>(t) = S^>(t)\theta(t)$. Because this function is stored on a discrete time mesh and has finite support, its discontinuity in time brings a non-negligible computational error when computing the Fourier transform $\tilde{S}^>(\omega)$. This problem can be handled by substracting a function which Fourier transform is analytically known, for instance

$$f_s(t) = -if_0\theta(t)\left[e^{-\gamma t - i\epsilon_1 t} - 2e^{-\frac{\gamma t}{2} - i\epsilon_2 t}\right], \tag{12.19a}$$

$$f_s(\omega) = \frac{f_0}{\omega - \epsilon_1 + i\gamma} - \frac{2f_0}{\omega - \epsilon_2 + \frac{i\gamma}{2}}. \tag{12.19b}$$

f_0, ϵ_1,ϵ_2 and γ are determined in order to compensate for the discontinuities of $\tilde{S}^>$ and $\partial_t\tilde{S}^>$. $\tilde{R}^>(\omega)$ is obtained using Eq. (12.18a) and we recover $R^>$ through $R^>(\omega) = 2i\text{Im}\tilde{R}^>(\omega)$. A new $R^>(t)$ is determined using a simple Fourier transform.

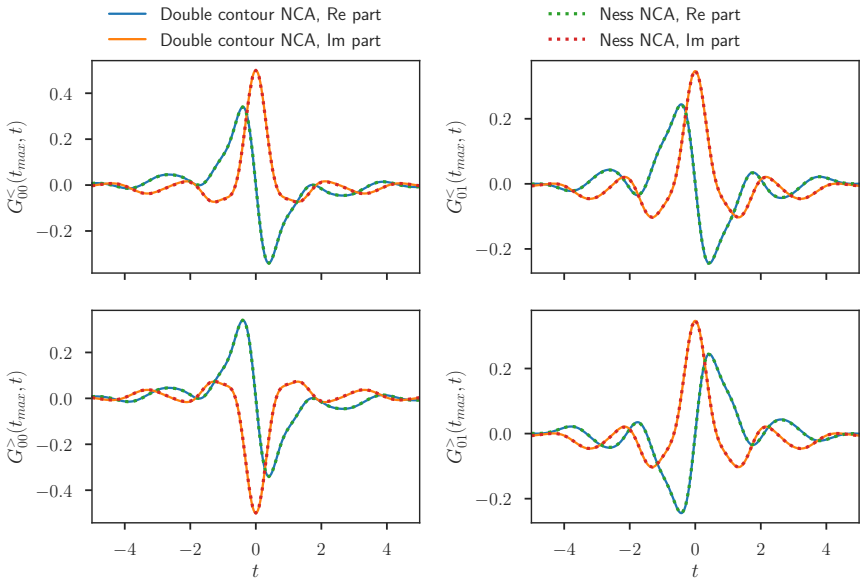

Figure 12.3 – Diagonal and off-diagonal components of the lesser and greater components of the Green's function $G(t)$ in the steady-state regime for a half-filled two-orbital model.

Once $R^>(t)$ has been fully converged, we construct $\bar{R}^>(t)$. To obtain its Fourier transform, we use

$$f_r(t) = -if_0\theta(-t)\left[e^{\gamma t - i\epsilon_1 t} - 2e^{\frac{\gamma t}{2} - i\epsilon_2 t}\right], \tag{12.20a}$$

$$f_r(\omega) = -\frac{f_0}{\omega - \epsilon_1 - i\gamma} + \frac{2f_0}{\omega - \epsilon_2 - \frac{i\gamma}{2}}, \tag{12.20b}$$

where f_0, ϵ_1,ϵ_2 and γ are determined in order to compensate for the discontinuities of $\bar{R}^>$and $\partial_t \bar{R}^>$.

Lesser component

The equations to solve for the greater components are

$$R^<(\omega) = -\left[\omega\mathbf{1} - \mathcal{H}_{\text{loc}} - \tilde{S}^>(\omega)\right]^{-1} S^<(\omega)\bar{R}^>(\omega), \tag{12.21a}$$

$$S^<(t) = -i\sum_{ab}\left(d_a^\dagger R^<(t) d_b \Delta^<_{ab}(t) - d_a R^<(t) d_b^\dagger \Delta^>_{ba}(-t)\right). \tag{12.21b}$$

These are solved iteratively, using Fourier transforms to go back and forth between real and frequency space. Note also that if $R^<$ is a solution to these equations, so is any function proportional to it. However, because the partition function is proportional to this component of the propagator, both will yield the same Green's function. This is a manifestation of the initial condition problem addressed above, and the fact that the physical solution is independent of it. We choose the solution that satisfies $Z = 1$ to guarantee its unicity, as it is the value we expect in the Keldysh formalism.

12.2.3 Benchmark

Let us revisit the previous benchmark of Section 12.1.2 where we performed a quench in U in a multi-orbital system. First, the density per spin obtained in the steady-state calculation is indeed found to be 0.5, as expected in the half-filled case. We plot in Fig. 12.3 the greater and lesser components of the steady-state Green's function $G(t)$ for $t \in [-5, 5]$. Full blue and orange lines are extracted from the out-of-equilibrium solver on the Keldysh contour, while the green and red dashed lines are the results of the steady-state method. Both results lie on top of each other. In this example, the steady-state solver is more than 100 times faster than its out-of-equilibrium counterpart, as it only has to solve a single time evolution.

12.3 Current through a quantum dot

The model used to benchmark the algorithms in Sections 12.1.2 and 12.2.3 reaches an equilibrium state in the long-time limit, that could be studied simply by using the equilibrium NCA solver presented in Section 11.1. In order to check the validity of our algorithms in an out-of-equilibrium steady-state, let us now consider the current flowing through a quantum dot.

A single energy level is located between a left (L) and a right (R) lead, that are both considered infinite and uncorrelated. The Hamiltonian of the system is

$$\mathcal{H} = -\mu \sum_{\sigma} d_{\sigma}^{\dagger} d_{\sigma} + U n_{d\uparrow} n_{d\downarrow} + \sum_{\substack{\sigma \mathbf{k} \\ a \in \{L,R\}}} \gamma_{\mathbf{k}} \left(c_{\sigma \mathbf{k} a}^{\dagger} d_{\sigma} + \text{h.c.} \right), \tag{12.22}$$

where $d_{\sigma}^{\dagger}$ (resp. d_{σ}) creates (resp. annhilates) an electron with spin σ on the dot, $n_{d\sigma} = d_{\sigma}^{\dagger} d_{\sigma}$ is the density operator, and $c_{\sigma \mathbf{k} a}^{\dagger}$ (resp. $c_{\sigma \mathbf{k} a}$) creates (resp. annihilates) an electron with spin σ and momentum $\mathbf{k}$ in the $a = L, R$ lead. μ is the chemical potential of the system, U the Coulomb repulsion and $\gamma_{\mathbf{k}}$ a momentum-dependent hopping term between the impurity level and the leads.

At $t = -\infty$, $\gamma_{\mathbf{k}}$ is considered to be null and the leads are both at equilibrium with respective chemical potentials μ_L and μ_R. The hoppings are then turned on and we let the system evolve until it reaches a steady-state. If $\mu_L > \mu_R$, a current will flow from the left lead to the right lead. We assume that

$$\mu_L = \mu + \frac{V}{2}, \quad \mu_R = \mu - \frac{V}{2}, \tag{12.23}$$

so that the chemical potential difference is symmetric around the impurity level. The noninteracting Green's function of the a lead for particles with spin σ, momentum $\mathbf{k}$ is denoted $g_{\sigma \mathbf{k} a}$.

The current per spin is [106]

$$I_{\sigma} = \frac{i}{2} \sum_{\mathbf{k}} \gamma_{\mathbf{k}} \left[\langle c_{\sigma \mathbf{k} L}^{\dagger} d_{\sigma} \rangle - \langle d_{\sigma}^{\dagger} c_{\sigma \mathbf{k} L} \rangle + d_{\sigma}^{\dagger} c_{\sigma \mathbf{k} R} \rangle - \langle c_{\sigma \mathbf{k} R}^{\dagger} d_{\sigma} \rangle \right]. \tag{12.24}$$

We introduce the Green's functions

$$G^{<}_{d \to a, \sigma \mathbf{k}}(t - t') = i \langle c_{\sigma \mathbf{k} a}^{\dagger}(t) d_{\sigma}(t') \rangle, \tag{12.25a}$$

$$G^{<}_{a \to d, \sigma \mathbf{k}}(t - t') = i \langle d_{\sigma}^{\dagger}(t) c_{\sigma \mathbf{k} a}(t') \rangle. \tag{12.25b}$$

These are related to the noninteracting Green's functions of the leads through [106, 95]

$$G^{<}_{d \to a, \sigma \mathbf{k}}(\omega) = \gamma_{\mathbf{k}} \left[g^{<}_{\sigma \mathbf{k} a}(\omega) G^{++}_{\sigma}(\omega) - g^{--}_{\sigma \mathbf{k} a}(\omega) G^{<}_{\sigma}(\omega) \right], \tag{12.26a}$$

$$G^{<}_{a \to d, \sigma \mathbf{k}}(\omega) = \gamma_{\mathbf{k}} \left[g^{++}_{\sigma \mathbf{k} a}(\omega) G^{<}_{\sigma}(\omega) - g^{<}_{\sigma \mathbf{k} a}(\omega) G^{--}_{\sigma}(\omega) \right]. \tag{12.26b}$$

Introducing the left and right hybridization functions $\Delta_{\sigma a} = \sum_{\mathbf{k}} \gamma_{\mathbf{k}}^2 g_{\sigma \mathbf{k} a}$, we finally obtain

$$I_{\sigma} = \frac{1}{2} \int \frac{\mathrm{d}\omega}{2\pi} \left[\left(\Delta^{<}_{\sigma L}(\omega) - \Delta^{<}_{\sigma R}(\omega) \right) G^{>}_{\sigma}(\omega) - \left(\Delta^{>}_{\sigma L}(\omega) - \Delta^{>}_{\sigma R}(\omega) \right) G^{<}_{\sigma}(\omega) \right]. \tag{12.27}$$

Let us now compute the current that flows through the quantum dot as a function of V with all three NCA algorithms presented in this Thesis. The retarded hybridization functions, $\Delta^{R}_{\sigma a}$, are initialized to a semicircular density of states of width $12D$, where $D = 1$ is our energy unit. The Keldysh component is obtained through the fluctuation-dissipation theorem, see Eq. (9.6),

$$\Delta^{K}_{\sigma L}(\omega) = \tanh\left(\frac{\beta(\omega - V/2)}{2} \right) \left[\Delta^{R}_{\sigma L}(\omega) - \left(\Delta^{R}_{\sigma L}(\omega) \right)^{*} \right], \tag{12.28a}$$

$$\Delta^{K}_{\sigma R}(\omega) = \tanh\left(\frac{\beta(\omega + V/2)}{2} \right) \left[\Delta^{R}_{\sigma R}(\omega) - \left(\Delta^{R}_{\sigma R}(\omega) \right)^{*} \right]. \tag{12.28b}$$

The greater and lesser components are then

$$\Delta^{>}_{\sigma a}(\omega) = \frac{1}{2} \left[\Delta^{K}_{\sigma a}(\omega) + \Delta^{R}_{\sigma a}(\omega) - \left(\Delta^{R}_{\sigma a}(\omega) \right)^{*} \right], \tag{12.29a}$$

$$\Delta^{<}_{\sigma a}(\omega) = \frac{1}{2} \left[\Delta^{K}_{\sigma a}(\omega) - \Delta^{R}_{\sigma a}(\omega) + \left(\Delta^{R}_{\sigma a}(\omega) \right)^{*} \right]. \tag{12.29b}$$

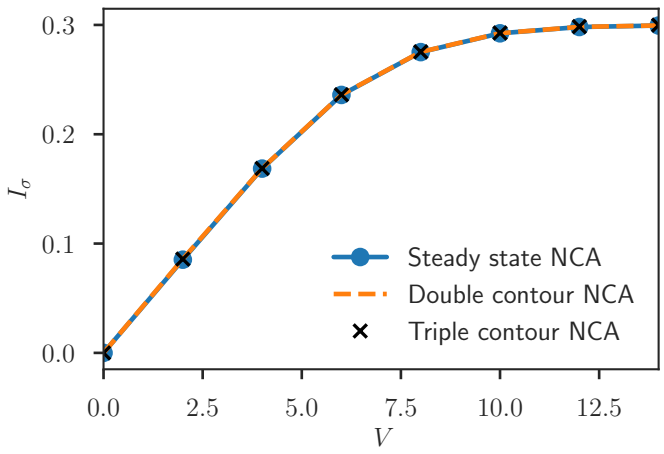

Figure 12.4 – Current flowing through a quantum to as a function of the chemical potential difference V between the leads. $\beta = 2$, $U = 3$, $\mu = 1.5$.

In the Baym-Kadanoff code, the left and right Matsubara hybridization function are also initialized to a semicircular density of states of width $12D$, and the mixed component is

$$\Delta^{\rceil}_{\sigma a}(t, \tau) = \Delta^{R}_{\sigma a}(t)\Delta^{M}_{\sigma a}(\beta - \tau). \tag{12.30}$$

In all cases, the full hybridization function is the sum of the left and right ones

$$\Delta_\sigma = \Delta_{\sigma L} + \Delta_{\sigma R}. \tag{12.31}$$

We choose $\beta = 2$, $U = 3$, $\mu = 1.5$. The IV-characteristics of the quantum dot is plotted in Fig. 12.4 using the steady-state solver (blue dots), the Keldysh contour formulation (dashed orange lines) and finally the full triple contour calculation presented in the previous Chapter (black crosses). When the chemical potential difference V is 0, no current is flowing trough the system. As the bandwidth of the semicircular density of states of the leads is 12, the current saturates for voltages $V \geq 12$. All three methods perfectly agree in their long-time limit.

Chapter 13

Electric-field-driven insulator-to-metal transition in Ca_2RuO_4

In a world relying more than ever on electronic devices, developing new materials to store and process data has become of paramount importance. Among currently investigated materials, strongly correlated systems are promising candidates as they display novel quantum phenomena, such as Mott transitions [74]. Applying pressure is a suitable tuning method to drive such transitions, however achieving high pressure conditions outside a laboratory proves to be difficult. A natural alternative is to apply an electric field E to the Mott insulator, resulting in a so-called "switching" to a metallic state.

Some transition metal oxides have already been proposed as candidates to build resistance RAM [105, 169], but they still require low temperature and/or high voltage (typically 1-100 kV/cm) [79, 75, 185, 156, 68]. To develop practical switching devices, recent experimental papers have focused on Ca_2RuO_4 as a promising candidate. Its transition indeed appears to be driven at room temperature using a dry-battery level voltage, resulting in a threshold field $E_{\text{th}} \sim 40$ V/cm [115, 142, 122].

This Chapter first aims at summarizing Ca_2RuO_4's properties and presenting experimental results concerning its electric-field induced insulator-to-metal transition. In a second part, we motivate a minimal model and present preliminary results using the NCA approximation presented in the previous Chapters.

13.1 Ca_2RuO_4: basic properties and model Hamiltonian

Ca_2RuO_4 is a layered perovskite with RuO_2 planes forming a square lattice. The space group of this material is *Pbca* [50, 23], which combines a rotation of the RuO_6 octahedra around the c-axis with a tilt around the b-axis (see Fig. 13.1a). Ruthenium atoms are in a $4d^4$ configuration. A structural transition occurs at $T_S \sim 356$K: above T_S, RuO_6 octahedra have a long c-axis (*L-Pbca* structure), while below T_S they have a short c-axis (*S-Pbca* structure).

Ca_2RuO_4 is part of a family of Ruthenium-based compounds with chemical formulae $Sr_{n+1}Ru_nO_{3n+1}$ and $Ca_{n+1}Ru_nO_{3n+1}$ [66], that exhibit remarkable properties: unconventional superconductivity [98], variety of magnetic phases [118, 29], nematicity and metal-insulator transitions [2, 114, 154, 50, 116, 117]. We are specifically interested in the metal-insulator transition occurring at $T_M \sim 357$K (see Fig. 13.1b), that has been shown to be caused by the structural transition between long and short RuO_6 octahedra [2, 58].

This material can be described by the following three-band Hubbard-Kanamori Hamiltonian for the t_{2g} orbitals [1] [78, 58, 155]

$$\begin{aligned}\mathcal{H} = &\sum_{ia\sigma} \epsilon_a n_{ia\sigma} - \sum_{\substack{a\sigma \\ \langle ij \rangle}} \gamma_a c^\dagger_{ia\sigma} c_{ja\sigma} + J \sum_{i,a\neq b} \left(c^\dagger_{ia\uparrow} c_{ib\uparrow} c^\dagger_{ib\downarrow} c_{ia\downarrow} + c^\dagger_{ia\uparrow} c_{ib\uparrow} c^\dagger_{ia\downarrow} c_{ib\downarrow} \right) \\ &+ U \sum_{ia} n_{ia\uparrow} n_{ia\downarrow} + (U-2J) \sum_{i,a\neq b} n_{ia\uparrow} n_{ib\uparrow} + (U-3J) \sum_{i\sigma,a<b} n_{ia\sigma} n_{ib\sigma}.\end{aligned} \tag{13.1}$$

1. For a broad introduction to Hund's metals, see Section 1.1.2.

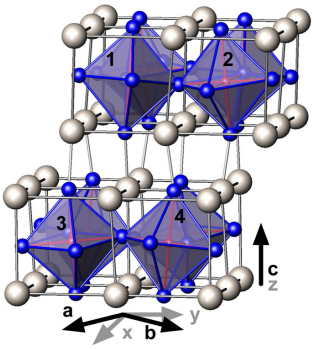

(a) Ca_2RuO_4 *Pbca* crystal structure. Pink dots denote ruthenium atoms, blue ones oxygen atoms, and white ones calcium atoms. [58]

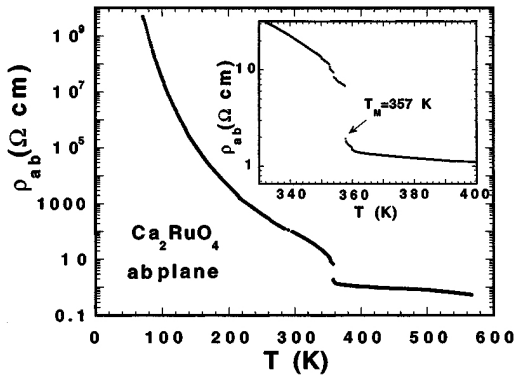

(b) Ca_2RuO_4 *ab* plane electrical resistivity as a function of temperature. *Inset:* Detail of the abrupt jump at $T_M \sim 357$K, that coincides with the structural transition between long and short octahedra. [2]

Figure 13.1

Figure 13.2 – Sketch of the effect of the structural transition on the t_{2g} orbitals in Ca_2RuO_4.

Here $a = xy, xz, yz$ denotes one of the t_{2g} orbitals, $c^\dagger_{ia\sigma}$ (resp. $c_{ia\sigma}$) creates (resp. destroys) an electron on site i, orbital a, spin σ, and $n_{ia\sigma} = c^\dagger_{ia\sigma}c_{ia\sigma}$ is the number operator. ϵ_a is the energy level of orbital a and γ_a the hopping amplitude to neighbouring sites. [2] For both *S-Pbca* and *L-Pbca* structure, the xy-bandwidth is twice as large as the xz/yz one: $4\gamma_{xy} \sim 2.6$ eV and $4\gamma_{xz/yz} \sim 1.3$ eV. $U \sim 2.3$ eV is the Coulomb repulsion and $J \sim 0.4$ eV the Hund's coupling.

Above T_M, the three t_{2g} orbitals roughly have the same energy: $\epsilon_{xy/xz/yz} = \epsilon$. Because Ru atoms have a $4d^4$ configuration, Ca_2RuO_4 is in a metallic state. As $T_M \sim T_S$, the octahedra shorten and the xy orbital is pushed to lower energy, which results is an effective crystal-field splitting $\Delta \sim 0.3$ eV with the xz/yz orbitals: $\epsilon_{xz/yz} = \epsilon$ and $\epsilon_{xy} = \epsilon - \Delta$. The xy orbital is completely filled, and the xz/yz ones are half-filled. The Coulomb repulsion and the Hund's coupling have been shown to open a gap and therefore create a Mott insulator in the material [58, 155]. This mechanism is illustrated in Fig. 13.2.

Apart from temperature, Ca_2RuO_4's insulator-to-metal transition can also be driven by a 0.5 GPa pressure at room temperature [114, 66]. Sr substitution also shows that the ground state of $Ca_{2-x}Sr_xRuO_4$ varies from a Mott insulator ($x < 0.2$) to an unconventional superconductor ($x = 2$) [98]. However, none of these techniques can be easily engineered in an electronic device.

13.2 Electric-field driven material

It has recently been discovered that the switching from an insulator to a metal can be driven by surprisingly small electric fields, and can be stably repeated at least three thousand times, opening a new realm of possible industrial applications for Ca_2RuO_4. The easiest way to create a metal from a Mott insulator using an electric field is through Zener breakdown, i.e. by applying a voltage at least as big as the energy gap. As the latter is 0.2 eV and the lattice spacing is 5.45 Å, this would lead a threshold energy $E_{\text{th}} \sim 4$MV/cm [115].

Nakamura *et al.* [115] first explored the effet of an applied electric-field on Ca_2RuO_4 at $T = 295\text{K} < T_S$. The current-voltage (IV) characteristics they obtained is presented in Fig. 13.3a. Red (resp. blue)

2. Only hoppings between orbitals of the same type are allowed.

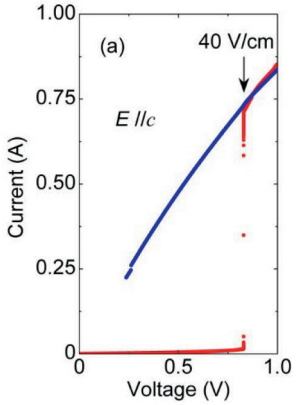

(a) IV characteristics, $T = 295$K. [115]

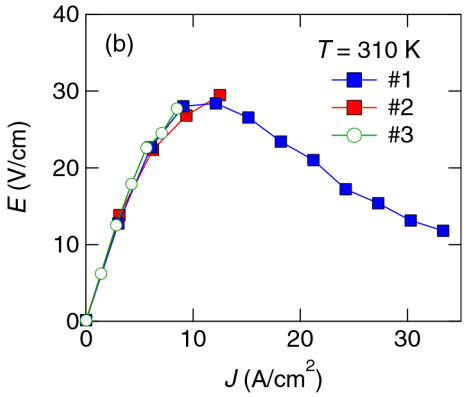

(b) Electric field E as function of current J. [122]

Figure 13.3 – Out-of-equilibrium properties of electric-field- and current-driven Ca_2RuO_4.

dots correspond to an increasing (resp. decreasing) voltage, showing a large hysteresis during the voltage sweeps. At $V \sim 0.8$V, the current jumps abruptly, signalling the switching. This corresponds to a surprisingly low value of the threshold field $E_{\text{th}} \sim 40$V/cm. X-ray diffraction measurements confirm that this switching is accompanied by a bulk first-order structural transition.

Okazaki *et al.* [122] were able to follow the unstable region of the hysteresis by inducing current instead of voltage in the material. Their results at T = 310K are presented in Fig. 13.3b, different symbols corresponding to different samples. The $E - J$ curve exhibits a peak at $E_{\text{th}} \sim 30$V/cm, which is very close to the reported value in Ref. [115]. The non-monotonous behaviour confirms an intrinsic non-linearity in Ca_2RuO_4 and shows that the current is a more appropriate control parameter.

As the metal-insulator transition is also driven by temperature, one should be careful not to induce Joule heating in the material. In Ref. [115], the authors compared the switching obtained using pulses of different lengths (10 to 100 ms), showing that the latter, and therefore the heat induced, is not a decisive factor. However, a recent study pointed out that localized heating can occur, caused by flowing currents, and lead to a misinterpretation of the electric-field induced results [103].

In order to settle this discussion, it is therefore desirable to construct a theoretical model for Ca_2RuO_4 and compute the value of the voltage one needs to apply in order to drive the insulator-to-metal transition.

13.3 Theoretical model

13.3.1 From a static electric field to a linear voltage drop

To keep notations simple, let us first consider the example of a simple 1D chain, that will naturally extend to the 3D case. An electric field is applied along the axis of the chain, $\mathbf{E} = E\mathbf{u_x}$ with $E > 0$. In the temporal gauge, the vector potential $\mathbf{A}$ and the scalar potential ϕ respectively write

$$\mathbf{A}(t) = -Et\mathbf{u_x}\,, \qquad \phi(\mathbf{x}, t) = 0. \tag{13.2}$$

The vector potential is then incorporated in the Hamiltonian as a Peierls term, a phase that modifies the hopping amplitudes [49]. Labelling $\mathcal{H}_{\text{int}}$ the interaction part of Eq. (13.1), the system subject to an electric field is thus described by the following time-dependent Hamiltonian [3]

$$\mathcal{H}_{\text{temp}}(t) = \sum_{ja\sigma} \epsilon_a n_{ja\sigma} + \mathcal{H}_{\text{int}} - \sum_{ja\sigma} \gamma_a \left(e^{iVt} c^\dagger_{j+1a\sigma} c_{ja\sigma} + \text{ h.c.} \right), \tag{13.3}$$

where $V = Es > 0$ with s the lattice spacing.

3. We add the subscript 'temp' to the Hamiltonian to specify that we work in the temporal gauge.

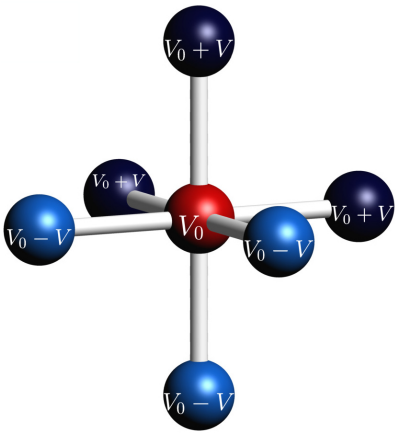

Figure 13.4 – Voltage drop in a 3D material subject to an electric-field applied along the body-diagonal direction. The central atom (red) is at voltage V_0. Its three neighbors depicted in darker blue are at $V_0 + V$, and its three neighbors in lighter blue at $V_0 - V$. [102]

The corresponding action for the system writes

$$\begin{aligned}\mathcal{S}_{\text{temp}} = &\int \sum_{ja\sigma} c^{\dagger}_{ja\sigma}(t)\left(\epsilon_a - i\partial_t\right) c_{ja\sigma}(t) + \int \mathcal{H}_{\text{int}}(c^{\dagger}_{ja\sigma}(t), c_{ja\sigma}(t)) \\ &- \int \sum_{ja\sigma} \gamma_a \left(e^{iVt} c_{j+1a\sigma}(t) c_{ja\sigma}(t) + \text{h.c.}\right).\end{aligned} \tag{13.4}$$

We now introduce the following gauge transformation

$$c_{ja\sigma} \to e^{ijVt} c_{ja\sigma}, \tag{13.5}$$

in order to rewrite the action of the system in the Coulomb gauge

$$\begin{aligned}\mathcal{S}_{\text{Coul}} = &\int \sum_{ja\sigma} c^{\dagger}_{ja\sigma}(t)\left(\epsilon_a - i\partial_t + jV\right) c_{ja\sigma}(t) + \int \mathcal{H}_{\text{int}}(c^{\dagger}_{ja\sigma}(t), c_{ja\sigma}(t)) \\ &- \int \sum_{ja\sigma} \gamma_a \left(c_{j+1a\sigma}(t) c_{ja\sigma}(t) + \text{h.c.}\right).\end{aligned} \tag{13.6}$$

When subject to a static electric field, the system is therefore equivalently described by the time-dependent Hamiltonian of Eq. (13.3) or the following time-independent Hamiltonian

$$\mathcal{H}_{\text{Coul}} = \sum_{ja\sigma} (\epsilon_a + jV) n_{ja\sigma} + \mathcal{H}_{\text{int}} - \sum_{\substack{\langle jl\rangle \\ a\sigma}} \gamma_a c^{\dagger}_{ja\sigma} c_{la\sigma}. \tag{13.7}$$

This equation simply describes the material being subject to a linear voltage drop along the x direction, where V is the voltage difference between two adjacent sites.

This construction naturally extends to the 3D case: if the electric field is applied along the body-diagonal direction (111), it will create layers of atoms with a given voltage, as depicted in Fig. 13.4. Considering an atom with voltage V_0, its (1,0,0), (0,1,0) and (0,0,1) neighbours will have voltage $V_0 + V$, while the (-1,0,0), (0,-1,0) and (0,0,-1) ones will bear voltage $V_0 - V$.

13.3.2 DMFT setup

The Hamiltonian from Eq. (13.6) describes the t_{2g} orbitals of the Ru atoms on the full lattice, in the presence of a static electric field. However, as we have already seen thoroughly through this Thesis, solving exactly the fully interacting problem is beyond what is possible with modern algorithms. We therefore

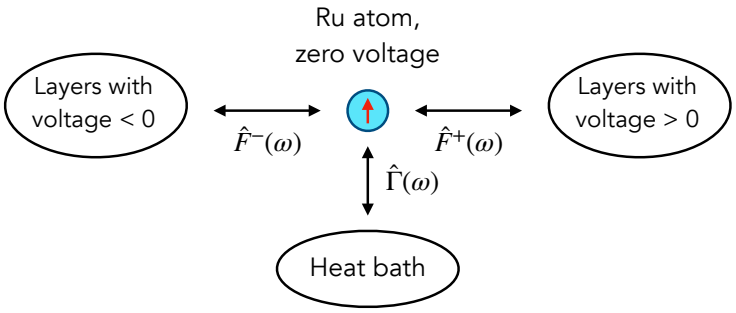

Figure 13.5 – DMFT embedding of a single Ru atom.

consider the Dynamical Mean-Field Theory (DMFT) approximation:[4] an isolated Ru atom, considered as an impurity, is self-consistently embedded into the lattice. We can formally consider that we single out an atom with voltage 0, so that the local Hamiltonian describing the energy levels and interactions of the t_{2g} orbitals is

$$\begin{aligned}\mathcal{H}_{\text{loc}} = &-\sum_{\sigma a}\epsilon_a n_{\sigma a} + U\sum_{a} n_{\uparrow a}n_{\downarrow a} + (U-2J)\sum_{a\neq b} n_{\uparrow a}n_{\uparrow b} \\ &+ (U-3J)\sum_{\sigma,a<b} n_{\sigma a}n_{\sigma a} + J\sum_{a\neq b}\left(d^\dagger_{\uparrow a}d_{\uparrow b}d^\dagger_{\downarrow b}d_{\downarrow a} + d^\dagger_{\uparrow b}d_{\uparrow b}d^\dagger_{\downarrow a}d_{\downarrow b}\right).\end{aligned} \tag{13.8}$$

Note that we write creation and annihilation operators for the orbital a, spin σ, $d^\dagger_{\sigma a}$ and $d_{\sigma a}$ as it is the usual convention in the literature for impurities. The density operator is then $n_{\sigma a} = d^\dagger_{\sigma a}d_{\sigma a}$.

The embedding of the impurity is sketched in Fig. 13.5. As there is a voltage drop in the system, we introduce two functions $\hat{F}^{+}_{\sigma a}(\omega)$ and $\hat{F}^{-}_{\sigma a}(\omega)$ that describe the hybridization of the Ru atom with layers bearing voltages respectively positive and negative. As we only allow hoppings between orbitals of the same type, see Eq. (13.1), these hybridization functions are diagonal in σ and a. We also introduce a flat heat bath $\hat{\Gamma}(\omega)$ for the system to thermalize, as the electric field brings energy to the material [11, 95, 102]

$$\Gamma^R_{\sigma a}(\omega) = -i\Gamma, \tag{13.9a}$$

$$\Gamma^K_{\sigma a}(\omega) = -2i\Gamma\tanh\left(\frac{\beta\omega}{2}\right). \tag{13.9b}$$

In the following, we consider $\Gamma = 0.1$. The full hybridization of the system then takes the form

$$\hat{\Delta}_{\sigma a}(\omega) = \hat{F}^{+}_{\sigma a}(\omega) + \hat{F}^{-}_{\sigma a}(\omega) + \hat{\Gamma}_{\sigma a}(\omega). \tag{13.10}$$

In order to close the self-consistency equations, we choose to work on a Bethe lattice. Due to its tree-like structure, we can easily assign a zero voltage to the central site, and set half of its neighbours at potential $+V$ and the other half at potential $-V$, so that the above construction stays unchanged. The hybridization functions to the positive and negative voltage layers write

$$\hat{F}^{\pm}_{\sigma a}(\omega) = \gamma_a^2\hat{G}^{\pm}_{\sigma a}(\omega), \tag{13.11}$$

where $\hat{G}^{\pm}$ is the Green's function of sites on the $\pm V$ layers (neighbours of the impurity). Such an approximation has been shown to yield physical results in Refs. [102, 126]. We also assume that the system is uniform and has reached a well-defined steady-state in the presence of current [95, 102]

$$\hat{G}^{\pm}_{\sigma a}(\omega) = \hat{G}_{\sigma a}(\omega \pm V). \tag{13.12}$$

We therefore have derived a closed set of equations in order to obtain the local Green's function of the material in the long-time limit where a steady state has settled. Provided the steady-state impurity solver we presented in Chapter 12, these equations can be solved self-consistently according to the following iterating scheme:

4. For a complete introduction to DMFT, see Chapter 2.

$$\hat{\Delta}_{\sigma a}(\omega) = \hat{\Gamma}_{\sigma a}(\omega) + \hat{F}^{+}_{\sigma a}(\omega) + \hat{F}^{-}_{\sigma a}(\omega) \longrightarrow \text{Impurity solver}$$

$$\uparrow \qquad\qquad \downarrow$$

$$\hat{F}^{\pm}_{\sigma a}(\omega) = \gamma_a^2 \hat{G}_{\sigma a}(\omega \pm V) \longleftarrow \hat{G}_{\sigma a}(\omega)$$

The electronic current per spin is derived in Appendix E.1 and writes

$$J_\sigma = \sum_a \gamma_a^2 \int \frac{\mathrm{d}\omega}{2\pi} G^{<}_{\sigma a}(\omega) \left[G^{>}_{\sigma a}(\omega + V) - G^{>}_{\sigma a}(\omega - V) \right]. \tag{13.13}$$

Equilibrium limit

At equilibrium, there is no voltage drop in the system, and no heat bath is required for thermalization. Eq. (13.10) therefore reduces to

$$\Delta_{\sigma a}(i\omega_n) = 2\gamma_a^2 G_{\sigma a}(i\omega_n) \tag{13.14}$$

The DMFT approximation is solved self-consistently according to the same iterating scheme as presented above.

13.3.3 Determining the crystal field splitting across the transition

The local Hamiltonian $\mathcal{H}_{\text{loc}}$ describing the t_{2g} orbitals on a single Ru atom, Eq. (13.8), depends explicitly on the crystal-field Δ, as $\epsilon_{xz} = \epsilon_{yz} = \epsilon_{xy} + \Delta$. The induction of voltage in Ca_2RuO_4 is expected to drive the insulator-to-metal transition and therefore reduce this splitting of the bands. In order to model this effect, we introduce the Hamiltonian of the lattice as an elastic term

$$\mathcal{H}_{\text{latt}} = \frac{k}{2} Q^2, \tag{13.15}$$

where Q is the structural mode amplitude and k its stiffness. Labelling $\hat{P}_\sigma = \hat{n}_{\sigma xy} - \frac{1}{2}\left(\hat{n}_{\sigma xz} + \hat{n}_{\sigma yz}\right)$ the polarization operator, the coupling to the electrons takes the form

$$\mathcal{H}_{\text{e-l}} = \frac{\Delta}{2} \sum_\sigma \hat{P}_\sigma[Q]. \tag{13.16}$$

We can assume the crystal field to be linearly dependent on the structure mode Q

$$\Delta = gQ, \tag{13.17}$$

where g is the electron-lattice coupling parameter. Such a linear relation has been checked using DFT calculations in various complex oxide metals [124, 55]. At equilibrium, and in the long-time limit where a steady state is established, Q is obtained by minimizing the total energy

$$kQ = \frac{g}{2} \sum_\sigma \left(\hat{P}_\sigma[Q] - \hat{P}_\sigma[Q=0] \right). \tag{13.18}$$

As $\hat{P}_\uparrow = \hat{P}_\downarrow$, this equation can be equivalently rewritten for the crystal-field splitting as

$$\hat{P}_\uparrow[\Delta] = \hat{P}_\uparrow[\Delta = 0] + \frac{k}{g^2}\Delta. \tag{13.19}$$

The constants k and g only depend on the structure of the material, and thus can be obtained from varying q in DFT calculations. We however choose in this work a heuristic determination of the k/g^2 ratio at equilibrium (see below for more details). For an induced voltage $V \neq 0$, the value of the effective crystal field is then obtained by intersecting the polarization vs Δ curve with Eq. (13.19).

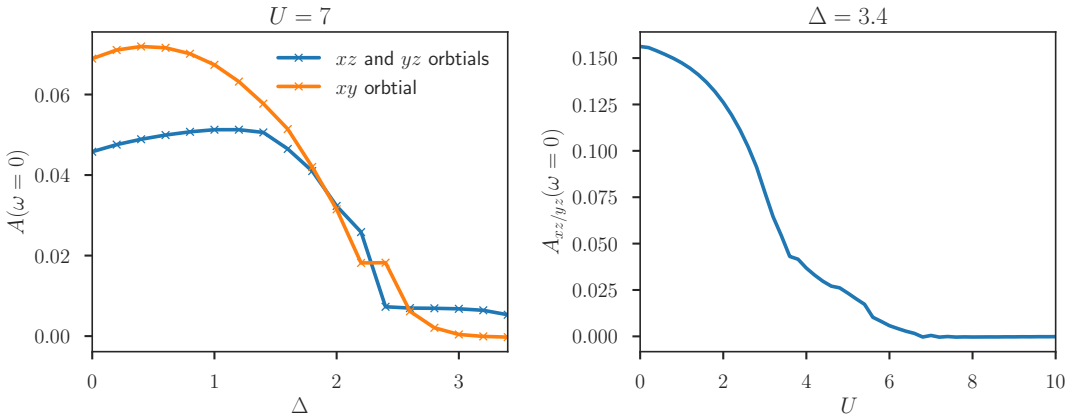

Figure 13.6 – Equilibrium zero-frequency extrapolation of the spectral function $A(\omega)$ as a function of Δ for $U = 7$ (*left*), and as a function of U for $\Delta = 3.4$ (*right*). $\beta = 10$.

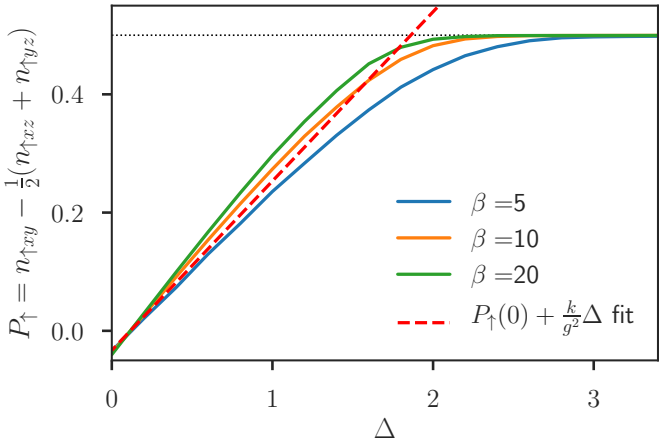

Figure 13.7 – Equilibrium evolution of the polarization for $\uparrow$ spins as a function of Δ for different temperatures. The red dashed line is the linear fit condition from Eq. (13.19). $U = 7$.

13.4 Preliminary results

13.4.1 Equilibrium

First, we choose a set of parameters in order to address the physical regime of the electric-field driven material. As emphasized in Section 13.1, the xy bandwidth is twice as large as the xz/yz ones, so that we choose $\gamma_{xz/yz} = 1$ to be our energy unit, and $\gamma_{xy} = 2$. The ratio of the Hund's coupling to the Coulomb repulsion is considered to be $J/U = 0.1$, and we place the metal-insulator transition induced by the structural change between long and short octahedra at $\beta = 10$.

At this temperature and $U = 7$, we plot in Fig. 13.6 (*left*) the evolution of spectral intensity at zero frequency as a function of crystal-field splitting for the xz and yz orbitals (blue curve) and for the xy orbital (orange curve). All three bands are metallic at $\Delta = 0$ and become insulating as Δ reaches values higher than 3. As explained in Section 13.1, the xy orbital becomes completely filled, while a Mott gap opens in the other two orbitals. To justify the latter, we plot in Fig. 13.6 (*right*) the evolution of $A_{xy/yz}(\omega = 0)$ as a function of the Coulomb repulsion for $\Delta = 3.4$. These bands have a metallic character at $U = 0$ and undergo a Mott transition with $U_c \sim 6$. Full Matsubara Green's functions are presented in Appendix E.2 for completeness.

We fix $U = 7$ as it seems to be a reasonable choice to describe the insulating system at equilibrium.

We plot in Fig. 13.7 the polarization for $\uparrow$ spins, $P_\uparrow = n_{\uparrow xy} - \frac{1}{2}(n_{\uparrow xy} + n_{\uparrow yz})$, as a function of crystal-

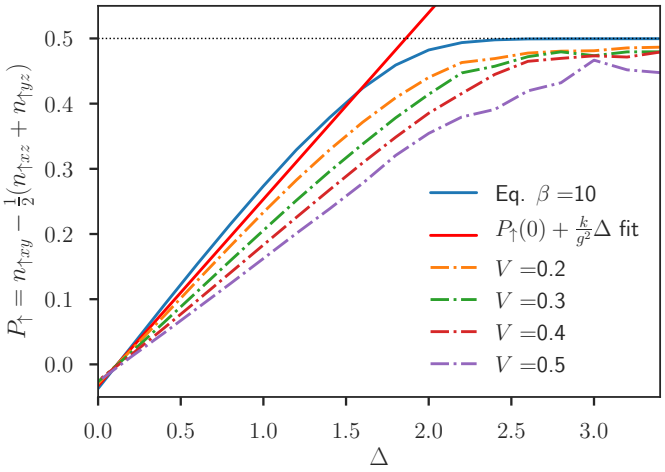

Figure 13.8 – Evolution of the polarization for $\uparrow$ spins as a function of Δ for the equilibrium and the voltage-driven system. The red dashed line is the linear fit condition from Eq. (13.19).

field splitting for $\beta = 5$ (blue), $\beta = 10$ (orange) and $\beta = 20$ (green). As mentioned above, the structural transition is considered to happen at $\beta = 10$. We therefore fit $P_\uparrow(0) + (k/g^2)\Delta$ from Eq. (13.19) between the $\beta = 5$ and 10 curves (red dashed line). It intersects the blue curve only at $\Delta = 0$, so that the system is in the long octahedra phase and is therefore a metal at $\beta = 5$. On the other hand, it intersects the orange and green curves for $\Delta \neq 0$, meaning the system has ordered in the short octahedra phase and is a metal for β higher than 10. This fit yields $k/g^2 \sim 0.29$.

Note that the equilibrium solution of Eq. (13.19) for $\beta = 10$ is $\Delta \sim 1.6$. For this value of the crystal field, the system is actually a polarized metal and not an insulator according to Fig. 13.6 (*left*). A higher value of the Coulomb repulsion should therefore be used to correctly describe the metal-insulator transition, but we keep this value for now as it has been used in the out-of-equilibrium calculations we present next.

13.4.2 Out-of-equilibrium

We now move to the study of Ca_2RuO_4 subject to a voltage difference V. The inverse temperature is set to $\beta = 10$ and the Coulomb repulsion to $U = 7$.

In Fig. 13.8 is plotted the evolution of $P_\uparrow$ as function of the crystal field for different values of the voltage V (dotted lines), together with the equilibrium solution (green) and the $P_\uparrow(0) + (k/g^2)\Delta$ fit (red line). The latter intersects all the voltage-driven curves at $\Delta = 0$, which means the out-of-equilibrium system is a metal. Applying an electric field to the insulating system drives the insulator-to-metal transition, as expected from experiments. The values of V studied are high and should be lowered. However, the steady-state NCA equations used here are hard to converge as one lowers the voltage. The support of the local states propagators $R^>(t)$ and $R^<(t)$ indeed becomes larger and, as these functions oscillate in time, this requires good precision on both their time and frequency representations.

More efficients way of solving the steady-state NCA equations therefore have to be developed in order to reach low voltages. Among the ideas under current development are a multiprocessor parallelization and the use logarithmic grids for Fourier transforms.

Part VI

Conclusions and perspectives

Chapter 14

Conclusion

In this Thesis, we have considered two complementary approaches in the development of new algorithms to study strongly correlated systems in and out of equilibrium. On the one hand, we started from experiments in realistic materials and developed methods to reproduce their emerging properties. On the other hand, we studied minimal models that we turned into pure algorithmic problems for which we searched the most efficient and accurate algorithms.

Following the first approach, photoemission data on Sr_2IrO_4 led us to identify the orbital characters of the bands located near the Fermi surface and construct an effective tight-binding model to describe them. We then used existing techniques to incorporate correlations, through a cellular extension of DMFT and a hybridization-expansion impurity solver. This allowed us to justify a strong momentum-space differentiation of the electronic structure at low doping level. The Fermi surface consists of pockets centered around $(\pi/2, \pi/2)$ while a pseudogap opens near $(\pi, 0)$. We found an excellent qualitative agreement between our results and the photoemission experiments that motivated this work. Further studies should be conducted to gain more insight on the influence of electronic correlations, as well as the elusive superconductivity of this material.

In a very different context, we got interested in the surprisingly low fields required to drive the insulator-to-metal transition in the Hund's metal Ca_2RuO_4. Reexpressing the effects of the static electric field as a linear voltage drop in the material, we presented a DMFT approximation for the nonequilibrium steady-state that settles at long times. In order to solve the quantum impurity problem, we decided to use NCA, a systematic approximation in the hybridization expansion that analytically sums a subset of diagrams. We derived the infinite-time limit of these equations and designed a solver that directly works in the steady-state regime. The preliminary results we presented for the electric-field driven metal-to-insulator transition in Ca_2RuO_4 are very promising. This project is still under current investigation.

The second approach led us to study new developments in determinant Monte Carlo algorithms for fermionic systems. At equilibrium, we presented an algorithm that allows the computation of dynamical quantities such as the self-energy of full lattice systems. We regrouped a factorial number of diagrams into an exponential sum of determinants, hence drastically reducing the fermionic sign problem. By comparing results for the two-dimensional Hubbard model with those obtained from diagrammatic Monte Carlo, we showed that we can reach higher perturbation orders and greater accuracy for the same computational effort.

Similar ideas were explored in the out-of-equilibrium version of this algorithm. We revisited the real-time diagrammatic quantum Monte Carlo algorithm in the LO basis, and showed that vacuum diagrams automatically vanish in this formalism without the need of an exponential sum. In an importance sampling procedure, we pointed out that this allows the algorithm to directly reach the steady-state limit as only interaction times in the vicinity of the measurement time contribute. Massive cancellations between LO configurations however bring a huge sign problem. We tried to reduce the overall error bar by regrouping contributions in order to optimize the sign problem, both using heuristic patterns and machine learning techniques. We were able to greatly reduce the variance, but not enough to compete with the original algorithm formulated on the Keldysh contour.

In all these diagrammatic methods, we only computed contributions to the perturbation series. The

latter tend to become divergent for large interactions as poles appear in the complex plane. An equally difficult algorithmic challenge thus consists in using resummation techniques to evaluate the series beyond its convergence radius and should be addressed next.

Despite these current limitations, new algorithms have changed the way theoreticians study strongly correlated systems. The years to come will undoubtedly bring new exciting developments that will allow us to gain a deeper understanding of the exciting phenomena taking place in these compounds. This paves the way to design new materials, such as solar cells or batteries, that will efficiently store data or energy. In a world relying more than ever on electronic devices but that should reinvent itself in the face of climate change, these developments will thus bring inventive solutions that have to be engineered hand-in-hand with the experimental teams.

Appendices

Appendix A

Appendix to Chapter 4

A.1 Green's functions and self-energy in the four doping regimes

In Fig. A.1, we show the Matsubara frequency Green's functions and self-energies in the four doping regimes discussed in the main text. These regimes are here associated with four different values of the chemical potential corresponding to the four rows of the figure.

For $\mu = 1$ eV the system is a Mott insulator, as can be seen from the insulating character of the two components of the Green's function $G_{\pm}$. Let us note that the real parts of the self-energies are very different, which is responsible for the opening of the Mott gap (see main text). Increasing the doping, we enter a pseudogap phase. At $\mu = 1.2$ eV, the even component of the Green's function has an insulating behavior while the odd one is metallic. At $\mu = 1.34$ eV, the system is in a differentiate regime. Both components of the Green's function are now metallic but the self-energies are still quite differentiated. Going to even larger dopings we finally reach the uniform Fermi liquid state. Hence at $\mu = 1.5$ eV, we see that G_+ and G_- are both metallic and that the self-energies tend to be identical.

A.2 Absence of a Mott insulator with the standard periodization scheme

The usual periodization of the self-energy writes

$$\tilde{\Sigma}^{\text{latt}}(i\omega_n, \mathbf{k}) = \begin{pmatrix} \Sigma_{AA} & \Sigma_{AB} \times f(\mathbf{k}) \\ \Sigma_{AB} \times f^*(\mathbf{k}) & \Sigma_{AA} \end{pmatrix}, \tag{A.1}$$

where

$$f(\mathbf{k}) = \frac{1}{4}\left(1 + e^{-ik_x} + e^{-ik_y} + e^{-i(k_x+k_y)}\right) \tag{A.2a}$$

$$= \cos\frac{k_x}{2}\cos\frac{k_y}{2}e^{-i\frac{k_x+k_y}{2}}. \tag{A.2b}$$

$\mathbf{k} = (k_x, k_y)$ is expressed in the reduced Brillouin zone. We see from Fig. 3.4 that the degeneracy of the $(\pi/2, \pi/2) - (\pi, 0)$ path in the full Brillouin zone has to be lifted in order to create a Mott insulating gap. However $f(\mathbf{k}) = 0$ along this path and the self-energy has the following expression

$$\tilde{\Sigma}^{\text{latt}}(i\omega_n, \mathbf{k}) = \Sigma_{AA} \times \mathbf{1}_{2\times 2}. \tag{A.3}$$

Hence the self-energy only renormalizes the chemical potential in the quasiparticle equation (Eq. (4.7)) at $\omega = 0$, forbidding any lifting of the degeneracy between the quasiparticle bands and therefore any gap in the band structure.

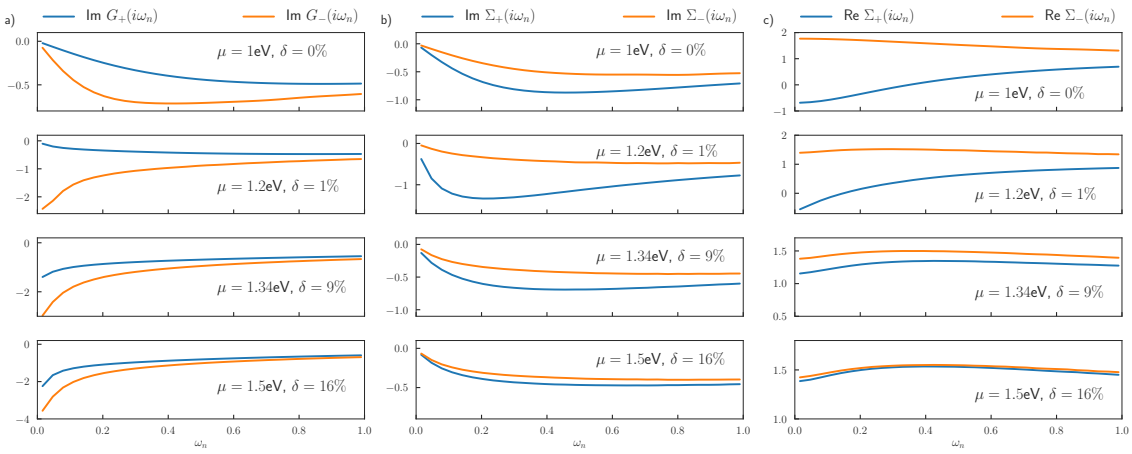

Figure A.1 – Evolution in the even - odd basis of a) the imaginary part of the Green's function $G_{\pm}(i\omega_n)$, b) the imaginary part of the self-energy $\Sigma_{\pm}(i\omega_n)$, c) the real part of $\Sigma_{\pm}(i\omega_n)$ as a function of the Matsubara frequency ω_n. On all plots, the even (odd) contribution is plotted in blue (orange).

Appendix B

Appendix to Chapter 7

B.1 Derivation of the equations of motion

Here we show that Eq. (7.3) can be obtained from the equations of motion of the Green's function. For concreteness, we consider the two-dimensional Hubbard model

$$\mathcal{H} = -t \sum_{\langle i,j\rangle\sigma} c^\dagger_{i\sigma} c_{j\sigma} + U \sum_i n_{i\uparrow} n_{i\downarrow} = \mathcal{H}_{\rm hop} + \mathcal{H}_{\rm int}, \tag{B.1}$$

where $c^\dagger_{i\sigma}$ creates a spin-σ electron on the site i of a square lattice, $t > 0$ is the nearest-neighbor hopping and U the onsite interaction. Note that the derivation below yields the same result for an interacting impurity coupled to a bath or for the Hubbard atom.

The equation of motion for the imaginary-time Green's function of two operators A and B, $G_{A,B}(\tau) = -\langle T_\tau A(\tau) B(0)\rangle$, is given by

$$\partial_\tau G_{A,B}(\tau) = -\delta(\tau)\langle\{A(\tau), B(0)\}\rangle - \langle T_\tau [\mathcal{H}, A](\tau) B(0)\rangle, \tag{B.2}$$

which, in Matsubara frequencies, writes

$$i\omega_n G_{A,B}(i\omega_n) = -G_{[\mathcal{H},A],B}(i\omega_n) + \langle\{A, B\}\rangle. \tag{B.3}$$

Let us note for later use that, by writing $G_{A,B}(\tau) = -\langle T_\tau A(0) B(-\tau)\rangle$, one obtains a similar expression that involves a commutator between the Hamiltonian and B rather than A

$$i\omega_n G_{A,B}(i\omega_n) = G_{A,[\mathcal{H},B]}(i\omega_n) + \langle\{A, B\}\rangle. \tag{B.4}$$

The equation of motion (Eq. (B.3)) for the one-particle Green's function $G^\sigma_{ij} \equiv -\langle T_\tau c_{i\sigma}(\tau) c^\dagger_{j\sigma}(0)\rangle$ is

$$i\omega_n G^\sigma_{ij} = -G_{[\mathcal{H},c_{i\sigma}],c^\dagger_{j\sigma}} + \langle\{c_{i\sigma}, c^\dagger_{j\sigma}\}\rangle. \tag{B.5}$$

Using the expression for the commutators

$$[\mathcal{H}_{\rm hop}, c_{i\sigma}] = t \sum_{\langle a,b\rangle} c_{b\sigma}\delta_{ia}, \tag{B.6a}$$

$$[\mathcal{H}_{\rm int}, c_{i\sigma}] = -U n_{i\bar\sigma} c_{i\sigma}, \tag{B.6b}$$

we find that

$$i\omega_n G^\sigma_{ij} = -t \sum_{\langle a,b\rangle} \delta_{ia} G^\sigma_{bj} + U G_{n_{i\bar\sigma}c_{i\sigma},c^\dagger_{j\sigma}} + \delta_{ij}, \tag{B.7a}$$

$$\sum_{\langle a,b\rangle} \left(i\omega_n \delta_{ib} + t\delta_{ia}\right) G^\sigma_{bj} = U G_{n_{i\bar\sigma}c_{i\sigma},c^\dagger_{j\sigma}} + \delta_{ij}. \tag{B.7b}$$

Introducing the correlator $F_{ij}^{\sigma} = UG_{n_{i\bar{\sigma}}c_{i\sigma},c_{j\sigma}^{\dagger}}$ the above equation can be rewritten in matrix form as

$$F_{\sigma} = (g_{\sigma}^{-1} - G_{\sigma}^{-1})G_{\sigma} = \Sigma_{\sigma}G_{\sigma}. \tag{B.8}$$

Note that this definition of F_{σ} is consistent with Eq. (7.10). We can now apply Eq. (B.4) to F_{ij}^{σ}

$$i\omega_n F_{ij}^{\sigma} = UG_{n_{i\bar{\sigma}}c_{i\sigma},[\mathcal{H},c_{j\sigma}^{\dagger}]} + U\left\langle\{n_{i\bar{\sigma}}c_{i\sigma}, c_{j\sigma}^{\dagger}\}\right\rangle. \tag{B.9}$$

Using the commutators

$$[\mathcal{H}_{\text{hop}}, c_{j\sigma}^{\dagger}] = -t\sum_{\langle a,b\rangle} c_{a\sigma}^{\dagger}\delta_{bj}, \tag{B.10a}$$

$$[\mathcal{H}_{\text{int}}, c_{j\sigma}^{\dagger}] = Un_{j\bar{\sigma}}c_{j\sigma}^{\dagger}, \tag{B.10b}$$

we find that

$$\sum_{\langle a,b\rangle}(i\omega_n\delta_{aj} + t\delta_{bj})\,F_{ia}^{\sigma} = U^2G_{n_{i\bar{\sigma}}c_{i\sigma},n_{j\bar{\sigma}}c_{j\sigma}^{\dagger}} + \langle n_{i\bar{\sigma}}\rangle\delta_{ij}. \tag{B.11}$$

Introducing the correlator $\bar{F}_{ij}^{\sigma} \equiv U^2G_{n_{i\bar{\sigma}}c_{i\sigma},n_{j\bar{\sigma}}c_{j\sigma}^{\dagger}}$ and the Hartree term $\Sigma_{ij}^{H,\sigma} = \langle n_{i\bar{\sigma}}\rangle\delta_{ij}$ the equation above becomes

$$F_{\sigma}g_{\sigma}^{-1} = \bar{F}_{\sigma} + \Sigma_{\sigma}^{H}. \tag{B.12}$$

Using Eq. (B.8) for F_{σ} and Dyson's equation we obtain

$$F_{\sigma}g_{\sigma}^{-1} = \Sigma_{\sigma}G_{\sigma}(G_{\sigma}^{-1} + \Sigma_{\sigma}) = \Sigma_{\sigma} + \Sigma_{\sigma}G_{\sigma}\Sigma_{\sigma}, \tag{B.13}$$

which yields the final result

$$\Sigma_{\sigma} = \Sigma_{\sigma}^{H} + \bar{F}_{\sigma} - \Sigma_{\sigma}G_{\sigma}\Sigma_{\sigma}. \tag{B.14}$$

This is the relation between the self-energy and the correlator $\bar{F}_{\sigma}$ used in Eq. (7.3). The definitions of $\bar{F}_{\sigma}$ and Σ_{σ}^{H} are respectively consistent with Eqs. (7.4) and (7.2).

B.2 Explicit cancellation of connected diagrams at order 3

Let us explicitly show the cancellation of non-self-energy diagrams in Eq. (7.9) for the specific case $V = \{x_1\}$ at order 3 in U. We start by considering

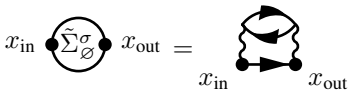

(B.15)

The first term $\bar{F}_V^{\sigma}(x_{\text{out}}, x_{\text{in}})$ in Eq. (7.9) corresponds to all connected diagrams with two external points x_{in} and x_{out} and one internal interaction vertex x_1:

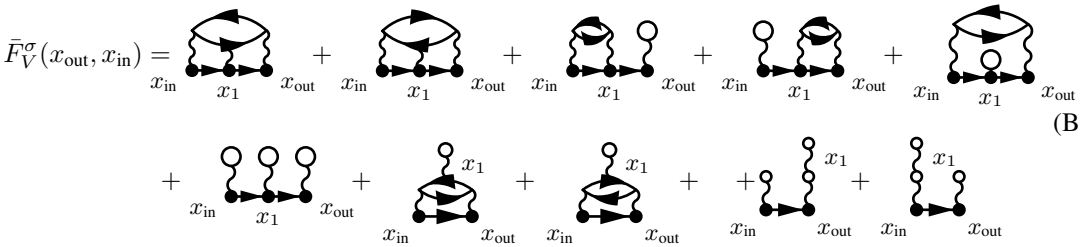

(B.16)

From this sum, we subtract the second and third terms of Eq. (7.9). The former gives

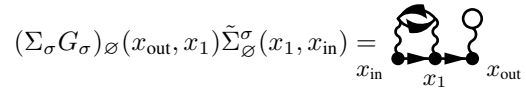

(B.17)

while the latter's contribution is the sum of

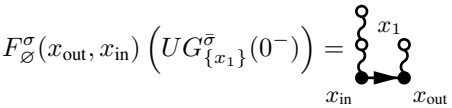

(B.18)

and of

$$F^{\sigma}_{\{t_1\}}(x_{\text{out}}, x_{\text{in}}) \left(UG^{\bar{\sigma}}_{\varnothing}(0^-)\right) =$$

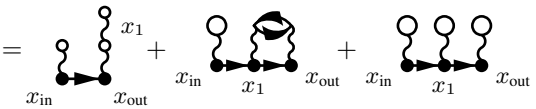

(B.19)

We see that the remaining contributions to the self-energy are only those that are one-particle irreducible.

Appendix C

Appendix to Chapter 9

C.1 Benchmark against the $\pm$ and CDet algorithms

The table below benchmarks the contributions to the density between the CDet algorithm of Chapter 6, the $\pm$ algorithm of Chapter 8, and the LO and mixed algorithms introduced in Chapter 9. We consider an energy level ϵ_d coupled to a bath described by a semi-circular density of states of bandwidth $4D$. We take D as our energy unit, and parameters are $\beta = 100$, $\gamma^2 = 0.04$, $\epsilon_d = -0.36$, $U = 1.2$, as well as a uniform α-shift $\alpha = 0.3$. Computation effort is 240 CPU*hours for each perturbation order.

	CDet	$\pm$
Order 1	$-1.7013633 \pm 5.2 \times 10^{-6}$	$-1.7013355 \pm 2.4 \times 10^{-6}$
Order 2	$14.473091 \pm 4.5 \times 10^{-5}$	$14.472669 \pm 7.4 \times 10^{-5}$
Order 3	-33.35593 ± 0.00025	-33.3544 ± 0.0022
Order 4	-431.3204 ± 0.0097	-431.304 ± 0.039
Order 5	5095.483 ± 0.094	5094.46 ± 0.82
Order 6	-16185.97 ± 0.30	-16166 ± 11
Order 7	-164346 ± 16	-164111 ± 175
Order 8	$2.22929 \times 10^6 \pm 162$	$2.2319 \times 10^6 \pm 2.0 \times 10^3$
Order 9	$-7.87625 \times 10^6 \pm 782$	$-7.850 \times 10^6 \pm 3.0 \times 10^4$

	LO	mixed
Order 1	$-1.7013405 \pm 2.9 \times 10^{-6}$	$-1.7013402 \pm 3.8 \times 10^{-6}$
Order 2	14.47295 ± 0.00020	14.47278 ± 0.00012
Order 3	-33.3462 ± 0.0077	-33.3534 ± 0.0047
Order 4	-431.17 ± 0.36	-431.271 ± 0.054
Order 5	5097 ± 10	5094.4 ± 1.1
Order 6	-16337 ± 364	-16170 ± 22
Order 7	-158102 ± 10331	-164949 ± 253
Order 8	$1.68 \times 10^6 \pm 5.0 \times 10^5$	$2.2207 \times 10^6 \pm 6.9 \times 10^4$
Order 9	EB $\simeq$ result	$-8.12 \times 10^6 \pm 1.6 \times 10^5$

Appendix D

Appendix to Chapter 11

D.1 Path-integral representation of R

Let $\mathcal{H}$ be the full Hamiltonian of the embedded system. We consider an initial coherent state of the full system $|\phi_i\rangle$ with eigenvalues $\phi_{\alpha i}$, and a final coherent state $\langle\phi_f|$ with eigenvalues $\phi^*_{\alpha f}$. Here α is a composite index that denotes all the possible operators on the impurity and in the bath. The propagator between these two states is defined at imaginary time τ as

$$\mathcal{U}_{fi}(\tau) = -\langle\phi_f|e^{-\tau\mathcal{H}}|\phi_i\rangle. \tag{D.1}$$

We want to represent $\mathcal{U}_{fi}$ as a path integral and follow here the steps of Ref. [119]. We start by breaking the integral between 0 and τ into M time steps of size $\epsilon = \tau/M$

$$\mathcal{U}_{fi}(\tau) = -\lim_{M\to\infty}\langle\phi_f|\left(e^{-\epsilon\mathcal{H}}\right)^M|\phi_i\rangle. \tag{D.2}$$

By inserting $M-1$ times the closure relation

$$1 = \prod_\alpha \mathrm{d}\phi^*_\alpha \mathrm{d}\phi_\alpha e^{-\sum_\alpha \phi^*_\alpha\phi_\alpha}|\phi\rangle\langle\phi|, \tag{D.3}$$

and labeling $\phi_0 = \phi_i$, $\phi_M = \phi_f$, we obtain

$$\mathcal{U}_{fi}(\tau) = -\lim_{M\to\infty}\left(\prod_{j=1}^{M-1}\prod_\alpha \mathrm{d}\phi^*_{\alpha j}\mathrm{d}\phi_{\alpha j}\right)e^{-\sum_{j=1}^{M-1}\sum_\alpha \phi^*_{\alpha j}\phi_{\alpha j}}\prod_{j=1}^{M}\langle\phi_j|e^{-\epsilon\mathcal{H}}|\phi_{j-1}\rangle. \tag{D.4}$$

The product of average values between two consecutive states is

$$\prod_{j=1}^{M}\langle\phi_j|e^{-\epsilon\mathcal{H}}|\phi_{j-1}\rangle = \exp\left(\sum_{j=1}^{M}\left[\sum_\alpha \phi^*_{\alpha j}\phi_{\alpha j-1} - \epsilon\mathcal{H}(\phi^*_{\alpha j},\phi_{\alpha j-1})\right]\right). \tag{D.5}$$

The set $\{\phi_{\alpha 0},\ldots,\phi_{\alpha M}\}$ is now represented by a trajectory $\phi_\alpha(\tau)$ and we introduce

$$\phi^*_{\alpha j}\frac{(\phi_{\alpha j}-\phi_{\alpha j-1})}{\epsilon} = \phi^*_\alpha(\tau)\partial_\tau\phi_\alpha(\tau), \tag{D.6a}$$

$$\mathcal{H}(\phi^*_{\alpha j},\phi_{\alpha j-1}) = \mathcal{H}(\phi^*_\alpha(\tau),\phi_\alpha(\tau)). \tag{D.6b}$$

The propagator $\mathcal{U}$ now takes the well-known form of a path-integral

$$\begin{aligned}\mathcal{U}_{fi}(\tau) = -\int_{\phi_\alpha(0)=\phi_\alpha i}^{\phi^*_\alpha(\tau)=\phi^*_{\alpha f}}\mathcal{D}\left[\phi^*_\alpha(\tau'),\phi_\alpha(\tau')\right]e^{\sum_\alpha \phi^*_\alpha(\tau)\phi_\alpha(\tau)}\\ \times\exp\left(\int_0^\tau \mathrm{d}\tau'\left[\sum_\alpha \phi^*_\alpha(\tau')\partial_{\tau'}\phi_\alpha(\tau') - \mathcal{H}\left(\phi^*_\alpha(\tau'),\phi_\alpha(\tau')\right)\right]\right),\end{aligned} \tag{D.7}$$

where

$$\int_{\phi_\alpha(0)}^{\phi_\alpha(\tau)} \mathcal{D}\left[\phi_\alpha^*(\tau'),\phi_\alpha(\tau')\right] = \lim_{M\to\infty} \int \prod_{j=1}^{M-1}\prod_{\alpha} \mathrm{d}\phi_{\alpha j}^* \mathrm{d}\phi_{\alpha j}. \tag{D.8}$$

In order to specify the local propagator for impurity states, we write explicitly $\mathcal{H}$ as

$$\mathcal{H} = \mathcal{H}_{\text{loc}} + \sum_{\mathbf{k}a}\left(\Gamma_{\mathbf{k}a} c_{\mathbf{k}a}^\dagger d_a + \text{ h.c.}\right) + \sum_{\mathbf{k}a} \epsilon_{\mathbf{k}a} c_{\mathbf{k}a}^\dagger c_{\mathbf{k}a}, \tag{D.9}$$

where $\mathcal{H}_{\text{loc}}$ is the local Hamiltonian of the impurity, $d_a^\dagger$ (resp. d_a) the creation (resp. annihilation) operator on the impurity, a being a composite index encoding the different degrees of freedom. $c_{\mathbf{k}a}^\dagger$ (resp. $c_{\mathbf{k}a}$) creates (resp. annihilates) an electron in the bath with momentum $\mathbf{k}$, and $\Gamma_{\mathbf{k}a}$ is a hopping amplitude between the impurity and the bath. In this formalism, the hybridization function takes the form

$$\Delta_a(i\omega_n) = \sum_{\mathbf{k}} \frac{|\Gamma_{\mathbf{k}a}|^2}{i\omega_n - \epsilon_{\mathbf{k}a}}. \tag{D.10}$$

We can now rewrite Eq. (D.7) by separating the Grassmann variables for the c and the d operators. We are interested in the propagator R_{fi} between two coherent states of the impurity, that we label $|\Phi_i\rangle$, with eigenvalues Φ_{ai}, and $\langle\Phi_f|$, with eigenvalues Φ_{af}^*. Identifying Grassmann variables with the corresponding operators, the propagator has the following path-integral representation

$$\begin{aligned} R_{fi}(\tau) = -\int_{d_a(0)=\Phi_{ai}}^{d_a^\dagger(\tau)=\Phi_{af}^*} & \mathcal{D}\left[d_a^\dagger(\tau'),d_a(\tau')\right] e^{\sum_a d_a^\dagger(\tau)d_a(\tau)} \\ & \times \exp\left(\int_0^\tau \mathrm{d}\tau' \left[\sum_a d_a^\dagger(\tau')\partial_\tau' d_a(\tau') - \mathcal{H}_{\text{loc}}(d_a^\dagger(\tau'),d_a(\tau'))\right]\right) \\ \times \int_{c_{\mathbf{k}a}(0)=-c_{\mathbf{k}a}(\tau)} & \mathcal{D}\left[c_{\mathbf{k}a}^\dagger(\tau'),c_{\mathbf{k}a}\right] \exp\left(\int_0^\tau \mathrm{d}\tau' \sum_{\mathbf{k}a}\left[c_{\mathbf{k}a}^\dagger(\tau')\partial_{\tau'} c_{\mathbf{k}a}(\tau')\right.\right. \\ & \left.\left. -(\Gamma_{\mathbf{k}a} c_{\mathbf{k}a}^\dagger(\tau') d_a(\tau') + \text{ h.c.}) - \epsilon_{\mathbf{k}a} c_{\mathbf{k}a}^\dagger(\tau') c_{\mathbf{k}a}(\tau')\right]\right) \end{aligned} \tag{D.11}$$

Integrating out the c variables yields

$$\begin{aligned} R_{fi}(\tau) = -\int_{d_a(0)=\Phi_{ai}}^{d_a^\dagger(\tau)=\Phi_{af}^*} & \mathcal{D}\left[d_a^\dagger(\tau'),d_a(\tau')\right] e^{\sum_a d_a^\dagger(\tau)d_a(\tau)} \\ & \times \exp\left(\int_0^\tau \mathrm{d}\tau' \left[\sum_a d_a^\dagger(\tau')\partial_\tau' d_a(\tau') - \mathcal{H}_{\text{loc}}(d_a^\dagger(\tau'),c_a(\tau'))\right]\right. \\ & \left. - \int_0^\tau \mathrm{d}\tau' \mathrm{d}\bar\tau \sum_a d_a^\dagger(\tau')\Delta_a(\tau'-\bar\tau) d_a(\bar\tau)\right) \end{aligned} \tag{D.12}$$

This path-integral expression for matrix elements motivates the expression of R as a time ordered-exponential of operators, Eq. (11.4).

Appendix E

Appendix to Chapter 13

E.1 Current computation

The electronic current per spin is defined as [106]

$$J_\sigma = \frac{i}{2}\sum_a \gamma_a \left[\langle d^\dagger_{\sigma a} c_{+\sigma a}\rangle - \langle c^\dagger_{+\sigma a} d_{\sigma a}\rangle + \langle c^\dagger_{-\sigma a} d_{\sigma a}\rangle - \langle d^\dagger_{\sigma a} c_{-\sigma a}\rangle\right], \tag{E.1}$$

where $c^\dagger_{\pm\sigma a}$ (resp. $c_{\pm\sigma a}$) is the creation (resp. annihilation) operator on the layer with voltage $\pm V$. We introduce the Green's functions

$$G^<_{d\to\pm,\sigma a}(t-t') = i\langle c^\dagger_{\pm\sigma a}(t) d_{\sigma a}(t')\rangle, \tag{E.2a}$$
$$G^<_{\pm\to d,\sigma a}(t-t') = i\langle d^\dagger_{\sigma a}(t) c_{\pm\sigma a}(t')\rangle. \tag{E.2b}$$

These are related to the impurity and the nonzero voltage layers through [106, 95]

$$\begin{aligned} G^<_{d\to\pm,\sigma a}(\omega) &= \gamma_a \left[\left(\hat{G}^\pm_{\sigma a}\right)^< (\omega) G^{++}_{\sigma a}(\omega) - \left(\hat{G}^\pm_{\sigma a}\right)^{--} (\omega) G^<_{\sigma a}(\omega)\right] \\ &= \gamma_a \left[G^<_{\sigma a}(\omega \pm V) G^{++}_{\sigma a}(\omega) - G^{--}_{\sigma a}(\omega \pm V) G^<_{\sigma a}(\omega)\right], \end{aligned} \tag{E.3}$$

$$\begin{aligned} G^<_{\pm\to d,\sigma a}(\omega) &= \gamma_a \left[\left(\hat{G}^\pm_{\sigma a}\right)^{++} (\omega) G^<_{\sigma a}(\omega) - \left(\hat{G}^\pm_{\sigma a}\right)^< (\omega) G^{--}_{\sigma a}(\omega)\right] \\ &= \gamma_a \left[G^{++}_{\sigma a}(\omega \pm V) G^<_{\sigma a}(\omega) - G^<_{\sigma a}(\omega \pm V) G^{--}_{\sigma a}(\omega)\right], \end{aligned} \tag{E.4}$$

where we used Eq. (13.12). Replacing these expressions in Eq. (E.1), one finally obtains

$$J_\sigma = \sum_a \gamma_a^2 \int \frac{\mathrm{d}\omega}{2\pi} G^<_{\sigma a}(\omega) \left[G^>_{\sigma a}(\omega + V) - G^>_{\sigma a}(\omega - V)\right]. \tag{E.5}$$

E.2 Equilibrium Green's functions

We plot in Fig. E.1 equilibrium Green's function at $\beta = 10$ and $U = 7$ for different values of the crystal-field Δ. We see a clear metal-to-insulator transition as the latter is increased.

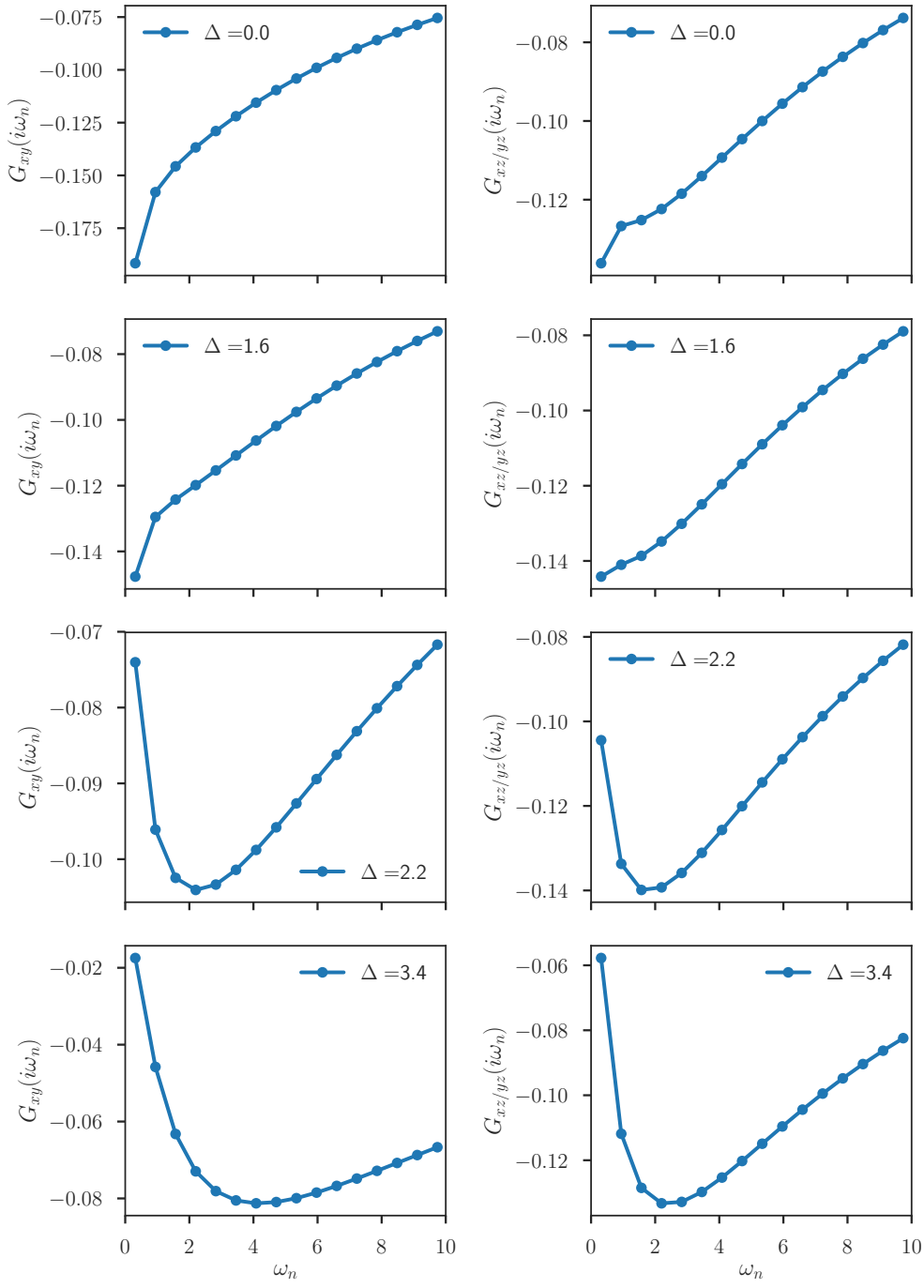

Figure E.1 – Ca_2RuO_4 equilibrium Green's functions using DMFT approximation coupled to a NCA solver for the xy orbital (*left*) and the xz/yz orbitals (*right*). $\beta = 10$, $U = 7$.

Part VII

Peer-reviewed papers

Pseudogap and electronic structure of electron-doped Sr_2IrO_4

Alice Moutenet,[1,2] Antoine Georges,[1,2,3,4] and Michel Ferrero[1,2]
[1]*Centre de Physique Théorique, École Polytechnique, CNRS, Université Paris-Saclay, 91128 Palaiseau, France*
[2]*Collège de France, 11 place Marcelin Berthelot, 75005 Paris, France*
[3]*Center for Computational Quantum Physics, Flatiron Institute, 162 Fifth Avenue, New York, New York 10010, USA*
[4]*Department of Quantum Matter Physics, University of Geneva, 24 Quai Ernest-Ansermet, 1211 Geneva 4, Switzerland*

(Received 26 January 2018; published 5 April 2018)

We present a theoretical investigation of the effects of correlations on the electronic structure of the Mott insulator Sr_2IrO_4 upon electron doping. A rapid collapse of the Mott gap upon doping is found, and the electronic structure displays a strong momentum-space differentiation at low doping level: The Fermi surface consists of pockets centered around $(\pi/2,\pi/2)$, while a pseudogap opens near $(\pi,0)$. Its physical origin is shown to be related to short-range spin correlations. The pseudogap closes upon increasing doping, but a differentiated regime characterized by a modulation of the spectral intensity along the Fermi surface persists to higher doping levels. These results, obtained within the cellular dynamical mean-field-theory framework, are discussed in comparison to recent photoemission experiments and an overall good agreement is found.

DOI: 10.1103/PhysRevB.97.155109

I. INTRODUCTION

Understanding the physical mechanism responsible for the pseudogap in cuprate superconductors, and its interplay with superconductivity, is still a central and very debated question in the field of strongly correlated materials. In this respect, the Sr_2IrO_4 iridate is a very interesting playground as it closely resembles these materials. It is indeed isostructural to La_2CuO_4 [1] and its low-energy electronic structure is well described by a single half-filled band because of strong spin-orbit (SO) coupling, as shown by electronic structure calculations in the local density approximation (LDA) [2,3]. Angular resolved photoemission spectroscopy (ARPES), optical spectroscopy, and resonant inelastic x-ray scattering experiments [2,4–7] as well as scanning tunneling microscopy [8] demonstrate that the ground state of this material is a Mott insulator. This conclusion is also supported by electronic structure calculations taking into account electronic correlations [3,9]. The similarity between the low-energy electronic structure of Sr_2IrO_4 and that of cuprates has led to the quest for superconductivity upon doping in this material [10–13].

The electronic configuration of the Ir^{4+} ions is $\{Xe\}f^{14}5d^5$ and Sr_2IrO_4 crystallizes in the K_2NiF_4 tetragonal structure, as La_2CuO_4 or Sr_2RhO_4 [1]. The IrO_6 octahedra are rotated about the c axis by $\sim$11 deg, generating a doubled unit cell [14]. The $5d^5$ electronic configuration would naively lead to a metallic state in a band theory approach. Sr_2RhO_4, having an identical atomic arrangement with nearly the same lattice constants and bond angles, is indeed found to be a Fermi-liquid metal [15]. Sr_2IrO_4, however, has a very strong SO coupling, a property which was shown to modify the electronic structure near the Fermi level in $5d$ systems [3,9,16–18]. This compound then effectively reduces to a half-filled $j_{\text{eff}} = 1/2$ single band near the Fermi surface, a configuration which makes it prone to the opening of a Mott gap as a result of repulsive interactions.

As the noninteracting Fermi surface of this material is electronlike, the hole-doped regime of high-Tc cuprates is to be compared with the electron-doped one of Sr_2IrO_4. Several experimental groups performed ARPES measurements on Sr_2IrO_4 to investigate the doped compound further [5–7,19]. Spectral intensity at the Fermi surface exhibits a strong momentum differentiation leading to the appearance of pockets in the "nodal" region located around $(\pi/2,\pi/2)$ [5,19], while the ARPES spectra in the "antinodal" region around $(\pi,0)$ are suggestive of a pseudogap [5]. Note that the nodal/antinodal terminology is inherited from the cuprate context and does not refer to the nodes of a superconducting gap—currently, no unambiguous evidence of superconductivity has been established.

In this paper, we construct a theoretical model of the low-energy electronic structure of doped Sr_2IrO_4, treating electronic correlation effects in the framework of cellular dynamical mean-field theory (CDMFT) [20,21]. The Fermi-surface spectral intensity maps displayed in Fig. 1 summarize key aspects of our results. Four successive doping regimes are found: The Mott-insulating state (not displayed in Fig. 1) evolves into a metal with strong nodal-antinodal differentiation at low doping. In this regime, the Fermi surface consists of pockets around $(\pi/2,\pi/2)$ [Figs. 1(a) and 1(b)], while the antinodal region displays a pseudogap, as shown below. Increasing doping further, spectral intensity appears near the antinodes, still with a pronounced differentiation [Fig. 1(c)]. A full Fermi surface, close to the uniform noninteracting one, is recovered at higher doping [Fig. 1(d)].

Previous theoretical studies addressed the issue of nodal-antinodal differentiation in this material. Reference [22] discussed the formation of nodal pockets but could not study the pseudogap due to the limitation of the slave-boson method. Reference [23] described the formation of the pseudogap as a phenomenon associated with long-range antiferromagnetic fluctuations using the fluctuation exchange approximation. The present work is able to capture both phenomena in a strongly-correlated regime dominated by short-range correlations.

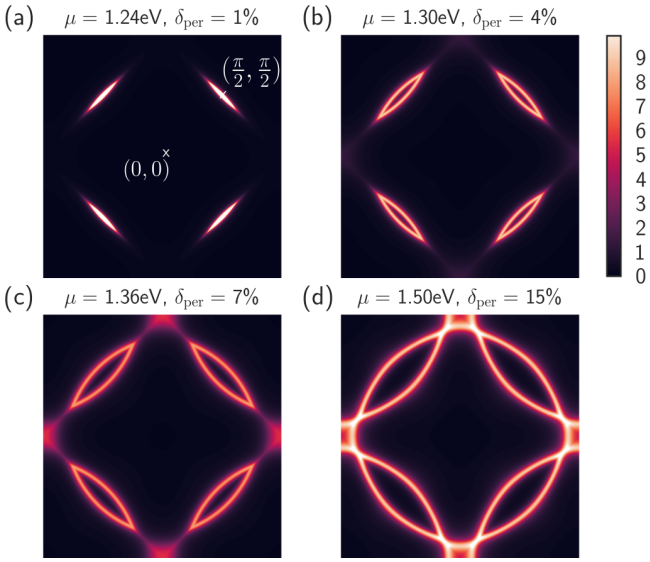

FIG. 1. Spectral intensity at the Fermi surface illustrating the evolution of the electronic structure upon increasing doping level, as described in the text. At low doping, the Fermi surface only consists of pockets near $(\pi/2,\pi/2)$ and a pseudogap is found near the antinodes. Results are obtained within CDMFT and a periodized self-energy for $U = 2$ eV at $T = 58$ K.

This paper is organized as follows. In Sec. II, we briefly summarize the tight-binding (TB) model of the electronic structure established in previous works and derive an effective model for the $j_{\rm eff} = 1/2$ states. In Sec. III, we introduce correlations in this model and explain how to deal with these within the CDMFT scheme. We discuss results of such CDMFT calculations in Sec. IV and particularly the emergence of the four doping regimes sketched above. In order to restore translational symmetry which is broken in CDMFT, we introduce a periodization scheme for the self-energy in Sec. V. This allows for a calculation of the spectral intensities, which are found to be in good agreement with the existing ARPES measurements. We also discuss the spectral signatures of the antinodal pseudogap. In Sec. VI, we compute and discuss the quasiparticle band structure. Section VII is devoted to a discussion and concluding remarks.

II. TIGHT-BINDING MODEL

In this section, we describe the electronic band structure of Sr_2IrO_4, derive an effective model for the $j_{\rm eff} = 1/2$ states, and emphasize that the low-energy states can be described by a single-band tight-binding model defined on a periodic lattice with a single atom per unit cell.

Our starting point is the tight-binding (TB) model introduced in Refs. [24,25] describing t_{2g} bands in the presence of spin-orbit coupling. Because of the rotation of the IrO_6 octahedra around the c axis, the Sr_2IrO_4 unit cell is composed of two inequivalent sites A and B. The tight-binding Hamiltonian is then written as

$$\mathcal{H}_0 = \sum_{\mathbf{k}\in \mathrm{RBZ}} \psi^\dagger_{\mathbf{k}} H_0(\mathbf{k}) \psi_{\mathbf{k}}, \tag{1}$$

where the momentum sum is over the $\sqrt{2}\times\sqrt{2}$ reduced Brillouin zone and the components of $\psi_{\mathbf{k}}$ are the electron annihilation operators for all 12 orbitals in the unit cell, $\{c_{\mathbf{k}\tau\alpha\sigma} | \tau = A,B; \alpha = d_{xy},d_{yz},d_{zx}; \sigma = \uparrow,\downarrow\}$. It is convenient to order the basis according to $(c_{Ad_{xy}\uparrow}, c_{Ad_{yz}\downarrow}, c_{Ad_{zx}\downarrow}, [A \leftrightarrow B])$ followed by their time-reversed partners ($[\uparrow\leftrightarrow\downarrow]$). There is no coupling between these two blocks as the system is time-reversal invariant and we can thus only consider the first half of the basis, taking into account that all bands are twofold degenerate. The remaining 6×6 tight-binding matrix H_0 is written as

$$H_0(\mathbf{k}) = \begin{pmatrix} O(\mathbf{k}) & P(\mathbf{k}) \\ P^\dagger(\mathbf{k}) & O(\mathbf{k}) \end{pmatrix}, \tag{2}$$

where P describes the hopping part of the Hamiltonian,

$$P(\mathbf{k}) = e^{-i\frac{k_x+k_y}{2}} \begin{pmatrix} -4t_1(\mathbf{k}) & 0 & 0 \\ 0 & -2t_2(\mathbf{k}) & 0 \\ 0 & 0 & -2t_3(\mathbf{k}) \end{pmatrix}, \tag{3}$$

with $t_1(\mathbf{k}) = t_0 \cos\frac{k_x}{2}\cos\frac{k_y}{2}$, $t_2(\mathbf{k}) = t_0\cos\frac{k_x+k_y}{2}$, and $t_3(\mathbf{k}) = t_0\cos\frac{k_x-k_y}{2}$. Here, $\mathbf{k} = (k_x,k_y)$ is expressed in terms of the reciprocal vectors forming the reduced Brillouin zone. O describes the on-site part of the Hamiltonian. It includes the spin-orbit coupling $\lambda\,\mathbf{L}_i\cdot\mathbf{S}_i$ and reads

$$O(\mathbf{k}) = \begin{pmatrix} \Delta_t + e_1(t_1(\mathbf{k})/t_0)^2 & \lambda/2 & -i\lambda/2 \\ \lambda/2 & 0 & -i\lambda/2 \\ i\lambda/2 & i\lambda/2 & 0 \end{pmatrix}, \tag{4}$$

where Δ_t is an on-site energy difference of the d_{xy} orbital relative to d_{yz} and d_{zx}, and λ is the spin-orbit coupling parameter. The additional term $e_1(t_1/t_0)^2$ accounts for the hybridization between d_{xy} and $d_{x^2-y^2}$ [24]. In the following, we consider $\Delta_t = 0.15$ eV, $t_0 = 0.35$ eV, $e_1 = -1.5$ eV, and $\lambda = 0.57$ eV. It has been shown that these values yield a band structure in good agreement with LDA+SO calculations [5,24].

We plot in Fig. 2 (upper panel) the six bands resulting from the diagonalization of $H_0(\mathbf{k})$ along the $(0,0)-(\pi/2,\pi/2)-(\pi,0)-(0,0)$ path of the full Brillouin zone. When the eigenvalues are projected on the $j_{\rm eff} = 1/2$ states,

$$\left| j_{\rm eff} = \frac{1}{2}, \pm\frac{1}{2} \right\rangle = \mp\frac{1}{\sqrt{3}}[|d_{xy},\pm\rangle \pm (|d_{yz}\rangle,\mp) \pm i|d_{zx},\mp\rangle)], \tag{5}$$

it can be seen that the low-energy bands essentially have $j_{\rm eff} = 1/2$ character, as highlighted in Refs. [2,5,24,25]. It is therefore natural to look for an effective reduced 2×2 Hamiltonian describing these states.

To do so, we rewrite H_0 in the following basis $(|\frac{1}{2},\frac{1}{2}\rangle_A$, $|\frac{1}{2},\frac{1}{2}\rangle_B$, $|\frac{3}{2},\frac{1}{2}\rangle_A$, $|\frac{3}{2},\frac{1}{2}\rangle_B$, $|\frac{3}{2},\frac{-3}{2}\rangle_A$, $|\frac{3}{2},\frac{-3}{2}\rangle_B)$:

$$H_0(\mathbf{k}) = \begin{pmatrix} H_{1/2}(\mathbf{k}) & M(\mathbf{k}) \\ M^\dagger(\mathbf{k}) & H_{3/2}(\mathbf{k}) \end{pmatrix}, \tag{6}$$

where the exact expressions of $H_{1/2}$, M, and $H_{3/2}$ are given in Appendix A. An effective Hamiltonian is then obtained by projecting H_0 onto the $j_{\rm eff} = 1/2$ subspace,

$$H^{\rm eff}_{1/2}(\mathbf{k}) = H_{1/2}(\mathbf{k}) + M(\mathbf{k})[E\times \mathbf{1}_{4\times 4} - H_{3/2}(\mathbf{k})]^{-1} M^\dagger(\mathbf{k}), \tag{7}$$

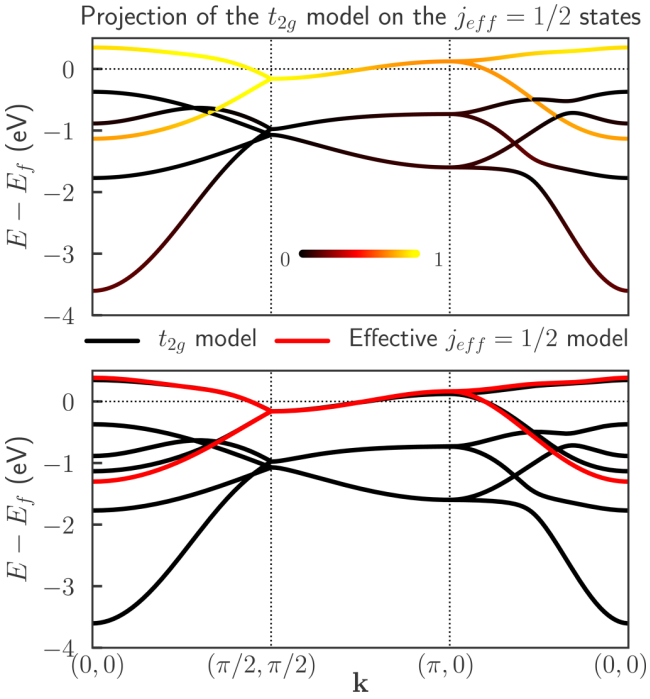

FIG. 2. Upper panel: Projection of the tight-binding model for the t_{2g} bands [Eq. (2)] on the $j_{\rm eff} = 1/2$ states. The value of the projection ranges from 0 (black) to 1 (yellow). Lower panel: Comparison between the full t_{2g} model (black lines) and the effective $j_{\rm eff} = 1/2$ model from Eq. (7) (red lines) with $E = 0$. On both panels, bands are plotted in reciprocal space, along the (0,0)-(π/2,π/2)-(π,0)-(0,0) path of the full Brillouin zone. $\Delta_t = 0.15$ eV, $t_0 = 0.35$ eV, $e_1 = -1.5$ eV, and $\lambda = 0.57$ eV.

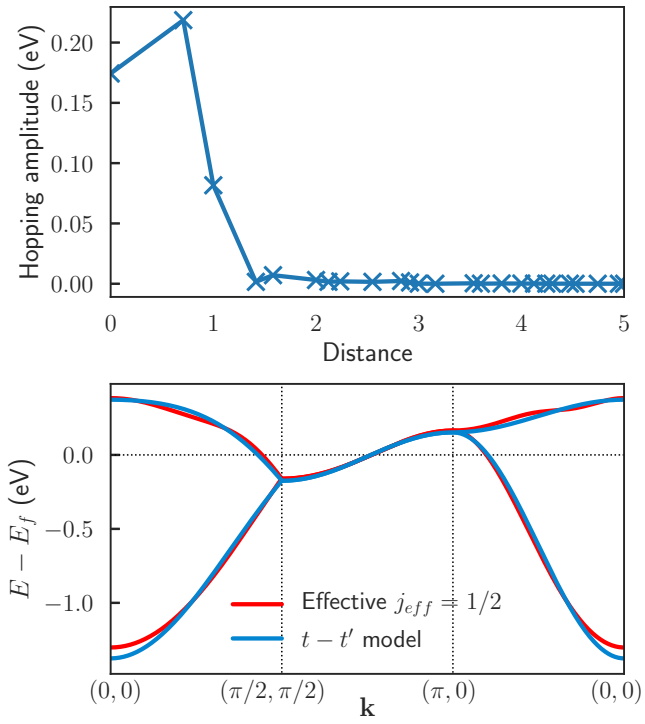

FIG. 3. Upper panel: Real-space hopping amplitudes of the effective $j_{\rm eff} = 1/2$ Hamiltonian with respect to the distance (the intersite distance is normalized to 1). Lower panel: Comparison between the effective $j_{\rm eff} = 1/2$ bands (red) with $E = 0$ and the folded dispersion obtained by keeping only the nearest- and next-nearest-neighbor hopping terms ($t = -0.219$ eV and $t' = -0.082$ eV, respectively). Bands are plotted in reciprocal space, along the (0,0)-(π/2,π/2)-(π,0)-(0,0) path of the full Brillouin zone. $\Delta_t = 0.15$ eV, $t_0 = 0.35$ eV, $e_1 = -1.5$ eV, and $\lambda = 0.57$ eV.

where $\mathbf{1}_{4\times4}$ is the 4×4 unit matrix and E is an energy scale that is adjusted in order to best match the original band structure.

While it is difficult to have a compact expression for this reduced Hamiltonian, one can easily diagonalize $H^{\rm eff}_{1/2}$ numerically for every $\mathbf{k}$ point of interest. This is shown (red lines) in Fig. 2 (lower panel) together with the complete t_{2g} band structure (black lines). The effective model appears to be in excellent agreement with the two low-energy bands exhibiting a $j_{\rm eff} = 1/2$ character.

As mentioned earlier, the Sr_2IrO_4 crystal has a two-atom unit cell and we expressed the tight-binding models above in the reduced Brillouin zone in order to make contact with experiments. Let us, however, emphasize that all sites are actually equivalent from a purely electronic point of view in these models. An inspection of the band structure in the reduced Brillouin zone indeed reveals that it results from the folding of half as many bands defined over the full Brillouin zone. This can be seen, e.g., from the degeneracy of the bands along the $(\pi/2,\pi/2) - (\pi,0)$ path of the full Brillouin zone. As a result, the effective model in Eq. (7) can be written as a simple tight-binding model on a square lattice,

$$\mathcal{H}^{\rm TB}_{1/2} = \sum_{ij} t_{ij} c^\dagger_i c_j, \tag{8}$$

where the hopping amplitudes t_{ij} are shown as a function of the distance $|i - j|$ in Fig. 3 (upper panel). We see that one obtains a good approximation of the band structure by only keeping the nearest- and next-nearest-neighbor hopping terms (for an almost perfect agreement, it is necessary to keep eight hopping parameters). This yields the simple energy dispersion:

$$\epsilon(\mathbf{k}) = \epsilon_0 + 2t(\cos k_x + \cos k_y) + 4t' \cos k_x \cos k_y, \tag{9}$$

where $\epsilon_0 = -0.174$ eV, $t = -0.219$ eV, $t' = -0.082$ eV, and $\mathbf{k} = (k_x,k_y)$ is now expressed in the basis of the *full* Brillouin zone. The folding of this band in the reduced Brillouin zone is shown together with the effective $j_{\rm eff} = 1/2$ band structure previously derived in Fig. 3 (lower panel). Let us mention that a similar tight-binding model was derived in Ref. [26] with the difference that the $d_{x^2-y^2}$ admixture was not included in their work.

In the following, we use the effective Hamiltonian derived in Eq. (7) $\mathcal{H}^{\rm eff}_{1/2} = \sum_{\mathbf{k}} H^{\rm eff}_{1/2}(\mathbf{k})$ to describe the low-energy excitations of the system.

III. INTRODUCING CORRELATIONS

We model the effect of electronic correlations in Sr_2IrO_4 with a Hubbard Hamiltonian that introduces an energy cost for having two electrons on the same Ir atom,

$$\mathcal{H} = \mathcal{H}^{\rm eff}_{1/2} + U \sum_{i,\tau} n_{i\tau\uparrow} n_{i\tau\downarrow}, \tag{10}$$

where $n_{i\tau\sigma}$ is the occupation number on the $j_z = \sigma$ orbital of the Ir atom $\tau = A,B$ in the unit cell i. In the following, we

use $U = 2$ eV [5,24] and a temperature $T = 1/\beta = 1/200$ eV $\simeq 58$ K. This model is studied using cellular dynamical mean-field theory [20,21]: The original lattice Hamiltonian (10) is mapped on a two-site auxiliary cluster model embedded in a self-consistent medium. The self-energy of the cluster model $\Sigma_{\tau,\tau'}$ is used to construct an approximation of the lattice self-energy where only intra-unit-cell components are nonvanishing, i.e., $\Sigma^{\rm latt}_{i\tau,i\tau'} = \Sigma_{\tau,\tau'}$. Note that the orbitals at sites A and B are electronically equivalent and therefore $\Sigma_{AA} = \Sigma_{BB}$ and $\Sigma_{AB} = \Sigma_{BA}$. We then have the following expression for the lattice Green's function:

$$\hat{G}^{\rm latt}(i\omega_n,\mathbf{k}) = \left\{(i\omega_n+\mu)\mathbf{1} - H^{\rm eff}_{1/2}(\mathbf{k}) - \hat{\Sigma}(i\omega_n)\right\}^{-1}, \quad (11)$$

where $\mathbf{k}$ is defined in the reduced Brillouin zone and both $\hat{G}^{\rm latt}$ and $\hat{\Sigma}$ are 2×2 matrices associated with the two Ir atoms in the unit cell. The CDMFT self-consistency imposes that the cluster Green's function $\hat{G}$ be the same as the unit-cell Green's function of the lattice,

$$\hat{G}(i\omega_n) = \sum_{\mathbf{k}\in \rm RBZ} \left\{(i\omega_n+\mu)\mathbf{1} - H^{\rm eff}_{1/2}(\mathbf{k}) - \hat{\Sigma}(i\omega_n)\right\}^{-1}. \quad (12)$$

We use a continuous-time hybridization-expansion-based quantum Monte Carlo impurity solver (CT-HYB) [27–30] to find the solution of the two-site cluster model, and the self-consistent equation (12) is solved iteratively [21]. More details are given in Appendix C. Codes necessary for the numerical calculations were developed using the TRIQS [31] library.

IV. THE FOUR DOPING REGIMES

We first investigate the cluster quantities $\hat{G}$ and $\hat{\Sigma}$ obtained by solving the CDMFT equations. These quantities can be expressed in the basis $\{|\frac{1}{2},\frac{1}{2}\rangle_A, |\frac{1}{2},\frac{1}{2}\rangle_B\}$ of the $j_{\rm eff} = 1/2$ orbitals on sites A and B. However, because A and B are electronically equivalent, it is convenient to work in the basis $\{|+\rangle,|-\rangle\}$ of even and odd combinations of the $j_{\rm eff} = 1/2$ orbitals, defined by

$$|\pm\rangle = \frac{1}{\sqrt{2}}\left(\left|\frac{1}{2},\frac{1}{2}\right\rangle_A \pm \left|\frac{1}{2},\frac{1}{2}\right\rangle_B\right). \quad (13)$$

In this basis, both $\hat{G}$ and $\hat{\Sigma}$ are diagonal (see Appendix C),

$$\hat{G} = \begin{pmatrix} G_+ & 0 \\ 0 & G_- \end{pmatrix}, \quad \hat{\Sigma} = \begin{pmatrix} \Sigma_+ & 0 \\ 0 & \Sigma_- \end{pmatrix}. \quad (14)$$

As we will discuss later, $G_\pm$ and $\Sigma_\pm$ have a direct physical interpretation. The physics close to the node $(\pi/2,\pi/2)$ is indeed essentially controlled by G_- and Σ_-, while the physics at the antinode $(\pi,0)$ is controlled by G_+ and Σ_+. The reason for this, anticipating Sec. VI and Fig. 10, is that the nodal Fermi-surface pocket at $(\pi/2,\pi/2)$ is associated with the upper band (which has an antibonding/odd character), while the nodal states are associated with the lower bonding band with even character. The analysis of these quantities will reveal the existence of four distinct regimes upon doping: a Mott-insulator phase, a pseudogap regime, a differentiation region, and, finally, a uniform Fermi-liquid state.

The electronic density n is shown as a function of the chemical potential μ in Fig. 4 (blue curve). It displays a clear plateau at $n = 1$ for μ between 0.56 and 1.16 eV, confirming

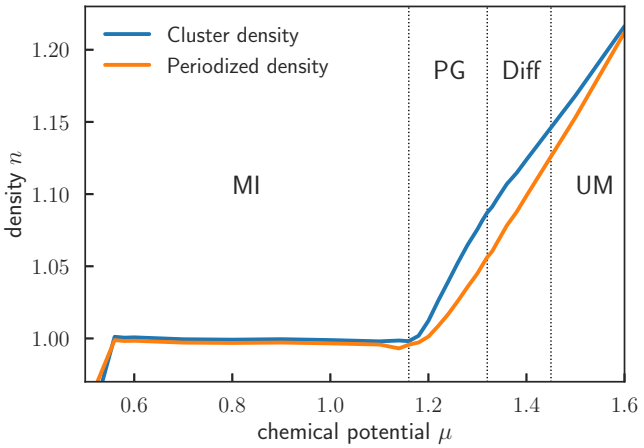

FIG. 4. Density of states as a function of the chemical potential μ. The cluster density is plotted in blue, while the periodized one is plotted in orange. Dotted lines separate the four doping regimes: below $\mu = 1.16$ eV is the Mott-insulating phase (MI), between $\mu = 1.16$ and $\mu = 1.32$ eV is the pseudogap regime (PG), between $\mu = 1.32$ and $\mu = 1.45$ eV is the differentiation region (Diff), and above $\mu = 1.45$ eV is the uniform metal (UM). Results are obtained with a two-site CDMFT calculation for $U = 2$ eV, $T = 58$ K.

that the system is a Mott insulator at half filling [2,3,9]. The width of the plateau, $\simeq$0.6 eV, is consistent with the recent experiment of Ref. [6].

Figures 5 and 6 display the spectral intensities $A_\pm(\omega = 0)$ at the Fermi level as well as the zero-frequency self-energies $\Sigma_\pm(\omega = 0)$ as a function of the chemical potential μ. These quantities are obtained by extrapolating to zero Matsubara frequency results obtained by Monte Carlo:

$$A_\pm(0) = -\frac{1}{\pi}\lim_{i\omega_n\to 0} {\rm Im}G_\pm(i\omega_n), \quad (15)$$

$$\Sigma_\pm(0) = \lim_{i\omega_n\to 0} \Sigma_\pm(i\omega_n). \quad (16)$$

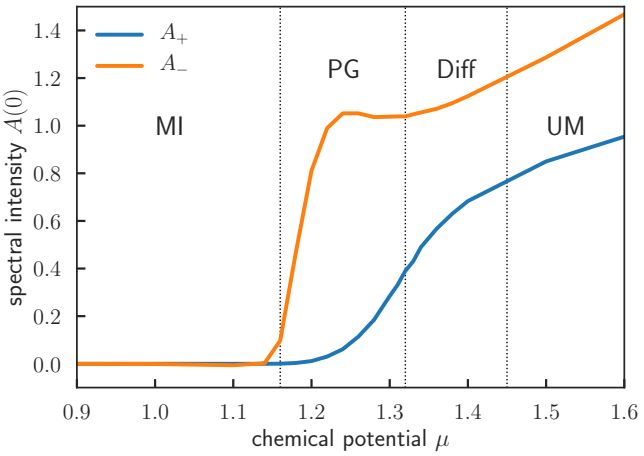

FIG. 5. Spectral intensity at the Fermi level $A(0)$ as a function of the chemical potential μ. The even (odd) contribution is plotted in blue (orange). Dotted lines separate the four doping regimes (see Fig. 4). Results are obtained with a two-site CDMFT calculation for $U = 2$ eV, $T = 58$ K.

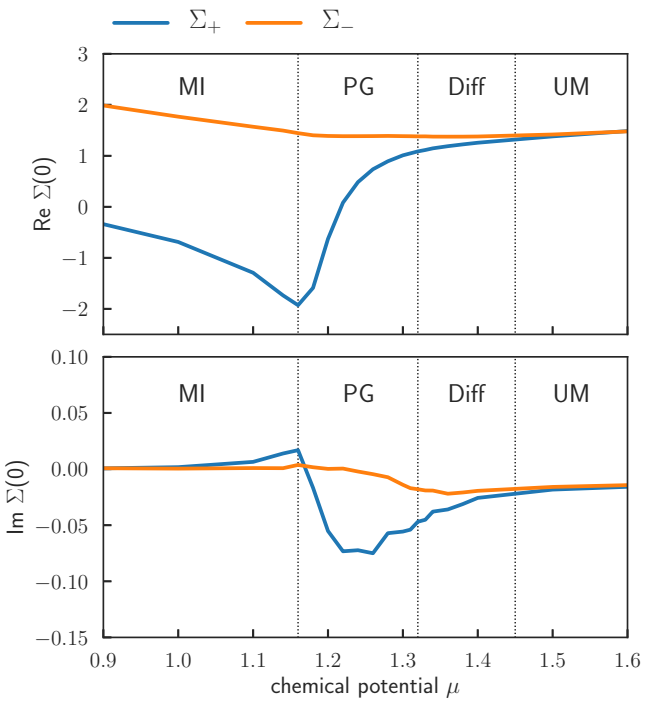

FIG. 6. Extrapolation at zero frequency of the real part (upper panel) and imaginary part (lower panel) of the self-energy $\Sigma(i\omega_n)$ as a function of the chemical potential μ. The even (odd) contribution is plotted in blue (orange). Dotted lines separate the four doping regimes (see Fig. 4). Results are obtained with a two-site CDMFT calculation for $U = 2$ eV, $T = 58$ K.

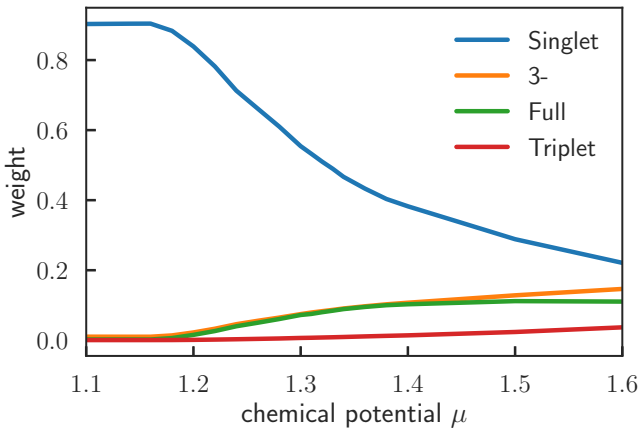

FIG. 7. Statistical weights of states dominating the Monte Carlo sampling on the dimer cluster of the CDMFT approach, as a function of the chemical potential μ. The dominant state is found to be the two-electron intersite singlet (blue). As doping level is increased, the three-electron odd-parity state catches up, denoted here as 3− (orange), as well as the fully occupied state (green), while the two-electron triplet state (red) has a smaller weight. Other contributions are negligible.

For completeness, we have included plots of the Matsubara frequency Green's functions and self-energies for several chemical potentials in Appendix B.

These results allow one to identify four distinct doping regimes. For chemical potentials smaller than $\mu = 1.16$ eV, the system is in a Mott-insulating regime and both the even (+) and odd (−) components of the spectral intensity at the Fermi level are zero, $A_{\pm}(0) = 0$ (also both Matsubara Green's functions $G_{\pm}(i\omega_n)$ have clear insulating character; see Appendix B). This is compatible with the location of the Mott plateau in Fig. 4. Correlation effects are especially visible in the very different values of the real parts of the self-energies, while both imaginary parts vanish. As a result, the effective low-energy band structure is split by the real parts of the self-energy in Eq. (12) and no excitations exist at $\omega = 0$. More precisely, the quasiparticle equation

$$\det\left\{(\omega+\mu)\mathbf{1} - H^{\text{eff}}_{1/2}(\mathbf{k}) - \hat{\Sigma}(\omega)\right\} = 0 \qquad (17)$$

has no solutions at $\omega = 0$ for all values of $\mathbf{k}$.

When μ lies between 1.16 and 1.32 eV, we enter a *pseudogap* regime. The even component of the Green's function, which provides a coarse-grained picture of the physics close to the antinode $\mathbf{k} = (\pi,0)$, maintains its insulating character ($A_+(0) = 0$), while the odd component, describing the nodal region close to $\mathbf{k} = (\pi/2,\pi/2)$, becomes metallic ($A_-(0) \neq 0$). This describes a metal that only has coherent quasiparticles close to the node. Antinodal particles are suppressed by lifetime effects, as can be seen from the more negative imaginary part of the even self-energy $\mathrm{Im}\Sigma_+(0)$ reaching -0.1 eV in Fig. 6, while $\mathrm{Im}\Sigma_-(0)$ remains very small. We show below that the spectral function exhibits a pseudogap at $\mathbf{k} = (\pi,0)$ in this region. This regime is very reminiscent of the pseudogap region of cuprate superconductors.

As the electron doping is further increased, for $1.32 \leqslant \mu \leqslant 1.45$ eV, spectral weight starts appearing in $A_+(0)$, an indication that quasiparticles start forming at the antinode as well. However, there are still visible differences between the even and odd components of the self-energies (see also Appendix B). The regime is therefore characterized by a visible $\mathbf{k}$-space differentiation where lifetime effects are stronger at the antinode than at the node [$\mathrm{Im}\Sigma_+(0) < \mathrm{Im}\Sigma_-(0)$], but do not completely destroy quasiparticles.

Eventually, for μ above 1.45 eV, a uniform metallic regime settles where both self-energies are identical and $\mathbf{k}$-space differentiation has disappeared. This regime would be well described by a single-site dynamical mean-field theory (DMFT) calculation.

It should be emphasized that boundaries delimiting these different regimes correspond to crossovers and hence are defined here in a qualitative manner.

The physical mechanism responsible for the formation of the pseudogap and the strong nodal-antinodal dichotomy observed at low doping can be revealed by studying the many-body states associated with the two-site cluster. Calculating these states' histogram, we identify those that contribute most to the stochastic sampling within the CT-HYB quantum impurity solver. This is shown in Fig. 7, from which it is clear that the system is dominated by the intradimer singlet state at low-doping levels. This is a strong indication that physics in this regime is governed by the formation of short-range antiferromagnetic correlations between neighboring sites.

V. FERMI SURFACE AND PSEUDOGAP

We now turn to the study of the fermiology of the system. Within CDMFT, the lattice Green's function given by Eq. (11) breaks translational symmetry [20], hence making a direct comparison to momentum-resolved ARPES experiments difficult. The reason for the symmetry breaking is that the lattice self-energy in CDMFT only has components inside a unit cell, but not between different unit cells. A natural way to restore the translational symmetry is to *periodize* the self-energy by propagating the intersite contribution Σ_{AB} over all links on the lattice. However, an artifact of this periodization scheme is that it prevents the formation of a Mott insulator and gives a wrong description of the low-doping physics (see Appendix D for more details). We therefore design a different periodization that yields much more physical results and preserves the existence of the Mott insulator. In this scheme, the lattice self-energy is given by

$$\tilde{\Sigma}^{\text{latt}}(i\omega_n,\mathbf{k}) = \begin{pmatrix} \Sigma_{AA} & \Sigma_{AB} \times e^{-i\frac{k_1+k_2}{2}} \\ \Sigma_{AB} \times e^{i\frac{k_1+k_2}{2}} & \Sigma_{AA} \end{pmatrix}, \quad (18)$$

where $\mathbf{k} = (k_1,k_2)$ is expressed in the reduced Brillouin zone. With this self-energy, we then define a periodized lattice Green's function $\tilde{G}^{\text{latt}}$ according to

$$\tilde{G}^{\text{latt}}(i\omega_n,\mathbf{k}) = \left\{ i\omega_n + \mu - H^{\text{eff}}_{1/2}(\mathbf{k}) - \tilde{\Sigma}^{\text{latt}}(i\omega_n,\mathbf{k}) \right\}^{-1}. \quad (19)$$

This Green's function preserves all the symmetries of the lattice and will be the basis of our analysis below.

As a consistency check, we first compute in Fig. 4 the electronic density n as a function of μ obtained from $\tilde{G}$ (orange curve). Comparing it to the cluster density (blue curve) discussed in Sec. IV, we see that plateaus at $n = 1$ match well, confirming the existence of a Mott insulator within our periodization scheme. However, the periodized density generally has slightly lower values compared to the cluster density for a given chemical potential. In the following, we discuss our results for specific values of μ and thus indicate two corresponding values of the electron doping: the cluster and the periodized one (δ_{cluster} and δ_{per}, respectively).

We plot in Fig. 1 the spectral intensity at the Fermi surface for four values of the chemical potential. At small doping levels, for $\mu \leqslant 1.30$ eV, nodal pockets with coherent quasiparticles develop, while the antinodal intensity is completely suppressed. For these values of μ, we are in the pseudogap regime discussed above. A closer inspection of the spectral function at $\mathbf{k} = (\pi,0)$ for $\mu = 1.30$ eV indeed confirms the presence of a clear pseudogap: Fig. 8 shows the leading edge of the spectrum being shifted away from zero energy. As discussed above, we attribute its formation to short-range antiferromagnetic correlations (manifested here as the dominance of intersite singlet dimer formation in our cluster, as revealed by the histogram of states).

As the electron doping is increased, the $(\pi/2,\pi/2)$ pockets grow and spectral intensity starts to appear around $(\pi,0)$ [see Fig. 1(c)], leading to an extension of the Fermi surface over the Brillouin zone. Quasiparticles are, however, far more incoherent and broader at the antinode, as can be seen from

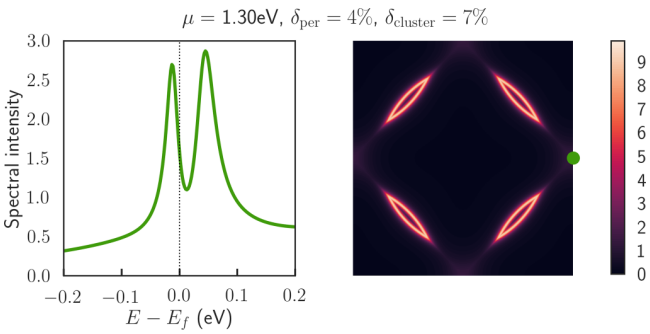

FIG. 8. Left panel: Spectral intensity $\text{Tr}A(\omega,\mathbf{k}_{\text{AN}})$ [energy distribution curve (EDC)] at the antinode $\mathbf{k}_{\text{AN}} = (\pi,0)$ for $\mu = 1.3$ eV. Right panel: Spectral intensity at the Fermi surface with a periodized self-energy for the same μ. $U = 2$ eV, $T = 58$ K.

momentum cuts across the node or the antinode (Fig. 9). While sharp coherent quasiparticles are found at the node, those at the antinode display a lower spectral intensity that is broadened over a greater region of $\mathbf{k}$ space. This corresponds to the momentum-differentiation regime introduced above.

At larger doping, the self-energy finally becomes uniform and the resulting Fermi surface displays coherent quasiparticles both at the node and the antinode, as shown in Fig. 1(d).

VI. ELECTRONIC BAND STRUCTURE

We now turn to an analysis of the dispersion of quasiparticle bands in Sr_2IrO_4. This requires one to analytically continue the imaginary-frequency data to the real axis. We use Padé approximants [32] to find $\tilde{\Sigma}^{\text{latt}}(\omega,\mathbf{k})$ from the knowledge of the periodized lattice self-energy $\tilde{\Sigma}^{\text{latt}}(i\omega_n,\mathbf{k})$. The resulting band structure is shown in Fig. 10 where we compare the insulating state at $\mu = 0.8$ eV [Figs. 10(a) and 10(c)] and the electron doped state at $\mu = 1.36$ eV, $\delta_{\text{per}} = 7\%$, $\delta_{\text{cluster}} = 10\%$ [Figs. 10(b) and 10(d)]. In Figs. 10(a) and 10(b), we show the noninteracting bands obtained by diagonalizing the TB+SO Hamiltonian $H^{\text{eff}}_{1/2}$ (dashed lines) and the quasiparticle bands

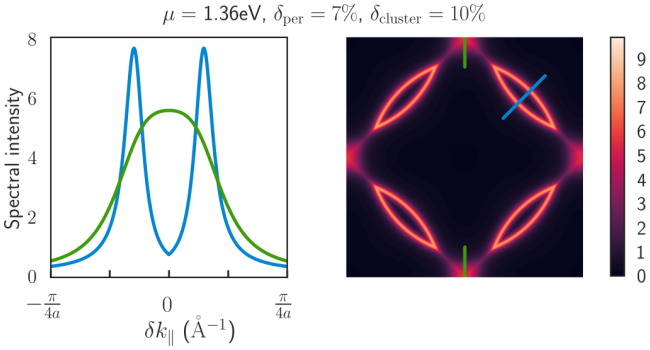

FIG. 9. Left panel: Spectral intensity at the Fermi surface $\text{Tr}A(\omega = 0,\mathbf{k})$ [momentum distribution curve (MDC)] for $\mu = 1.36$ eV taken along the nodal (blue) and the antinodal (green) directions. Corresponding cuts are shown with the same color code on the right panel. Right panel: Spectral intensity at the Fermi surface with a periodized self-energy for the same μ. $U = 2$ eV, $T = 58$ K.

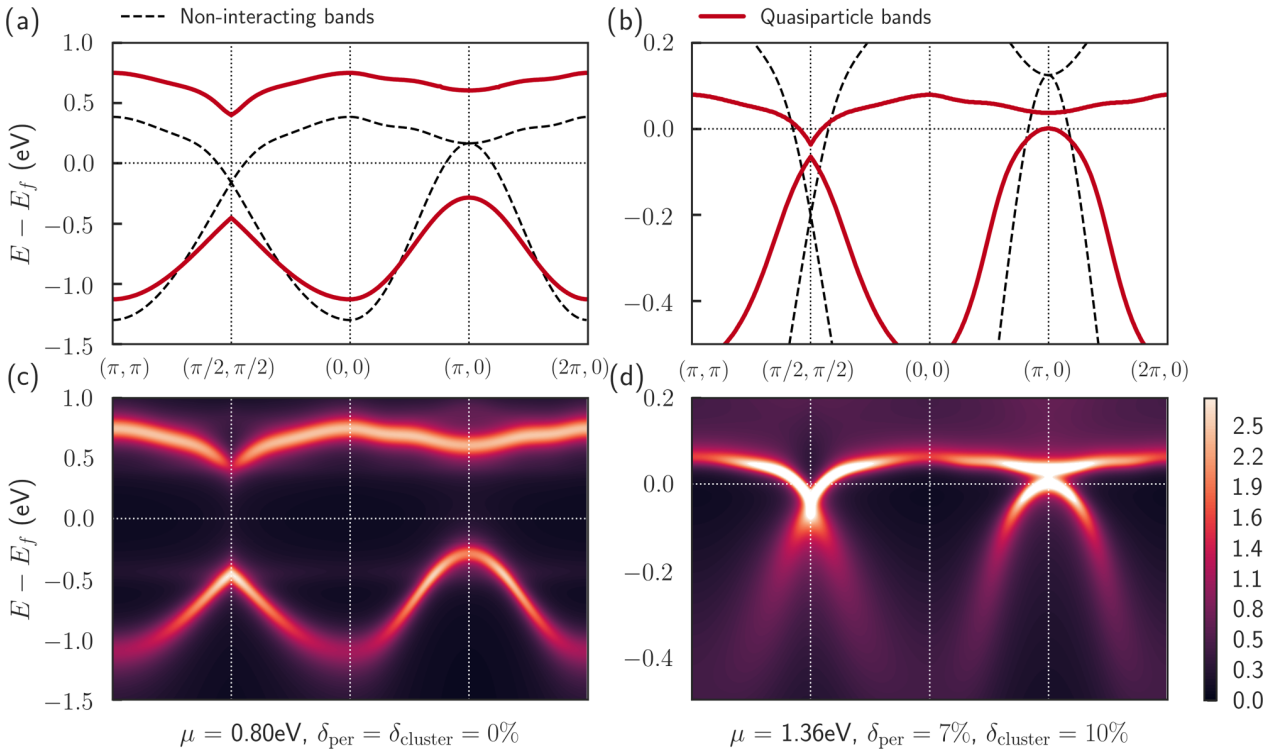

FIG. 10. Band dispersion of the (a),(c) insulating ($\mu = 0.8$ eV) and (b),(d) doped ($\mu = 1.36$ eV) Sr_2IrO_4. Periodized self-energies are analytically continued from Padé approximants. Upper panels: Comparison between the noninteracting bands obtained from the TB+SO Hamiltonian $H^{\rm eff}_{1/2}$ (dashed lines) and the quasiparticle bands. Lower panels: Spectral intensities, generalizing Fig. 1 away from the Fermi surface. All panels follow the (π,π)-$(\pi/2,\pi/2)$-(0,0)-$(\pi,0)$-$(2\pi,0)$ path in the full Brillouin zone. $U = 2$ eV, $T = 58$ K.

obtained from the solutions of

$$\det\left\{(\omega+\mu)\mathbf{1} - H^{\rm eff}_{1/2}(\mathbf{k}) - \tilde{\Sigma}^{\rm latt}(\omega,\mathbf{k})\right\} = 0. \qquad (20)$$

Bands are plotted along the (π,π)-$(\pi/2,\pi/2)$-(0,0)-$(\pi,0)$-$(2\pi,0)$ path of the full Brillouin zone. Figures 10(c) and 10(d) display the corresponding total spectral intensity, $\mathrm{Tr}\hat{A}(\omega,\mathbf{k})$.

In the insulating region, the Mott gap is clearly visible. The band structure indicates that correlation effects have split the original noninteracting bands. This is compatible with the observation that at $\mu = 0.8$ eV, the cluster self-energies take very different values, $\mathrm{Re}\Sigma_+(0) \neq \mathrm{Re}\Sigma_-(0)$. Lifetime effects are also not very strong and the bands are fairly coherent, consistent with the fact that $\mathrm{Im}\Sigma_\pm(0) \simeq 0$. The top of the lower band is located at $\simeq -0.4$ eV at the node and at $\simeq -0.2$ eV at the antinode. There is a direct gap to the unoccupied states of the order of 0.8 eV at $\mathbf{k} = (\pi/2,\pi/2)$, while the smallest overall gap is indirect and of the order of 0.6 eV. Note that the latter value is consistent with the width of the Mott plateau in Fig. 4.

As we move to the doped region, the Mott gap first closes at the nodal point $\mathbf{k} = (\pi/2,\pi/2)$ and the quasiparticle bands merge. The crossing of the upper band at two points close to $(\pi/2,\pi/2)$ is a signature of the pocket seen in the previous spectral intensities. Around these points, a clear renormalization of the Fermi velocities by a factor 1/4 is visible as compared to the noninteracting bands. For $\mu = 1.36$ eV, there is still a gap between the bands at $\mathbf{k} = (\pi,0)$, but the lower band just reaches the Fermi level yielding some antinodal spectral weight. It is interesting to note that the correlation effects are much stronger on the lower band than on the upper band. Quasiparticles are then better defined at $(\pi/2,\pi/2)$ (where they correspond to a crossing of the upper band) than at $(\pi,0)$ (where they are associated with the lower band). This is explained by the fact that the physics of the lower band is mainly controlled by the cluster self-energy Σ_+, while the upper band is controlled by Σ_-. As a result, the larger negative imaginary part of Σ_+ (see Fig. 6) induces stronger lifetime effects at the antinode,

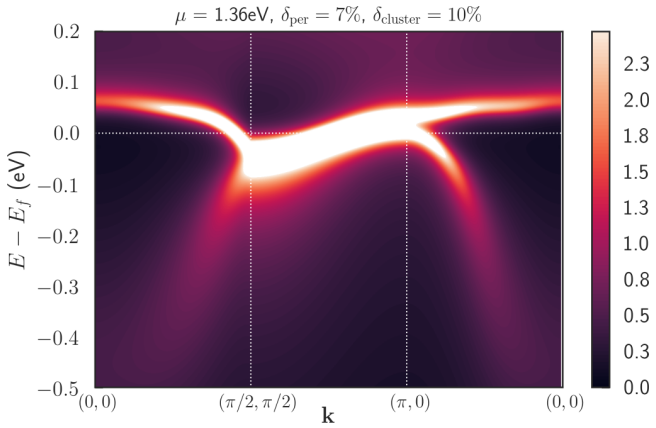

FIG. 11. Spectral intensity of the doped compound ($\mu = 1.36$ eV) along the degenerate path (0,0)-$(\pi/2,\pi/2)$-$(\pi,0)$-(0,0) in the full Brillouin zone. Periodized self-energies are analytically continued from Padé approximants. $U = 2$ eV, $T = 58$ K.

while the smaller imaginary part of Σ_- maintains coherent quasiparticles at the node.

We finally display in Fig. 11 a spectral intensity map along the $(\pi/2,\pi/2)-(\pi,0)$ Brillouin zone path, which corresponds to the path along which the noninteracting bands are degenerate. ARPES data along this path have not appeared in print to our knowledge, and our results could be useful in the context of future analysis of ARPES experiments.

VII. DISCUSSION AND CONCLUSIONS

Finally, we discuss the comparison of our results with ARPES and other experiments on doped Sr_2IrO_4.

Overall, there is excellent qualitative agreement. Comparing Figs. 10(a) and 10(b), a clear "collapse" of the Mott gap is found upon doping the insulator (i.e., the two bands become much closer to each other). This effect was reported in ARPES experiments [5,6]: It is clearly apparent, for example, in Figs. 2(g) and 2(h) of Ref. [5] in which the top of the band at $(\pi/2,\pi/2)$ moves from about -0.4 eV to about -0.1 eV (band crossing) upon doping. In fact, the location of the top of the band at the "node" (-0.4 eV) and "antinode" (-0.2 eV) is in good quantitative agreement with the values reported in Ref. [5]. The rather round and spread behavior of the band at the node quite agrees with the experiments even if the nodal part does not appear to be as narrow as it is observed.

The nodal-antinodal differentiation and formation of a pseudogap near the antinode is also consistent with the experimental observations [5,19]. Here, we have shown that the physical origin of the pseudogap is indeed the same as in cuprate superconductors, namely, short-range spin correlations (see, e.g., Refs. [33,34] for recent theoretical studies).

The value of the interaction parameter $U = 2$ eV for which we chose to perform our calculations should also be discussed in the context of experimental measurements, especially of experimental determinations of the Mott gap. With this value, we find a Mott gap which is indirect and of the order of $\sim$0.6 eV—corresponding to the transition between the top of the lower Hubbard band at $(\pi,0)$ and the bottom of the upper Hubbard band at $(\pi/2,\pi/2)$ in Fig. 10(a), and also to the width of the Mott plateau in Fig. 4. The value of the optical gap would be slightly larger. In Ref. [6], Sr_2IrO_4 was studied under both hole (Rh) and electron (La) doping, allowing for a determination of a Mott gap of the order of 0.7 eV, in rather good agreement with the present work. Optical spectroscopy measurements (see, e.g., Fig. 4 in Ref. [2]) do reveal a sharp increase of absorption in that frequency range, but a rather slow onset of the optical conductivity is observed with spectral weight below this scale, possibly suggesting a significantly smaller value of the actual gap (although a precise determination is difficult). This suggests that the value of U used in the present work may be a bit too large. Accordingly, we note that the Fermi-surface renormalizations obtained above appear to be somewhat larger than the values reported in Ref. [5].

An *ab initio* determination of the screened U appropriate for the low-energy model used here, as well as a more systematic study of this model as a function of U, would be desirable in future work. In connection with the latter, a study of the possible superconducting instability as a function of U can be performed within cluster extensions of DMFT [CDMFT or dynamical cluster approximation (DCA)] for the present model and would shed light on the elusive superconductivity of doped Sr_2IrO_4.

ACKNOWLEDGMENTS

We are grateful to Felix Baumberger, Alberto de la Torre, Sara Ricco, and Anna Tamai for sharing with us their experimental results and for numerous discussions. We also acknowledge discussions with Luca Perfetti, Véronique Brouet, Dirk van der Marel, Nimrod Bachar, and Silke Biermann, and thank the CPHT computer support team for their help. This work has been supported by the European Research Council Grant No. ERC-319286-QMAC and the Swiss National Science Foundation (NCCR MARVEL). The Flatiron Institute (A.G.) is supported by the Simons Foundation.

APPENDIX A: EXPRESSION OF H_0 IN THE j BASIS

Labeling $l(\mathbf{k}) = e^{-i\frac{k_x+k_y}{2}}$, we have

$$H_{1/2}(\mathbf{k}) = \begin{pmatrix} \frac{1}{3}\left[\Delta_t + e_1\left(\frac{t_1(\mathbf{k})}{t_0}\right)^2\right] + \lambda & -\frac{8}{3}l(\mathbf{k})t_1(\mathbf{k}) \\ -\frac{8}{3}l^\dagger(\mathbf{k})t_1(\mathbf{k}) & \frac{1}{3}\left[\Delta_t + e_1\left(\frac{t_1(\mathbf{k})}{t_0}\right)^2\right] + \lambda \end{pmatrix}, \tag{A1}$$

$$M^\dagger(\mathbf{k}) = \begin{pmatrix} -\frac{\sqrt{2}}{3}\left[\Delta_t + e_1\left(\frac{t_1(\mathbf{k})}{t_0}\right)^2\right] & \frac{2\sqrt{2}}{3}l(\mathbf{k})t_1(\mathbf{k}) \\ \frac{2\sqrt{2}}{3}l^\dagger(\mathbf{k})t_1(\mathbf{k}) & -\frac{\sqrt{2}}{3}\left[\Delta_t + e_1\left(\frac{t_1(\mathbf{k})}{t_0}\right)^2\right] \\ 0 & \frac{2}{\sqrt{6}}l(\mathbf{k})[t_2(\mathbf{k}) - t_3(\mathbf{k})] \\ \frac{2}{\sqrt{6}}l^\dagger(\mathbf{k})[t_2(\mathbf{k}) - t_3(\mathbf{k})] & 0 \end{pmatrix}, \tag{A2}$$

and

$$H_{3/2}(\mathbf{k}) = \begin{pmatrix} \frac{2}{3}\left[\Delta_t + e_1\left(\frac{t_1(\mathbf{k})}{t_0}\right)^2\right] - \frac{\lambda}{2} & -\frac{10}{3}l(\mathbf{k})t_1(\mathbf{k}) & 0 & \frac{l(\mathbf{k})}{\sqrt{3}}[t_2(\mathbf{k}) - t_3(\mathbf{k})] \\ -\frac{10}{3}l^\dagger(\mathbf{k})t_1(\mathbf{k}) & \frac{2}{3}\left[\Delta_t + e_1\left(\frac{t_1(\mathbf{k})}{t_0}\right)^2\right] - \frac{\lambda}{2} & \frac{l^\dagger(\mathbf{k})}{\sqrt{3}}[t_2(\mathbf{k}) - t_3(\mathbf{k})] & 0 \\ 0 & \frac{l(\mathbf{k})}{\sqrt{3}}[t_2(\mathbf{k}) - t_3(\mathbf{k})] & -\frac{\lambda}{2} & -2l(\mathbf{k})t_1(\mathbf{k}) \\ \frac{l^\dagger(\mathbf{k})}{\sqrt{3}}[t_2(\mathbf{k}) - t_3(\mathbf{k})] & 0 & -2l^\dagger(\mathbf{k})t_1(\mathbf{k}) & -\frac{\lambda}{2} \end{pmatrix}. \tag{A3}$$

APPENDIX B: GREEN'S FUNCTIONS AND SELF-ENERGY IN THE FOUR DOPING REGIMES

In Fig. 12, we show the Matsubara frequency Green's functions and self-energies in the four doping regimes discussed in the main text. Here these regimes are associated with four different values of the chemical potential corresponding to the four rows of the figure.

For $\mu = 1$ eV, the system is a Mott insulator, as can be seen from the insulating character of the two components of the Green's function $G_\pm$. Let us note that the real parts of the self-energies are very different, which is responsible for the opening of the Mott gap (see main text). Increasing the doping, we enter a pseudogap phase. At $\mu = 1.2$ eV, the even component of the Green's function has an insulating behavior, while the odd one is metallic. At $\mu = 1.34$ eV, the system is in a differentiated regime. Both components of the Green's function are now metallic, but the self-energies are still quite differentiated. Going to even larger dopings, we finally reach the uniform Fermi-liquid state. Hence, at $\mu = 1.5$ eV, we see that G_+ and G_- are both metallic and that the self-energies tend to be identical.

APPENDIX C: SOLVING CDMFT EQUATIONS

In order to solve the CDMFT equations, it is convenient to work in the $\pm$ basis introduced in Eq. (13). In this basis, the lattice Green's function is

$$\hat{G}^{\text{latt}}_\pm(i\omega_n,\mathbf{k}) = \{(i\omega_n + \mu)\mathbf{1} - H^{\text{eff}}_\pm(\mathbf{k}) - \hat{\Sigma}_\pm(i\omega_n)\}^{-1}, \tag{C1}$$

where $H^{\text{eff}}_\pm(\mathbf{k})$ is the effective $j_{\text{eff}} = 1/2$ Hamiltonian expressed in the $\pm$ basis and the cluster self-energy is diagonal because the A and B sites are electronically equivalent,

$$\hat{\Sigma}_\pm(i\omega_n) = \begin{pmatrix} \Sigma_+(i\omega_n) & 0 \\ 0 & \Sigma_-(i\omega_n) \end{pmatrix}. \tag{C2}$$

Note that for a given $\mathbf{k}$ point, $\hat{G}^{\text{latt}}_\pm(i\omega_n,\mathbf{k})$ is not diagonal. One can, however, show that for a generic 2×2 diagonal matrix $\mathcal{M}$,

$$\sum_{\mathbf{k}\in\text{RBZ}} [H^{\text{eff}}_\pm(\mathbf{k}) + \mathcal{M}]^{-1} \tag{C3}$$

is a diagonal matrix too. As a result, the CDMFT self-consistency given by Eq. (12) becomes diagonal and reads

$$\hat{G}_\pm(i\omega_n) = \sum_{\mathbf{k}\in\text{RBZ}} \{(i\omega_n + \mu)\mathbf{1} - H^{\text{eff}}_\pm(\mathbf{k}) - \hat{\Sigma}_\pm(i\omega_n)\}^{-1}, \tag{C4}$$

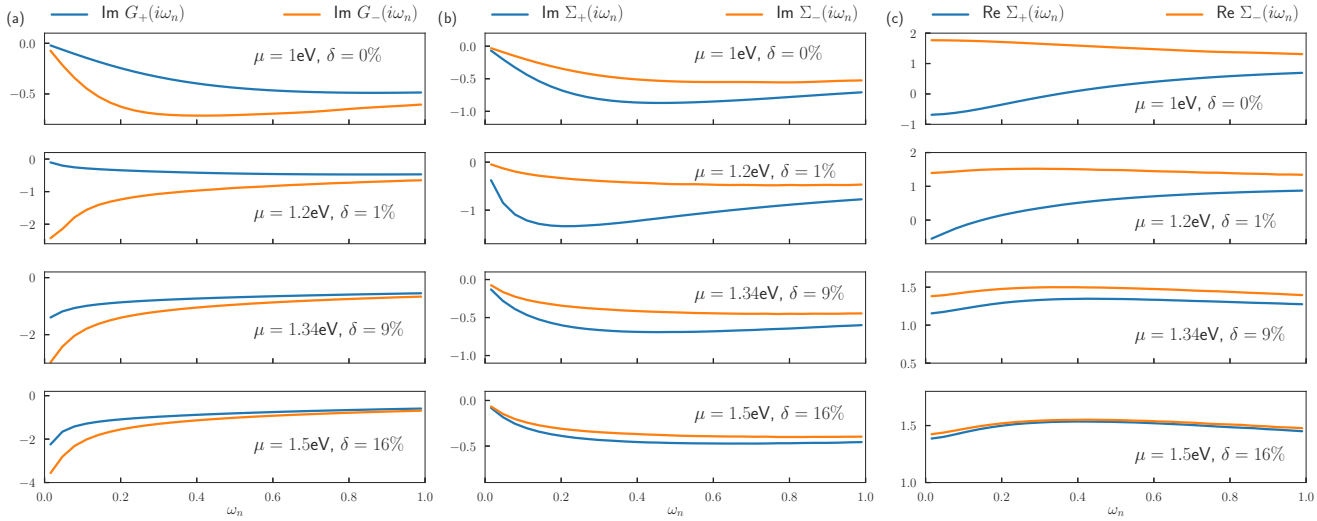

FIG. 12. Evolution in the even-odd basis of (a) the imaginary part of the Green's function $G_\pm(i\omega_n)$, (b) the imaginary part of the self-energy $\Sigma_\pm(i\omega_n)$, and (c) the real part of $\Sigma_\pm(i\omega_n)$ as a function of the Matsubara frequency ω_n. On all plots, the even (odd) contribution is plotted in blue (orange). All quantities are depicted for different values of the chemical potential, from top to bottom panels, respectively: $\mu = 1$ eV and an electron doping $\delta = 0\%$; $\mu = 1.2$ eV, $\delta = 1\%$; $\mu = 1.34$ eV, $\delta = 9\%$; and $\mu = 1.5$ eV, $\delta = 1.6\%$. Results were obtained for $U = 2$ eV, $T = 54$ K.

where both cluster quantities $\hat{G}_\pm$ and $\hat{\Sigma}_\pm$ are diagonal. This equation is solved iteratively in the following way: At the iteration step n, the quantum impurity model is described by a noninteracting Green's function $G^{(n)}_{0,\pm}$ and a local interaction Hamiltonian that has the following expression in the $\pm$ basis:

$$\mathcal{H}^{\text{int}} = \frac{U}{2}\sum_{s=\pm}(n_{s\uparrow}n_{s\downarrow} + n_{s\uparrow}n_{\bar{s}\downarrow} + c^\dagger_{s\uparrow}c^\dagger_{s\downarrow}c_{\bar{s}\downarrow}c_{\bar{s}\uparrow} + c^\dagger_{s\uparrow}c^\dagger_{\bar{s}\downarrow}c_{s\downarrow}c_{\bar{s}\uparrow}). \tag{C5}$$

This cluster model is solved using the CT-HYB quantum impurity solver. This solver directly works in the $\pm$ basis. It yields both the cluster Green's functions $G^{(n)}_\pm$ and self-energies $\Sigma^{(n)}_\pm$. The self-consistency condition is used to construct a local diagonal lattice Green's function,

$$\hat{G}^{(n)}_{\text{loc},\pm}(i\omega_n) = \sum_{\mathbf{k}\in\text{RBZ}} \{(i\omega_n+\mu)\mathbf{1} - H^{\text{eff}}_\pm(\mathbf{k}) - \hat{\Sigma}^{(n)}_\pm(i\omega_n)\}^{-1}. \tag{C6}$$

This allows one to get a new expression for the noninteracting cluster Green's function, via a modified Dyson equation:

$$\left[G^{(n+1)}_{0,\pm}\right]^{-1} = \left[G^{(n)}_{\text{loc},\pm}\right]^{-1} + \Sigma^{(n)}_\pm. \tag{C7}$$

This procedure is iterated until convergence.

APPENDIX D: ABSENCE OF A MOTT INSULATOR WITH THE STANDARD PERIODIZATION SCHEME

The usual periodization of the self-energy is written as

$$\tilde{\Sigma}^{\text{latt}}(i\omega_n,\mathbf{k}) = \begin{pmatrix} \Sigma_{AA} & \Sigma_{AB}\times f(\mathbf{k}) \\ \Sigma_{AB}\times f^*(\mathbf{k}) & \Sigma_{AA}\end{pmatrix}, \tag{D1}$$

where

$$f(\mathbf{k}) = \frac{1}{4}\left(1 + e^{-ik_x} + e^{-ik_y} + e^{-i(k_x+k_y)}\right) \tag{D2a}$$

$$= \cos\frac{k_x}{2}\cos\frac{k_y}{2}e^{-i\frac{k_x+k_y}{2}}. \tag{D2b}$$

$\mathbf{k} = (k_1,k_2)$ is expressed in the reduced Brillouin zone. We see from Fig. 2 that the degeneracy of the $(\pi/2,\pi/2)-(\pi,0)$ path in the full Brillouin zone has to be lifted in order to create a Mott-insulating gap. However, $f(\mathbf{k}) = 0$ along this path and the self-energy has the following expression:

$$\tilde{\Sigma}^{\text{latt}}(i\omega_n,\mathbf{k}) = \Sigma_{AA}\times\mathbf{1}_{2\times2}. \tag{D3}$$

Hence, the self-energy only renormalizes the chemical potential in the quasiparticle equation [Eq. (20)] at $\omega = 0$, forbidding any lifting of the degeneracy between the quasiparticle bands and therefore any gap in the band structure.

[1] J. J. Randall, L. Katz, and R. Ward, J. Am. Chem. Soc. **79**, 266 (1957).
[2] B. J. Kim, H. Jin, S. J. Moon, J.-Y. Kim, B.-G. Park, C. S. Leem, J. Yu, T. W. Noh, C. Kim, S.-J. Oh, J.-H. Park, V. Durairaj, G. Cao, and E. Rotenberg, Phys. Rev. Lett. **101**, 076402 (2008).
[3] C. Martins, M. Aichhorn, L. Vaugier, and S. Biermann, Phys. Rev. Lett. **107**, 266404 (2011).
[4] J. Kim, D. Casa, M. H. Upton, T. Gog, Y.-J. Kim, J. F. Mitchell, M. van Veenendaal, M. Daghofer, J. van den Brink, G. Khaliullin, and B. J. Kim, Phys. Rev. Lett. **108**, 177003 (2012).
[5] A. de la Torre, S. McKeown Walker, F. Y. Bruno, S. Riccó, Z. Wang, I. Gutierrez Lezama, G. Scheerer, G. Giriat, D. Jaccard, C. Berthod, T. K. Kim, M. Hoesch, E. C. Hunter, R. S. Perry, A. Tamai, and F. Baumberger, Phys. Rev. Lett. **115**, 176402 (2015).
[6] V. Brouet, J. Mansart, L. Perfetti, C. Piovera, I. Vobornik, P. Le Fèvre, F. Bertran, S. C. Riggs, M. C. Shapiro, P. Giraldo-Gallo, and I. R. Fisher, Phys. Rev. B **92**, 081117(R) (2015).
[7] K. Terashima, M. Sunagawa, H. Fujiwara, T. Fukura, M. Fujii, K. Okada, K. Horigane, K. Kobayashi, R. Horie, J. Akimitsu, E. Golias, D. Marchenko, A. Varykhalov, N. L. Saini, T. Wakita, Y. Muraoka, and T. Yokoya, Phys. Rev. B **96**, 041106 (2017).
[8] J. Nichols, N. Bray-Ali, A. Ansary, G. Cao, and K.-W. Ng, Phys. Rev. B **89**, 085125 (2014).
[9] H. Zhang, K. Haule, and D. Vanderbilt, Phys. Rev. Lett. **111**, 246402 (2013).
[10] H. Watanabe, T. Shirakawa, and S. Yunoki, Phys. Rev. Lett. **110**, 027002 (2013).
[11] Y. Yang, W.-S. Wang, J.-G. Liu, H. Chen, J.-H. Dai, and Q.-H. Wang, Phys. Rev. B **89**, 094518 (2014).
[12] Y. K. Kim, N. H. Sung, J. D. Denlinger, and B. J. Kim, Nat. Phys. **12**, 37 (2015).
[13] Y. J. Yan, M. Q. Ren, H. C. Xu, B. P. Xie, R. Tao, H. Y. Choi, N. Lee, Y. J. Choi, T. Zhang, and D. L. Feng, Phys. Rev. X **5**, 041018 (2015).
[14] M. K. Crawford, M. A. Subramanian, R. L. Harlow, J. A. Fernandez-Baca, Z. R. Wang, and D. C. Johnston, Phys. Rev. B **49**, 9198 (1994).
[15] T. Vogt and D. Buttrey, J. Solid State Chem. **123**, 186 (1996).
[16] D. J. Singh, P. Blaha, K. Schwarz, and J. O. Sofo, Phys. Rev. B **65**, 155109 (2002).
[17] K. Rossnagel and N. V. Smith, Phys. Rev. B **73**, 073106 (2006).
[18] H. J. Xiang and M.-H. Whangbo, Phys. Rev. B **75**, 052407 (2007).
[19] Y. K. Kim, O. Krupin, J. D. Denlinger, A. Bostwick, E. Rotenberg, Q. Zhao, J. F. Mitchell, J. W. Allen, and B. J. Kim, Science **345**, 187 (2014).
[20] G. Kotliar, S. Y. Savrasov, G. Pálsson, and G. Biroli, Phys. Rev. Lett. **87**, 186401 (2001).
[21] A. Georges, G. Kotliar, W. Krauth, and M. J. Rozenberg, Rev. Mod. Phys. **68**, 13 (1996).
[22] A. Hampel, C. Piefke, and F. Lechermann, Phys. Rev. B **92**, 085141 (2015).
[23] H. Wang, S.-L. Yu, and J.-X. Li, Phys. Rev. B **91**, 165138 (2015).
[24] H. Jin, H. Jeong, T. Ozaki, and J. Yu, Phys. Rev. B **80**, 075112 (2009).
[25] J.-M. Carter, V. Shankar V., and H.-Y. Kee, Phys. Rev. B **88**, 035111 (2013).
[26] H. Watanabe, T. Shirakawa, and S. Yunoki, Phys. Rev. Lett. **105**, 216410 (2010).
[27] P. Seth, I. Krivenko, M. Ferrero, and O. Parcollet, Comput. Phys. Commun. **200**, 274 (2016).
[28] P. Werner, A. Comanac, L. de' Medici, M. Troyer, and A. J. Millis, Phys. Rev. Lett. **97**, 076405 (2006).

[29] P. Werner and A. J. Millis, Phys. Rev. B **74**, 155107 (2006).
[30] E. Gull, A. J. Millis, A. I. Lichtenstein, A. N. Rubtsov, M. Troyer, and P. Werner, Rev. Mod. Phys. **83**, 349 (2011).
[31] O. Parcollet, M. Ferrero, T. Ayral, H. Hafermann, I. Krivenko, L. Messio, and P. Seth, Comput. Phys. Commun. **196**, 398 (2015).
[32] H. J. Vidberg and J. W. Serene, J. Low Temp. Phys. **29**, 179 (1977).
[33] O. Gunnarsson, T. Schäfer, J. P. F. LeBlanc, E. Gull, J. Merino, G. Sangiovanni, G. Rohringer, and A. Toschi, Phys. Rev. Lett. **114**, 236402 (2015).
[34] W. Wu, M. Ferrero, A. Georges, and E. Kozik, Phys. Rev. B **96**, 041105 (2017).

Determinant Monte Carlo algorithms for dynamical quantities in fermionic systems

Alice Moutenet,[1,2] Wei Wu,[1,2] and Michel Ferrero[1,2]
[1]*Centre de Physique Théorique, Ecole Polytechnique, CNRS, Université Paris-Saclay, 91128 Palaiseau, France*
[2]*Collège de France, 11 Place Marcelin Berthelot, 75005 Paris, France*

(Received 18 January 2018; revised manuscript received 30 January 2018; published 12 February 2018)

We introduce and compare three different Monte Carlo determinantal algorithms that allow one to compute dynamical quantities, such as the self-energy, of fermionic systems in their thermodynamic limit. We show that the most efficient approach expresses the sum of a factorial number of one-particle-irreducible diagrams as a recursive sum of determinants with exponential complexity. By comparing results for the two-dimensional Hubbard model with those obtained from state-of-the-art diagrammatic Monte Carlo, we show that we can reach higher perturbation orders and greater accuracy for the same computational effort.

DOI: 10.1103/PhysRevB.97.085117

I. INTRODUCTION

Perturbation expansions are at the heart of many important developments in many-body physics. They appear both in the construction of new theoretical frameworks and in the design of numerical algorithms that have greatly contributed to push further our understanding of interacting quantum systems.

Continuous-time quantum Monte Carlo algorithms [1] such as CT-INT [2,3], CT-AUX [4], or CT-HYB [5,6] are examples of such algorithms. They have been a breakthrough in finding solutions of quantum impurity problems and have opened a new realm for the development of extensions of dynamical mean-field theory [7–12].

One of the reasons for the success of these algorithms is that they are based on a perturbation expansion of the partition function Z. The contributions to Z can be reorganized into determinants that effectively sum a factorial number of perturbation diagrams. As a result, large perturbation orders can be computed and, for smaller clusters, the strong-coupling, low-temperature regime can be addressed. These methods are, however, limited by the number of sites that can be treated in the auxiliary quantum impurity cluster. For large clusters the fermionic sign problem [13] becomes very severe as temperature is decreased or interaction increased [14], and it is very difficult to extrapolate the solution of the infinite size system from a limited number of small clusters.

An alternative and complementary approach is to investigate quantum systems directly in their thermodynamic limit, as in the DiagMC [15–19] algorithm that has also benefited from great advances. With this approach, controlled results were obtained, e.g., for the normal phase of the unitary Fermi gas [20,21], the ground-state phase diagram of the Hubbard model in the weak-coupling regime away from half-filling [22–25], and even in parts of its phase diagram where a pseudogap has already formed [26].

In this method, the perturbation series is written directly for the physical quantity of interest, for example, the self-energy. Contributions to the series are given by individual perturbation Feynman diagrams (one-particle-irreducible ones for the self-energy) that are sampled stochastically. While the sign alternation between individual diagrams is a necessary condition for the convergence of the series, it introduces a fermionic sign problem that makes it difficult to precisely compute high-order coefficients of the series. Another difficulty of the DiagMC approach is that it can be challenging to resum the perturbation series and obtain converged results even if many coefficients are known with great accuracy.

In order to reduce the sign problem of the DiagMC, a connected determinant algorithm (CDet) has been recently introduced in Ref. [27]. The key idea of the approach is to express the sum of a factorial number of connected perturbation diagrams as a sum of determinants (a similar strategy is used in an algorithm for correlated out-of-equilibrium systems) [28]. The physical quantity of interest is then obtained by stochastically sampling these contributions. This algorithm has been shown to scale as 3^n with the perturbation order n. It has proven to give quantitative improvements in the computation of static properties such as pressure [27]. However, no computation of dynamical quantities with the CDet approach has been attempted so far.

In this article, we introduce and compare three different Monte Carlo determinantal algorithms that allow one to compute dynamical quantities of a fermionic system. Two of them are directly based on the CDet approach, while the third algorithm, which we will show is the most efficient, is a generalization of the CDet approach to one-particle-irreducible (1PI) diagrams. It directly samples the contributions to the self-energy with a recursive algorithm scaling as $n^2 3^n$. By comparing results for the two-dimensional Hubbard model with those obtained from DiagMC, we will show that this new approach leads to much smaller error bars for the same numerical effort. It therefore represents an important alternative to compute dynamical quantities.

The article is organized as follows. In Sec. II, we briefly summarize the CDet approach introduced in Ref. [27], as it will be one of the building blocks of our proposal. In Sec. III, we present three algorithms that allow one to derive dynamical quantities. We discuss their practical implementation as a Monte Carlo method in Sec. IV. We then compare and discuss the results of these algorithms and of the DiagMC for the

two-dimensional Hubbard model in Sec. V. We finally conclude in Sec. VI.

II. CONNECTED DETERMINANT APPROACH

First, we briefly summarize the CDet approach introduced in Ref. [27] as it is one of the building blocks of our proposed algorithms. This approach provides a general scheme to compute connected correlators. For concreteness, we consider in this article models described by a noninteracting Green's function G_0 and a local interaction vertex $Un_\uparrow n_\downarrow$. This is the case, for example, in the Hubbard model, in some quantum impurity problems, or in the simple case of an isolated Hubbard atom (that we will later use for benchmark purposes).

In a diagrammatic approach, a perturbation series in the interaction U is constructed. Correlation functions $\mathcal{C}$ of two operators A and B, defined as

$$\mathcal{C}(x_{\text{out}},x_{\text{in}}) \equiv -\langle T_\tau B(x_{\text{out}})A(x_{\text{in}})\rangle, \tag{1}$$

where T_τ is the time-ordering operator and x denotes a vertex, are then expressed as a sum of *connected* diagrams. In real space and imaginary time, x writes (i,τ) for the Hubbard model, where i describes the lattice position and $\tau \in [0,\beta]$ the imaginary time ($\beta = 1/T$ being the inverse temperature). At a given order n in the perturbation series, a diagram contributing to $\mathcal{C}(x_{\text{out}},x_{\text{in}})$ is characterized by the set of its internal vertices $V = \{x_1,\ldots,x_n\}$, where x_l is associated with the lth interaction vertex. The topology of such a diagram is given by two adjacency matrices describing the way the interaction vertices and the external vertices x_{in} and x_{out} are connected.

In the standard DiagMC [15–19] technique, individual connected diagrams are stochastically sampled in a way that preserves their connectivity, with a probability given by the absolute value of their contribution to $\mathcal{C}(x_{\text{out}},x_{\text{in}})$. Note that even if some diagrams share the same vertices, they may have alternating signs from one topology to another, which is one of the ingredients leading to a significant sign problem in this approach. The idea of the CDet algorithm is to regroup *all* diagrams sharing the same internal vertices V in a contribution $\mathcal{C}_V(x_{\text{out}},x_{\text{in}})$ and then stochastically sample the sets V. The stochastic weight of this group of diagrams in the Monte Carlo sampling of $\mathcal{C}(x_{\text{out}},x_{\text{in}})$ is the absolute value of their sum, which is only a function of V.

One could naturally expect that summing this factorial number of diagrams would come with a factorial cost, but it was shown [27] that it can actually be achieved exponentially. The sum of connected diagrams entering $\mathcal{C}_V(x_{\text{out}},x_{\text{in}})$ is expressed as the sum of *all* diagrams (connected and disconnected ones) from which the disconnected components are recursively subtracted. This can be formalized as follows:

$$\mathcal{C}_V(x_{\text{out}},x_{\text{in}}) = \mathcal{D}_V(x_{\text{out}},x_{\text{in}}) - \sum_{S\subsetneq V} \mathcal{C}_S(x_{\text{out}},x_{\text{in}})\mathcal{D}_{V\setminus S}(\varnothing),$$

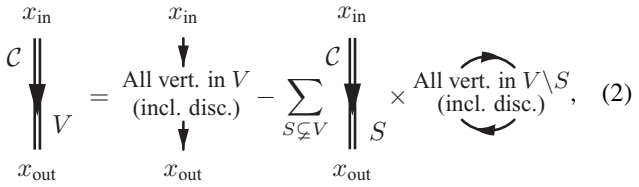

(2)

where $\mathcal{D}_V(x_{\text{out}},x_{\text{in}})$ denotes the sum of all diagrams (including disconnected ones) with internal vertices V, external vertices x_{in} and x_{out}. $D_V(\varnothing)$ is the sum of all diagrams with vertices V and no external vertices. The cancellation of disconnected diagrams is illustrated in the second line of Eq. (2). A key feature of this recursive sum is that $\mathcal{D}_V$ terms can be expressed as determinants (and hence with a polynomial computational cost) [29].

Algorithmically, the evaluation of $\mathcal{C}_V(x_{\text{out}},x_{\text{in}})$ at order n is done in two steps. First, determinants $\mathcal{D}_S$ are computed for all subsets S of V, with a total effort $2^n n^3$. The leading complexity, however, comes from the progressive computation, from low to high orders, of $\mathcal{C}_S$. More precisely, if all $\mathcal{C}_{S'}$ are known for subsets S' with less than $p \leqslant n$ vertices, one can compute a given p-order $\mathcal{C}_S$ using Eq. (2) with $V = S$, in 2^p operations [see right-hand side (rhs) of Eq. (2)]. This has to be done for all the $\binom{n}{p}$ subsets S at order p before computing contributions at the next order $p+1$. The final result is obtained when this has been done for all $p \leqslant n$ and the leading complexity of the algorithm to compute $\mathcal{C}_V(x_{\text{out}},x_{\text{in}})$ is therefore $\sum_{p=0}^{n}\binom{n}{p}2^p = 3^n$.

Note that a similar cancellation of disconnected diagrams had been introduced in a quantum Monte Carlo algorithm for correlated out-of-equilibrium systems [28] where connected correlators are expressed as a sum of 2^n determinants thanks to Keldysh diagrammatic techniques.

The CDet approach leads to an important reduction of statistical error with respect to the DiagMC and has allowed for great progress in the computation of static properties, such as pressure in the Hubbard model [27]. This method, however, has not yet been used to compute dynamical quantities.

In the following, we will investigate how this can be done. We could examine, e.g., the Green's function but choose instead to focus on the self-energy Σ that is a more irreducible object where signatures of numerical noise are clearer. Other single-particle quantities can then be computed from Σ. A straightforward way to obtain Σ is to compute the Green's function G with the CDet approach and derive the self-energy through Dyson's equation. However, even if one can compute G with great accuracy, its inversion in Dyson's equation leads to an amplification of the statistical noise and, as we will show below, the resulting Σ can only be accurately obtained for low orders. It is therefore desirable to look for other techniques to compute the self-energy. This is the purpose of the following section.

III. SELF-ENERGY COMPUTATION

We introduce three different techniques to compute dynamical quantities. In order to compare their efficiencies, we focus on the self-energy Σ^σ (here σ denotes the spin) that they yield, because numerical noise is particularly visible in this quantity. First, we use Dyson's equation to obtain the self-energy from a computation of the Green's function using the CDet technique. We then present a diagrammatic method that allows us to compute the self-energy recursively from the knowledge of a different correlator $\bar{F}$ that can still be computed using the CDet. We finally introduce an extension of the CDet algorithm that efficiently computes the sum of all *one-particle-irreducible* diagrams of a perturbation series

and therefore allows us to directly stochastically sample the contributions to the self-energy. As we discuss in Sec. V, the latter allows for a much better determination of dynamical quantities.

A. Dyson's equation

The most straightforward way to compute the self-energy Σ^σ is to first compute the Green's function G^σ using the CDet algorithm and then use Dyson's equation,

$$\Sigma^\sigma = \left(G_0^\sigma\right)^{-1} - (G^\sigma)^{-1}. \tag{3}$$

We show in Sec. V that it is very difficult to obtain precise data with this method because of the inversion of G that dramatically increases the noise.

B. Equations of motion

We present a diagrammatic approach to compute the self-energy based on the computation of a different correlator with the CDet algorithm. Let us first write the self-energy as the sum of a constant Hartree term and a frequency-dependent part

$$\Sigma^\sigma(x_{\text{out}},x_{\text{in}}) \equiv \Sigma^{H,\sigma}\,\delta_{x_{\text{in}},x_{\text{out}}} + \tilde{\Sigma}^\sigma(x_{\text{out}},x_{\text{in}}). \tag{4}$$

We recall that x is a combined index, e.g., (i,τ) for the Hubbard model, where i is the lattice site and τ the imaginary time. The Hartree term contribution is given by

$$\Sigma^{H,\sigma} \equiv U G^{\bar\sigma}(0^-) = \tag{5}$$

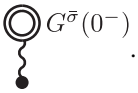

It can be directly computed from the knowledge of the Green's function $G^{\bar\sigma}$, which is a connected correlator that can be obtained from Eq. (2). The self-energy Σ^σ can then be obtained recursively using the following expression:

$$\Sigma^\sigma = \Sigma^{H,\sigma} + \bar{F}^\sigma - \Sigma^\sigma G^\sigma \Sigma^\sigma, \tag{6a}$$

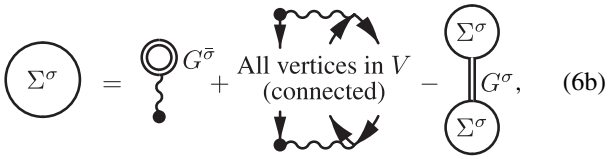

(6b)

where the correlation function $\bar{F}^\sigma$ is defined by

$$\bar{F}^\sigma(x_{\text{out}},x_{\text{in}}) \equiv -U^2\langle T_\tau n_{\bar\sigma} c_\sigma(x_{\text{out}}) n_{\bar\sigma} c_\sigma^\dagger(x_{\text{in}})\rangle. \tag{7}$$

Equation (6) can be derived from the equations of motion (EOM) of the Green's function, as detailed in Appendix A, and we will use this terminology in the following to unambiguously refer to this method. It has a simple diagrammatic interpretation [see the second line of Eq. (6)] that illustrates how 1PI diagrams are isolated. Indeed, according to Eq. (4), the self-energy is the sum of contributions with a single external vertex (Hartree term $\Sigma^{H,\sigma}$) and contributions with two external vertices ($\tilde{\Sigma}^\sigma$). The former is easy to compute, and the latter is the sum of all 1PI diagrams with two external vertices. The term $\bar{F}^\sigma$ on the rhs of Eq. (6) represents the sum of *all connected* diagrams with the same external vertices as $\tilde{\Sigma}^\sigma$. From this, one then has to subtract all non-1PI diagrams, which can always be expressed in the form $\Sigma^\sigma G^\sigma \Sigma^\sigma$.

We now reorganize the equation above in order to be able to compute the contributions to the self-energy at a given perturbation order just from the knowledge of the contributions to $\bar{F}^\sigma$ and $\Sigma^{H,\sigma}$. We first multiply Eq. (6) by G_0^σ on the right and we obtain

$$\Sigma^\sigma G_0^\sigma = \Sigma^{H,\sigma} G_0^\sigma + \bar{F}^\sigma G_0^\sigma - \Sigma^\sigma G^\sigma \Sigma^\sigma G_0^\sigma. \tag{8}$$

Reorganizing the terms,

$$\bar{F}^\sigma G_0^\sigma + \Sigma^{H,\sigma} G_0^\sigma = \Sigma^\sigma\left[G_0^\sigma + G^\sigma \Sigma^\sigma G_0^\sigma\right] = \Sigma^\sigma G^\sigma. \tag{9}$$

Substituting this expression for $\Sigma^\sigma G^\sigma$ in Eq. (6), we find

$$\Sigma^\sigma = \Sigma^{H,\sigma} + \bar{F}^\sigma - \left[\bar{F}^\sigma G_0^\sigma + \Sigma^{H,\sigma} G_0^\sigma\right]\Sigma^\sigma. \tag{10}$$

This equation allows us to recursively compute the contributions to the self-energy at all perturbation orders. Indeed, because $\bar{F}^\sigma$ is at least of order 2 in U and $\Sigma^{H,\sigma}$ is at least of order 1 in U, the computation of the contribution to the self-energy at order n on the left-hand side can be obtained from the knowledge of the contributions to $\bar{F}$ and the contributions to the self-energy at strictly lower orders $< n$ on the rhs. As a result, the left-hand side contributions can be computed without any inversion, and there is no noise amplification as in Dyson's equation. We can therefore expect this approach to be more efficient.

The algorithm is implemented by computing the Green's function G^σ and the correlator $\bar{F}^\sigma$ using the CDet algorithm. Then, Eq. (10) is used to recursively compute the contributions to Σ^σ at a given order. As we use the CDet algorithm to obtain two correlators and the self-energy is only computed in a postprocessing part, the complexity of this algorithm naturally scales as 3^n.

C. Determinantal approach to sum all 1PI diagrams

We now introduce an extension of the CDet algorithm to efficiently compute the sum of all one-particle irreducible diagrams of a perturbation series. At a given perturbation order n in the interaction U, a self-energy diagram is characterized by $x_{\text{in}}, x_{\text{out}}$, its internal interaction vertices $V = \{x_1,\ldots,x_{n-2}\}$, and the adjacency matrices that connect the vertices. Note that we choose $n-2$ points in the set of internal vertices V because x_{in} and x_{out} both carry an interaction vertex as well. We wish to group all diagrams that share the same internal vertices V into a contribution $\Sigma_V^\sigma(x_{\text{out}},x_{\text{in}})$ so that

$$\begin{aligned}\Sigma^\sigma(x_{\text{out}},x_{\text{in}}) &= \sum_V \Sigma_V^\sigma(x_{\text{out}},x_{\text{in}}) \\ &= \sum_V \left(\Sigma_V^{H,\sigma}\,\delta_{x_{\text{in}},x_{\text{out}}} + \tilde{\Sigma}_V^\sigma(x_{\text{out}},x_{\text{in}})\right).\end{aligned} \tag{11}$$

The contribution $\Sigma_V^\sigma(x_{\text{out}},x_{\text{in}})$ is theoretically a sum of a factorial number of diagrams, but we will express it with the help of a recursion, very much in the spirit of Ref. [27], that only involves connected correlators that can be computed with exponential effort using Eq. (2). The numerical effort to obtain $\Sigma_V^\sigma(x_{\text{out}},x_{\text{in}})$ will then turn out to also be exponential.

The frequency-dependent part of the self-energy $\tilde{\Sigma}^\sigma_V(x_{\rm out},x_{\rm in})$ can be expressed *via* the following recursive formula

$$\tilde{\Sigma}^\sigma_V(x_{\rm out},x_{\rm in}) = \bar{F}^\sigma_V(x_{\rm out},x_{\rm in}) - \sum_{\substack{x'\in V\\ S\subseteq V\setminus\{x'\}\\ S'=V\setminus(S\cup\{x'\})}} F^\sigma_{S'}(x_{\rm out},x')\tilde{\Sigma}^\sigma_S(x',x_{\rm in}) - \sum_{\substack{S\subseteq V\\ S'=V\setminus S}} F^\sigma_{S'}(x_{\rm out},x_{\rm in})\big(UG^{\bar\sigma}_S(0^-)\big), \tag{12a}$$

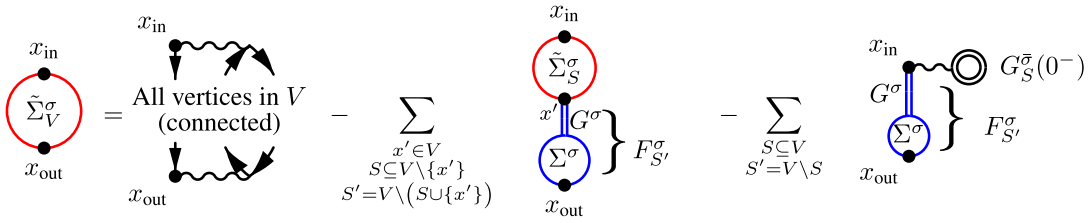

(12b)

where the correlation function F^σ is given by [30]

$$F^\sigma(x_{\rm out},x_{\rm in}) = \Sigma^\sigma G^\sigma(x_{\rm out},x_{\rm in}) \tag{13}$$

$$\equiv -U\langle T_\tau n_{\bar\sigma} c_\sigma(x_{\rm out})c^\dagger_\sigma(x_{\rm in})\rangle, \tag{14}$$

and $\bar{F}^\sigma$ by Eq. (7). The starting point of the recursion is the order-2 diagram

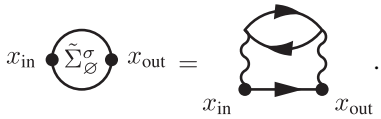

(15)

The second line of Eq. (12) illustrates the cancellation of non-1PI diagrams. The self-energy contributions $\tilde{\Sigma}^\sigma_V$ that are calculated recursively are indicated as red circles, while blue diagrams correspond to the correlation function $F^\sigma = \Sigma^\sigma G^\sigma$. An explicit example of this formula at third order is shown in Appendix C. Let us note that, in this formula, the starting point of the recursion is already an order-2 diagram, while it is an order-0 diagram in Eq. (2), justifying a set V with $n-2$ vertices.

The first term $\bar{F}^\sigma_V(x_{\rm out},x_{\rm in})$ on the rhs of Eq. (12) is the contribution to the correlation function $\bar{F}^\sigma(x_{\rm out},x_{\rm in})$ for the set of internal vertices V. It is the sum of all connected diagrams that have interaction vertices at $x_{\rm in}$, $x_{\rm out}$ and all $x\in V$ as interaction vertices. In order to obtain the contributions to the self-energy $\tilde{\Sigma}^\sigma_V(x_{\rm out},x_{\rm in})$, one has to subtract from this term all diagrams that are not 1PI. These can be expressed in the form $\Sigma^\sigma G^\sigma \Sigma^\sigma = F^\sigma\Sigma^\sigma = F^\sigma(\Sigma^{H,\sigma}+\tilde{\Sigma}^\sigma)$, and there are therefore two families of diagrams to subtract for a given set of vertices V: first all terms $F^\sigma_{S'}(x_{\rm out},x_{\rm in})\Sigma^{H,\sigma}_S$ such that $S\sqcup S' = V$, then all terms $F^\sigma_{S'}(x_{\rm out},x')\tilde{\Sigma}^\sigma_S(x',x_{\rm in})$ such that $S\sqcup\{x'\}\sqcup S' = V$. In the latter family, note that $S\subsetneq V$ is a proper subset of V, so that the calculation of $\tilde{\Sigma}^\sigma_V$ involves only some $\tilde{\Sigma}^\sigma_S$ that have been previously computed in the recursion.

We have therefore derived a recursive formula for the contributions $\tilde{\Sigma}^\sigma_V(x_{\rm out},x_{\rm in})$ that involves the computation of only connected correlation functions. The recursion is completed in two steps. First, all correlators $\bar{F}^\sigma$, F^σ, and G^σ have to be enumerated, the main effort coming from the F^σ_S that have to be computed for all pairs of external vertices [as a consequence of the explicit use of an intermediate vertex point x' in Eq. (12)]. The computational cost for the precomputation is therefore dominated by $n^2 3^n$. Second, the recursion has to be implemented, as in the CDet, by computing the contributions $\tilde{\Sigma}^\sigma_S$ starting from low to higher orders. At a given order p, it takes an effort $p2^p$ to get a given $\tilde{\Sigma}^\sigma_S(x',x_{\rm in})$. This has to be done for all subsets S at order p and all x' before computing contributions at the next order $p+1$ and requires a total effort $\binom{n}{p}p^2 2^p$. All in all the recursion will take $\sum_{p=0}^n\binom{n}{p}p^2 2^p$ with a complexity $n^2 3^n$. The leading complexity of the algorithm is therefore $n^2 3^n$.

We will show in Sec. V that despite this additional n^2 factor, this method leads to smaller error bars compared to the approaches above. It also gives more accurate results than the state-of-the-art DiagMC calculations for the same computational effort.

IV. MONTE CARLO IMPLEMENTATION

In this section, we describe how to compute the different quantities that appear in the algorithms above using a Monte Carlo (MC) method. We generically denote these quantities as $\mathcal{M}^\sigma$. The quantities that need to be computed depend on the algorithm considered. The Green's function G^σ has to be computed for all three approaches. In addition, $\bar{F}^\sigma$ must be computed for the equations of motion algorithm and $\tilde{\Sigma}^\sigma$ for the direct sampling of the self-energy. We write $\mathcal{M}^\sigma$ as a sum over all contributions described by a set V_m with m internal vertices:

$$\mathcal{M}^\sigma(x_{\rm out},x_{\rm in}) = \sum_{m=0}^\infty\sum_{V_m}\mathcal{M}^\sigma_{V_m}(x_{\rm out},x_{\rm in}). \tag{16}$$

Note that a configuration with m internal vertices contributes, in the perturbation series in U, to the coefficient of order $n=m$ for the Green's function, $n=m+1$ for F^σ and $n=m+2$ for $\tilde{\Sigma}^\sigma$.

In order to compute $\mathcal{M}^\sigma(x_{\rm out},x_{\rm in})$, we stochastically generate Monte Carlo configurations that sample the rhs terms of the sum. A configuration $\mathfrak{C}$ is described by the number of internal vertices m, the spin σ, and the set of all vertices,

$$\mathfrak{C} = \{m;\sigma;x_{\rm in},x_{\rm out};x_1,\ldots,x_m\}, \tag{17}$$

and its weight in the Monte Carlo sampling is

$$w_{\mathfrak{C}} = \left|\mathcal{M}^\sigma_{V_m}(x_{\rm out},x_{\rm in})\right|. \tag{18}$$

We use a standard Metropolis [31] algorithm to generate a Markov chain distributed according to $w_{\mathfrak{C}}$. For concreteness,

we consider the case of the Hubbard model where $x = (i, \tau)$. Starting from a given $\mathfrak{C}$, a new configuration $\mathfrak{C}'$ is proposed by applying one of the following Monte Carlo updates:

(i) Pick one of the interaction vertices in $\mathfrak{C}$ and change its position and imaginary time. One can increase the probability of the move being accepted by choosing a new position either among the neighbors of the chosen vertex or from a Gaussian distribution. The imaginary time can be chosen uniformly.

(ii) Flip the spin $\sigma \to \bar{\sigma}$.

(iii) Remove a randomly chosen internal interaction vertex from $\mathfrak{C}$.

(iv) Add a new internal interaction vertex in $\mathfrak{C}$. The new lattice site can be chosen from a Gaussian distribution around the center of gravity of the vertices in $\mathfrak{C}$. The imaginary time can be chosen with uniform probability.

The new configuration $\mathfrak{C}'$ is accepted or rejected with the usual Metropolis ratio

$$p^{\text{accept}}_{\mathfrak{C}\to\mathfrak{C}'} = \min\left(1, \frac{T_{\mathfrak{C}'\mathfrak{C}}\, w_{\mathfrak{C}'}}{T_{\mathfrak{C}\mathfrak{C}'}\, w_{\mathfrak{C}}}\right), \tag{19}$$

where $T_{\mathfrak{C}\mathfrak{C}'}$ is the probability to propose $\mathfrak{C}'$ after $\mathfrak{C}$.

This algorithm will sample the configurations according to the weights $w_{\mathfrak{C}}$; however, it is necessary to normalize the result. To do so, it is convenient to restrict the Monte Carlo simulation to only two consecutive orders, m and $m+1$. A vertex can be added (resp. removed) only if the current $\mathfrak{C}$ is at order m (resp. $m+1$). In the lowest order m the following normalization quantity is measured

$$\mathcal{N}_m = \sum_{x_{\text{in}}, x_{\text{out}}, \sigma} \sum_{V_m} \left|\mathcal{M}^{\sigma}_{V_m}(x_{\text{out}}, x_{\text{in}})\right|, \tag{20}$$

while at order $m+1$, both $\mathcal{N}_{m+1}$ and the contribution to $\mathcal{M}^{\sigma}$ are measured. The knowledge of the expected value for $\mathcal{N}_m$ allows us to find the normalization factor and obtain a normalized value for the contribution to $\mathcal{M}^{\sigma}$ and $\mathcal{N}_{m+1}$ at order $m+1$. The latter can then be used to normalize a further simulation at orders $m+1$ and $m+2$, and so on. The contribution at $m = 0$, for instance, the pair-bubble diagram for the self-energy, can be computed analytically, allowing for a precise determination of $\mathcal{N}_0$.

We performed several calculations for the special case of a single correlated site (especially for benchmarking purposes). In that situation, it is possible to restrict the simulation to a fixed order m and propose updates that change only the spin σ and the imaginary time of a randomly chosen interaction vertex. The normalization is obtained by computing an integral whose value is known. The simple choice

$$\mathcal{I}_m = \sum_{\sigma} \int_0^{\beta} d\tau_{\text{in}} d\tau_{\text{out}} d\tau_1 \ldots d\tau_m = 2\beta^{m+2}$$

turns out to provide a good normalization.

Let us note that statistical errors in the normalization factor propagate from one order to the other. One must therefore be careful in the computation of error bars using, e.g., a binning or jackknife analysis.

V. RESULTS

In this section, we present actual computations of the self-energy according to the implementations described in Sec. III. For clarity, we respectively denote by Dyson, EOM, and ΣDet the use of Dyson's equation, the equations of motion, and the direct calculation of the self-energy from the sum of 1PI diagrams.

We consider two models in the following. The first is a single correlated electronic level, that we will refer to as a Hubbard atom, described by the Hamiltonian

$$\mathcal{H}_{\text{atom}} = U n_{\uparrow} n_{\downarrow} + \epsilon, \tag{21}$$

where n_{σ} is the number of the spin-σ fermion, U is the onsite repulsion, and ϵ the energy of the electronic level. This model has an analytical solution and allows us to both benchmark and compare the different methods introduced above. The second model is the prototypical two-dimensional Hubbard model given by

$$\mathcal{H}_{\text{Hubbard}} = -t \sum_{\langle i,j\rangle\sigma} c^{\dagger}_{i\sigma} c_{j\sigma} + U \sum_i n_{i\uparrow} n_{i\downarrow}, \tag{22}$$

where $c^{\dagger}_{i\sigma}$ creates a spin-σ electron on site i of a square lattice, $t > 0$ is the nearest-neighbor hopping, and U is the onsite interaction. This is the model that we eventually aim to solve in its thermodynamic limit (infinite lattice). In our results, $t = 1$ will be our energy unit. Note that in the computations of the Hubbard model, we use an α shift that redefines the noninteracting propagator [3,26,28,32].

We first benchmark our results against both analytical and standard DiagMC [15–19] solutions and verify the theoretical complexity of our models in Appendix B. We then compare the three different methods between them, showing that ΣDet performs better both on the isolated atom and on the lattice. This method is finally shown to also improve state-of-the-art results from recent DiagMC calculations.

A. Comparison with Dyson's equation

Until now, no dynamical quantities have been computed with the CDet algorithm and it is therefore instructive to see how the use of Dyson's equation compares to the calculation of the self-energy from the EOM and ΣDet methods.

We first consider the Hubbard atom. Figure 1 shows the contribution to the imaginary part of the Matsubara frequency self-energy $\tilde{\Sigma}^{\sigma}(i\omega_n)$ from perturbation order 8. The direct measurement of the self-energy and the EOM method yield results that have very small error bars (smaller than the symbol size) and that are in perfect agreement (both curves lie on top of one another). In contrast, starting from the Green's function as obtained by Eq. (2), the results for the self-energy display large statistical errors that increase with the Matsubara frequency index. The reason is simple and expected: when Dyson's equation is used to compute the self-energy, there is an amplification of the numerical noise because of the inversion of the Green's function. In practice, it becomes quickly impossible to obtain accurate data. This is problematic, because large error bars make it very difficult, e.g., to analytically continue the results to the real axis.

Figure 2 shows results for the two-dimensional Hubbard model on a 32×32 lattice (for $\beta t = 2$ the Hubbard model is in its thermodynamic limit on this lattice). At order 3, the contribution to the self-energy taken at the first Matsubara frequency $i\omega_0$ obtained from ΣDet on a chosen path in the

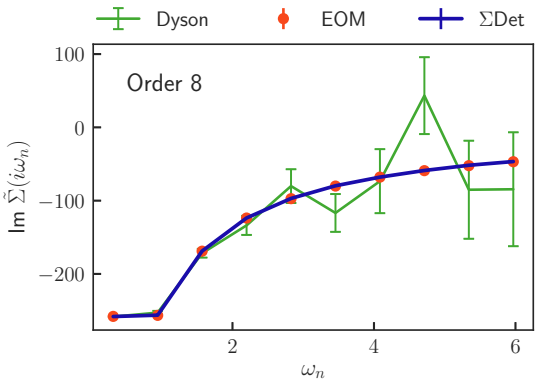

FIG. 1. Imaginary part of the Hubbard atom self-energy at order 8 in U as obtained from Dyson's equation (green), the equations of motion approach (orange), and the direct self-energy measurement (blue). We use $\beta = 10$, $U = 1$, $\epsilon = -0.2$. All simulations lasted 120 CPU hours.

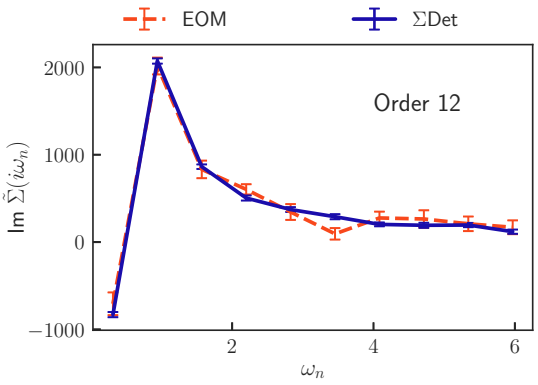

FIG. 3. Imaginary part of the Hubbard atom self-energy at order 12 in U as obtained from the equations of motion approach (orange) and the direct self-energy measurement (blue). We use $\beta = 10$, $U = 1$, $\epsilon = -0.2$. All simulations lasted 120 CPU hours.

Brillouin zone is in perfect agreement with the EOM method, and error bars for both methods are very small (smaller than symbol size, both curves being on top). The computation of Σ^σ from the Green's function is noisier. Error bars actually increase with the Matsubara frequency index when using Dyson's equation, resulting in reasonable results only for the first few frequencies even for small perturbation orders. Again, the reason for this large noise is the amplification due to the inversion of the Green's function. Also, on the lattice, a direct measurement of the self-energy has the advantage of mainly sampling fairly local diagrams. Indeed, at a temperature $T = t/2$, the self-energy very quickly vanishes for nonlocal components. The same is not true for the Green's function that has a slower decay; its stochastic sampling is therefore less efficient.

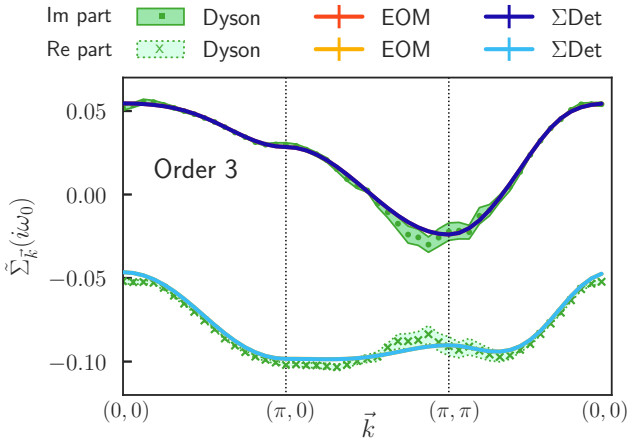

FIG. 2. Hubbard model self-energy at the first Matsubara frequency $\tilde{\Sigma}_{\vec{k}}(i\omega_0)$ along the $\vec{k} = (0,0) \to (\pi,0) \to (\pi,\pi) \to (0,0)$ path at order 3 in U, as obtained from Dyson's equation (green), the equations of motion approach (orange), and the direct self-energy measurement (blue). We use a 32×32 lattice with $\beta t = 2$, $U = 4t$, $\mu = 0$ and a uniform α shift $\alpha_\uparrow = \alpha_\downarrow = 1.53t$. All simulations lasted 120 CPU hours.

B. Comparison between the equations of motion and the direct sampling of the self-energy

We now compare the use of equations of motion to the direct sampling of the self-energy expressed as a sum of 1PI diagrams (ΣDet). It is not clear which method is more efficient, as the ΣDet allows for a precise cancellation of diagrams and directly samples the quantity of interest but scales as $n^2 3^n$, while the EOM method cancels diagrams on average but has a better scaling as 3^n.

We first consider the Hubbard atom. In Fig. 3 we show the contribution to the imaginary part of the Matsubara frequency $\tilde{\Sigma}^\sigma(i\omega_n)$ at order 12 for both methods. The equations of motion method has error bars that are seen to be about 1 order of magnitude greater than the ΣDet ones. In order to quantify the efficiency more accurately, we plot in Fig. 4 the variance at the first Matsubara frequency ω_0 as a function of the perturbation order for both methods. We see from this plot that ΣDet performs better at low perturbation order, and that both methods tend to become equivalent at higher orders.

The comparison of the resulting self-energies on the lattice Hubbard model (Fig. 5) shows an even more pronounced

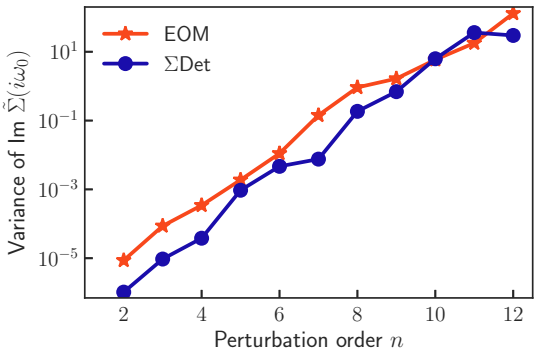

FIG. 4. Variance of the imaginary part of the Hubbard atom self-energy at the first Matsubara frequency. Orange lines with stars is the result of the equations of motion. Blue line with dots corresponds to the direct self-energy measurement. We use $\beta = 10$, $U = 1$, $\epsilon = -0.2$.

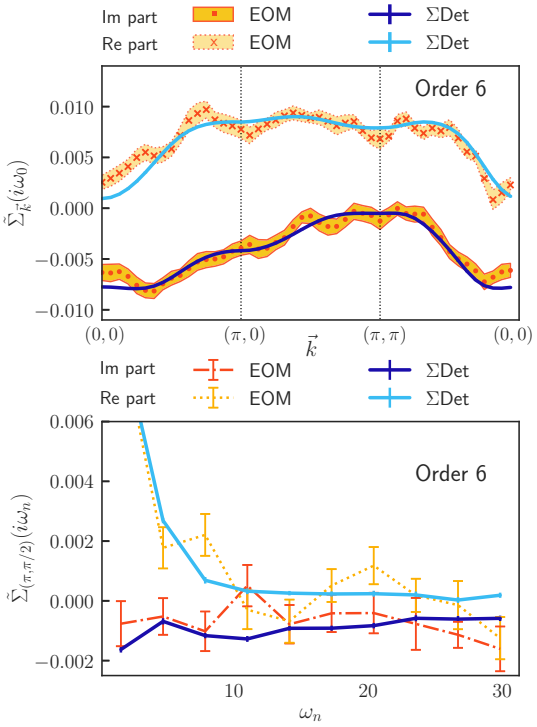

FIG. 5. Hubbard model self-energy at order 6 in U on a 32×32 lattice with $\beta t = 2$, $U = 4t$, $\mu = 0$ and with a uniform α shift $\alpha_\uparrow = \alpha_\downarrow = 1.53t$. Blue symbols are results for the direct self-energy measurement; orange symbols are results from the equations of motion approach. Upper panel: Self-energy at the first Matsubara frequency $\tilde{\Sigma}_{\vec{k}}(i\omega_0)$ along the $\vec{k} = (0,0) \to (\pi,0) \to (\pi,\pi) \to (0,0)$ path. Lower panel: Self-energy as a function of $i\omega_n$ at $\vec{k} = (\pi,\pi/2)$. All simulations lasted 120 CPU hours.

difference between the two approaches. At order 6, the contribution to the self-energy taken at the first Matsubara frequency (upper panel) obtained from ΣDet on a chosen path in the Brillouin zone is very well converged and the error bars for this method are very small (smaller than symbol size). The computation of Σ^σ from the equations of motion is less accurate, even if it agrees with the ΣDet within its error bars. We then look at the Matsubara frequency evolution for a given reciprocal lattice vector $\vec{k} = (\pi,\pi/2)$. The error bar for the EOM method is seen to be large for all Matsubara frequencies. To be quantitative, we plot in Fig. 6 the variance at the first Matsubara frequency ω_0 for this same value of $\vec{k} = (\pi,\pi/2)$ as function a of the perturbation order. We see from this plot that ΣDet always performs better than the EOM method, by about 1 order of magnitude.

We believe the explanation for this behavior comes from two ingredients. First, the cancellation of non-one-particle-irreducible diagrams is done *on average* in the EOM approach, while it is exact in the ΣDet algorithm and therefore more efficient to measure the self-energy. This is particularly visible on the lattice that has more degrees of freedom. Second, the self-energy Σ^σ is more local on the lattice than the correlator $\bar{F}$. Hence the direct MC sampling of the self-energy still performs better, even though its numerical complexity is greater by a factor n^2. Let us note here that the EOM approach could be

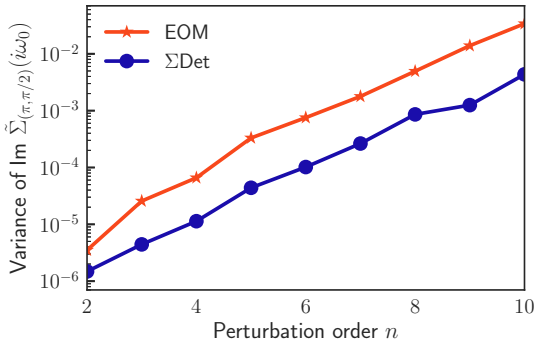

FIG. 6. Variance of the imaginary part of the Hubbard model self-energy Im $\tilde{\Sigma}_{(\pi,\pi/2)}(i\omega_0)$. Orange lines with stars is the result equations of motion. Blue line with dots corresponds to the direct self-energy measurement. We use a 32×32 lattice with $\beta t = 2$, $U = 4t$, $\mu = 0$ and with a uniform α shift $\alpha_\uparrow = \alpha_\downarrow = 1.53t$.

useful in the context of the real-time algorithm of Ref. [28]. There the complexity of the EOM approach would be 2^n while a direct self-energy approach would scale as $n^2 3^n$. It may well be that the EOM approach is more efficient in that case.

C. Comparison between ΣDet and DiagMC algorithms

As the direct calculation of the self-energy ΣDet proves to be a very accurate method to get the self-energy, it is natural to compare it to the state-of-the-art DiagMC results on the two-dimensional Hubbard model. To this end, we compute in Fig. 7 the contribution to the first Matsubara frequency ω_0 of the self-energy at perturbation order 7 for both ΣDet and DiagMC methods. Error bars at this perturbation order, the highest currently reachable with DiagMC techniques, are much smaller with the ΣDet algorithm than with the standard DiagMC approach for simulations of the same length. This algorithm canceling directly non-1PI diagrams in the MC sampling is therefore an interesting alternative to the current diagrammatic Monte Carlo approach.

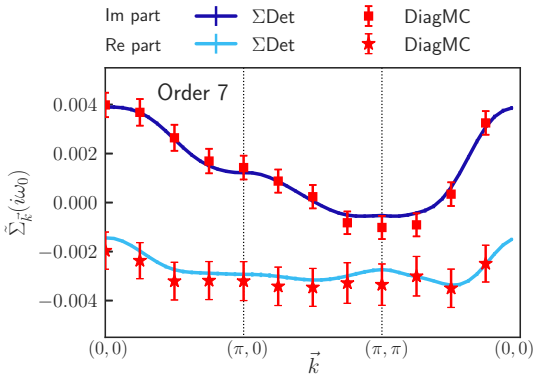

FIG. 7. Hubbard model self-energy at the first Matsubara frequency $\tilde{\Sigma}_{\vec{k}}(i\omega_0)$ along the $\vec{k} = (0,0) \to (\pi,0) \to (\pi,\pi) \to (0,0)$ path at order 7 in U, as obtained from DiagMC (red) and the direct self-energy measurement (blue). We use a 32×32 lattice with $\beta t = 2$, $U = 4t$, $\mu = 0$ and a uniform α shift $\alpha_\uparrow = \alpha_\downarrow = 1.53t$. Simulations lasted 1440 CPU hours for the ΣDet and 4000 CPU hours for the DiagMC.

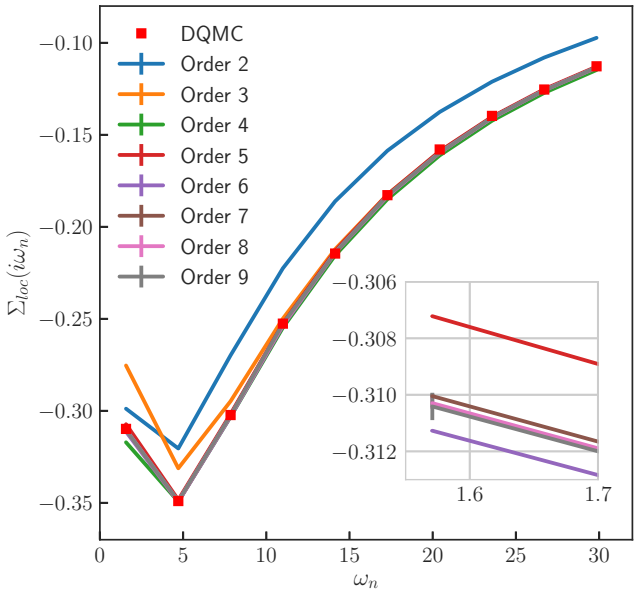

FIG. 8. Imaginary part of the local lattice self-energy $\Sigma^{\sigma}_{\mathrm{loc}}(i\omega_n)$ as a function of Matsubara frequency, as computed using k orders, with $k = 2, \ldots, 9$. The red squares are results obtained from DQMC (error bars are smaller than the symbol size). Inset: Zoom on the first Matsubara frequency. It is seen that the results are converged with an error bar smaller than 1%. We use a 32×32 lattice with $\beta t = 2, U = 4t, \mu = 0$ and with a uniform α shift $\alpha_{\uparrow} = \alpha_{\downarrow} = 1.53t$. The discrete time interval in DQMC is $\Delta\tau = 1/32$.

As a final illustration of the method, we compute contributions up to order 9. The resummed local self-energy is shown in Fig. 8. We observe that with a reasonable choice for the α shift, one can completely converge the results with an uncertainty below 1%.

VI. CONCLUSION

We have introduced and compared three methods to compute the self-energy of fermionic systems. Two of them rely on the computation of correlators using the CDet technique, while the third one is an extension of the CDet that allows one to sum all diagrams that share the same interaction vertices and are one-particle irreducible. This allows us to design a Monte Carlo scheme that directly samples the contributions to the self-energy. This ΣDet algorithm has an exponential complexity $n^2 3^n$ where n is the perturbation order. We have shown that even if it has higher complexity, an approach that computes the self-energy directly leads to much smaller error bars with respect to the use of Dyson's equation or more sophisticated equations of motion (nevertheless, the latter could be useful in the context of real-time quantum Monte Carlo algorithms) [28].

With the parameters that we have discussed above, $\beta = 2/t$, $U = 4t$, and $\mu = 0$ (corresponding to a total density $n = 0.66$), the direct self-energy measurement also leads to much smaller error bars than the usual DiagMC algorithm on the two-dimensional Hubbard model and sets the current state of the art of these approaches. In practice, one can completely converge the results for 9 orders with an uncertainty below 1%. Note that for these parameters, other approaches, such as determinant quantum Monte Carlo (DQMC) [33], also converge (see Fig. 8). It is therefore important to more systematically compare the ΣDet approach, the DiagMC, and other algorithms in different regimes of parameters in order to determine in what regions of the Hubbard model solutions can be converged. Work is in progress along these lines. (See also the recent article of Šimkovic and Kozik [34].)

Finally, further progress is still needed to be able to reach stronger coupling regimes and lower temperatures. While the summation over all topologies certainly reduces the sign problem, the stochastic integration over imaginary times still yields large error bars at high orders. It is therefore necessary to investigate how this sign problem could be reduced.

ACKNOWLEDGMENTS

We would like to acknowledge valuable feedback from the participants of the Diagrammatic Monte Carlo Workshop held at the Flatiron Institute, June 2017, where this work was first presented, and we are particularly grateful for discussions with A. Georges, E. Kozik, R. Rossi, F. Šimkovic, and X. Waintal. We are especially indebted to O. Parcollet for suggesting improvements to our work. This work has been supported by the Simons Foundation within the Many Electron Collaboration framework (W.W.) and the European Research Council through Grant No. ERC-319286-QMAC (A.M.). Our codes were developed using the TRIQS [35] library. We would also like to thank the computing staff at CPHT for their help.

APPENDIX A: EQUATIONS OF MOTION

Here we show that Eq. (6) can be obtained from the equations of motion of the Green's function. For concreteness, we consider the two-dimensional Hubbard model

$$\mathcal{H} = -t \sum_{\langle i,j\rangle\sigma} c^{\dagger}_{i\sigma} c_{j\sigma} + U \sum_{i} n_{i\uparrow} n_{i\downarrow} \tag{A1a}$$

$$\equiv \mathcal{H}_{\mathrm{hop}} + \mathcal{H}_{\mathrm{int}}, \tag{A1b}$$

where $c^{\dagger}_{i\sigma}$ creates a spin-σ electron on the site i of a square lattice, $t > 0$ is the nearest-neighbor hopping, and U the onsite interaction. Note that the derivation below yields the same result for an interacting impurity coupled to a bath or for the Hubbard atom. These models are used in the article to benchmark and compare results from the different methods introduced in Sec. III.

We define the imaginary-time Green's function of two operators A and B as $G_{A,B}(\tau) = -\langle T_\tau A(\tau) B(0)\rangle$. The equation of motion for G is given by

$$\partial_\tau G_{A,B}(\tau) = -\delta(\tau)\langle\{A(\tau), B(0)\}\rangle - \langle T_\tau [\mathcal{H}, A](\tau) B(0)\rangle, \tag{A2}$$

which, in Matsubara frequencies, is written

$$i\omega_n G_{A,B}(i\omega_n) = -G_{[\mathcal{H},A],B}(i\omega_n) + \langle\{A, B\}\rangle. \tag{A3}$$

Let us note for later use that by writing $G_{A,B}(\tau) = -\langle T_\tau A(0) B(-\tau)\rangle$, one obtains a similar expression that involves a commutator between the Hamiltonian and B rather than A,

$$i\omega_n G_{A,B}(i\omega_n) = G_{A,[\mathcal{H},B]}(i\omega_n) + \langle\{A, B\}\rangle. \tag{A4}$$

The equation of motion [Eq. (A3)] for the one-particle Green's function $G^{\sigma}_{ij} \equiv -\langle T_\tau c_{i\sigma}(\tau) c^{\dagger}_{j\sigma}(0)\rangle$ is

$$i\omega_n G^{\sigma}_{ij} = -G_{[\mathcal{H},c_{i\sigma}],c^{\dagger}_{j\sigma}} + \langle\{c_{i\sigma}, c^{\dagger}_{j\sigma}\}\rangle. \tag{A5}$$

Using the expression for the commutators

$$[\mathcal{H}_{\text{hop}}, c_{i\sigma}] = t\sum_{\langle a,b\rangle} c_{b\sigma}\delta_{ia}, \tag{A6a}$$

$$[\mathcal{H}_{\text{int}}, c_{i\sigma}] = -U n_{i\bar{\sigma}} c_{i\sigma}, \tag{A6b}$$

we find that

$$i\omega_n G^{\sigma}_{ij} = -t\sum_{\langle a,b\rangle}\delta_{ia} G^{\sigma}_{bj} + U G_{n_{i\bar{\sigma}}c_{i\sigma},c^{\dagger}_{j\sigma}} + \delta_{ij}, \tag{A7a}$$

$$\sum_{\langle a,b\rangle}(i\omega_n\delta_{ib} + t\delta_{ia}) G^{\sigma}_{bj} = U G_{n_{i\bar{\sigma}}c_{i\sigma},c^{\dagger}_{j\sigma}} + \delta_{ij}. \tag{A7b}$$

Introducing the correlator $F^{\sigma}_{ij} \equiv U G_{n_{i\bar{\sigma}}c_{i\sigma},c^{\dagger}_{j\sigma}}$, the equation above can be rewritten in matrix form as

$$F^{\sigma} = \left(G_0^{\sigma -1} - G^{\sigma -1}\right) G^{\sigma} = \Sigma^{\sigma} G^{\sigma}. \tag{A8}$$

Note that this definition of F^{σ} is consistent with Eq. (13). We can now apply Eq. (A4) to F^{σ}_{ij},

$$i\omega_n F^{\sigma}_{ij} = U G_{n_{i\bar{\sigma}}c_{i\sigma},[\mathcal{H},c^{\dagger}_{j\sigma}]} + U\langle\{n_{i\bar{\sigma}}c_{i\sigma}, c^{\dagger}_{j\sigma}\}\rangle. \tag{A9}$$

Using the commutators

$$[\mathcal{H}_{\text{hop}}, c^{\dagger}_{j\sigma}] = -t\sum_{\langle a,b\rangle} c^{\dagger}_{a\sigma}\delta_{bj}, \tag{A10a}$$

$$[\mathcal{H}_{\text{int}}, c^{\dagger}_{j\sigma}] = U n_{j\bar{\sigma}} c^{\dagger}_{j\sigma}, \tag{A10b}$$

we find that

$$\sum_{\langle a,b\rangle}(i\omega_n\delta_{aj} + t\delta_{bj}) F^{\sigma}_{ia} = U^2 G_{n_{i\bar{\sigma}}c_{i\sigma},n_{j\bar{\sigma}}c^{\dagger}_{j\sigma}} + \langle n_{i\bar{\sigma}}\rangle\delta_{ij}. \tag{A11}$$

Introducing the correlator $\bar{F}^{\sigma}_{ij} \equiv U^2 G_{n_{i\bar{\sigma}}c_{i\sigma},n_{j\bar{\sigma}}c^{\dagger}_{j\sigma}}$ and the Hartree term $\Sigma^{H,\sigma}_{ij} = \langle n_{i\bar{\sigma}}\rangle\delta_{ij}$ the equation above becomes

$$F^{\sigma} G_0^{\sigma -1} = \bar{F}^{\sigma} + \Sigma^{H,\sigma}. \tag{A12}$$

Using Eq. (A8) for F^{σ} and Dyson's equation we have that

$$F^{\sigma} G_0^{\sigma -1} = \Sigma^{\sigma} G^{\sigma}(G^{\sigma -1} + \Sigma^{\sigma}) = \Sigma^{\sigma} + \Sigma^{\sigma} G^{\sigma}\Sigma^{\sigma}, \tag{A13}$$

which yields the final result

$$\Sigma^{\sigma} = \Sigma^{H,\sigma} + \bar{F}^{\sigma} - \Sigma^{\sigma} G^{\sigma}\Sigma^{\sigma}. \tag{A14}$$

This is the relation between the self-energy and the correlator $\bar{F}^{\sigma}$ used in Eq. (6). The definitions of $\bar{F}^{\sigma}$ and $\Sigma^{H,\sigma}$ are respectively consistent with Eqs. (7) and (5).

APPENDIX B: BENCHMARKS

Here, we present benchmarks for the three methods introduced in the main text and we check their theoretical complexity. We first consider the simple problem of a Hubbard atom. The self-energy is given by

$$\Sigma^{\sigma}(i\omega_n) = \langle n_{\bar{\sigma}}\rangle U + \frac{\langle n_{\bar{\sigma}}\rangle(1 - \langle n_{\bar{\sigma}}\rangle)U^2}{i\omega_n - \epsilon - (1 - \langle n_{\bar{\sigma}}\rangle)U}, \tag{B1}$$

and the contributions to $\tilde{\Sigma}(i\omega_n)$ at different orders in U can be computed analytically. In Fig. 9, we show results for the contributions to $\tilde{\Sigma}(i\omega_n)$ at order 5 as obtained from the proposed algorithms. The results clearly agree with the analytical values within the error bars.

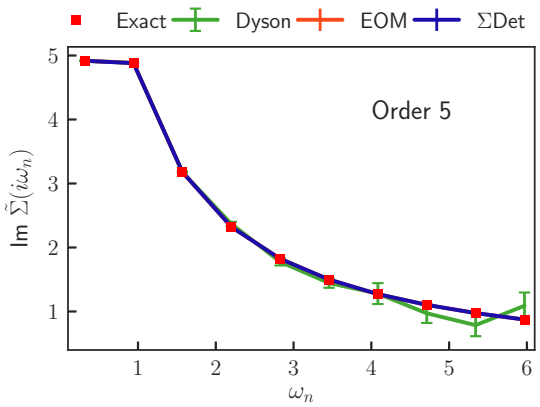

FIG. 9. Benchmark of the contribution to the Matsubara frequency self-energy $\tilde{\Sigma}(i\omega_n)$ for the Hubbard atom at order 5 in the perturbation series in U. Red squares are the analytical solution. Green lines are obtained from a calculation of the Green's function with Eq. (2). Orange line is the result of the equations of motion and lies on top of the blue curve corresponding to the direct self-energy measurement. We use $\beta = 10$, $U = 1$, $\epsilon = -0.2$. All simulations lasted 1200 CPU hours.

Next we consider the Hubbard model on a 32×32 square lattice. In Fig. 10 we plot the momentum-dependent

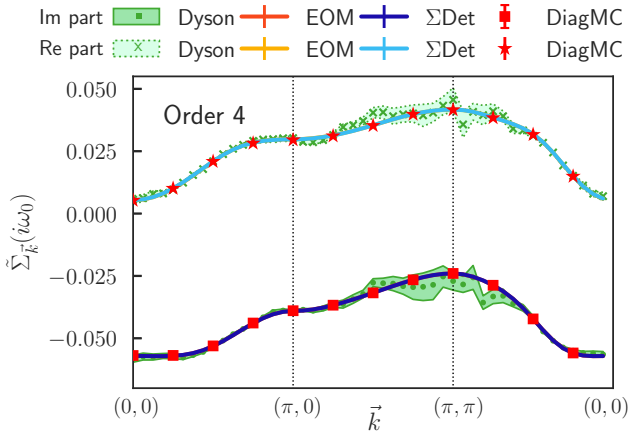

FIG. 10. Hubbard model self-energy at the first Matsubara frequency $\tilde{\Sigma}_{\vec{k}}(i\omega_0)$ along the $\vec{k} = (0,0) \to (\pi,0) \to (\pi,\pi) \to (0,0)$ path at order 4 in U, as obtained from DiagMC (red), Dyson's equation (green), the equations of motion approach (orange), and the direct self-energy measurement (blue). We use a 32×32 lattice with $\beta t = 2$, $U = 4t$, $\mu = 0$ and a uniform α shift $\alpha_{\uparrow} = \alpha_{\downarrow} = 1.53t$. The DiagMC simulation lasted 400 CPU hours, while all other simulations lasted 1440 CPU hours.

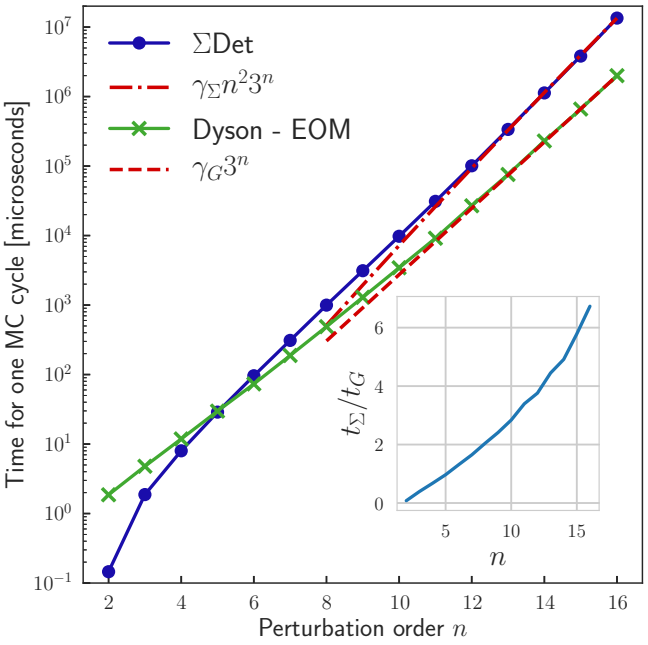

FIG. 11. Comparison of the time for one Monte Carlo cycle (in microseconds) between the direct accumulation of the self-energy (blue curve with dots) and the computation of the Green's function using CDet (green curve with dots), on a semilog scale, as a function of the perturbation order n. Each curve is fitted by its expected high-n behavior: $\gamma_\Sigma n^2 3^n$ for the ΣDet (dotted red line) and $\gamma_G 3^n$ for Dyson (dashed red line), where $\gamma_G = 0.0464$ and $\gamma_\Sigma = 0.0012$ are implementation-dependent constants. Inset: Ratio of the time of one MC cycle for ΣDet (t_Σ) and for the CDet (t_G), as a function of the perturbation order n.

self-energy $\tilde{\Sigma}_{\vec{k}}(i\omega_0)$ at its first Matsubara frequency along the $\vec{k} = (0,0) \to (\pi,0) \to (\pi,\pi) \to (0,0)$ path of the Brillouin zone. Results from the three approaches are are shown at order 4 and compared to results obtained using the standard DiagMC [15–19] algorithm. (This implementation of the algorithm has been benchmarked and used in earlier calculations, see, e.g., Ref. [26].) Results agree with the benchmark DiagMC calculation within error bars.

A measurement of the time to perform one MC step allows us to study the complexity of the algorithms. This is shown in Fig. 11, where the time for a single step is shown both for the direct measurement of the self-energy using the ΣDet and for the measurement of G using the CDet, that is then used in Dyson's equation. We know that the EOM method takes twice the CDet complexity, so we consider these two methods together in this study. The expected high-order behavior in $n^2 3^n$ for the self-energy measurement and 3^n for the CDet is found. At smaller perturbation orders, the asymptotic behavior is not yet settled. At orders smaller than 5, the self-energy measurement takes less time mainly because the algorithm starts at order 2. [The recursion starts with the pair-bubble diagram, see Eq. (15) with $V = \varnothing$.] On the contrary, the CDet algorithm for the Green's function starts at order 0. As a consequence, the direct measurement of the self-energy is only about a factor 3 slower than the CDet approach at order 10 (see inset of Fig. 11), which is the order that is currently accessible with reasonable error bars.

APPENDIX C: CANCELLATION OF NON-SELF-ENERGY DIAGRAMS

Let us explicitly show the cancellation of non-self-energy diagrams in Eq. (12) for the specific case $V = \{x_1\}$ at order 3 in U. We start by considering

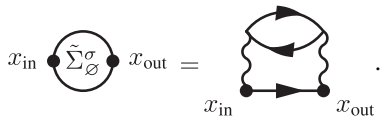

(C1)

The first term $\bar{F}^\sigma_V(x_{\text{out}},x_{\text{in}})$ in Eq. (12) corresponds to all connected diagrams with two external points x_{in} and x_{out} and one internal interaction vertex x_1:

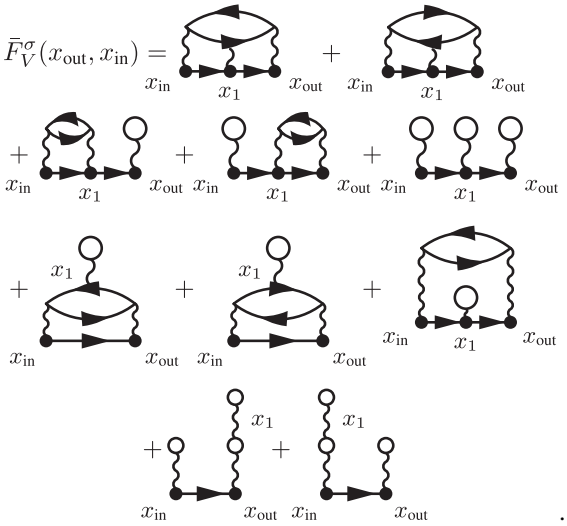

(C2)

From this sum, we subtract the second and third terms of Eq. (12). The former gives

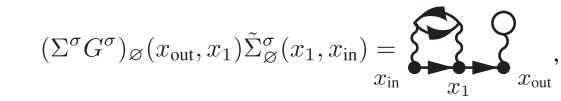

(C3)

while the latter's contribution is the sum of

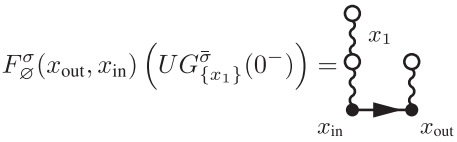

(C4)

and of

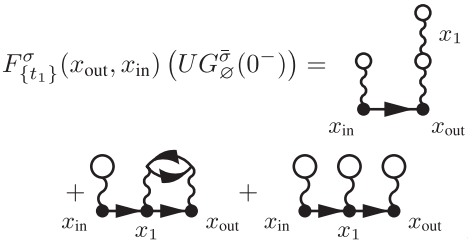

(C5)

We see that the remaining contributions to the self-energy that remain are only those diagrams that are one-particle irreducible.

[1] E. Gull, A. J. Millis, A. I. Lichtenstein, A. N. Rubtsov, M. Troyer, and P. Werner, Rev. Mod. Phys. **83**, 349 (2011).

[2] A. N. Rubtsov and A. I. Lichtenstein, J. Exp. Theor. Phys. Lett. **80**, 61 (2004).

[3] A. N. Rubtsov, V. V. Savkin, and A. I. Lichtenstein, Phys. Rev. B **72**, 035122 (2005).

[4] E. Gull, P. Werner, O. Parcollet, and M. Troyer, Europhys. Lett. **82**, 57003 (2008).

[5] P. Werner, A. Comanac, L. de' Medici, M. Troyer, and A. J. Millis, Phys. Rev. Lett. **97**, 076405 (2006).

[6] P. Werner and A. J. Millis, Phys. Rev. B **74**, 155107 (2006).

[7] A. Georges, G. Kotliar, W. Krauth, and M. J. Rozenberg, Rev. Mod. Phys. **68**, 13 (1996).

[8] G. Kotliar, S. Y. Savrasov, K. Haule, V. S. Oudovenko, O. Parcollet, and C. A. Marianetti, Rev. Mod. Phys. **78**, 865 (2006).

[9] M. H. Hettler, A. N. Tahvildar-Zadeh, M. Jarrell, T. Pruschke, and H. R. Krishnamurthy, Phys. Rev. B **58**, R7475(R) (1998).

[10] A. I. Lichtenstein and M. I. Katsnelson, Phys. Rev. B **62**, R9283(R) (2000).

[11] G. Kotliar, S. Y. Savrasov, G. Pálsson, and G. Biroli, Phys. Rev. Lett. **87**, 186401 (2001).

[12] T. Maier, M. Jarrell, T. Pruschke, and M. H. Hettler, Rev. Mod. Phys. **77**, 1027 (2005).

[13] M. Troyer and U.-J. Wiese, Phys. Rev. Lett. **94**, 170201 (2005).

[14] J. P. F. LeBlanc, A. E. Antipov, F. Becca, I. W. Bulik, G. K.-L. Chan, C.-M. Chung, Y. Deng, M. Ferrero, T. M. Henderson, C. A. Jiménez-Hoyos, E. Kozik, X.-W. Liu, A. J. Millis, N. V. Prokof'ev, M. Qin, G. E. Scuseria, H. Shi, B. V. Svistunov, L. F. Tocchio, I. S. Tupitsyn *et al.* (Simons Collaboration on the Many-Electron Problem), Phys. Rev. X **5**, 041041 (2015).

[15] N. V. Prokof'ev and B. V. Svistunov, Phys. Rev. Lett. **81**, 2514 (1998).

[16] N. Prokof'ev and B. Svistunov, Phys. Rev. Lett. **99**, 250201 (2007).

[17] E. Kozik, K. V. Houcke, E. Gull, L. Pollet, N. Prokof'ev, B. Svistunov, and M. Troyer, Europhys. Lett. **90**, 10004 (2010).

[18] K. V. Houcke, E. Kozik, N. Prokof'ev, and B. Svistunov, Phys. Procedia **6**, 95 (2010), Computer Simulations Studies in Condensed Matter Physics XXI .

[19] E. Bourovski, N. Prokof'ev, and B. Svistunov, Phys. Rev. B **70**, 193101 (2004).

[20] K. Van Houcke, F. Werner, E. Kozik, N. Prokof'ev, B. Svistunov, M. J. H. Ku, A. T. Sommer, L. W. Cheuk, A. Schirotzek, and M. W. Zwierlein, Nat. Phys. **8**, 366 (2012).

[21] E. Burovski, N. Prokof'ev, B. Svistunov, and M. Troyer, Phys. Rev. Lett. **96**, 160402 (2006).

[22] J. Gukelberger, L. Huang, and P. Werner, Phys. Rev. B **91**, 235114 (2015).

[23] Y. Deng, E. Kozik, N. V. Prokof'ev, and B. V. Svistunov, Europhys. Lett. **110**, 57001 (2015).

[24] F. Šimkovic, X.-W. Liu, Y. Deng, and E. Kozik, Phys. Rev. B **94**, 085106 (2016).

[25] F. Šimkovic, Y. Deng, N. V. Prokof'ev, B. V. Svistunov, I. S. Tupitsyn, and E. Kozik, Phys. Rev. B **96**, 081117 (2017).

[26] W. Wu, M. Ferrero, A. Georges, and E. Kozik, Phys. Rev. B **96**, 041105 (2017).

[27] R. Rossi, Phys. Rev. Lett. **119**, 045701 (2017).

[28] R. E. V. Profumo, C. Groth, L. Messio, O. Parcollet, and X. Waintal, Phys. Rev. B **91**, 245154 (2015).

[29] R. Rossi, N. Prokof'ev, B. Svistunov, K. V. Houcke, and F. Werner, Europhys. Lett. **118**, 10004 (2017).

[30] R. Bulla, A. C. Hewson, and T. Pruschke, J. Phys.: Condens. Matter **10**, 8365 (1998).

[31] N. Metropolis, A. W. Rosenbluth, M. N. Rosenbluth, A. H. Teller, and E. Teller, J. Chem. Phys. **21**, 1087 (1953).

[32] R. Rossi, F. Werner, N. Prokof'ev, and B. Svistunov, Phys. Rev. B **93**, 161102 (2016).

[33] R. Blankenbecler, D. J. Scalapino, and R. L. Sugar, Phys. Rev. D **24**, 2278 (1981).

[34] F. Simkovic IV. and E. Kozik, arXiv:1712.10001.

[35] O. Parcollet, M. Ferrero, T. Ayral, H. Hafermann, I. Krivenko, L. Messio, and P. Seth, Comput. Phys. Commun. **196**, 398 (2015).

Cancellation of vacuum diagrams and the long-time limit in out-of-equilibrium diagrammatic quantum Monte Carlo

Alice Moutenet,[1,2,3] Priyanka Seth,[4] Michel Ferrero,[1,2] and Olivier Parcollet[3,4]
[1]*CPHT, CNRS, Ecole Polytechnique, Institut Polytechnique de Paris, Route de Saclay, 91128 Palaiseau, France*
[2]*Collège de France, 11 place Marcelin Berthelot, 75005 Paris, France*
[3]*Center for Computational Quantum Physics, Flatiron Institute, 162 Fifth Avenue, New York, New York 10010, USA*
[4]*Institut de Physique Théorique (IPhT), CEA, CNRS, UMR 3681, 91191 Gif-sur-Yvette, France*

(Received 26 April 2019; published 14 August 2019)

We express the recently introduced real-time diagrammatic quantum Monte Carlo [Phys. Rev. B **91**, 245154 (2015)] in the Larkin-Ovchinnikov basis in Keldysh space. Based on a perturbation expansion in the local interaction U, the special form of the interaction vertex allows us to write diagrammatic rules in which vacuum Feynman diagrams directly vanish: This reproduces the main property of the previous algorithm, without the cost of the exponential sum over Keldysh indices. In an importance sampling procedure, this implies that only interaction times in the vicinity of the measurement time contribute, and such an algorithm can directly address the long-time limit needed in the study of steady states in out-of-equilibrium systems. We then implement and discuss different variants of Monte Carlo algorithms in the Larkin-Ovchinnikov basis. A sign problem reappears, showing that the cancellation of vacuum diagrams has no direct impact on it.

DOI: 10.1103/PhysRevB.100.085125

I. INTRODUCTION

The development of high-precision and controlled computational methods for nonequilibrium models in strongly-correlated regimes is a subject of growing interest in theoretical condensed-matter physics. Recent years have seen significant experimental progress with quantum transport through mesoscopic systems [1], metal-insulator transitions driven by an electric field [2], or light-induced superconductivity [3–7].

Powerful tools have been designed for the study of quantum systems at equilibrium. Notably, the combination of dynamical mean-field theory [8–10] and state-of-the-art continuous-time quantum Monte Carlo (QMC) algorithms such as CT-INT [11,12], CT-AUX [13], or CT-HYB [14,15] have allowed for great advances. When considering out-of-equilibrium systems, however, early attempts to construct similar perturbation-expansion-based real-time QMC algorithms encountered an exponential sign problem that prevented them from reaching long times and large interactions [16–20]. Other approaches such as the density matrix renormalization group (DMRG) [21–23] also struggle in the long-time limit due to entanglement growth. There is therefore still a great need for high-precision numerical methods that would be able to access the nonequilibrium steady states of strongly-interacting quantum systems.

Current efforts to build real-time quantum Monte Carlo methods mainly explore two routes: the inchworm algorithm [24–30] and the so-called "diagrammatic" QMC [31–33] which is the subject of this paper. Using an expansion of physical quantities in powers of the interaction U, this algorithm has been shown to directly address the infinite-time steady states. The name "diagrammatic" refers to its imaginary-time counterparts that were historically constructing a Markov chain in the space of Feynman diagrams [34–37].

First introduced in Ref. [31], the real-time diagrammatic QMC algorithm stochastically samples physical quantities using an importance sampling. At a given perturbation order n, its key idea is to regroup a factorial number of Feynman diagrams in a sum over Keldysh indices of 2^n determinants. This exponential sum has been shown to cancel vacuum diagrams, a property also used in recent diagrammatic QMC methods in imaginary time [38–40]. As a direct consequence, the Monte Carlo sampling only involves interaction times in a neighborhood around the measurement time $t_{\max}$: We talk about the *clusterization* of times. The computation of the Monte Carlo weight is exponential in the perturbation order but *uniform in time*, at any temperature. The algorithm can therefore address long, even infinite, times in the computation of contributions to the perturbation theory. This method was recently generalized to compute the Green's function and tested in quantum impurity models [32,33]. The current form of the algorithm is able to compute the Kondo resonance at low temperature in the strongly-correlated Kondo regime.

Coefficients of the expansion being written in terms of high-dimensional integrals of the sum of determinants, its exponential scaling limits our capability to compute high orders with great precision (we typically are limited to 10 of them). Even though nonperturbative information and Bayesian techniques can overcome noise amplification occurring in the resummation of the series [33], this can prevent the algorithm from reaching very large U.

In this paper, we show that we can obtain the cancellation of diagrams and the long time clusterization property *without* summing an exponential number of terms. Using the Larkin-Ovchinnikov (LO) basis in Keldysh space, we rewrite the integrand as a sum of 4^n determinants, but we show that diagrammatic rules in this basis are such that *every* diagram has the clusterization property. In other words, the elimination

of vacuum diagrams is directly achieved in the diagrammatics without the need of an exponential sum. We then implement and compare two Monte Carlo algorithms based on this mathematical property. Both sample single determinants at a polynomial cost, but then one measures in the LO basis (LO algorithm) while the other measures in the original basis (mixed algorithm). We obtain that a simple implementation of the real-time diagrammatic QMC in the Larkin-Ovchinnikov basis leads to a severe sign problem, which is reduced in the mixed algorithm. This shows that the main effect of the exponential sum of determinants, beyond the cancellation of vacuum disconnected diagrams, is to reduce the sign problem of this class of algorithms.

This paper is organized as follows. First, we present in Sec. II the usual Keldysh formalism in the $\{\pm\}$ basis, briefly summarize the diagrammatic rules, and then derive the cancellation of vacuum diagrams and the clusterization of the density when summing over Keldysh indices. We follow the same structure in Sec. III where we introduce the Larkin-Ovchinnikov basis, showing that all vacuum diagrams are equal to zero, so that density contributions directly clusterize around the measurement time. We then detail in Sec. IV the Monte Carlo implementation of the original algorithm presented in Ref. [31] ($\pm$ algorithm) and two algorithms based on the Larkin-Ovchinnikov formalism (LO and mixed algorithms). In Sec. V we compute the density of an impurity level coupled to a bath, present the results of all three algorithms, and explain the origin of the observed error bars. We finally conclude in Sec. VI.

II. KELDYSH FORMALISM

We work in the Keldysh formalism [41–44]. In this framework, operators act on the Keldysh contour $\mathcal{C}$ consisting of a forward branch, from an initial time t_0 (that we take equal to 0 in the following) to a given time $t_{\max}$, and a backward branch, from $t_{\max}$ to t_0. The system is initially prepared at equilibrium without interactions. A Keldysh point k on $\mathcal{C}$ is defined as a pair $k \equiv (t, \alpha)$ with a time $t \in [0, t_{\max}]$ and a Keldysh index $\alpha \in \{\pm\}$ indicating which branch is to be considered. The $+$ (resp. $-$) index denotes the forward (resp. backward) branch, as depicted below.

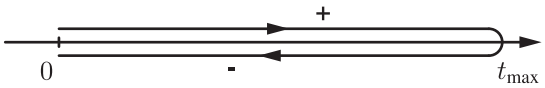

Note that both branches are along the real axis and are displaced only for graphical purposes. In the following, Greek letters refer to $\pm$ indices unless otherwise stated. We define a contour operator $T_{\mathcal{C}}$ that follows the arrows on the above picture: $T_{\mathcal{C}}$ coincides with the usual time-ordering operator T on the $+$ branch, with the anti-time ordered operator $\check{\mathrm{T}}$ on the $-$ branch, and considers all Keldysh points on the backward branch to be later than points on the forward branch.

The formalism we develop in this section is valid for any general model described by a noninteracting Green's function g and a density-density interaction. However, for the sake of simplicity, we consider interacting electrons on a single energy level. The operator c_σ (resp. $c_\sigma^\dagger$) destroys (resp. creates) an electron with spin $\sigma = \uparrow, \downarrow$. The interaction term, turned on at $t = 0$, is given by the interaction vertex $U n_\uparrow n_\downarrow$, where $n_\sigma \equiv c_\sigma^\dagger c_\sigma$ is the density operator.

We define the time-dependent Green's function

$$\hat{G}_\sigma(t, t') \equiv -i\langle T_{\mathcal{C}} c_\sigma(t) c_\sigma^\dagger(t')\rangle, \tag{1}$$

where $c_\sigma^{(\dagger)}(t)$ is the Heisenberg representation of $c_\sigma^{(\dagger)}$ and the average is taken with respect to the initial noninteracting state. The Green's function takes the form of a 2×2 matrix in the $\{\pm\}$ basis: $\hat{G}_\sigma = \begin{pmatrix} G_\sigma^{++} & G_\sigma^{<} \\ G_\sigma^{>} & G_\sigma^{--} \end{pmatrix}$, where

$$G_\sigma^{<}(t, t') \equiv i\langle c_\sigma^\dagger(t') c_\sigma(t)\rangle, \tag{2a}$$

$$G_\sigma^{>}(t, t') \equiv -i\langle c_\sigma(t) c_\sigma^\dagger(t')\rangle, \tag{2b}$$

$$G_\sigma^{++}(t, t') \equiv -i\langle \mathrm{T} c_\sigma(t) c_\sigma^\dagger(t')\rangle, \tag{2c}$$

$$G_\sigma^{--}(t, t') \equiv -i\langle \check{\mathrm{T}} c_\sigma(t) c_\sigma^\dagger(t')\rangle. \tag{2d}$$

Throughout the paper, noninteracting Green's functions will be denoted by lower case letters, interacting ones by upper case letters, and a $\hat{}$ denotes a matrix.

A. Diagrammatic rules

In this paper, we construct perturbation series in the interaction U for physical observables of interest. Computing contributions at different perturbation orders relies on the evaluation of Feynman diagrams obeying rules that we briefly summarize.

A straight line represents a noninteracting Green's function

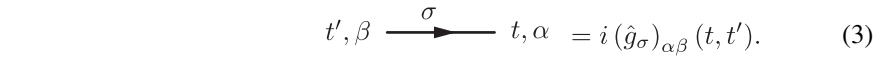

(3)

Because the interaction has the form $U n_\uparrow n_\downarrow$, an interaction vertex is characterized by a single Keldysh point $\{t, \alpha\}$, and the indices of the four legs all have to be equal to the Keldysh index α

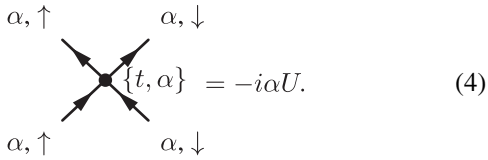

(4)

Hence, for every interaction time t, there are two possible vertices. The sum of the different $\{\pm\}$ configurations can be written in the $\mathcal{H}_\uparrow \otimes \mathcal{H}_\downarrow$ space, in the form

$$-iU(m_+ \otimes m_+ - m_- \otimes m_-), \tag{5}$$

where $m_+ = \begin{pmatrix} 1 & 0 \\ 0 & 0 \end{pmatrix}$ and $m_- = \begin{pmatrix} 0 & 0 \\ 0 & 1 \end{pmatrix}$ are matrices in the $\{\pm\}$ basis, and $\mathcal{H}_\sigma$ is the Hilbert space for spin σ. Furthermore, an interaction of the form $h c_\sigma^\dagger c_\sigma$ in the Hamiltonian would give rise to two-leg vertices of the form

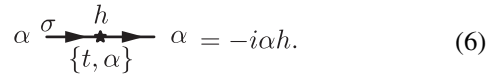

(6)

These do not appear directly in the diagrammatics but will be formally useful when deriving the expression of the fermionic bubble. The sum over Keldysh indices reads $-ih(m_+ - m_-)$ in both $\mathcal{H}_\uparrow$ and $\mathcal{H}_\downarrow$ spaces.

With the expression of the four-leg interaction vertex, the following fermionic bubble reads

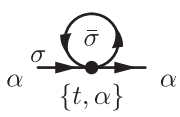

$$= \alpha U g^{\alpha\alpha}_{\bar{\sigma}}(t,t). \tag{7}$$

Because of the form of the interaction term, we have

$$g^{\alpha\alpha}_{\sigma}(t,t) = g^{<}_{\sigma}(t,t). \tag{8}$$

Hence, the above diagram reduces to $\alpha U g^{<}_{\bar{\sigma}}(t,t)$, which can be formulated as a two-leg vertex with a $iUg^{<}_{\bar{\sigma}}(t,t)$ field

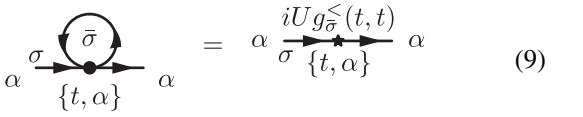

(9)

If $\mathcal{M}$ is the quantity we want to compute (later on the density), its perturbation expansion is given by $\mathcal{M} = \sum_n \mathcal{M}_n U^n$. Because of the form of the interaction vertex, we have

$$\mathcal{M}_n = \int_{\mathcal{C}} \mathrm{d}k_1 \ldots \mathrm{d}k_n \, \mathcal{M}^{\pm}_n(k_1, \ldots, k_n) \tag{10}$$

$$= \int_0^{t_{\max}} \mathrm{d}t_1 \ldots \mathrm{d}t_n \sum_{\alpha_1 \ldots \alpha_n} \mathcal{M}^{\pm}_n(\{t_i, \alpha_i\}_{1 \leqslant i \leqslant n}), \tag{11}$$

where $\mathcal{M}^{\pm}_n(\{t_i, \alpha_i\}_{1 \leqslant i \leqslant n})$ can be expressed as a product of determinants, their precise form depending on the measured quantity. Throughout this paper, the $\pm$ superscript will denote quantities expressed in the $\{\pm\}$ basis. Moreover times integrated over are always considered ordered.

B. Cancellation of vacuum diagrams when summing over Keldysh indices

Due to the forward-backward nature of the contour $\mathcal{C}$, the partition function Z is exactly equal to 1 in the real-time Keldysh formalism. Expressing Z as a series in U ($Z = \sum_n Z_n U^n$), this property implies that all Z_n are vanishing for $n \geqslant 1$. Because of the form of Eq. (10), this cancellation involves both the integral over times and the sum over Keldysh indices. However, it was proven by Profumo and co-workers in Ref. [31] that only the latter is needed. For all $n \geqslant 1$, $\{t_1, \ldots, t_n\} \in [0, t_{\max}]^n$,

$$\sum_{\alpha_1 \ldots \alpha_n} Z^{\pm}_n(\{t_i, \alpha_i\}_{1 \leqslant i \leqslant n}) = 0, \tag{12}$$

where

$$Z^{\pm}_n(\{t_i, \alpha_i\}_{1 \leqslant i \leqslant n}) = (-i\alpha_1) \ldots (-i\alpha_n) \times i^n i^n \times \prod_{\sigma} \det \left[(\hat{g}_{\sigma})_{\alpha_i \alpha_j}(t_i, t_j) \right]_{1 \leqslant i,j \leqslant n}. \tag{13}$$

Each $(-i\alpha_k)$ comes from Eq. (4), and the two i^n factors from the fact that a straight line actually represents an $i\hat{g}$ [Eq. (3)].

For every configuration of times $\{t_1, \ldots, t_n\}$, vacuum diagrams therefore cancel when performing the explicit 2^n sum over Keldysh indices. Recent developments in imaginary-time diagrammatic QMC also achieved, through an iterative procedure, the cancellation of vacuum (and, later on, non-one-particle irreducible) diagrams at every Monte Carlo step at an exponential cost in the perturbation order [38–40].

C. Density computation and clusterization

In the following, we compute the density d of electrons with spin $\uparrow$ on the impurity level at the end point of the Keldysh contour, $d \equiv \langle n_{\uparrow}(t_{\max}) \rangle$. In the $\{\pm\}$ basis, let us note that $d = (\hat{G}_{\uparrow})_{01}(t_{\max}, t_{\max})/i$. Hence we can represent the measurement vertex as a "special" vertex bearing time $t_{\max}$, such that the ingoing and outgoing Keldysh indices are 0 and 1:

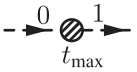

(14)

Note that the surrounding lines are dashed because they should bear a $\hat{g}$ propagator (instead of an $i\hat{g}$ one as in the rest of the formalism). The order-n contribution to d reads

$$d_n = \int_0^{t_{\max}} \mathrm{d}t_1 \ldots \mathrm{d}t_n \sum_{\alpha_1 \ldots \alpha_n} (-i\alpha_1) \ldots (-i\alpha_n) \times \frac{i^{n+1} i^n}{i^2} \prod_{\sigma} \det \mathcal{D}^{\pm}_{\sigma}(\{t_i, \alpha_i\}_{1 \leqslant i \leqslant n}), \tag{15}$$

where

$$\mathcal{D}^{\pm}_{\uparrow}(\{t_i, \alpha_i\}_{1 \leqslant i \leqslant n}) = \begin{pmatrix} \left[(\hat{g}_{\uparrow})_{\alpha_i \alpha_j}(t_i, t_j) \right]_{1 \leqslant i,j \leqslant n} & \begin{matrix} (\hat{g}_{\uparrow})_{\alpha_1 1}(t_1, t_{\max}) \\ \vdots \\ (\hat{g}_{\uparrow})_{\alpha_n 1}(t_n, t_{\max}) \end{matrix} \\ \begin{matrix} (\hat{g}_{\uparrow})_{0\alpha_1}(t_{\max}, t_1) & \ldots & (\hat{g}_{\uparrow})_{0\alpha_n}(t_{\max}, t_n) \end{matrix} & (\hat{g}_{\uparrow})_{01}(t_{\max}, t_{\max}) \end{pmatrix}, \tag{16}$$

and

$$\mathcal{D}^{\pm}_{\downarrow}(\{t_i, \alpha_i\}_{1 \leqslant i \leqslant n}) = \left[(\hat{g}_{\downarrow})_{\alpha_i \alpha_j}(t_i, t_j) \right]_{1 \leqslant i,j \leqslant n}. \tag{17}$$

Using the cancellation of vacuum diagrams when summing over Keldysh indices, we reproduce in Appendix A the argument of Ref. [31] showing that the computation of d_n only involves the sampling of interaction times close to $t_{\max}$. As a direct consequence, Monte Carlo algorithms implementing this sum in the calculation of the weight can address any measurement time $t_{\max}$, when earlier methods were limited to short-term measurements [16–20]. We talk about the *clusterization* of interaction times in the computation of the density.

III. LARKIN-OVCHINNIKOV FORMALISM

Starting from the expression of the Green's function in the $\{\pm\}$ basis, we define its counterpart in the LO basis, $\hat{G}^{\mathrm{LO}}$,

through the following transformation [42,45]

$$\hat{G}^{\mathrm{LO}}_{\sigma}(t,t') \equiv L^{\dagger}\tau_3 \hat{G}_{\sigma}(t,t')L, \tag{18}$$

where $L = \frac{1}{\sqrt{2}}\begin{pmatrix} 1 & 1 \\ -1 & 1 \end{pmatrix}$ and $\tau_3 = \begin{pmatrix} 1 & 0 \\ 0 & -1 \end{pmatrix}$. The Green's function now takes the 2×2 form $\hat{G}^{\mathrm{LO}}_{\sigma} = \begin{pmatrix} R_\sigma & K_\sigma \\ 0 & A_\sigma \end{pmatrix}$, where R, K, and A are, respectively, the retarded, Keldysh, and advanced Green's functions defined as

$$R_\sigma(t,t') \equiv -i\theta(t-t')\langle\{c_\sigma(t), c^{\dagger}_\sigma(t')\}\rangle, \tag{19a}$$

$$A_\sigma(t,t') \equiv i\theta(t'-t)\langle\{c_\sigma(t), c^{\dagger}_\sigma(t')\}\rangle, \tag{19b}$$

$$K_\sigma(t,t') \equiv -i\langle[c_\sigma(t), c^{\dagger}_\sigma(t')]\rangle. \tag{19c}$$

In this basis, the Keldysh index $\alpha \in \{\pm\}$ is replaced by an LO index 0 or 1. In the following, l will always denote such an index unless otherwise stated.

A. Diagrammatic rules

To expose the diagrammatic rules in this formalism, let us first determine from Eq. (5) the form of the four-leg interaction vertex in the LO basis. The m_+ and m_- matrices transform as

$$L^{\dagger}\tau_3 m_+ L = \frac{1}{2}\begin{pmatrix} 1 & 1 \\ 1 & 1 \end{pmatrix} \equiv \frac{1}{2}\tau_{\uparrow}, \tag{20a}$$

$$L^{\dagger}\tau_3 m_- L = \frac{1}{2}\begin{pmatrix} -1 & 1 \\ 1 & -1 \end{pmatrix} \equiv \frac{1}{2}\tau_{\downarrow}. \tag{20b}$$

Hence the sum of different LO contributions can be written

$$-\frac{iU}{4}(\tau_\uparrow \otimes \tau_\uparrow - \tau_\downarrow \otimes \tau_\downarrow) = -\frac{iU}{2}(\mathbf{1}\otimes\tau_\downarrow + \tau_\uparrow \otimes \mathbf{1}), \tag{21}$$

where $\mathbf{1}$ is the 2×2 identity matrix. Note that this is consistent with the symmetric form $-\frac{iU}{2}(\mathbf{1}\otimes\tau + \tau\otimes\mathbf{1})$ noted in Ref. [46], where $\tau = \begin{pmatrix} 0 & 1 \\ 1 & 0 \end{pmatrix}$. The rhs form of Eq. (21) is the one we will retain in the rest of this paper. We show in Secs. III B and III C that the identity part of the vertex is essential in the proof of the cancellation of vacuum diagrams and the clusterization of times in the computation of observables.

The key point of this expression of the vertex is that we can reduce the number of indices involved in the diagrammatics using the fact that $\tau_\uparrow$ and $\tau_\downarrow$ are rank-1 matrices: $\tau_\uparrow = v_\uparrow v_\uparrow^{\top}$ with $v_\uparrow = \begin{pmatrix} 1 \\ 1 \end{pmatrix}$ and $\tau_\downarrow = v_\downarrow(-v_\downarrow^{\top})$ with $v_\downarrow = \begin{pmatrix} 1 \\ -1 \end{pmatrix}$. We can therefore absorb the τ_σ part of the vertex in a redefinition of the noninteracting propagator (see below).

An LO vertex can then be characterized by a tuple $\{t, i_\tau, l\}$, where $t \in [0, t_{\max}]$, $i_\tau \in \{-1, 1\}$ and $l \in \{0, 1\}$. $i_\tau = 1$ (resp. -1) indicates that the $\uparrow$ (resp. $\downarrow$) spin is carrying the $\tau_\uparrow$ (resp. $\tau_\downarrow$) side, and l is the LO index entering the identity part of the vertex. We store the information about both the bare propagator $\hat{g}^{\mathrm{LO}}_\sigma = \begin{pmatrix} r_\sigma & k_\sigma \\ 0 & a_\sigma \end{pmatrix}$ and the nature of the vertices it is connected to in the form of a 3×3 matrix $\hat{\tilde{g}}_\sigma$. The two first indices corresponds to a connection to the identity (with $l = 0$ or 1), and the third one to the connection to a τ_σ:

$$\left(\hat{\tilde{g}}_\sigma\right)_{ll'} = \left(\hat{g}^{\mathrm{LO}}_\sigma\right)_{ll'}, \tag{22a}$$

$$\left(\hat{\tilde{g}}_\sigma\right)_{l2} = \left(\hat{g}^{\mathrm{LO}}_\sigma v_\sigma\right)_l, \tag{22b}$$

$$\left(\hat{\tilde{g}}_\sigma\right)_{2l} = \left(\sigma v_\sigma^{\top}\hat{g}^{\mathrm{LO}}_\sigma\right)_l, \tag{22c}$$

$$\left(\hat{\tilde{g}}_\sigma\right)_{22} = \sigma v_\sigma^{\top}\hat{g}^{\mathrm{LO}}_\sigma v_\sigma, \tag{22d}$$

with the convention that $\sigma = \uparrow$ should be understood as $+1$ and $\sigma = \downarrow$ as -1.

We obtain

$$\hat{\tilde{g}}_\sigma = \begin{pmatrix} r_\sigma & k_\sigma & r_\sigma + \sigma k_\sigma \\ 0 & a_\sigma & \sigma a_\sigma \\ \sigma r_\sigma & \sigma k_\sigma + a_\sigma & \sigma[r_\sigma + a_\sigma] + k_\sigma \end{pmatrix}. \tag{23}$$

To simplify upcoming equations, we express the indices of $\hat{\tilde{g}}_\uparrow$ and $\hat{\tilde{g}}_\downarrow$ at a vertex $\{t, i_\tau, l\}$ in the form of two composite indices $L^\uparrow$ and $L^\downarrow$:

$$L^\sigma = \begin{cases} 2 & \text{if } i_\tau = \sigma \\ l & \text{otherwise} \end{cases} \tag{24}$$

Note that this 3×3 form of the Green's function comes from the absorption of the τ_σ part of the vertex and has nothing to do with the Baym-Kadanoff L-shaped contour used in thermal real-time computations.

With this notation, a straight line represents a noninteracting (modified) Green's function

$$t', L'^{\sigma} \xrightarrow{\ \sigma\ } t, L^\sigma = i\left(\hat{\tilde{g}}_\sigma\right)_{L^\sigma L'^\sigma}(t,t'). \tag{25}$$

As discussed previously, the interaction vertex, proportional to the identity in the $\{\pm\}$ basis, is now proportional to $\frac{\mathbf{1}\otimes\tau_\downarrow + \tau_\uparrow\otimes\mathbf{1}}{2}$ in the $\mathcal{H}_\uparrow \otimes \mathcal{H}_\downarrow$ space

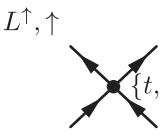

$$= -\frac{iU}{2}\left(\delta_{i_\tau 1}\delta_{L^\uparrow 2}\delta_{L^\downarrow l} + \delta_{i_\tau -1}\delta_{L^\downarrow 2}\delta_{L^\uparrow l}\right). \tag{26}$$

As $m_+ - m_-$ transforms into the 2×2 identity matrix in the LO basis, a two-leg vertex is simply characterized by an interaction time t and an LO index l. A term $hc^{\dagger}_\sigma c_\sigma$ in the Hamiltonian would therefore give rise to the following vertex

$$L^\sigma \xrightarrow[\{t,l\}]{\sigma\ \ h\ \ \sigma} L^\sigma = -ih\delta_{L^\sigma l}. \tag{27}$$

With this expression of the interaction vertex, the following fermionic bubble

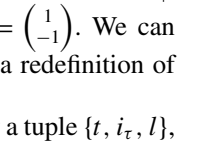

evaluates to

$$\frac{U}{2}\delta_{L^\sigma 2}[r_{\bar\sigma}(t,t) + a_{\bar\sigma}(t,t)] + \frac{U}{2}\delta_{L^\sigma l}[\bar\sigma r_{\bar\sigma}(t,t) + \bar\sigma a_{\bar\sigma}(t,t) + k_{\bar\sigma}(t,t)]. \tag{28}$$

For the equal-time limit of the retarded, Keldysh, and advanced Green's function, we choose a convention which ensures the consistency between the $\{\pm\}$ and LO basis. We consider

$$k_\sigma(t,t) = 2g^{<}_\sigma(t,t), \tag{29a}$$

$$r_\sigma(t,t) = a_\sigma(t,t) = 0, \tag{29b}$$

and we show that this is consistent with Eq. (8). Using Eq. (29), the above fermionic bubble reduces to $Ug^<_{\bar\sigma}(t,t)\delta_{L^\sigma l}$. It can be rewritten as a two-leg vertex with a $iUg^<_{\bar\sigma}(t,t)$ field

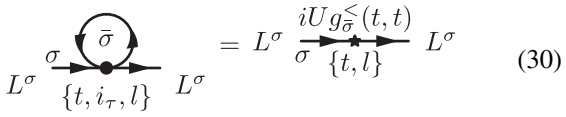

(30)

This equation is, up to a change of basis, the same as Eq. (9). The choice of equal time limit described in Eq. (29) is therefore consistent with the $\{\pm\}$ basis formalism.

The order-n contribution to the quantity $\mathcal{M}$ we want to measure in an expansion in U is similar to Eq. (10) but has to take account of the new form of the vertex

$$\mathcal{M}_n = \int_0^{t_{\max}} \mathrm{d}t_1 \dots \mathrm{d}t_n \sum_{\substack{i_{\tau_1} \dots i_{\tau_n} \\ l_1 \dots l_n}} \mathcal{M}_n^{\mathrm{LO}}(\{t_i, i_{\tau_i}, l_i\}_{1\leqslant i\leqslant n}), \quad (31)$$

where the $\mathcal{M}_n^{\mathrm{LO}}(\{t_i, i_{\tau_i}, l_i\}_{1\leqslant i\leqslant n})$ can once again be expressed as a product of determinants, their precise form depending on the computed quantity. This formalism leads to 4^n LO configurations for a given set of n interaction times, to be compared with 2^n possible configurations in the $\pm$ basis. However, we show in the next section that vacuum diagrams now directly cancel in this formalism, without the actual need to perform an explicit sum over all configurations.

B. Cancellation of vacuum diagrams

In this section, we show the main result of this paper: Contributions to the partition function are directly equal to zero in the LO basis. For all $n \geqslant 1$, $\{t_1, \dots, t_n\} \in [0, t_{\max}]^n$, $\{i_{\tau_1}, \dots, i_{\tau_n}\} \in \{-1, 1\}^n$, $\{l_1, \dots, l_n\} \in \{0, 1\}^n$,

$$Z_n^{\mathrm{LO}}\left(\{t_i, i_{\tau_i}, l_i\}_{1\leqslant i\leqslant n}\right) = 0, \quad (32)$$

where the contributions to the partition function are

$$Z_n^{\mathrm{LO}}\left(\{t_i, i_{\tau_i}, l_i\}_{1\leqslant i\leqslant n}\right) = \left(-\frac{i}{2}\right)^n i^n i^n \prod_\sigma \det\left[(\hat{\hat g}_\sigma)_{L_i^\sigma L_j^\sigma}(t_i, t_j)\right]_{1\leqslant i,j\leqslant n}. \quad (33)$$

Each $-\frac{i}{2}$ comes from Eq. (26) and the two i^n factors from the fact that a straight line actually represents an $i\hat{\hat g}$ [Eq. (25)].

Let us consider an order $n \geqslant 1$ diagram contributing to Z. The interaction times are denoted $t_1, \dots, t_n$. We introduce $\hat t = \max_i t_i$ and $\hat\imath$ such that $t_{\hat\imath} = \hat t$. We label σ the spin on the identity side of the $(\mathbf{1}\otimes\tau_\downarrow + \tau_\uparrow \otimes \mathbf{1})/2$ interaction vertex at $\hat t$ and l the corresponding LO index. We consider the diagrammatic line following spin σ. If $\hat t$ is surrounded by no other interaction vertex, the diagram is then proportional to

$$(\hat{\hat g}_\sigma)_{ll}(\hat t, \hat t) = \delta_{l0} r_\sigma(\hat t, \hat t) + \delta_{l1} a_\sigma(\hat t, \hat t) = 0. \quad (34)$$

In the case where $\hat t$ is surrounded by at least one other interaction vertex, we label its surrounding interaction times (that can be equal) t_i and t_j, i, $j \neq \hat\imath$, with corresponding composite indices L_i^σ, L_j^σ. We then obtain

$$(\hat{\hat g}_\sigma)_{L_j^\sigma l}(t_j, \hat t) = \delta_{L_j^\sigma 2}\delta_{l1}[\sigma k_\sigma(t_j, \hat t) + a_\sigma(t_j, \hat t)] + \delta_{L_j^\sigma 1}\delta_{l1} a_\sigma(t_j, \hat t) + \delta_{L_j^\sigma 0}\delta_{l1} k_\sigma(t_j, \hat t), \quad (35)$$

and

$$(\hat{\hat g}_\sigma)_{l L_i^\sigma}(\hat t, t_i) = \delta_{L_i^\sigma 2}\delta_{l0}[r_\sigma(\hat t, t_i) + \sigma k_\sigma(\hat t, t_i)] + \delta_{L_i^\sigma 1}\delta_{l0} k_\sigma(\hat t, t_i) + \delta_{L_i^\sigma 0}\delta_{l0} r_\sigma(\hat t, t_i). \quad (36)$$

The full diagram is then proportional to $\delta_{l0}\delta_{l1} = 0$. Hence every diagram contributing to Z in the LO basis is exactly equal to 0. This formalism *directly cancels vacuum diagrams*.

Finally, we note that this proof relies only on having the identity on one side of the interaction vertex and not on the explicit contraction with $\tau_\uparrow, \tau_\downarrow$. Had we kept the diagrammatics with $\hat g$ lines instead of $\hat{\hat g}$ ones, we would also obtain the cancellation of vacuum diagrams.

C. Density computation and clusterization

In order to understand how to write the density of $\uparrow$ electrons on the energy level in the LO basis, we use the following property of the Keldysh formalism: The average value of an operator does not depend on the branch of $\mathcal{C}$ where it is computed. Considering d on the $+$ branch of the contour, the computation of the density can be understood as the action of the m_+ matrix in the $\{\pm\}$ basis, which transforms in the $\frac{1}{2}\tau_\uparrow$ matrix in the LO basis according to Eq. (20a). Hence we can represent the measurement vertex as a "special" interaction vertex at time $t_{\max}$ with $i_\tau = 1$:

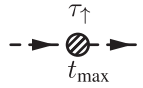

(37)

As previously, surrounding lines are dashed because they bear a $\hat{\hat g}$ (and not an $i\hat{\hat g}$). Hence the order-n contribution to d reads

$$d_n = \int_0^{t_{\max}} \mathrm{d}t_1 \dots \mathrm{d}t_n \sum_{\substack{i_{\tau_1} \dots i_{\tau_n} \\ l_1 \dots l_n}} \left(-\frac{i}{2}\right)^n \frac{i^{n+1} i^n}{i^2} \times \prod_\sigma \det \mathcal{D}_\sigma^{\mathrm{LO}}\left(\{t_i, i_{\tau_i}, l_i\}_{1\leqslant i\leqslant n}\right). \quad (38)$$

The $\mathcal{D}_\sigma^{\mathrm{LO}}$ matrices are defined as

$$\mathcal{D}_\uparrow^{\mathrm{LO}}\left(\{t_i, i_{\tau_i}, l_i\}_{1\leqslant i\leqslant n}\right) = \begin{pmatrix} & & (\hat{\hat g}_\uparrow)_{L_1^\uparrow 2}(t_1, t_{\max}) \\ \left[(\hat{\hat g}_\uparrow)_{L_i^\uparrow L_j^\uparrow}(t_i, t_j)\right]_{1\leqslant i,j\leqslant n} & & \vdots \\ & & (\hat{\hat g}_\uparrow)_{L_n^\uparrow 2}(t_n, t_{\max}) \\ (\hat{\hat g}_\uparrow)_{2L_1^\uparrow}(t_{\max}, t_1) & \dots & (\hat{\hat g}_\uparrow)_{2L_n^\uparrow}(t_{\max}, t_n) \quad (\hat{\hat g}_\uparrow)_{22}(t_{\max}, t_{\max}) \end{pmatrix}, \quad (39)$$

and

$$\mathcal{D}_\downarrow^{\mathrm{LO}}\left(\{t_i, i_{\tau_i}, l_i\}_{1\leqslant i\leqslant n}\right) = \left[(\hat{\hat g}_\downarrow)_{L_i^\downarrow L_j^\downarrow}(t_i, t_j)\right]_{1\leqslant i,j\leqslant n}. \quad (40)$$

Before considering the clusterization of interaction times, we note that half of the contributions to the density vanish. Let us consider a given set $\{t_i, i_{\tau_i}, l_i\}_{1\leqslant i\leqslant n}$ of LO vertices at order n, and let us label $\hat{t} = \max_i t_i$ and $\hat{i}$ such that $t_{\hat{i}} = \hat{t}$. If $i_{\tau_{\hat{i}}} = 1$, then the $\downarrow$ spin is carrying the identity side of the vertex. As we measure the density on the $\uparrow$ spin, the argument used in the cancellation vacuum diagrams (see III B) applies again and $\mathcal{D}^{\mathrm{LO}}_{\downarrow}(\{t_i, i_{\tau_i}, l_i\}_{1\leqslant i\leqslant n})$ is the $n\times n$ null matrix. If $i_{\tau_{\hat{i}}} = -1$, the contribution does not vanish. Hence, when computing the density, at every order n and for every set of n interaction times, $4^n/2$ LO configurations (out of 4^n) are exactly zero.

The clusterization of interaction times around $t_{\max}$ in the calculation of the density is then a direct consequence of the cancellation of vacuum diagrams and is very similar to the proof in the $\{\pm\}$ basis (now without the exponential sum). Let n be a given perturbation order and $t_1 < t_2 < \cdots < t_n$ n interaction times. Let us assume that the first j times are located far away from the measurement time $t_{\max}$ and that the last $n-j$ times are located in the vicinity of $t_{\max}$. We can formally consider

$$\forall 1 \leqslant i \leqslant j, \quad |t_i - t_{\max}| \to \infty. \tag{41}$$

Because the Green's function is a local quantity in time, this means that for all $t \in \{t_1, \ldots, t_j\}, t' \in \{t_{j+1}, \ldots, t_n; t_{\max}\}$

$$\|\hat{\hat{g}}_\sigma(t,t')\| \to 0, \quad \|\hat{\hat{g}}_\sigma(t',t)\| \to 0. \tag{42}$$

We therefore have

$$\prod_\sigma \det \mathcal{D}^{\mathrm{LO}}_\sigma\left(\{t_i, i_{\tau_i}, l_i\}_{1\leqslant i\leqslant n}\right) \simeq \prod_\sigma \det A_\sigma \prod_\sigma \det B_\sigma, \tag{43}$$

with

$$A_\sigma = \left[(\hat{\hat{g}})_{L_i^\sigma L_{i'}^\sigma}(t_i, t_{i'})\right]_{1\leqslant i,i'\leqslant j}, \tag{44a}$$

$$B_\downarrow = \left[(\hat{\hat{g}})_{L_i^\downarrow L_{i'}^\downarrow}(t_i, t_{i'})\right]_{j+1\leqslant i,i'\leqslant n}, \tag{44b}$$

and $B_\uparrow$ is the $\left[(\hat{\hat{g}})_{L_i^\uparrow L_{i'}^\uparrow}(t_i, t_{i'})\right]_{j+1\leqslant i,i'\leqslant n}$ matrix where a last line and column corresponding to $t_{\max}$ are added, similar to Eq. (39). However, $\prod_\sigma \det A_\sigma$ is a contribution to Z at order j, and it vanishes according to (32). Therefore $\prod_\sigma \det D_\sigma \simeq 0$, and this proves the clusterization of times around $t_{\max}$ in the computation of the density. In the next section, we present different algorithms to stochastically sample Eqs. (15) and (38).

IV. MONTE CARLO IMPLEMENTATION

In this section, we describe how to compute the density d introduced above using quantum Monte Carlo (MC) techniques. We present three different algorithms to compute this quantity, one using the $\pm$ algorithm presented in Ref. [31] and the other two based on the LO formalism presented above.

A. Monte Carlo algorithms

We first describe how to stochastically generate MC configurations to sample the order-n contribution, d_n, as expressed in Eqs. (15) and (38). The $\pm$ algorithm works directly on the Keldysh contour. A configuration $\mathfrak{c}$ is determined by a given perturbation order n and a set of n interaction times (and *not* Keldysh points): $\mathfrak{c} = \{n; t_1, \ldots, t_n\}$. The contribution to d_n of a given configuration is

$$w^\pm_{\mathfrak{c}} = -i^{n+1} \sum_{\alpha_1\ldots\alpha_n} \alpha_1 \ldots \alpha_n \prod_\sigma \det \mathcal{D}^\pm_\sigma(\{t_i, \alpha_i\}_{1\leqslant i\leqslant n}). \tag{45}$$

In the Monte Carlo, configurations are sampled stochastically according to their weight, which we choose to be $|w^\pm_{\mathfrak{c}}|$. We then have

$$d_n = \int_0^{t_{\max}} \mathrm{d}t_1 \ldots \mathrm{d}t_n\, w^\pm_{\mathfrak{c}} \propto \sum_{\mathfrak{c}}^{\mathrm{MC}\,\pm} \operatorname{sign} w^\pm_{\mathfrak{c}}. \tag{46}$$

Note that it was shown in Ref. [31] that $w^\pm_{\mathfrak{c}} \in \mathbb{R}$.

In the LO algorithm, a configuration $\mathfrak{c}$ is now determined by a given perturbation order n and a set of n interaction LO vertices: $\mathfrak{c} = \{n; y_1, \ldots, y_n\}$, where $y_i = \{t_i, i_{\tau_i}, l_i\}$. Because the density is a real quantity, the contributions to d_n of a configuration $\mathfrak{c}$ can be written as

$$w^{\mathrm{LO}}_{\mathfrak{c}} = -\frac{1}{2^{n+1}} \mathrm{Re}\left(i^{n+1} \prod_\sigma \det \mathcal{D}^{\mathrm{LO}}_\sigma(\mathfrak{c})\right). \tag{47}$$

If $|w^{\mathrm{LO}}_{\mathfrak{c}}|$ is the statistical weight of $\mathfrak{c}$ in the Monte Carlo process, then

$$d_n = \int_0^{t_{\max}} \mathrm{d}t_1 \ldots \mathrm{d}t_n \sum_{\substack{i_{\tau_1}\ldots i_{\tau_n}\\ l_1\ldots l_n}} w^{\mathrm{LO}}_{\mathfrak{c}} \propto \sum_{\mathfrak{c}}^{\mathrm{MC\,LO}} \operatorname{sign} w^{\mathrm{LO}}_{\mathfrak{c}}. \tag{48}$$

The third algorithm that we study is a mixed algorithm that samples the configurations according to their LO weight $|w^{\mathrm{LO}}_{\mathfrak{c}}|$ but computes d_n in the original $\{\pm\}$ basis, from the contributions $w^\pm_{\mathfrak{c}}$ at the sampled times. A configuration $\mathfrak{c}$ is then determined by a given perturbation order n and a set of n interaction LO vertices: $\mathfrak{c} = \{n; y_1, \ldots, y_n\}$ and the MC weight is $|w^{\mathrm{mixed}}_{\mathfrak{c}}| = |w^{\mathrm{LO}}_{\mathfrak{c}}|$, so that

$$\begin{aligned} d_n &= \frac{1}{\mathcal{N}} \int_0^{t_{\max}} \mathrm{d}t_1 \ldots \mathrm{d}t_n \sum_{\substack{i_{\tau_1}\ldots i_{\tau_n}\\ l_1\ldots l_n}} \left|w^{\mathrm{LO}}_{\mathfrak{c}}\right| \frac{w^\pm_{\mathfrak{c}}}{\left|w^{\mathrm{LO}}_{\mathfrak{c}}\right|} \\ &\propto \frac{1}{\mathcal{N}} \sum_{\mathfrak{c}}^{\mathrm{MC\ mixed}} \frac{w^\pm_{\mathfrak{c}}}{\left|w^{\mathrm{LO}}_{\mathfrak{c}}\right|}, \end{aligned} \tag{49}$$

where $\mathcal{N}$ is the number of nonzero LO configurations. When computing the density, $\mathcal{N} = 4^n/2$ at order n (see Sec. III C).

In all three techniques, we use a standard Metropolis algorithm [47] to generate Markov chains distributed according to the weights $|w_{\mathfrak{c}}|$. Starting from a given configuration $\mathfrak{c}$, a new configuration $\mathfrak{c}'$ is proposed according to one of the following two Monte Carlo updates:

(1) Remove a randomly chosen interaction time (for the $\pm$ algorithm) or interaction LO vertex (for the LO and mixed algorithms) from $\mathfrak{c}$.

(2) Add a new interaction time (for the $\pm$ algorithm) or an interaction LO vertex (for the LO and mixed algorithms). In all three techniques, because of the clusterization of times around $t_{\max}$, we choose the new interaction time according to a Cauchy law (see below). We randomly choose the i_τ and l indices.

The new configuration $\mathfrak{c}'$ is accepted or rejected with the usual Metropolis ratio

$$p^{\text{accept}}_{\mathfrak{c}\to\mathfrak{c}'} = \min\left(1, \frac{T_{\mathfrak{c}'\mathfrak{c}}|w_{\mathfrak{c}'}|}{T_{\mathfrak{c}\mathfrak{c}'}|w_{\mathfrak{c}}|}\right), \tag{50}$$

where $T_{\mathfrak{c}\mathfrak{c}'}$ is the probability to propose $\mathfrak{c}'$ after $\mathfrak{c}$.

B. Proposition of times

We have shown previously that times clusterize around $t_{\max}$. It is therefore more efficient to propose times located around it compared to uniformly distributed between 0 and $t_{\max}$. We consider a Cauchy law determined by two parameters t_0 and a

$$\rho(t) = \frac{1}{C}\frac{1}{1+\left(\frac{t-t_0}{a}\right)^2}. \tag{51}$$

C is a normalization factor such that the integral of ρ between 0 and $t_{\max}$ gives 1, defined as $C = a[C_2 - C_1]$, where $C_1 = \arctan\left(-\frac{t_0}{a}\right)$ and $C_2 = \arctan\left(\frac{t_{\max}-t_0}{a}\right)$.

To obtain a new time that follows this probability law, one can perform these three steps:

(1) Choose a random number u uniformly distributed between 0 and 1.

(2) Construct

$$x = \frac{1}{2} + \frac{1}{\pi}[(1-u)C_1 + uC_2], \tag{52}$$

uniformly distributed between $\frac{1}{2} + \frac{1}{\pi}C_1$ and $\frac{1}{2} + \frac{1}{\pi}C_2$.

(3) Compute

$$t = t_0 + a\tan\left(\pi\left(x - \tfrac{1}{2}\right)\right), \tag{53}$$

distributed between 0 and $t_{\max}$ according to ρ.

The parameters t_0 and a are then fitted to the 1D projection of times visited by the Monte Carlo, accumulated during the first part of the computation.

C. Redefinition of noninteracting propagators

As shown in previous works [12,31,48,49], there is some freedom in the choice of the noninteracting propagator used to construct the perturbation expansion, since the interaction can be redefined as

$$Un_\uparrow n_\downarrow = U(n_\uparrow - \alpha)(n_\downarrow - \alpha) + U\alpha(n_\uparrow + n_\downarrow) + \text{const.} \tag{54}$$

Note that in this subsection α *does not* denote a Keldysh index but a scalar, in order to be consistent with the existing literature. In particular, it was shown that α can strongly modify the radius of convergence of the perturbation series [31,48]. This redefinition of the interaction term in Eq. (54) is taken into account by subtracting α on the diagonal of the determinants as explained and proved in Ref. [31]. The second term in Eq. (54) acts as a shift in the chemical potential and can be absorbed in a redefinition of the noninteracting propagators.

Let us first consider the LO basis. This shift acts a diagonal term in the self-energy and hence in

$$\left(\hat{g}^{\text{LO}}_\sigma\right)^{-1} = \begin{pmatrix} r_\sigma^{-1} & -k_\sigma/|r_\sigma|^2 \\ 0 & a_\sigma^{-1} \end{pmatrix}. \tag{55}$$

α therefore modifies r_σ and a_σ into

$$\bar{r}_\sigma(\omega) = [r(\omega)^{-1} - U\alpha]^{-1}, \tag{56}$$

$$\bar{a}_\sigma(\omega) = [a(\omega)^{-1} - U\alpha]^{-1}. \tag{57}$$

As $k_\sigma/|r_\sigma|^2$ is not impacted by the shift, the modified Keldysh Green's function is then

$$\bar{k}_\sigma(\omega) = \left|\frac{\bar{r}_\sigma(\omega)}{r_\sigma(\omega)}\right|^2 k_\sigma(\omega). \tag{58}$$

From these expressions, we can then deduce the modified Green's functions in the $\{\pm\}$ basis through a change of basis transformation.

D. Normalization procedure

All Monte Carlo algorithms presented above compute the order-n contribution to the density d, however the MC results need to be normalized. Hence we restrict our calculation to two consecutive orders, n and $n+1$, and a time or vertex can be added (resp. removed) only if the current configuration $\mathfrak{c}$ is at order n (resp. $n+1$). We measure both the density (d_n and d_{n+1}) and a normalization factor (η_n and η_{n+1}). In all algorithms, the normalization factor is chosen to be the sum of the absolute value of the contributions to the density:

$$\eta_n \propto \sum_{\mathfrak{c}}^{\text{MC}} |w_{\mathfrak{c}}|, \tag{59}$$

where the proportionality constant is the same as in the calculation of d_n. If $\tilde{d}_n$ and $\tilde{\eta}_n$ are the unrenormalized sums of the contributions accumulated in the Monte Carlo procedure, then the normalized values for d_n and η_n are obtained as

$$d_{n+1} = \frac{\eta_n}{\tilde{\eta}_n}\tilde{d}_{n+1}; \qquad \eta_{n+1} = \frac{\eta_n}{\tilde{\eta}_n}\tilde{\eta}_{n+1}, \tag{60}$$

and η_n is then used to normalize the following simulation between orders $n+1$ and $n+2$. The lowest order is computed analytically to close the equations.

V. RESULTS

A. Density

In this section, we present actual computations of the density according to the algorithms described in the previous section and compare their efficiency. In the following, we consider an energy level ϵ_d coupled to a bath described by a semicircular density of states of bandwidth $4t$. The Green's function describing this bath is defined on the complex plane as [8]

$$g_{\text{bath}}(\zeta) = \frac{\zeta - \text{sgn}(\text{Im}\zeta)\sqrt{\zeta^2 - 4t^2}}{2t^2}. \tag{61}$$

The noninteracting retarded Green's function of the impurity level is

$$r_\sigma(\omega) = \frac{1}{\omega - \epsilon_d - \gamma^2 g_{\text{bath}}(\omega)}, \tag{62}$$

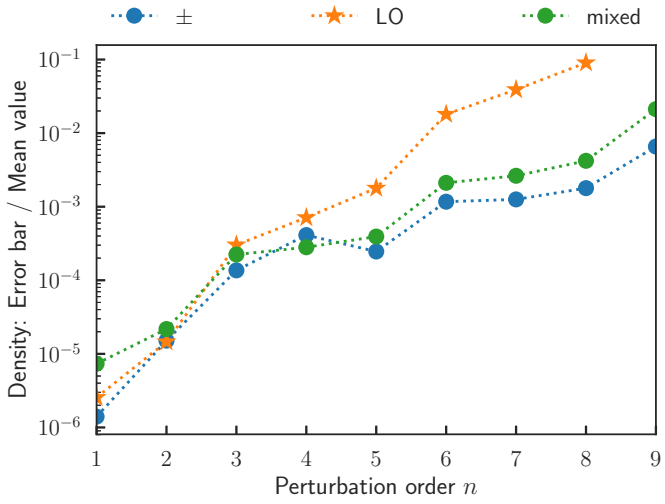

FIG. 1. Comparison of the error bar divided by the mean value in a density computation, for the three different MC algorithms considered: the one working in the Keldysh ± basis (blue dots), the one in the LO basis (orange stars), and the mixed algorithm (green dots, see text). $t = 1$, $\beta t = 100$, $\gamma^2 = 0.04t^2$, $\epsilon_d = -0.36t$, $U = 1.2t$, $\alpha = 0.3$. Computational effort is 240 CPU*hours for every order.

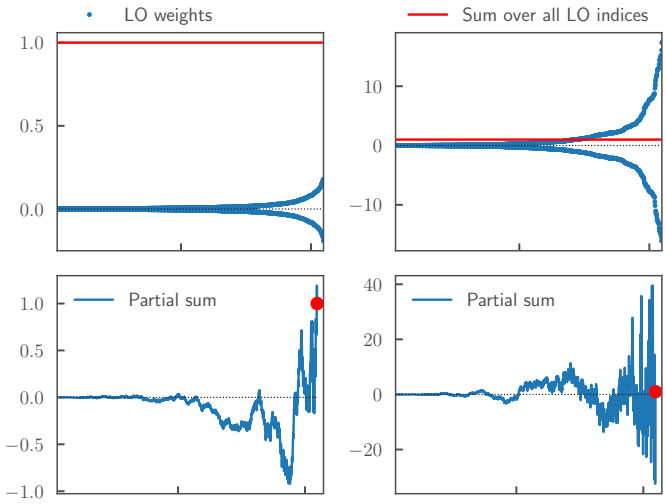

FIG. 2. Upper panel: Sorted array of the LO weights according to their absolute value (blue dots) and their sum (red line), normalized to 1. Lower panel: Partial sum of the above LO weights, from left to right, the red dot being the last point, by definition 1. Left panels correspond to the $T_1 = \{273.2, 277.8, 280.9, 331.7, 366.4, 390.5\}$ time configuration, and the right panels to $T_2 = \{338.3, 343.2, 366.9, 369.7, 393.9, 394.5\}$. Order 7, $t_{\max} = 400$.

where γ is a coupling term between the energy level and the bath. The Keldysh Green's function is then deduced using the fluctuation-dissipation theorem

$$k_\sigma(\omega) = \tanh\left(\frac{\beta\omega}{2}\right)[r_\sigma(\omega) - r_\sigma^*(\omega)]. \tag{63}$$

In the following, $t = 1$ is our energy unit. We consider $\beta t = 100$, $\gamma^2 = 0.04t^2$, $\epsilon_d = -0.36t$. Electrons on the impurity experience a local Coulomb interaction $U = 1.2t$. We choose the α shift to be $\alpha = 0.3$ (see Sec. IV C), such that $U\alpha = -\epsilon_d$. The bath being particle-hole symmetric, this creates a shifted retarded Green's function $\bar{r}(\omega)$ that is itself particle-hole symmetric [see Eq. (56)]. However, we have checked that this particular choice of α does not influence our conclusions. We provide in Appendix B a table benchmarking the LO and mixed algorithms against the original ± algorithm. This shows in particular that the LO and mixed algorithms yield correct results and that we can indeed reach long times in the LO algorithm without an exponential sum of determinants.

Our main result is shown in Fig. 1 where we compare the relative error bar in the density computation as a function of the perturbation order. Blue dots denote the ± algorithm, orange stars the LO algorithm, and green dots the mixed algorithm. The order-9 relative error is not shown for the LO algorithm as it exceeds 1 and is therefore meaningless. In all three cases, dotted lines are guides to the eye. The computational time is 240 CPU*hours for each order.

We see that all three relative error bars increase with perturbation order. This can either come from the increasing difficulty of computing the series coefficients, or an error propagation coming from the normalization factor η. We plot in Appendix C the relative error bar on η, which is much smaller than the final relative error on the density, showing that the latter mainly comes from the increasing difficulty to compute higher order coefficients. Moreover, the LO relative error bars very quickly become much larger than the ± ones, their difference nearly reaching two orders of magnitude at order 8. The mixed algorithm is found to perform better than the LO algorithm but its error bars slowly grow larger than the ± ones. This is surprising, as one could have expected to at least gain the decorrelation time over the algorithm of Ref. [31]. We discuss the origin of the error bars in both algorithms in the next section.

B. The return of the sign problem

In this section, we discuss the origin of the large variance in the computation of the density in the LO algorithm in terms of a sign problem in the Monte Carlo sampling and we show how this impacts the error bars of the mixed algorithm.

In the upper panel of Fig. 2, we plot as blue dots the nonzero LO weights for two different time configurations, sorted according to their absolute value. The left and right panel correspond to two different time configurations (Cf caption). In both cases, the red line indicates the full sum over all LO indices, normalized to 1 (which coincides with the ± weight). The lower panel shows the partial sum, from left to right, of the LO weights plotted above. The last point, equal to 1 by construction, is emphasized as a red dot. As roughly half of the weights are positive and half negative, we see that the sum of the LO weights over the indices at fixed time configuration is characterized by a massive cancellation. This is the origin of the large error bar in the Monte-Carlo, i.e., another manifestation of the sign problem. Furthermore, the partial sum shows that there is no clear feature or cutoff from which one could extract the value of the full sum.

Let us now turn to the mixed algorithm. In both the left and right panels of Fig. 2, the sum over all LO indices, which coincides with the ± weight, is normalized to 1. However, in

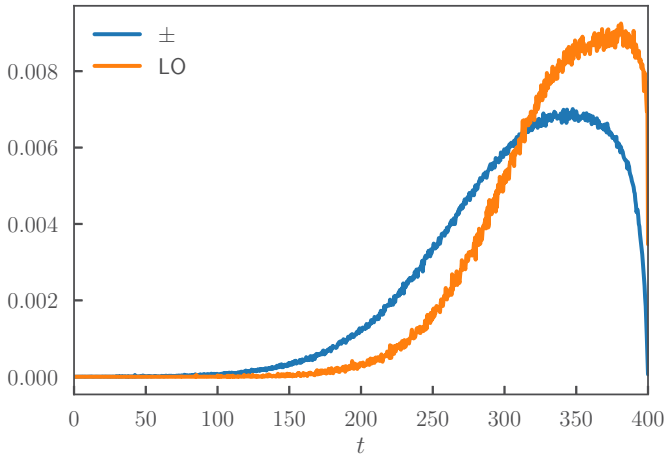

FIG. 3. Histograms of the times visited by the Monte Carlo algorithms, projected in one dimension. Order 9, $t_{\max} = 400$.

the left panel, the weights of the different LO configurations are small compared to the final result, reaching at most 20% of it. In the right panel, those same weights are much bigger, reaching up to 1700% of the full sum. Hence the Monte Carlo implemented in the LO basis does not sample the same time configurations as the algorithm in the {±} basis. This is illustrated in Fig. 3 where the histograms of the times visited by the Monte Carlo, projected in one dimension, are plotted for both the ± algorithm (blue line) and LO one (orange line). First, we observe the clusterization of times proved at the beginning of this paper: Interaction times contributing to the density tend to be in the vicinity of $t_{\max}$. Then, we see that some times located far away from the measurement but still contributing significantly to the ± algorithm are almost never visited in the LO algorithm. On the other hand, times close to $t_{\max}$ are more sampled in the latter. As times visited by the mixed algorithm coincide with the LO ones, this explains the difference in error bars between the mixed and ± algorithms observed in Fig. 1.

VI. CONCLUSION

In conclusion, the explicit sum over the Keldysh indices of the original ± algorithm of Ref. [31] has two functions: (i) it allows us to reach the very long times due to the clusterization of the integrand caused by the cancellation of vacuum diagrams; (ii) it strongly reduces the error bar by performing a massive cancellation of terms. In this paper, we have shown that one can obtain the first properties for each determinant using the Larkin-Ovchinnikov basis, hence without the exponentially large sum of determinants. A direct implementation of the algorithm in the LO basis indeed reaches the steady state but also has an error bar growing quickly with the order n due to a sign problem. An interesting possibility would be the existence of an optimum between the LO and original ± algorithms, using partial groupings of terms in the LO basis with less than 2^n terms that would reduce the sign problem and yields a better scaling than the original algorithm in the {±} basis. Work is in progress in this direction.

ACKNOWLEDGMENTS

We are grateful to Xavier Waintal and Antoine Georges for useful discussions. This work was partly supported by the European Research Council Grant No. ERC-278472-MottMetals (P.S., O.P.). The Flatiron Institute is a division of the Simons Foundation. Part of this work was performed using HPC resources from GENCI (Grant No. A0050510609).

APPENDIX A: CLUSTERIZATION OF THE DENSITY IN THE {±} BASIS

We reproduce here the argument of Ref. [31] showing that the cancellation of vacuum diagrams when summing over Keldysh indices implies the clusterization of interaction times near $t_{\max}$. Let n be a given perturbation order, and $t_1 < t_2 < \cdots < t_n$ n interaction times. Let's assume that the first j times are located far away from the measurement time $t_{\max}$ and that the last $n - j$ times are located in the vicinity of $t_{\max}$. We can formally consider

$$\forall 1 \leqslant i \leqslant j, \quad |t_i - t_{\max}| \to \infty. \tag{A1}$$

Because the Green's function is a local quantity, this means that for all $t \in \{t_1, \ldots, t_j\}, t' \in \{t_{j+1}, \ldots, t_n; t_{\max}\}$

$$||\hat{g}_\sigma(t, t')|| \to 0, \quad ||\hat{g}_\sigma(t', t)|| \to 0. \tag{A2}$$

We therefore have

$$\sum_{\alpha_1 \ldots \alpha_n} \alpha_1 \ldots \alpha_n \prod_\sigma \det \mathcal{D}^{\pm}_\sigma\left(\{t_i, i_{\tau_i}, l_i\}_{1 \leqslant i \leqslant n}\right)$$
$$\simeq \sum_{\alpha_1 \ldots \alpha_j} \alpha_1 \ldots \alpha_j \prod_\sigma \det A_\sigma \sum_{\alpha_{j+1} \ldots \alpha_n} \alpha_{j+1} \ldots \alpha_n \prod_\sigma \det B_\sigma, \tag{A3}$$

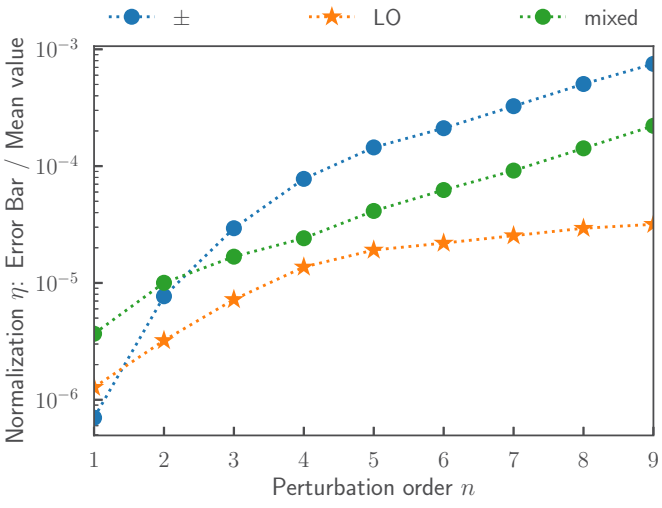

FIG. 4. Comparison of the error bar divided by the mean value of the normalization coefficient, for the three different MC algorithms considered: the one working in the Keldysh ± basis (blue dots), the one in the LO basis (orange stars) and the mixed algorithm (green dots). $t = 1$, $\beta t = 100$, $\gamma^2 = 0.04t^2$, $\epsilon_d = -0.36t$, $U = 1.2t$, $\alpha = 0.3$. Computational effort is 240 CPU*hours for every order.

with

$$A_\sigma = \left[(\hat{g}_\sigma)_{\alpha_i\alpha'_i}(t_i, t_{i'})\right]_{1\leqslant i,i'\leqslant j}, \tag{A4a}$$

$$B_\downarrow = \left[(\hat{g}_\downarrow)_{\alpha_i\alpha'_i}(t_i, t_{i'})\right]_{j+1\leqslant i,i'\leqslant n}, \tag{A4b}$$

and $B_\uparrow$ is the $[(\hat{g}_\uparrow)_{\alpha_i\alpha'_i}(t_i, t_{i'})]_{j+1\leqslant i,i'\leqslant n}$ matrix where a last line and column corresponding to $t_{\max}$ are added, similar to Eq. (16). However, $\sum_{\alpha_1\ldots\alpha_j} \alpha_1\ldots\alpha_j \prod_\sigma \det A_\sigma$ is a contribution to Z at order j, and it vanishes according to (12). Therefore $\sum_{\alpha_1\ldots\alpha_n} \alpha_1\ldots\alpha_n \prod_\sigma \det D^\pm_\sigma \simeq 0$, and this proves the clusterization of times in around $t_{\max}$ in the computation of the density.

APPENDIX B: BENCHMARK

The table below benchmarks the contributions to the density between the $\pm$, LO, and mixed algorithms. We take $t = 1$ as our energy unit, and parameters are $\beta t = 100$, $\gamma^2 = 0.04t^2$, $\epsilon_d = -0.36t$, $U = 1.2t$, $\alpha = 0.3$. Computation effort is 240 CPU*hours for each perturbation order.

	$\pm$	LO	mixed
Order 1	$-1.7013454 \pm 0.00014\%$	$-1.7013431 \pm 0.00026\%$	$-1.7013466 \pm 0.00073\%$
Order 2	$14.47243 \pm 0.0015\%$	$14.47252 \pm 0.0015\%$	$14.47214 \pm 0.0022\%$
Order 3	$-33.3479 \pm 0.014\%$	$-33.3610 \pm 0.030\%$	$-33.3583 \pm 0.022\%$
Order 4	$-431.09 \pm 0.041\%$	$-431.51 \pm 0.071\%$	$-431.30 \pm 0.028\%$
Order 5	$5094.7 \pm 0.025\%$	$5100.6 \pm 0.18\%$	$5092.6 \pm 0.039\%$
Order 6	$-16173 \pm 0.12\%$	$-15802 \pm 1.8\%$	$-16171 \pm 0.21\%$
Order 7	$-1.6411 \times 10^5 \pm 0.13\%$	$-1.6595 \times 10^5 \pm 3.9\%$	$-1.6554 \times 10^5 \pm 0.26\%$
Order 8	$2.2332 \times 10^7 \pm 0.18\%$	$2.1071 \times 10^7 \pm 9.0\%$	$2.2316 \times 10^7 \pm 0.42\%$
Order 9	$-7.865 \times 10^7 \pm 0.66\%$	$2.852 \times 10^7 \pm 240\%$	$-8.079 \times 10^7 \pm 2.1\%$

APPENDIX C: ORIGIN OF ERROR BAR

We have seen in Sec. IV D that the contributions to the density have to be normalized by a factor η, see Eq. (60). To verify that the error bars on the density are not due to this normalization factor, we plot its relative error bars in Fig. 4. Blue dots denote the $\pm$ algorithm, orange stars the LO algorithm, and green dots the mixed algorithm. Comparing it to Fig. 1, we see that the relative error bars on η are much smaller than the ones on the density.

[1] R. M. Potok, I. G. Rau, H. Shtrikman, Y. Oreg, and D. Goldhaber-Gordon, Nature (London) **446**, 167 (2007).

[2] F. Nakamura, M. Sakaki, Y. Yamanaka, S. Tamaru, T. Suzuki, and Y. Maeno, Sci. Rep. **3**, 2536 (2013).

[3] D. Fausti, R. I. Tobey, N. Dean, S. Kaiser, A. Dienst, M. C. Hoffmann, S. Pyon, T. Takayama, H. Takagi, and A. Cavalleri, Science **331**, 189 (2011).

[4] D. Nicoletti, E. Casandruc, Y. Laplace, V. Khanna, C. R. Hunt, S. Kaiser, S. S. Dhesi, G. D. Gu, J. P. Hill, and A. Cavalleri, Phys. Rev. B **90**, 100503(R) (2014).

[5] E. Casandruc, D. Nicoletti, S. Rajasekaran, Y. Laplace, V. Khanna, G. D. Gu, J. P. Hill, and A. Cavalleri, Phys. Rev. B **91**, 174502 (2015).

[6] D. Nicoletti and A. Cavalleri, Adv. Opt. Photonics **8**, 401 (2016).

[7] D. Nicoletti, D. Fu, O. Mehio, S. Moore, A. S. Disa, G. D. Gu, and A. Cavalleri, Phys. Rev. Lett. **121**, 267003 (2018).

[8] A. Georges, G. Kotliar, W. Krauth, and M. J. Rozenberg, Rev. Mod. Phys. **68**, 13 (1996).

[9] G. Kotliar, S. Y. Savrasov, K. Haule, V. S. Oudovenko, O. Parcollet, and C. A. Marianetti, Rev. Mod. Phys. **78**, 865 (2006).

[10] H. Aoki, N. Tsuji, M. Eckstein, M. Kollar, T. Oka, and P. Werner, Rev. Mod. Phys. **86**, 779 (2014).

[11] A. N. Rubtsov and A. I. Lichtenstein, J. Exp. Theor. Phys. Lett. **80**, 61 (2004).

[12] A. N. Rubtsov, V. V. Savkin, and A. I. Lichtenstein, Phys. Rev. B **72**, 035122 (2005).

[13] E. Gull, P. Werner, O. Parcollet, and M. Troyer, Europhys. Lett. **82**, 57003 (2008).

[14] P. Werner, A. Comanac, L. de' Medici, M. Troyer, and A. J. Millis, Phys. Rev. Lett. **97**, 076405 (2006).

[15] P. Werner and A. J. Millis, Phys. Rev. B **74**, 155107 (2006).

[16] L. Mühlbacher and E. Rabani, Phys. Rev. Lett. **100**, 176403 (2008).

[17] P. Werner, T. Oka, and A. J. Millis, Phys. Rev. B **79**, 035320 (2009).

[18] P. Werner, T. Oka, M. Eckstein, and A. J. Millis, Phys. Rev. B **81**, 035108 (2010).

[19] M. Schiró and M. Fabrizio, Phys. Rev. B **79**, 153302 (2009).

[20] M. Schiró, Phys. Rev. B **81**, 085126 (2010).

[21] S. R. White, Phys. Rev. Lett. **69**, 2863 (1992).

[22] S. R. White, Phys. Rev. B **48**, 10345 (1993).

[23] U. Schollwöck, Rev. Mod. Phys. **77**, 259 (2005).

[24] G. Cohen, D. R. Reichman, A. J. Millis, and E. Gull, Phys. Rev. B **89**, 115139 (2014).
[25] G. Cohen, E. Gull, D. R. Reichman, and A. J. Millis, Phys. Rev. Lett. **112**, 146802 (2014).
[26] G. Cohen, E. Gull, D. R. Reichman, and A. J. Millis, Phys. Rev. Lett. **115**, 266802 (2015).
[27] H.-T. Chen, G. Cohen, and D. R. Reichman, J. Chem. Phys. **146**, 054105 (2017).
[28] H.-T. Chen, G. Cohen, and D. R. Reichman, J. Chem. Phys. **146**, 054106 (2017).
[29] A. E. Antipov, Q. Dong, J. Kleinhenz, G. Cohen, and E. Gull, Phys. Rev. B **95**, 085144 (2017).
[30] A. Boag, E. Gull, and G. Cohen, Phys. Rev. B **98**, 115152 (2018).
[31] R. E. V. Profumo, C. Groth, L. Messio, O. Parcollet, and X. Waintal, Phys. Rev. B **91**, 245154 (2015).
[32] C. Bertrand, O. Parcollet, A. Maillard, and X. Waintal, arXiv:1903.11636.
[33] C. Bertrand, S. Florens, O. Parcollet, and X. Waintal, arXiv:1903.11646.
[34] N. V. Prokof'ev and B. V. Svistunov, Phys. Rev. Lett. **81**, 2514 (1998).
[35] N. Prokof'ev and B. Svistunov, Phys. Rev. Lett. **99**, 250201 (2007).
[36] K. V. Houcke, E. Kozik, N. Prokof'ev, and B. Svistunov, Physics Procedia **6**, 95 (2010), computer Simulations Studies in Condensed Matter Physics XXI.
[37] E. Bourovski, N. Prokof'ev, and B. Svistunov, Phys. Rev. B **70**, 193101 (2004).
[38] R. Rossi, Phys. Rev. Lett. **119**, 045701 (2017).
[39] A. Moutenet, W. Wu, and M. Ferrero, Phys. Rev. B **97**, 085117 (2018).
[40] F. Simkovic IV. and E. Kozik, arXiv:1712.10001.
[41] J. Schwinger, J. Math. Phys. **2**, 407 (1961).
[42] L. V. Keldysh, Zh. Eksp. Teor. Fiz. **47**, 1515 (1965) [Sov. Phys. JETP **20**, 1018 (1965)].
[43] J. Rammer and H. Smith, Rev. Mod. Phys. **58**, 323 (1986).
[44] A. Kamenev and A. Levchenko, Adv. Phys. **58**, 197 (2009).
[45] A. Larkin and Y. Ovchinnikov, in *Nonequilibrium Superconductivity*, edited by D. Langenberg and A. Larkin (Elsevier, Amsterdam, 1986).
[46] G. Biroli and O. Parcollet, Phys. Rev. B **65**, 094414 (2002).
[47] N. Metropolis, A. W. Rosenbluth, M. N. Rosenbluth, A. H. Teller, and E. Teller, J. Chem. Phys. **21**, 1087 (1953).
[48] W. Wu, M. Ferrero, A. Georges, and E. Kozik, Phys. Rev. B **96**, 041105(R) (2017).
[49] R. Rossi, F. Werner, N. Prokof'ev, and B. Svistunov, Phys. Rev. B **93**, 161102(R) (2016).

Bibliography

[1] I.L. Aleiner, P.W. Brouwer, and L.I. Glazman. Quantum effects in Coulomb blockade. *Physics Reports*, 358(5):309 – 440, 2002.

[2] C. S. Alexander, G. Cao, V. Dobrosavljevic, S. McCall, J. E. Crow, E. Lochner, and R. P. Guertin. Destruction of the Mott insulating ground state of Ca_2RuO_4 by a structural transition. *Phys. Rev. B*, 60:R8422–R8425, Sep 1999.

[3] H. Alloul, T. Ohno, and P. Mendels. ^{89}Y NMR evidence for a Fermi-liquid behavior in $YBa_2Cu_3O_{6+x}$. *Phys. Rev. Lett.*, 63:1700–1703, Oct 1989.

[4] Frithjof B. Anders. Steady-State Currents through Nanodevices: A Scattering-States Numerical Renormalization-Group Approach to Open Quantum Systems. *Phys. Rev. Lett.*, 101:066804, Aug 2008.

[5] Frithjof B. Anders and Avraham Schiller. Real-Time Dynamics in Quantum-Impurity Systems: A Time-Dependent Numerical Renormalization-Group Approach. *Phys. Rev. Lett.*, 95:196801, Oct 2005.

[6] Frithjof B. Anders and Avraham Schiller. Spin precession and real-time dynamics in the Kondo model: Time-dependent numerical renormalization-group study. *Phys. Rev. B*, 74:245113, Dec 2006.

[7] P. W. Anderson. Localized Magnetic States in Metals. *Phys. Rev.*, 124:41–53, Oct 1961.

[8] P. W. Anderson. More Is Different. *Science*, 177(4047):393–396, 1972.

[9] Andrey E. Antipov, Qiaoyuan Dong, Joseph Kleinhenz, Guy Cohen, and Emanuel Gull. Currents and Green's functions of impurities out of equilibrium: Results from inchworm quantum Monte Carlo. *Phys. Rev. B*, 95:085144, Feb 2017.

[10] Hideo Aoki, Naoto Tsuji, Martin Eckstein, Marcus Kollar, Takashi Oka, and Philipp Werner. Nonequilibrium dynamical mean-field theory and its applications. *Rev. Mod. Phys.*, 86:779–837, Jun 2014.

[11] Camille Aron, Cedric Weber, and Gabriel Kotliar. Impurity model for non-equilibrium steady states. *Phys. Rev. B*, 87:125113, Mar 2013.

[12] Thomas Ayral and Olivier Parcollet. Mott physics and spin fluctuations: A unified framework. *Phys. Rev. B*, 92:115109, Sep 2015.

[13] Thomas Ayral and Olivier Parcollet. Mott physics and spin fluctuations: A functional viewpoint. *Phys. Rev. B*, 93:235124, Jun 2016.

[14] Corentin Bertrand, Serge Florens, Olivier Parcollet, and Xavier Waintal. Reconstructing Nonequilibrium Regimes of Quantum Many-Body Systems from the Analytical Structure of Perturbative Expansions. *Phys. Rev. X*, 9:041008, Oct 2019.

[15] Corentin Bertrand, Olivier Parcollet, Antoine Maillard, and Xavier Waintal. Quantum Monte Carlo algorithm for out-of-equilibrium Green's functions at long times. *Phys. Rev. B*, 100:125129, Sep 2019.

[16] N. E. Bickers. Review of techniques in the large-N expansion for dilute magnetic alloys. *Rev. Mod. Phys.*, 59:845–939, Oct 1987.

[17] N. E. Bickers, D. L. Cox, and J. W. Wilkins. Self-consistent large-N expansion for normal-state properties of dilute magnetic alloys. *Phys. Rev. B*, 36:2036–2079, Aug 1987.

[18] Giulio Biroli and Olivier Parcollet. Out-of-equilibrium dynamics of a quantum Heisenberg spin glass. *Phys. Rev. B*, 65:094414, Feb 2002.

[19] Andreas Björklund, Thore Husfeldt, Petteri Kaski, and Mikko Koivisto. Fourier Meets Möbius: Fast Subset Convolution. In *Proceedings of the Thirty-Ninth Annual ACM Symposium on Theory of Computing*, pages 67–74, New York, NY, USA, 2007. Association for Computing Machinery.

[20] R. Blankenbecler, D. J. Scalapino, and R. L. Sugar. Monte Carlo calculations of coupled boson-fermion systems. I. *Phys. Rev. D*, 24:2278–2286, Oct 1981.

[21] Aviel Boag, Emanuel Gull, and Guy Cohen. Inclusion-exclusion principle for many-body diagrammatics. *Phys. Rev. B*, 98:115152, Sep 2018.

[22] Evgueni Bourovski, Nikolay Prokof'ev, and Boris Svistunov. Truncated-determinant diagrammatic Monte Carlo for fermions with contact interaction. *Phys. Rev. B*, 70:193101, Nov 2004.

[23] M. Braden, G. André, S. Nakatsuji, and Y. Maeno. Crystal and magnetic structure of $\mathrm{Ca_2RuO_4}$: Magnetoelastic coupling and the metal-insulator transition. *Phys. Rev. B*, 58:847–861, Jul 1998.

[24] Véronique Brouet, Joseph Mansart, Luca Perfetti, Christian Piovera, Ivana Vobornik, Patrick Le Fèvre, Fran çois Bertran, Scott C. Riggs, M. C. Shapiro, Paula Giraldo-Gallo, and Ian R. Fisher. Transfer of spectral weight across the gap of $\mathrm{Sr_2IrO_4}$ induced by La doping. *Phys. Rev. B*, 92:081117, Aug 2015.

[25] Henrik Bruus and Karsten Flensberg. *Many-body quantum theory in condensed matter physics: an introduction*. Oxford University Press, 2004.

[26] R Bulla, A C Hewson, and Th Pruschke. Numerical renormalization group calculations for the self-energy of the impurity Anderson model. *Journal of Physics: Condensed Matter*, 10(37):8365–8380, sep 1998.

[27] R. Bulla, A.C. Hewson, and Th. Pruschke. Numerical renormalization group calculations for the self-energy of the impurity Anderson model. *Journal of Physics: Condensed Matter*, 10(37):8365, 1998.

[28] Ralf Bulla, Theo A. Costi, and Thomas Pruschke. Numerical renormalization group method for quantum impurity systems. *Rev. Mod. Phys.*, 80:395–450, Apr 2008.

[29] G. Cao, S. McCall, J. E. Crow, and R. P. Guertin. Observation of a Metallic Antiferromagnetic Phase and Metal to Nonmetal Transition in $\mathrm{Ca_3Ru_2}O_7$. *Phys. Rev. Lett.*, 78:1751–1754, Mar 1997.

[30] Jean-Michel Carter, Vijay Shankar V., and Hae-Young Kee. Theory of metal-insulator transition in the family of perovskite iridium oxides. *Phys. Rev. B*, 88:035111, Jul 2013.

[31] Jean-Michel Delisle Carter. *Interplay between spin-orbit coupling, electronic correlations and lattice distortions in perovskite iridates*. PhD thesis, University of Toronto, 2013.

[32] Hsing-Ta Chen, Guy Cohen, and David R. Reichman. Inchworm Monte Carlo for exact non-adiabatic dynamics. I. Theory and algorithms. *The Journal of Chemical Physics*, 146(5):054105, 2017.

[33] Hsing-Ta Chen, Guy Cohen, and David R. Reichman. Inchworm Monte Carlo for exact non-adiabatic dynamics. II. Benchmarks and comparison with established methods. *The Journal of Chemical Physics*, 146(5):054106, 2017.

[34] Xu Chen, Xiuyuan Cheng, and Stéphane Mallat. Unsupervised Deep Haar Scattering on Graphs. In *Proceedings of the 27th International Conference on Neural Information Processing Systems - Volume 1*, NIPS 14, pages 1709–1717, Cambridge, MA, USA, 2014. MIT Press.

[35] Guy Cohen, Emanuel Gull, David R. Reichman, and Andrew J. Millis. Green's Functions from Real-Time Bold-Line Monte Carlo Calculations: Spectral Properties of the Nonequilibrium Anderson Impurity Model. *Phys. Rev. Lett.*, 112:146802, Apr 2014.

[36] Guy Cohen, Emanuel Gull, David R. Reichman, and Andrew J. Millis. Taming the Dynamical Sign Problem in Real-Time Evolution of Quantum Many-Body Problems. *Phys. Rev. Lett.*, 115:266802, Dec 2015.

[37] Guy Cohen, David R. Reichman, Andrew J. Millis, and Emanuel Gull. Green's functions from real-time bold-line Monte Carlo. *Phys. Rev. B*, 89:115139, Mar 2014.

[38] Piers Coleman. New approach to the mixed-valence problem. *Phys. Rev. B*, 29:3035–3044, Mar 1984.

[39] M. K. Crawford, M. A. Subramanian, R. L. Harlow, J. A. Fernandez-Baca, Z. R. Wang, and D. C. Johnston. Structural and magnetic studies of Sr_2IrO_4. *Phys. Rev. B*, 49:9198–9201, Apr 1994.

[40] Sara M. Cronenwett, Tjerk H. Oosterkamp, and Leo P. Kouwenhoven. A Tunable Kondo Effect in Quantum Dots. *Science*, 281(5376):540–544, 1998.

[41] A. de la Torre, S. McKeown Walker, F. Y. Bruno, S. Riccó, Z. Wang, I. Gutierrez Lezama, G. Scheerer, G. Giriat, D. Jaccard, C. Berthod, T. K. Kim, M. Hoesch, E. C. Hunter, R. S. Perry, A. Tamai, and F. Baumberger. Collapse of the Mott Gap and Emergence of a Nodal Liquid in Lightly Doped Sr_2IrO_4. *Phys. Rev. Lett.*, 115:176402, Oct 2015.

[42] Luca de' Medici, Jernej Mravlje, and Antoine Georges. Janus-Faced Influence of Hund's Rule Coupling in Strongly Correlated Materials. *Phys. Rev. Lett.*, 107:256401, Dec 2011.

[43] Paul Adrien Maurice Dirac and Ralph Howard Fowler. Quantum mechanics of many-electron systems. *Proceedings of the Royal Society of London. Series A, Containing Papers of a Mathematical and Physical Character*, 123(792):714–733, 1929.

[44] Martin Eckstein, Marcus Kollar, and Philipp Werner. Thermalization after an Interaction Quench in the Hubbard Model. *Phys. Rev. Lett.*, 103:056403, Jul 2009.

[45] Martin Eckstein, Takashi Oka, and Philipp Werner. Dielectric Breakdown of Mott Insulators in Dynamical Mean-Field Theory. *Phys. Rev. Lett.*, 105:146404, Sep 2010.

[46] Martin Eckstein and Philipp Werner. Nonequilibrium dynamical mean-field calculations based on the noncrossing approximation and its generalizations. *Phys. Rev. B*, 82:115115, Sep 2010.

[47] Jack Edmonds. Paths, Trees, and Flowers. *Canadian Journal of Mathematics*, 17:449–467, 1965.

[48] Michel Ferrero, Pablo S. Cornaglia, Lorenzo De Leo, Olivier Parcollet, Gabriel Kotliar, and Antoine Georges. Pseudogap opening and formation of Fermi arcs as an orbital-selective Mott transition in momentum space. *Phys. Rev. B*, 80:064501, Aug 2009.

[49] Richard Phillips Feynman, Robert Benjamin Leighton, and Matthew Sands. *The Feynman lectures on physics; New millennium ed.* Basic Books, New York, NY, 2010. Originally published 1963-1965.

[50] O. Friedt, M. Braden, G. André, P. Adelmann, S. Nakatsuji, and Y. Maeno. Structural and magnetic aspects of the metal-insulator transition in $Ca_{2-x}Sr_xRuO_4$. *Phys. Rev. B*, 63:174432, Apr 2001.

[51] Tatsuya Fujii and Kazuo Ueda. Perturbative approach to the nonequilibrium Kondo effect in a quantum dot. *Phys. Rev. B*, 68:155310, Oct 2003.

[52] Harold N. Gabow. An Efficient Implementation of Edmonds' Algorithm for Maximum Matching on Graphs. *J. ACM*, 23(2):221–234, April 1976.

[53] Antoine Georges, Gabriel Kotliar, Werner Krauth, and Marcelo J. Rozenberg. Dynamical mean-field theory of strongly correlated fermion systems and the limit of infinite dimensions. *Rev. Mod. Phys.*, 68:13–125, Jan 1996.

[54] Antoine Georges, Luca de' Medici, and Jernej Mravlje. Strong Correlations from Hund's Coupling. *Annual Review of Condensed Matter Physics*, 4(1):137–178, 2013.

[55] Alexandru B. Georgescu, Oleg E. Peil, Ankit S. Disa, Antoine Georges, and Andrew J. Millis. Disentangling lattice and electronic contributions to the metal–insulator transition from bulk vs. layer confined $RNiO_3$. *Proceedings of the National Academy of Sciences*, 116(29):14434–14439, 2019.

[56] D. Goldhaber-Gordon, J. Göres, M. A. Kastner, Hadas Shtrikman, D. Mahalu, and U. Meirav. From the Kondo Regime to the Mixed-Valence Regime in a Single-Electron Transistor. *Phys. Rev. Lett.*, 81:5225–5228, Dec 1998.

[57] D. Goldhaber-Gordon, Hadas Shtrikman, D. Mahalu, David Abusch-Magder, U. Meirav, and M. A. Kastner. Kondo effect in a single-electron transistor. *Nature*, 391:156–159, 1998.

[58] E. Gorelov, M. Karolak, T. O. Wehling, F. Lechermann, A. I. Lichtenstein, and E. Pavarini. Nature of the Mott Transition in Ca_2RuO_4. *Phys. Rev. Lett.*, 104:226401, Jun 2010.

[59] N. Grewe and H. Keiter. Diagrammatic approach to the intermediate-valence compounds. *Phys. Rev. B*, 24:4420–4444, Oct 1981.

[60] Kent Griffin and Michael J. Tsatsomeros. Principal minors, Part I: A method for computing all the principal minors of a matrix. *Linear Algebra and its Applications*, 419(1):107 – 124, 2006.

[61] E. Gull, P. Werner, O. Parcollet, and M. Troyer. Continuous-time auxiliary-field Monte Carlo for quantum impurity models. *EPL (Europhysics Letters)*, 82(5):57003, 2008.

[62] Emanuel Gull, Andrew J. Millis, Alexander I. Lichtenstein, Alexey N. Rubtsov, Matthias Troyer, and Philipp Werner. Continuous-time Monte Carlo methods for quantum impurity models. *Rev. Mod. Phys.*, 83:349–404, May 2011.

[63] Emanuel Gull, Olivier Parcollet, and Andrew J. Millis. Superconductivity and the Pseudogap in the Two-Dimensional Hubbard Model. *Phys. Rev. Lett.*, 110:216405, May 2013.

[64] O. Gunnarsson, T. Schäfer, J. P. F. LeBlanc, E. Gull, J. Merino, G. Sangiovanni, G. Rohringer, and A. Toschi. Fluctuation Diagnostics of the Electron Self-Energy: Origin of the Pseudogap Physics. *Phys. Rev. Lett.*, 114:236402, Jun 2015.

[65] Hartmut Hafermann, Kelly R. Patton, and Philipp Werner. Improved estimators for the self-energy and vertex function in hybridization-expansion continuous-time quantum Monte Carlo simulations. *Phys. Rev. B*, 85:205106, May 2012.

[66] Hongxia Hao, Antoine Georges, Andrew J. Millis, Brenda Rubenstein, Qiang Han, and Hao Shi. Metal-Insulator and Magnetic Phase Diagram of Ca_2RuO_4 from Auxiliary Field Quantum Monte Carlo and Dynamical Mean Field Theory, 2019.

[67] W. K. Hastings. Monte Carlo sampling methods using Markov chains and their applications. *Biometrika*, 57(1):97–109, 04 1970.

[68] K. Hatsuda, T. Kimura, and Y. Tokura. Electric-field switching of orbital order in layered manganites. *Applied Physics Letters*, 83(16):3329–3331, 2003.

[69] K. Haule, S. Kirchner, J. Kroha, and P. Wölfle. Anderson impurity model at finite Coulomb interaction U: Generalized noncrossing approximation. *Phys. Rev. B*, 64:155111, Sep 2001.

[70] K. Haule and G. Kotliar. Coherence-incoherence crossover in the normal state of iron oxypnictides and importance of Hund's rule coupling. *New Journal of Physics*, 11(2):025021, feb 2009.

[71] M. H. Hettler, M. Mukherjee, M. Jarrell, and H. R. Krishnamurthy. Dynamical cluster approximation: Nonlocal dynamics of correlated electron systems. *Phys. Rev. B*, 61:12739–12756, May 2000.

[72] M. H. Hettler, A. N. Tahvildar-Zadeh, M. Jarrell, T. Pruschke, and H. R. Krishnamurthy. Nonlocal dynamical correlations of strongly interacting electron systems. *Phys. Rev. B*, 58:R7475–R7479, Sep 1998.

[73] Kris Van Houcke, Evgeny Kozik, N. Prokof'ev, and B. Svistunov. Diagrammatic Monte Carlo. *Physics Procedia*, 6(Supplement C):95 – 105, 2010. Computer Simulations Studies in Condensed Matter Physics XXI.

[74] Masatoshi Imada, Atsushi Fujimori, and Yoshinori Tokura. Metal-insulator transitions. *Rev. Mod. Phys.*, 70:1039–1263, Oct 1998.

[75] Y. Iwasa, T. Koda, Y. Tokura, S. Koshihara, N. Iwasawa, and G. Saito. Switching effect in organic charge transfer complex crystals. *Applied Physics Letters*, 55(20):2111–2113, 1989.

[76] Hosub Jin, Hogyun Jeong, Taisuke Ozaki, and Jaejun Yu. Anisotropic exchange interactions of spin-orbit-integrated states in Sr_2IrO_4. *Phys. Rev. B*, 80:075112, Aug 2009.

[77] Alex Kamenev and Alex Levchenko. Keldysh technique and non-linear σ-model: basic principles and applications. *Advances in Physics*, 58(3):197–319, 2009.

[78] Junjiro Kanamori. Electron Correlation and Ferromagnetism of Transition Metals. *Progress of Theoretical Physics*, 30(3):275–289, 09 1963.

[79] Teruo Kanki, Kenichi Kawatani, Hidefumi Takami, and Hidekazu Tanaka. Direct observation of giant metallic domain evolution driven by electric bias in VO_2 thin films on $TiO_2(001)$ substrate. *Applied Physics Letters*, 101(24):243118, 2012.

[80] A. A. Katanin, A. Toschi, and K. Held. Comparing pertinent effects of antiferromagnetic fluctuations in the two- and three-dimensional Hubbard model. *Phys. Rev. B*, 80:075104, Aug 2009.

[81] H. Keiter and J. C. Kimball. Diagrammatic Approach to the Anderson Model for Dilute Alloys. *Journal of Applied Physics*, 42(4):1460–1461, 1971.

[82] L. V. Keldysh. Diagram technique for nonequilibrium processes. *Zh. Eksp. Teor. Fiz.*, 47:1515–1527, 1964. [Sov. Phys. JETP20,1018(1965)].

[83] B. J. Kim, Hosub Jin, S. J. Moon, J.-Y. Kim, B.-G. Park, C. S. Leem, Jaejun Yu, T. W. Noh, C. Kim, S.-J. Oh, J.-H. Park, V. Durairaj, G. Cao, and E. Rotenberg. Novel $J_{\rm eff} = 1/2$ Mott State Induced by Relativistic Spin-Orbit Coupling in $\mathrm{Sr_2IrO_4}$. *Phys. Rev. Lett.*, 101:076402, Aug 2008.

[84] Jungho Kim, D. Casa, M. H. Upton, T. Gog, Young-June Kim, J. F. Mitchell, M. van Veenendaal, M. Daghofer, J. van den Brink, G. Khaliullin, and B. J. Kim. Magnetic Excitation Spectra of $\mathrm{Sr_2IrO_4}$ Probed by Resonant Inelastic X-Ray Scattering: Establishing Links to Cuprate Superconductors. *Phys. Rev. Lett.*, 108:177003, Apr 2012.

[85] Y. K. Kim, O. Krupin, J. D. Denlinger, A. Bostwick, E. Rotenberg, Q. Zhao, J. F. Mitchell, J. W. Allen, and B. J. Kim. Fermi arcs in a doped pseudospin-1/2 Heisenberg antiferromagnet. *Science*, 345(6193):187–190, 2014.

[86] G. Kotliar, S. Y. Savrasov, K. Haule, V. S. Oudovenko, O. Parcollet, and C. A. Marianetti. Electronic structure calculations with dynamical mean-field theory. *Rev. Mod. Phys.*, 78:865–951, Aug 2006.

[87] Gabriel Kotliar, Sergej Y. Savrasov, Gunnar Pálsson, and Giulio Biroli. Cellular Dynamical Mean Field Approach to Strongly Correlated Systems. *Phys. Rev. Lett.*, 87:186401, Oct 2001.

[88] E. Kozik, K. Van Houcke, E. Gull, L. Pollet, N. Prokof'ev, B. Svistunov, and M. Troyer. Diagrammatic Monte Carlo for correlated fermions. *EPL (Europhysics Letters)*, 90(1):10004, 2010.

[89] Werner Krauth. *Statistical mechanics: Algorithms and computations*. Oxford University Press, 2006.

[90] Y. Kuramoto. Self-consistent perturbation theory for dynamics of valence fluctuations. *Zeitschrift für Physik B Condensed Matter*, 53:37–52, 1983.

[91] David P. Landau and Kurt Binder. *A Guide to Monte Carlo Simulations in Statistical Physics*. Cambridge University Press, 4 edition, 2014.

[92] A.I. Larkin and Yu.N. Ovchinnikov. Vortex motion in Superconductors. In D.N. Langenberg and A.I. Larkin, editors, *Nonequilibrium Superconductivity*. Elsevier, 1986.

[93] J. P. F. LeBlanc, Andrey E. Antipov, Federico Becca, Ireneusz W. Bulik, Garnet Kin-Lic Chan, Chia-Min Chung, Youjin Deng, Michel Ferrero, Thomas M. Henderson, Carlos A. Jiménez-Hoyos, E. Kozik, Xuan-Wen Liu, Andrew J. Millis, N. V. Prokof'ev, Mingpu Qin, Gustavo E. Scuseria, Hao Shi, B. V. Svistunov, Luca F. Tocchio, I. S. Tupitsyn, Steven R. White, Shiwei Zhang, Bo-Xiao Zheng, Zhenyue Zhu, and Emanuel Gull. Solutions of the Two-Dimensional Hubbard Model: Benchmarks and Results from a Wide Range of Numerical Algorithms. *Phys. Rev. X*, 5:041041, Dec 2015.

[94] B Lenz, C Martins, and S Biermann. Spectral functions of $\mathrm{Sr_2IrO_4}$: theory versus experiment. *Journal of Physics: Condensed Matter*, 31(29):293001, may 2019.

[95] Jiajun Li, Camille Aron, Gabriel Kotliar, and Jong E. Han. Electric-Field-Driven Resistive Switching in the Dissipative Hubbard Model. *Phys. Rev. Lett.*, 114:226403, Jun 2015.

[96] A. I. Lichtenstein and M. I. Katsnelson. Antiferromagnetism and d-wave superconductivity in cuprates: A cluster dynamical mean-field theory. *Phys. Rev. B*, 62:R9283–R9286, Oct 2000.

[97] Daniel Loss and David P. DiVincenzo. Quantum computation with quantum dots. *Phys. Rev. A*, 57:120–126, Jan 1998.

[98] Y. Maeno, H. Hashimoto, K. Yoshida, S. Nishizaki, T. Fujita, J. G. Bednorz, and F. Lichtenberg. Superconductivity in a layered perovskite without copper. *Nature*, 372:532–534, Dec 1994.

[99] Thomas Maier, Mark Jarrell, Thomas Pruschke, and Matthias H. Hettler. Quantum cluster theories. *Rev. Mod. Phys.*, 77:1027–1080, Oct 2005.

[100] Cyril Martins, Markus Aichhorn, Loïg Vaugier, and Silke Biermann. Reduced Effective Spin-Orbital Degeneracy and Spin-Orbital Ordering in Paramagnetic Transition-Metal Oxides: $\mathrm{Sr_2IrO_4}$ versus $\mathrm{Sr_2RhO_4}$. *Phys. Rev. Lett.*, 107:266404, Dec 2011.

[101] Cyril Martins, Benjamin Lenz, Luca Perfetti, Veronique Brouet, François Bertran, and Silke Biermann. Nonlocal Coulomb correlations in pure and electron-doped $\mathrm{Sr_2IrO_4}$: Spectral functions, Fermi surface, and pseudo-gap-like spectral weight distributions from oriented cluster dynamical mean-field theory. *Phys. Rev. Materials*, 2:032001, Mar 2018.

[102] Anne Matthies, Jiajun Li, and Martin Eckstein. Control of competing superconductivity and charge order by nonequilibrium currents. *Phys. Rev. B*, 98:180502, Nov 2018.

[103] Giordano Mattoni, Shingo Yonezawa, and Yoshiteru Maeno. Diamagnetic-like response from localised heating of a paramagnetic material, 2020.

[104] Marjan Maček, Philipp T. Dumitrescu, Corentin Bertrand, Bill Triggs, Olivier Parcollet, and Xavier Waintal. Quantum Quasi-Monte Carlo, 2020.

[105] G. I. Meijer. Who Wins the Nonvolatile Memory Race? *Science*, 319(5870):1625–1626, 2008.

[106] Yigal Meir and Ned S. Wingreen. Landauer formula for the current through an interacting electron region. *Phys. Rev. Lett.*, 68:2512–2515, Apr 1992.

[107] Nicholas Metropolis, Arianna W. Rosenbluth, Marshall N. Rosenbluth, Augusta H. Teller, and Edward Teller. Equation of State Calculations by Fast Computing Machines. *The Journal of Chemical Physics*, 21(6):1087–1092, 1953.

[108] Alice Moutenet, Antoine Georges, and Michel Ferrero. Pseudogap and electronic structure of electron-doped $\mathrm{Sr_2IrO_4}$. *Phys. Rev. B*, 97:155109, Apr 2018.

[109] Alice Moutenet, Priyanka Seth, Michel Ferrero, and Olivier Parcollet. Cancellation of vacuum diagrams and the long-time limit in out-of-equilibrium diagrammatic quantum Monte Carlo. *Phys. Rev. B*, 100:085125, Aug 2019.

[110] Alice Moutenet, Wei Wu, and Michel Ferrero. Determinant Monte Carlo algorithms for dynamical quantities in fermionic systems. *Phys. Rev. B*, 97:085117, Feb 2018.

[111] Jernej Mravlje, Markus Aichhorn, Takashi Miyake, Kristjan Haule, Gabriel Kotliar, and Antoine Georges. Coherence-Incoherence Crossover and the Mass-Renormalization Puzzles in $\mathrm{Sr_2RuO_4}$. *Phys. Rev. Lett.*, 106:096401, Mar 2011.

[112] Lothar Mühlbacher and Eran Rabani. Real-Time Path Integral Approach to Nonequilibrium Many-Body Quantum Systems. *Phys. Rev. Lett.*, 100:176403, May 2008.

[113] E Müller-Hartmann. Self-consistent perturbation theory of the Anderson model: Ground state properties. *Zeitschrift für Physik B Condensed Matter*, 57:281–287, 1984.

[114] Fumihiko Nakamura, Tatsuo Goko, Masakazu Ito, Toshizo Fujita, Satoru Nakatsuji, Hideto Fukazawa, Yoshiteru Maeno, Patricia Alireza, Dominic Forsythe, and Stephen R. Julian. From Mott insulator to ferromagnetic metal: A pressure study of $\mathrm{Ca_2RuO_4}$. *Phys. Rev. B*, 65:220402, May 2002.

[115] Fumihiko Nakamura, Mariko Sakaki, Yuya Yamanaka, Sho Tamaru, Takashi Suzuki, and Yoshiteru Maeno. Electric-field-induced metal maintained by current of the Mott insulator $\mathrm{Ca_2RuO_4}$. *Scientific Reports*, 3:2536, 2013.

[116] S. Nakatsuji and Y. Maeno. Quasi-Two-Dimensional Mott Transition System $\mathrm{Ca_{2-x}Sr_xRuO_4}$. *Phys. Rev. Lett.*, 84:2666–2669, Mar 2000.

[117] S. Nakatsuji and Y. Maeno. Switching of magnetic coupling by a structural symmetry change near the Mott transition in $\mathrm{Ca_{2-x}Sr_xRuO_4}$. *Phys. Rev. B*, 62:6458–6466, Sep 2000.

[118] Satoru Nakatsuji, Shin-ichi Ikeda, and Yoshiteru Maeno. $\mathrm{Ca_2RuO_4}$: New Mott Insulators of Layered Ruthenate. *Journal of the Physical Society of Japan*, 66(7):1868–1871, 1997.

[119] John W. Negele and Henri Orland. *Quantum Many-Particle Systems*. Calif: Addison-Wesley Pub. Co., 1988.

[120] John Nichols, Noah Bray-Ali, Armin Ansary, Gang Cao, and Kwok-Wai Ng. Tunneling into the Mott insulator $\mathrm{Sr_2IrO_4}$. *Phys. Rev. B*, 89:085125, Feb 2014.

[121] M. R. Norman, D. Pines, and C. Kallin. The pseudogap: friend or foe of high T_c? *Advances in Physics*, 54(8):715–733, 2005.

[122] Ryuji Okazaki, Yasuo Nishina, Yukio Yasui, Fumihiko Nakamura, Takashi Suzuki, and Ichiro Terasaki. Current-Induced Gap Suppression in the Mott Insulator $\mathrm{Ca_2RuO_4}$. *Journal of the Physical Society of Japan*, 82(10):103702, 2013.

[123] Olivier Parcollet, Michel Ferrero, Thomas Ayral, Hartmut Hafermann, Igor Krivenko, Laura Messio, and Priyanka Seth. TRIQS: A toolbox for research on interacting quantum systems. *Computer Physics Communications*, 196(Supplement C):398 – 415, 2015.

[124] Oleg E. Peil, Alexander Hampel, Claude Ederer, and Antoine Georges. Mechanism and control parameters of the coupled structural and metal-insulator transition in nickelates. *Phys. Rev. B*, 99:245127, Jun 2019.

[125] Francesco Peronaci, Marco Schiró, and Olivier Parcollet. Resonant Thermalization of Periodically Driven Strongly Correlated Electrons. *Phys. Rev. Lett.*, 120:197601, May 2018.

[126] Francesco Petocchi, Sophie Beck, Claude Ederer, and Philipp Werner. Hund excitations and the efficiency of Mott solar cells. *Phys. Rev. B*, 100:075147, Aug 2019.

[127] John Preskill. Quantum Computing in the NISQ era and beyond. *Quantum*, 2:79, August 2018.

[128] Rosario E. V. Profumo, Christoph Groth, Laura Messio, Olivier Parcollet, and Xavier Waintal. Quantum Monte Carlo for correlated out-of-equilibrium nanoelectronic devices. *Phys. Rev. B*, 91:245154, Jun 2015.

[129] Nikolai V. Prokof'ev and Boris V. Svistunov. Polaron Problem by Diagrammatic Quantum Monte Carlo. *Phys. Rev. Lett.*, 81:2514–2517, Sep 1998.

[130] Nikolay Prokof'ev and Boris Svistunov. Bold Diagrammatic Monte Carlo Technique: When the Sign Problem Is Welcome. *Phys. Rev. Lett.*, 99:250201, Dec 2007.

[131] Th. Pruschke and N. Grewe. The Anderson model with finite Coulomb repulsion. *Zeitschrift für Physik B Condensed Matter*, 74:439–449, 1989.

[132] J. Rammer and H. Smith. Quantum field-theoretical methods in transport theory of metals. *Rev. Mod. Phys.*, 58:323–359, Apr 1986.

[133] John J. Randall, Lewis Katz, and Roland Ward. The Preparation of a Strontium-Iridium Oxide Sr2IrO41,2. *Journal of the American Chemical Society*, 79(2):266–267, 1957.

[134] R. Rossi, N. Prokof'ev, B. Svistunov, K. Van Houcke, and F. Werner. Polynomial complexity despite the fermionic sign. *EPL (Europhysics Letters)*, 118(1):10004, 2017.

[135] Riccardo Rossi. Determinant Diagrammatic Monte Carlo Algorithm in the Thermodynamic Limit. *Phys. Rev. Lett.*, 119:045701, Jul 2017.

[136] Riccardo Rossi, Fedor Šimkovic, and Michel Ferrero. Renormalized perturbation theory at large expansion orders, 2020.

[137] Riccardo Rossi, Félix Werner, Nikolay Prokof'ev, and Boris Svistunov. Shifted-action expansion and applicability of dressed diagrammatic schemes. *Phys. Rev. B*, 93:161102(R), Apr 2016.

[138] K. Rossnagel and N. V. Smith. Spin-orbit coupling in the band structure of reconstructed $1T-\mathrm{TaS}_2$. *Phys. Rev. B*, 73:073106, Feb 2006.

[139] A. N. Rubtsov and A. I. Lichtenstein. Continuous-time quantum Monte Carlo method for fermions: Beyond auxiliary field framework. *Journal of Experimental and Theoretical Physics Letters*, 80(1):61–65, Jul 2004.

[140] A. N. Rubtsov, V. V. Savkin, and A. I. Lichtenstein. Continuous-time quantum Monte Carlo method for fermions. *Phys. Rev. B*, 72:035122, Jul 2005.

[141] Andreas Rüegg, Emanuel Gull, Gregory A. Fiete, and Andrew J. Millis. Sum rule violation in self-consistent hybridization expansions. *Phys. Rev. B*, 87:075124, Feb 2013.

[142] Mariko Sakaki, Nobuo Nakajima, Fumihiko Nakamura, Yasuhisa Tezuka, and Takashi Suzuki. Electric-Field-Induced Insulator-Metal Transition in Ca_2RuO_4 Probed by X-ray Absorption and Emission Spectroscopy. *Journal of the Physical Society of Japan*, 82(9):093707, 2013.

[143] Thomas Schäfer, Nils Wentzell, Fedor Šimkovic IV, Yuan-Yao He, Cornelia Hille, Marcel Klett, Christian J. Eckhardt, Behnam Arzhang, Viktor Harkov, François-Marie Le Régent, Alfred Kirsch, Yan Wang, Aaram J. Kim, Evgeny Kozik, Evgeny A. Stepanov, Anna Kauch, Sabine Andergassen, Philipp Hansmann, Daniel Rohe, Yuri M. Vilk, James P. F. LeBlanc, Shiwei Zhang, A. M. S. Tremblay, Michel Ferrero, Olivier Parcollet, and Antoine Georges. Tracking the Footprints of Spin Fluctuations: A Multi-Method, Multi-Messenger Study of the Two-Dimensional Hubbard Model, 2020.

[144] Marco Schiró and Michele Fabrizio. Real-time diagrammatic Monte Carlo for nonequilibrium quantum transport. *Phys. Rev. B*, 79:153302, Apr 2009.

[145] Jörg Schmid, Jürgen Weis, Karl Eberl, and Klaus [v. Klitzing]. A quantum dot in the limit of strong coupling to reservoirs. *Physica B: Condensed Matter*, 256-258:182 – 185, 1998.

[146] U. Schollwoeck and S. R. White. Methods for Time Dependence in DMRG, 2006.

[147] Julian Schwinger. Brownian Motion of a Quantum Oscillator. *Journal of Mathematical Physics*, 2(3):407–432, 1961.

[148] Priyanka Seth, Igor Krivenko, Michel Ferrero, and Olivier Parcollet. TRIQS/CTHYB: A continuous-time quantum Monte Carlo hybridisation expansion solver for quantum impurity problems. *Computer Physics Communications*, 200:274 – 284, 2016.

[149] Kyle M. Shen, F. Ronning, D. H. Lu, F. Baumberger, N. J. C. Ingle, W. S. Lee, W. Meevasana, Y. Kohsaka, M. Azuma, M. Takano, H. Takagi, and Z.-X. Shen. Nodal Quasiparticles and Antinodal Charge Ordering in $Ca_{2-x}Na_xCuO_2Cl_2$. *Science*, 307(5711):901–904, 2005.

[150] Hao Shi and Shiwei Zhang. Symmetry in auxiliary-field quantum Monte Carlo calculations. *Phys. Rev. B*, 88:125132, Sep 2013.

[151] Hao Shi and Shiwei Zhang. Infinite variance in fermion quantum Monte Carlo calculations. *Phys. Rev. E*, 93:033303, Mar 2016.

[152] D. J. Singh, P. Blaha, K. Schwarz, and J. O. Sofo. Electronic structure of the pyrochlore metals $Cd_2Os_2O_7$ and $Cd_2Re_2O_7$. *Phys. Rev. B*, 65:155109, Mar 2002.

[153] G. Stefanucci and R. van Leeuwen. *Nonequilibrium Many-Body Theory of Quantum Systems: A Modern Introduction*. Cambridge University Press, 2013.

[154] P. Steffens, O. Friedt, P. Alireza, W. G. Marshall, W. Schmidt, F. Nakamura, S. Nakatsuji, Y. Maeno, R. Lengsdorf, M. M. Abd-Elmeguid, and M. Braden. High-pressure diffraction studies on Ca_2RuO_4. *Phys. Rev. B*, 72:094104, Sep 2005.

[155] D. Sutter, C. G. Fatuzzo, S. Moser, M. Kim, R. Fittipaldi, A. Vecchione, V. Granata, Y. Sassa, F. Cossalter, G. Gatti, M. Grioni, H. M. Ronnow, N. C. Plumb, C. E. Matt, M. Shi, M. Hoesch, T. K. Kim, T-R Chang, H-T Jeng, C. Jozwiak, A. Bostwick, E. Rotenberg, A. Georges, T. Neupert, and J. Chang. Hallmarks of Hund's coupling in the Mott insulator Ca_2RuO_4. *Nature Communications*, 8:15176, May 2017.

[156] Y. Taguchi, T. Matsumoto, and Y. Tokura. Dielectric breakdown of one-dimensional Mott insulators Sr_2CuO_3 and $SrCuO_2$. *Phys. Rev. B*, 62:7015–7018, Sep 2000.

[157] Amir Taheridehkordi, S. H. Curnoe, and J. P. F. LeBlanc. Optimal grouping of arbitrary diagrammatic expansions via analytic pole structure. *Phys. Rev. B*, 101:125109, Mar 2020.

[158] K. Terashima, M. Sunagawa, H. Fujiwara, T. Fukura, M. Fujii, K. Okada, K. Horigane, K. Kobayashi, R. Horie, J. Akimitsu, E. Golias, D. Marchenko, A. Varykhalov, N. L. Saini, T. Wakita, Y. Muraoka, and T. Yokoya. Evolution of the remnant Fermi-surface state in the lightly doped correlated spin-orbit insulator $Sr_{2-x}La_xIrO_4$. *Phys. Rev. B*, 96:041106, Jul 2017.

[159] A. Toschi, A. A. Katanin, and K. Held. Dynamical vertex approximation: A step beyond dynamical mean-field theory. *Phys. Rev. B*, 75:045118, Jan 2007.

[160] Matthias Troyer and Uwe-Jens Wiese. Computational Complexity and Fundamental Limitations to Fermionic Quantum Monte Carlo Simulations. *Phys. Rev. Lett.*, 94:170201, May 2005.

[161] Naoto Tsuji, Takashi Oka, Philipp Werner, and Hideo Aoki. Dynamical Band Flipping in Fermionic Lattice Systems: An ac-Field-Driven Change of the Interaction from Repulsive to Attractive. *Phys. Rev. Lett.*, 106:236401, Jun 2011.

[162] D. van der Marel and G. A. Sawatzky. Electron-electron interaction and localization in d and f transition metals. *Phys. Rev. B*, 37:10674–10684, Jun 1988.

[163] Dirk van der Marel. *The electronic structure of embedded transition metal atoms*. PhD thesis, University of Groningen, 1985.

[164] F. Verstraete and J. I. Cirac. Renormalization algorithms for Quantum-Many Body Systems in two and higher dimensions, 2004.

[165] F. Verstraete, V. Murg, and J.I. Cirac. Matrix product states, projected entangled pair states, and variational renormalization group methods for quantum spin systems. *Advances in Physics*, 57(2):143–224, 2008.

[166] H. J. Vidberg and J. W. Serene. Solving the Eliashberg equations by means of N-point Padé approximants. *J. Low Temp. Phys.*, 29:179–192, 1977.

[167] T. Vogt and D.J. Buttrey. Temperature Dependent Structural Behavior of Sr_2RhO_4. *Journal of Solid State Chemistry*, 123(1):186 – 189, 1996.

[168] Fedor Šimkovic and Evgeny Kozik. Determinant Monte Carlo for irreducible Feynman diagrams in the strongly correlated regime. *Phys. Rev. B*, 100:121102, Sep 2019.

[169] Rainer Waser and Masakazu Aono. Nanoionics-based resistive switching memories. *Nature Materials*, 6:833–840, 2007.

[170] Hiroshi Watanabe, Tomonori Shirakawa, and Seiji Yunoki. Microscopic Study of a Spin-Orbit-Induced Mott Insulator in Ir Oxides. *Phys. Rev. Lett.*, 105:216410, Nov 2010.

[171] Philipp Werner, Armin Comanac, Luca de' Medici, Matthias Troyer, and Andrew J. Millis. Continuous-Time Solver for Quantum Impurity Models. *Phys. Rev. Lett.*, 97:076405, Aug 2006.

[172] Philipp Werner, Emanuel Gull, Matthias Troyer, and Andrew J. Millis. Spin Freezing Transition and Non-Fermi-Liquid Self-Energy in a Three-Orbital Model. *Phys. Rev. Lett.*, 101:166405, Oct 2008.

[173] Philipp Werner and Andrew J. Millis. Hybridization expansion impurity solver: General formulation and application to Kondo lattice and two-orbital models. *Phys. Rev. B*, 74:155107, Oct 2006.

[174] Philipp Werner, Takashi Oka, Martin Eckstein, and Andrew J. Millis. Weak-coupling quantum Monte Carlo calculations on the Keldysh contour: Theory and application to the current-voltage characteristics of the Anderson model. *Phys. Rev. B*, 81:035108, Jan 2010.

[175] Philipp Werner, Takashi Oka, and Andrew J. Millis. Diagrammatic Monte Carlo simulation of nonequilibrium systems. *Phys. Rev. B*, 79:035320, Jan 2009.

[176] Steven R. White. Density matrix formulation for quantum renormalization groups. *Phys. Rev. Lett.*, 69:2863–2866, Nov 1992.

[177] Steven R. White. Density-matrix algorithms for quantum renormalization groups. *Phys. Rev. B*, 48:10345–10356, Oct 1993.

[178] G. C. Wick. The Evaluation of the Collision Matrix. *Phys. Rev.*, 80:268–272, Oct 1950.

[179] Alexander Wietek and Andreas M. Läuchli. Sublattice coding algorithm and distributed memory parallelization for large-scale exact diagonalizations of quantum many-body systems. *Phys. Rev. E*, 98:033309, Sep 2018.

[180] Kenneth G. Wilson. The renormalization group: Critical phenomena and the Kondo problem. *Rev. Mod. Phys.*, 47:773–840, Oct 1975.

[181] Ned S. Wingreen and Yigal Meir. Anderson model out of equilibrium: Noncrossing-approximation approach to transport through a quantum dot. *Phys. Rev. B*, 49:11040–11052, Apr 1994.

[182] D. Wolf. Simplified version of the cuprate superconductor phase diagram.

[183] Wei Wu, Michel Ferrero, Antoine Georges, and Evgeny Kozik. Controlling Feynman diagrammatic expansions: Physical nature of the pseudogap in the two-dimensional Hubbard model. *Phys. Rev. B*, 96:041105(R), Jul 2017.

[184] H. J. Xiang and M.-H. Whangbo. Cooperative effect of electron correlation and spin-orbit coupling on the electronic and magnetic properties of Ba_2NaOsO_6. *Phys. Rev. B*, 75:052407, Feb 2007.

[185] S. Yamanouchi, Y. Taguchi, and Y. Tokura. Dielectric Breakdown of the Insulating Charge-Ordered State in $La_{2-x}Sr_xNiO_4$. *Phys. Rev. Lett.*, 83:5555–5558, Dec 1999.

[186] Z. P. Yin, K. Haule, and G. Kotliar. Kinetic frustration and the nature of the magnetic and paramagnetic states in iron pnictides and iron chalcogenides. *Nature Materials*, 10:932–935, 2011.

[187] Hongbin Zhang, Kristjan Haule, and David Vanderbilt. Effective $J{=}1/2$ Insulating State in Ruddlesden-Popper Iridates: An LDA+DMFT Study. *Phys. Rev. Lett.*, 111:246402, Dec 2013.

[188] Shiwei Zhang. *Auxiliary-Field Quantum Monte Carlo for Correlated Electron Systems*, chapter 15. Verlag des Forschungszentrum Jülich, 2013.

[189] Manuel Zingl, Jernej Mravlje, Markus Aichhorn, Olivier Parcollet, and Antoine Georges. Hall coefficient signals orbital differentiation in the Hund's metal Sr_2RuO_4. *NPJ Quantum Materials*, 4:2397–4648, Jul 2019.

Titre : Nouveaux algorithmes pour l'étude des propriétés d'équilibre et hors d'équilibre des systèmes quantiques fortement corrélés

Mots clés : Physique - Matière condensée - Problème à N corps - Systèmes fortement corrélés - Algorithmes

Résumé : Quel est le point commun entre les étoiles formant une galaxie, les gouttes d'eau s'écoulant dans une rivière, et les électrons d'une céramique supraconductrice lévitant au-dessus d'un aimant ? Tous ces systèmes ne peuvent être décrits par le mouvement isolé d'une seule de leurs composantes. C'est l'ensemble des particules et de leurs interactions qui fait émerger leurs singulières propriétés : on parle du problème à N corps. Dans cette Thèse, nous nous intéressons aux propriétés des systèmes d'électrons fortement corrélés, dont la physique est gouvernée par les principes de la mécanique quantique. Les méthodes analytiques étant rapidement limitées, nous développons de nouvelles approches numériques afin de quantifier précisément les propriétés de matériaux dans lesquels les interactions entre particules deviennent importantes.
Nous nous intéressons tout d'abord aux propriétés d'équilibre de la pérovskite Sr_2IrO_4, un matériau structurellement équivalent au cuprate supraconducteur La_2CuO_4. Nous mettons en évidence l'existence d'un pseudogap et décrivons la structure électronique de ce matériau en fonction du dopage. Nous développons ensuite des extensions aux algorithmes de Monte Carlo déterminantaux pour l'étude de quantités dynamiques comme l'énergie propre, et nous montrons qu'il est possible de regrouper un nombre factoriel de diagrammes en une somme de déterminants, réduisant ainsi fortement le problème de signe fermionique.
Dans un deuxième temps, nous décrivons les systèmes fortement corrélés hors d'équilibre. Nous commençons par revisiter le Monte Carlo diagrammatique en temps réel dans une nouvelle base qui permet aux diagrammes du vide de s'annuler directement. Au cours d'un échantillonnage statistique, ceci permet d'atteindre la limite de long temps nécessaire à l'étude des états stationnaires des systèmes hors d'équilibre. Pour terminer, nous étudions la transition métal-isolant induite par un champ électrique de Ca_2RuO_4, qui coexiste avec une transition structurelle. Un algorithme basé sur l'approximation sans croisement nous permettent de calculer le courant en fonction du champ crystallin dans ce matériau.

Title: Novel algorithms for strongly correlated quantum systems in and out of equilibrium

Keywords: Physics - Condensed matter - Many-body problem - Strongly correlated systems - Algorithms

Abstract: What do stars in a galaxy, drops in a river, and electrons in a superconducting cuprate levitating above a magnet all have in common? All of these systems cannot be described by the isolated motion of one of their parts. These singular properties emerge from particles and their interactions as a whole: we talk about the *many-body problem*. In this Thesis, we focus on properties of strongly-correlated systems, that obey quantum mechanics. Analytical methods being rapidly limited in their understanding of these materials, we develop novel numerical techniques to precisely quantify their properties when interactions between particles become strong.
First, we focus on the equilibrium properties of the layered perovskite Sr_2IrO_4, a compound isostructural to the superconducting cuprate La_2CuO_4, where we prove the existence of a pseudogap and describe the electronic structure of this material upon doping. Then, in order to address the thermodynamic limit of lattice problems, we develop extensions of determinant Monte Carlo algorithms to compute dynamical quantities such as the self-energy. We show how a factorial number of diagrams can be regrouped in a sum of determinants, hence drastically reducing the fermionic sign problem.
In the second part, we turn to the description of nonequilibrium phenomena in correlated systems. We start by revisiting the real-time diagrammatic Monte Carlo recent advances in a new basis where all vacuum diagrams directly vanish. In an importance sampling procedure, such an algorithm can directly address the long-time limit needed in the study of steady states in out-of-equilibrium systems. Finally, we study the insulator-to-metal transition induced by an electric field in Ca_2RuO_4, which coexists with a structural transition. An algorithm based on the non-crossing approximation allows us to compute the current as a function of crystal-field splitting in this material.

Institut Polytechnique de Paris
91120 Palaiseau, France